Non-linear gravitational collapse in extended gravity theories

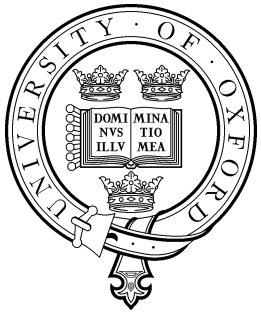

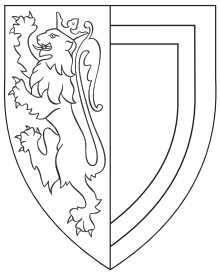

Francesca von Braun-Bates

Balliol College

University of Oxford

A thesis submitted for the degree of

Doctor of Philosophy

Trinity 2017

Acknowledgements

In 2001, Nadia Weiner Bloom (Lady Margaret Hall) suggested I might be "Oxbridge material"; a suggestion I dismissed as rapidly as one would dismiss the notion that the Earth is the centre of the Universe. In 2012, however, that suggestion became a reality when I began my Oxbridge journey at Balliol College.

While the ideas expressed in this Thesis are my own, the spine which binds it is the support from family and friends and collaboration with my colleagues, especially my amazing Supervisors. To Prof. Pedro Ferreira *muito obrigada* and to A/Prof. Julien Devriendt *merci beaucoup*! It was a long, winding but an unforgettable journey! Heartfelt thanks to my collaborators: Dr. Johannes Noller, Dr. Hans Winther and Dr. David Alonso.

To my fellow Balliolites: Ben *grātiās vōbīs agō* for the walks and the coffees; to Sam, Ashley, Hilary, Toli, Bernardo and Dr. Dave: thank you for looking out for me at Holywell. Nina and Yin, my "besties" in Centre Wing, I hope we shall always be friends. I shall miss my "Astro Group", Ricarda's birthday parties and my office mates in Room 650 in the DWB especially Becky, Laura and Ellen.

It was always a treat to catch up with visitors from Sydney and Dublin. Thank you to my Aunt Kerry for the lovely cards filled with encouragement and to the Nielsons for the Easter feast and giant chocolate rabbit.

Words cannot express my gratitude to my guardian angels at Holywell: the men of the "Night's Watch" Rob and Mark, the irreplacable Mark Howe, my mini-Mum Pauline, Brian and Amani: heartfelt thanks for your kindness and friendship to myself and my family. Special thanks to the Praefectus, Prof. Tom Melham, whose generosity to both myself and my family could never be repaid. Thank you also Sir Drummond, Katie S., Helen Young, Garret and Ashling for your assistance during my time in Oxford.

There are three people who deserve a special thank you for fostering my love of Physics. Tibor Molnar, Rowena Danziger A.M. and last but by no means least, John Trimble, my indefatigable Physics teacher at Ascham School. "Dr. Bruce" and "McKinnon" guided me through the Cosmology Distinction Course. I am grateful to Anne and Terrey Arcus A.M. for their gift of the Arcus Travelling Scholarship and to Dr. Ian Francis A.M. for his encouragement and support.

Finally, thank you to the travel agency, catering, laundry, ironing, butler service and bank of Mum and Dad, which never closed.

Veni, Vidi, Vivo!

Abstract

General Relativity is one theory amongst a wider range of plausible descriptions of the Universe. The aim of this thesis is to examine the behaviour of so-called screened theories, which are designed to avoid local tests of MG. We establish that these theories may be treated in a unified manner in the context of halo formation. A prerequisite for this is the clarification that the quasi-static approximation can be applied in cosmologically-plausible scenarios.

Amongst the plethora of MG theories, we select three, each of which exhibit a different form of screening. This describes a self-concealing property whereby each theory behaves like GR in the conditions of the local Universe. Only at regions of high energy density (chameleon), large coupling to matter (symmetron) or large derivatives of the scalar field (Vainshtein) does their modified behaviour emerge. We examine $f(\mathcal{R})$, symmetron and DGP gravity in the context of non-linear gravitational collapse for the remainder of the thesis.

Relativistic scalar fields are ubiquitous in our modern understanding of structure formation. They arise as candidates for dark energy and are at the heart of many modified theories of gravity. While there has been tremendous progress in calculating their effects on large scales there are still open questions on how to best quantify their effects on smaller scales where non-linear collapse becomes important. In these regimes, it has become the norm to use the quasi-static approximation in which the time evolution of perturbations in the scalar fields are discarded, akin to what is done in the context of non-relativistic fields in cosmology and the corresponding Newtonian limit. We show that considerable care must be taken in this regime by studying linearly perturbed scalar field cosmologies and quantifying the error that arise from taking the quasi-static limit. We focus on $f(R)$ and chameleon models to assess the impact of the quasi-static approximation and discuss how it might affect studying the non-linear growth of structure in N-body numerical simulations.

The halo mass function (HMF) $n(M)dM$ is the number n of haloes with mass in the range $[M, M + dM]$ per unit volume. It has two remarkable properties which render it a useful probe of extensions to general relativity (GR). On the one hand, it is (nearly-)universal, in the sense that it can be written in a form $f(\nu)$ which is (practically) insensitive to changes in redshift and cosmological parameters and redshift. We develop a method to generalise fitting functions derived in GR to a variety of screened MG

theories, in order to examine whether they are universal in the sense of being insensitive to MG. On the other hand, the HMF is sensitive to both the expansion history of the universe and the nonlinear behaviour of spherical collapse via the critical density parameter δ_c [40] and the matter power spectrum via the halo resolution $S(M)$ (both of which appear in ν). This greatly complicates the theoretical framework required to calculate ν, particularly given the sensitivity of chameleon MG to the surrounding environment. We explore a variety of new and existing methods to do so. Finally we re-calibrate the MG halo mass functions with the same rigour as has been done in GR.

An important indicator of modified gravity is the effect of the local environment on halo properties. This paper examines the influence of the local tidal structure on the halo mass function, the halo orientation, spin and the concentration-mass relation. We generalise the excursion set formalism to produce a halo mass function conditional on large-scale structure. Our model agrees well with simulations on large scales at which the density field is linear or weakly non-linear. Beyond this, our principal result is that $f(\mathcal{R})$ does affect halo abundances, the halo spin parameter and the concentration-mass relationship in an environment-independent way, whereas we find no appreciable deviation from ΛCDM for the mass function with fixed environment density, nor the alignment of the orientation and spin vectors of the halo to the eigenvectors of the local cosmic web. There is a general trend for greater deviation from ΛCDM in underdense environments and for high-mass haloes, as expected from chameleon screening.

Given the broad spectrum of MG theories, it is important to design new probes of MG. Despite the fact that we examine only three theories of MG, the techniques and methodology developed in this thesis can be applied to a wide variety of theories and can be extended to improve the results in this work.

Declaration

I carried out the work in this thesis at the Sub-Department of Astrophysics of the University of Oxford between Michaelmas 2012 and Trinity 2017 under the supervision of Professor Pedro Ferreira and Associate Professor Julien Devriendt. I declare that no part of this thesis has been submitted in support of another degree, diploma or other qualification at any university. Except where otherwise stated, the work in this thesis is all mine.

My research was partly funded by an Australian Postgraduate Award from the University of Sydney and I am grateful to Anne and Terrey Arcus A.M. for their gift of the Arcus Travelling Scholarship of which I was the recipient in 2014-15.

The following publications emerged from this thesis.

Chapter 3 is based upon:
Johannes Noller, Francesca von Braun-Bates, and Pedro G. Ferreira. "Relativistic scalar fields and the quasi-static approximation in theories of modified gravity". In: **Phys.Rev.** D89 (2014), p. 023521. DOI: 10.1103/PhysRevD.89.023521. arXiv: 1310.3266 [astro-ph.CO]

Chapters 4 and 5 are based upon:
F. von Braun-Bates et al. "The $f(R)$ halo mass function in the cosmic web". In: J. Cosmology Astropart. Phys. 3, 012 (Mar. 2017), p. 012. DOI: 10.1088/1475-7516/2017/03/012. arXiv: 1702.06817.

Chapters 4 and 6 are based upon a paper (under review in JCAP):
F. von Braun-Bates and J. Devriendt. "Universality of the halo mass function in screened gravity theories". In: **ArXiv e-prints** (Apr. 2018). arXiv: 1804.05387.

Contents

List of Figures

List of Tables

Chapter 1

Introduction

That gravity is not a force propagated through a static and infinite Universe but an inherent property of the spacetime which arises from describing the Universe as a geometric manifold, is perhaps the greatest insight of modern physics.

Einstein's theory of general relativity ([98]; henceforth GR) is now held as a dictum of twentieth century physics: not only a description of one of the four fundamental forces, but (alongside the Standard Model of particle physics) one of the two components of a "Grand Unified Theory" whence all physics might be derived. For the purpose of this thesis, GR has two remarkable qualities:

1. Its strong-field predictions remained largely un-testable to great accuracy until 60 years after its formulation. Weak-field tests available in the Solar System (e.g. the perihelion of Mercury, known to be discrepant from Newtonian predictions in 1843 [240], and the lensing deflection of the Sun first measured in 1919 [93]) operate on a scale of $\Phi_N \sim 10^{-6}$, where deviations from non-relativistic physics (let alone between competing relativistic theories) are expected to be small [118].

2. It provided a mathematical description of the Universe. This resulted in quantitative hypotheses which could be tested against predictions from Newtonian cosmology, e.g. the lensing deflection predicted by [249].

This combination lead to a plethora of extensions to GR, now termed modified or extended gravity theories (henceforth MG), which may be tested in all environments of the Universe. This thesis addresses the question of how certain plausible MG theories—having passed tests on both local and cosmological scales—can be examined on the intervening non-linear scales.

First we establish GR, both in terms of its physical principles and mathematical frame-

work, in Section 1.1. (More detail in given in Appendix A.) Then in Section 1.2 we show that GR is the simplest of a much richer space of models (thanks to Lovelock's Theorem) and broadly categorize some alternatives. Next we apply GR to quantify the concordance cosmology of ΛCDM in Section 1.3, including how to describe the effects of gravity in different regimes. This leads naturally to a discussion of MG cosmology in Section 1.4, from its motivation to its application in analytic, semi-analytic and numerical techniques. Finally we specify the problems addressed in this thesis in Section 1.5 with an overview of the structure.

1.1 General Relativity

Just as special relativity grew from attempts to reconcile Maxwell's equations with Galileo's principle of relativity, GR needed to reconcile Newton's gravitational equations with the principles of special relativity.

This task separates into several parts, which we shall address in this section.

1. The inherent non-linearity of a gravitational version of special relativity;
2. Dissatisfaction with theoretical properties of Newtonian gravity, e.g. action-at-a-distance, lack of Lorentz invariance and equality between inertial and gravitational mass.
3. Potentially observational problems with Newtonian gravity, e.g. the perihelion of Mercury, gravitational lensing, the behaviour of black holes.

We shall see that the principles behind GR (Appendix A.1) lead to a geometric description of gravity. The complexity of Item 1 is encapsulated in the Einstein field equations (Appendix A.3), which resolve the problematic features of Item 2. We can then address Item 3 by determining the behaviour of observables (matter, photons, *etc.*) under the influence of gravity via the geodesic equation (Appendix A.4).

The principles which enabled Einstein to reconcile the consequences of special relativity with the limitations of Newtonian gravity are well known. Newtonian gravity can be summarised in a form ostensibly similar to a co-ordinate approach to GR Definition A.1. This is particularly useful because there must be a set of conditions—now termed the weak-field limit—under which GR reproduces the behaviour of Newtonian gravity.

The weak-field limit operates in scales smaller than the horizon, in regimes where the gravitational potential is small. From Definition A.1 we see that non-uniform gravitational fields are observable, but uniform ones are not. This is due to the fact that

under Newtonian gravity the equation of motion of a freely-falling particle can be described in an inertial co-ordinate system (Eq. (A.1)) where the particle has a (passive) gravitational mass m_p and an inertial mass m_i. The experiments of Galileo, Newton and Eotvos [107] show the equality of these masses. Also Newton's 3rd law shows the equality of the active and passive gravitational masses (proof in Appendix A.1). Thus we obtain:

Theorem 1.1 (Equivalence of inertial and gravitational mass)**.** The inertial, active gravitational and passive gravitational masses of an object are equal. □

An important corollary is the universality of free-fall, known as early as Philoponus [107] that "if you take two weights differing by a very wide measure and drop them from the same height, then the ratio of the times of their motion does not correspond with the ratio of their masses....but the times will not differ at all from each other." Thus our GR-like formulation of Newtonian gravity leads to the weak equivalence principle (Definition A.4).

Similarly, GR must abide by the postulates of special relativity in any local reference frame. We summarise these in Definition A.2. Consequently, we obtain a (possibly infinite) set of privileged observers, each with their own inertial frame. In order for Items 3 and 4 to be satisfied, this specifies the allowed transformation between the inertial frames specified in Item 2. The invariance postulate Item 4 is known as Lorentz invariance (Eq. (A.3)). A physical law which remains unchanged under the transformation Eq. (A.3) is termed **Lorentz invariant**. The implications are not merely that definitions of distance and time may change between frames (to ensure the constancy of c) but that this difference between frames is what becomes meaningful, because there is no absolute frame privileged above all others. These postulates (Definition A.2) must hold locally in GR.

We now have the components for one of the two key results of GR, namely the Einstein equivalence principle (the equivalence principles are in Definition A.4). This describes the trajectories of particles given the geometry of spacetime and leads to the geodesic equation in Eq. (1.7) and Appendix A.4. Any theory which obeys the EEP is a valid description of gravity (i.e. which reconciles special relativity with Newtonian gravity [118]). However, the only theory which obeys the SEP is GR [255]. This is due to the corollary that the only gravitational field in the Universe is that provided by the metric $\mathbf{g}$ otherwise one could use the local gravitational effects (including the self-interaction of bodies which are not test masses) to distinguish between inertial reference frames. Once the spacetime geometry is specified, the equivalence principles dictate the acceleration produced by the curvature of the manifold.

The opposite problem—how the presence of gravitating bodies determines the curvature of the manifold—is the non-linearity problem mentioned at the beginning of this section. Specifically, if gravity causes an equivalent force to acceleration, then the geodesics which result correspond to a curved manifold equivalent to imposing a potential on a flat manifold. But this potential is itself a form of energy, which contributes to gravitation. Thus the GR field equations cannot retain the linearity of Newtonian gravity (proof in Appendix A.1). Instead, we are forced to construct a metric theory of gravity where the field equations are tensor (rather than scalar). We shall specify these in Appendix A.3 and Definition 1.2.

The second postulate of GR is the principle of general covariance. Generalising from the equations for special relativity, which take the same form in any vertical co-ordinate system, we require those for GR to take the same form in any co-ordinate system. Thus if satisfied in one co-ordinate system they hold in all others. Consequently they must be local, symmetric, rank-$(0,2)$ tensor equations [118], otherwise the Einstein equation and the geodesic equation cannot reduce to their special relativity behaviour in locally-inertial co-ordinates.

Having established the postulates of GR, we are now able to quantitatively generalise both Newtonian gravity and special relativity in the next two paragraphs.

The field equations of GR are most elegantly derived from a variation-of-least-action principle. This will be useful in subsequent sections (Section 1.2 and Chapter 2) because it is the approach commonly used to generalise GR to MG theories. We outline Hilbert's approach in Appendix A.2. In 4 dimensions, the only available quantity which is invariant under co-ordinate transformation in a scalar function of the metric and its derivatives, i.e. the Ricci scalar (up to a generic constant term). Applying modern notation, we obtain [41]:

$$S_{\mathrm{EH}}\left[g_{\mu\nu}\right] = \int \sqrt{g}\,\mathrm{d}^{\,4}x\ \left(R - 2\Lambda\right) = \int \sqrt{g}\,\mathrm{d}^{\,4}x\ G_{\mu\nu}\delta g^{\mu\nu} + \oint \cdots \tag{1.1}$$

where in the last equality we have recognised that additional boundary terms exist. These need to be carefully selected (see [41] for an explanation) if the action is to satisfy certain conditions on the boundary, but they do not contribute to the bulk action (hence to the Einstein equations). This is the Einstein-Hilbert action with the cosmological constant term included.

We obtain the complete Lagrangian for GR by generalising the source term. Nowadays, it is common to define the stress-energy tensor via the implicit relation [41]:

$$\delta S_M\left[\phi, g_{\mu\nu}\right] = -\frac{1}{2}\int \sqrt{g}\,\mathrm{d}^{\,4}x\ T_{\mu\nu}\delta g^{\mu\nu} \implies T_{\mu\nu} = -\frac{2}{\sqrt{g}}\frac{\delta}{\delta g^{\mu\nu}} S_M\left[\phi, g_{\mu\nu}\right] \tag{1.2}$$

where we have updated to modern notation and defined $\mathbf{T}$ to be the source of the field equations by construction. In this way we automatically obtain the desirable properties of $\mathbf{T}$ from those of $\mathbf{g}$: symmetry, covariance and conservation.

The complete action for GR in the presence of matter (along with its constraint equations) can be summarised as:

$$S_{\mathrm{GR}} \equiv \frac{1}{16\pi G_N} S_{\mathrm{EH}}\left[g_{\mu\nu}\right] + S_M\left[\phi, g_{\mu\nu}\right] \text{ where } \frac{\delta S_{\mathrm{GR}}}{\delta g^{\mu\nu}} = 0 \tag{1.3}$$

Having defined a complete Lagrangian for GR, we obtain the field equations by the usual route of varying the Lagrangian with respect to the metric and setting the derivative to zero (defined in Appendix A.3). The Lagrangian density $\mathcal{L}$ is given by the gravitational and the matter terms [118]:

$$\mathcal{L}_{\mathrm{GR}} = \sqrt{-g}\frac{R - 2\Lambda}{16\pi G_N} + \mathcal{L}_{\mathrm{matter}} \tag{1.4}$$

The first term is the Einstein-Hilbert Lagrangian density. We have normalised it by the factor of $16\pi G_N$ to account for the constant of proportionality κ between the Einstein tensor (obtained by setting the matter term to zero) and the stress-energy tensor (obtained by setting the gravitational term to zero). In this way, we obtain both sides of the Einstein equation Eq. (1.5) simultaneously.

On the right hand side of the Einstein equation, the stress-energy-momentum tensor $\mathbf{T}$ encapsulates the energy density, energy pressure and (both isotropic and anisotropic) stress due to the various components of the Universe. These components are simplified on cosmological scales to perfect fluids, whose form we delay until Section 1.3.

On the left hand side of the Einstein equation, the Einstein tensor $\mathbf{G}$ measures the compression of the metric in units of inverse-length squared. The Einstein tensor can also be derived geometrically. Recall that we are concerned with the relative motion between reference frames. The behaviour of infinitesimally-separated reference frames can be characterised by the method of parallel transport. In Definitions A.6 to A.8 we establish some definitions, which encapsulate the non-Euclidean geometry of the spacetime manifold. Not only does this reproduce the behaviour of inertial reference frames in special relativity but it also generalises to the non-inertial frames of GR.

The curvature of the spacetime manifold is described by the Riemann tensor and its contractions, the Ricci tensor and scalar respectively. We define these in Definition A.9. Covariant derivatives do not commute because the basis vectors are now functions of their co-ordinate chart (a situation familiar from spherical or cylindrical co-ordinates). We can now construct the Einstein tensor from the metric and its derivatives.

Definition 1.1 (Einstein tensor [223])**.** The most general rank-$(0,2)$ tensor with units of inverse-length squared is the Einstein tensor $\mathbf{G}$ defined by:

$$G_{\alpha\beta} \equiv R_{\alpha\beta} - \frac{1}{2} g_{\alpha\beta} \left(R - 2\Lambda\right)$$

where Λ is the gravitational part of the cosmological constant, R, $\mathbf{R}$ and $\mathbf{g}$ are the Ricci scalar, tensor and metric tensor respectively. □

While the cosmological constant can be neglected on astrophysical scales, its value becomes important on cosmological scales. We shall see that this leads to the cosmological constant problem in Section 1.4.1. Thus we have quantified the self-interaction of the spacetime manifold with its contents: the Einstein equation describes the gravitational curvature of spacetime caused by the presence of energy.

Definition 1.2 (GR field equations [41, 118, 223])**.** The field equation of GR is the Einstein equation:

$$G_{\alpha\beta} = \frac{c^4}{8\pi G_N} T_{\alpha\beta} \tag{1.5}$$

The integrability condition (the contracted Bianchi identity) combined with the Einstein equation produces the energy-momentum balance equation

$$\nabla_\alpha G^{\alpha\beta} = 0 \implies \nabla_\alpha T^{\alpha\beta} = 0 \tag{1.6}$$

Thus we have six independent, covariant equations for the metric (ten equations from Eq. (1.5) and four constraint equations Eq. (1.6)). □

Now we define the geodesic equation which described the trajectory of a particle given its local spacetime geometry. This is a straightforward generalisation of the Newtonian geodesic equation which we saw in Definition A.1 to accommodate the non-Euclidean nature of the manifold. Geodesics are those curves whose covariant acceleration is zero, i.e. which are parallel transported (Definition A.8). Applying the definition of the convective derivative in Definition A.7 to the four-velocity, we obtain the geodesic equation directly:

$$\frac{\mathrm{d}^2 x^\alpha}{\mathrm{d}\tau^2} + \Gamma^\alpha{}_{\beta\gamma} \frac{\mathrm{d}x^\beta}{\mathrm{d}\tau} \frac{\mathrm{d}x^\gamma}{\mathrm{d}\tau} = 0 \tag{1.7}$$

If the world-line describes a massive particle then the affine parameter τ is equivalent to the proper time. Thus we see that in the presence of gravity, objects are parallel transported along their world-lines.

GR provides us with the tools to mathematically describe the paths of observables in the Universe given its geometry. Accordingly, the challenge for cosmology is either:

1. To specify the energy contents of the Universe via **T** and solve the Einstein equation for the corresponding geometry, or

2. To specify the geometry of the Universe in **G** and solve the Einstein equation to find the contents of the Universe.

Both of these approaches are required to extract from the cosmological principle, the concordance cosmology of ΛCDM. We shall discuss this in Section 1.3. Meanwhile we shall see in the next section that GR is the simplest of a large family of gravitation theories. It is this family of theories which also fulfil Einstein's aim of reconciling Newtonian gravity with the postulates of special relativity. It is the aim of this thesis to demonstrate that one can distinguish GR from MG.

1.2 Beyond GR

Contrary to what one might naively expect, there are only a finite number of extensions to GR. In this section we first outline Lovelock's theorem, which states that the theory of GR is in some sense the simplest possible. This provides a set of conditions which must be broken by an MG theory. Next we categorise a selection of MG theories into families depending upon which condition they violate. Then we attempt a general definition of a theory of MG (in comparison to a GR cosmology with dark energy). Finally, we discuss the status of GR as a quantum theory.

1.2.1 Lovelock's theorem

Lovelock's theorem acts as an important guide for the development of MG theories. It asserts that GR is the only gravitational theorem to fulfil a certain series of conditions.

Theorem 1.2 (Lovelock's Theorem [171, 172])**.** The most general Lagrangian density of the form $\mathcal{L}\left(g_{\alpha\beta}, \partial g_{\alpha\beta}, \partial\partial g_{\alpha\beta}\right)$ which satisfies the following conditions:

1. The Euler-Lagrange equations are rank-$(0,2)$ tensor equations;

2. They are symmetric under exchange of indices;

3. They are divergence-free;

4. They are second order in derivatives of the metric;

5. The equations are local;

6. The spacetime manifold has four dimensions.

is given by

$$\mathcal{L} = \sqrt{g}\left[aR + b\epsilon^{\mu\nu\rho\lambda}R^{\alpha\beta}{}_{\mu\nu}R_{\alpha\beta\rho\lambda} + c\left(R^2 - 4R^{\mu}{}_{\nu}R^{\nu}{}_{\mu} + R^{\mu\nu}{}_{\rho\lambda}R^{\rho\lambda}{}_{\mu\nu}\right) + d\right]$$

for real constants a, b, c, d. □

To reproduce the Einstein-Hilbert action, we set $a = 1$ and $d = -2\Lambda$: the values of b and c are unimportant because neither the second nor the third term in Theorem 1.2 contribute to the Euler-Lagrange equations.

An important corollary of Lovelock's Theorem is the limitation it places upon the possible modifications to general relativity, which must retain the essential properties of the GR field equations. Namely, if one wishes to have rank-$(2, 0)$, divergence-free field equations, while retaining the existing symmetry of indices and a torsion-free manifold, then there are only four possible modifications to GR [70]:

1. Add derivatives of $\mathbf{g}$ above second order in the field equations;
2. Supplement or replace the metric tensor $\mathbf{g}$ with other fields;
3. Increase the dimensionality of space-time;
4. Permit non-local field equations;

or any combination thereof. This separates extended gravity theories into various families depending upon their relaxation of constraints on the field equations. However, a more pragmatic approach is to base the familial divisions upon the dynamical effects of modified gravity, e.g. the presence of extra fields in $\mathbf{T}$, or the ability of a theory to evade observational constraints. In this thesis, we concentrate on MG theories which naturally evade local (Solar System) constraints and can be represented by the addition of a scalar field coupled to matter to the stress-energy tensor, and each of which exhibits a different relaxation of Lovelock-related constraints. Such theories are termed screened modified gravity.

1.2.2 Examples of MG theories

This section provides a brief survey of currently viable MG theories. We categorise them according to Lovelock's theorem and explain potential problems with each violation. A selection of theories is presented in graphical form in Fig. 1.1. In Chapter 2 we will delve into the three MG theories used in this thesis: namely $f(\mathcal{R})$, Dvali-Gabadadze-Porrati (DGP) and Symmetron models.

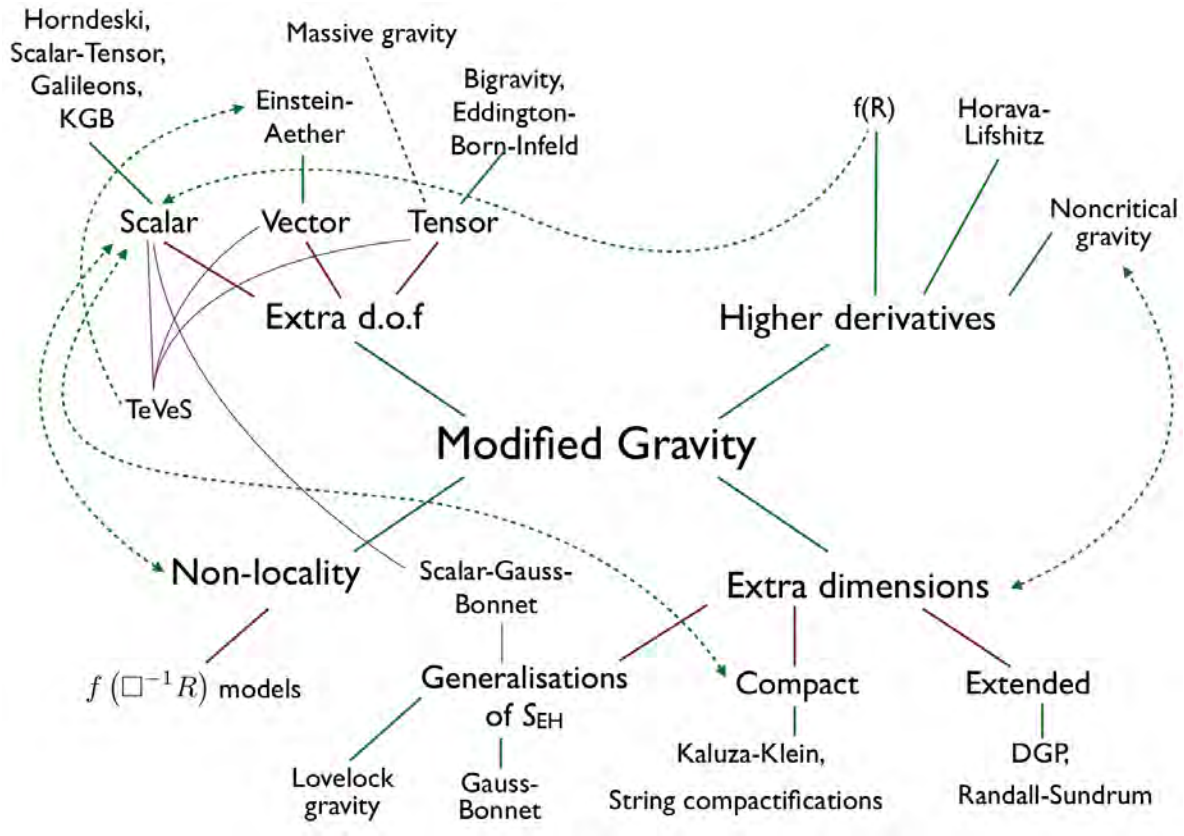

Figure 1.1: Schematic of the relations between a selection of extended gravity theories. Reproduced from [16] with permission.

1.2.2.1 Higher derivative theories

Higher derivative theories add extra spatial or temporal derivatives of order 3 or greater to the field equations. There are tight constraints on higher-order temporal derivatives due to Ostrogradski's theorem which places conditions on the Lagrangian to ensure that it is energetically stable. Adding higher order spatial derivatives violates Lorentz invariance, so we neglect these theories here.

Ostrogradski's theorem shows that new degrees of freedom without constraint relations run away to infinitely high energies [151]. Adding higher-order derivatives to a Lagrangian leads to a set of Euler-Lagrange equations with higher order, requiring more initial conditions to specify a solution. The corresponding Hamiltonian has extra canonical momenta, i.e. more degrees of freedom [151]. The Hamiltonian will be linear in these additional momenta, so there are no multiplications by other variables to limit the magnitude of these terms. Consequently, if a different mode is excited to infinitely high energy, the mode whose momentum appears linearly in the Hamiltonian can compensate without bound. This results in different modes running to infinite (but equal and opposite) energy states: a ghost phenomenon. This effect becomes worse with increasing derivative order because runaway is more entropically favoured. The general result of Ostrogradski's theorem is that a (non-degenerate) Lagrangian containing N-th

order derivatives of $\mathbf{q}$ requires $(N-1)$ constraints for the $(N-1)$ terms linear in $\mathbf{p}$ in its Hamiltonian if it is to avoid catastrophic energy instabilities [16]. Thus we see that it is difficult to build stable higher-derivative theories of gravity.

An example which does avoid the pitfalls of Ostrogradski's theorem is the class of $f(R,T,G)$ gravities. Of these, $f(\mathcal{R})$ is the most widely studied: it is this theory which is a focal point of this thesis, which we discuss in Chapter 2.

1.2.2.2 Additional degrees of freedom

A large class of MG theories is constructed by adding new scalar, vector or tensor fields to the gravitational action. If these fields are minimally coupled to the metric then they can be moved from the left to the right hand side of the Einstein equation and become an effective form of dark energy. If they are non-minimally space coupled to the metric then they introduce new kinetic terms into the action and the resulting terms and coupling constants can be tuned to agree with observations. This does not result in fine-tuning if one can find a physically motivated rationale for the values of the additional terms.

The traditional effective field theory approach of particle physics cannot be used in this context. This involves composing a Lagrangian from all possible terms in a power series in E/M, where in our case E/M equals $H_0/M_{\rm Pl}$ [16]. We see that at late times every term is hugely suppressed: in fact the only terms which survive are the usual Einstein-Hilbert term, a kinetic term for the scalar field and the scalar field potential. Thus we are faced with the same fine tuning as the new cosmological constant problem (discussed in Section 1.4.1).

Extra fields also risk the creation of ghosts, which are fields with the non-canonical sign in the kinetic term. These arise from adding extra fields with even spin (i.e. scalars or tensors), which have energy eigenvalues which are negative [70]. Since its energy is unbounded from below, the ghost particle—if coupled to non-ghost fields—can transfer its negative energy to physical particles (e.g. in quantum production of ghost–non-ghost pairs *in vacuo*). In order to "exorcise" the ghost, it must be either prevented from contributing a (potentially infinite) negative term to the Hamiltonian via [16]:

1. including constraints which bound ghost terms from below
2. coupling to matter above a cut-off energy scale (usually $M_{\rm Pl}$)
3. not coupling to matter (or other non-ghost fields)

Accordingly, some ghost fields can be included provided that the Hamiltonian remains positive below the cutoff scale.

If we limit ourselves to purely scalar fields, then the most general Lagrangian was found by Horndeski (although more general forms have since been discovered, with third-order time derivatives in their equations of motion) [151]:

$$L = \Sigma_{i=2}^{5} \alpha_i {}^{(i)}L \quad \text{where} \quad \phi_\mu \equiv \nabla_\mu \phi \quad \text{and} \quad \phi_{\mu\nu} \equiv \nabla_\nu \nabla_\mu \phi \tag{1.8a}$$

$${}^{(2)}L = G_2(\phi, X) \tag{1.8b}$$

$${}^{(3)}L = G_3(\phi, X)\Box\phi \tag{1.8c}$$

$${}^{(4)}L = G_4(\phi, X)R - 2\partial_X G_4(\phi, X)\left[\Box\phi^2 - \phi^{\mu\nu}\phi_{\mu\nu}\right] \tag{1.8d}$$

$${}^{(5)}L = G_5(\phi, X)G_{\mu\nu}\phi^{\mu\nu} + \frac{1}{3}\partial_X G_5(\phi, X)\left[\Box\phi^3 - 3\left(\Box\phi\right)\phi^{\mu\nu}\phi_{\mu\nu} + 2\phi^{\mu\nu}\phi_{\mu\sigma}\phi^{\sigma}{}_{\nu}\right] \tag{1.8e}$$

This unifies a variety of sub-models for different choices of the free functions G_i. The simplest of these is the cubic Galileon models, which we shall discuss in Chapter 2.

1.2.2.3 Additional dimensions

It is possible to formulate the field equations in manifolds which are not 4-dimensional. Manifolds with $N \leq 3$ dimensions are immediately ruled out, not only by trivial observation, but also by the degrees of freedom of the Riemann tensor. In theories with extra temporal dimensions, closed time-like curves can generate paradoxes and problems with causality [70]. We do not discuss them here. In theories with extra spatial dimensions $N \geq 4$ the Newtonian potential due to a point source $1/r^{N-3}$ is unstable [70]. Therefore these theories are only plausible if the extra dimensions do not manifest on local scales (otherwise we would have evidence from, e.g. unstable planetary orbits). There are three possibilities:

- promoting surface terms to volume terms in the generalised Einstein-Hilbert action
- adding compacted spatial dimensions
- adding extended spatial dimensions

and we discuss each in turn. A schematic summary is shown in Fig. 1.2.

Gauss-Bonnet cosmologies make use of the two terms in Lovelock's action Theorem 1.2 which only appear as surface terms in 4 dimensions [16]. In $N > 4$ dimensions these terms do propagate to the Euler-Lagrange equations. A corollary of Lovelock's theorem is that in D dimensions, there are $D/2$ unique Lagrangian densities which permit both

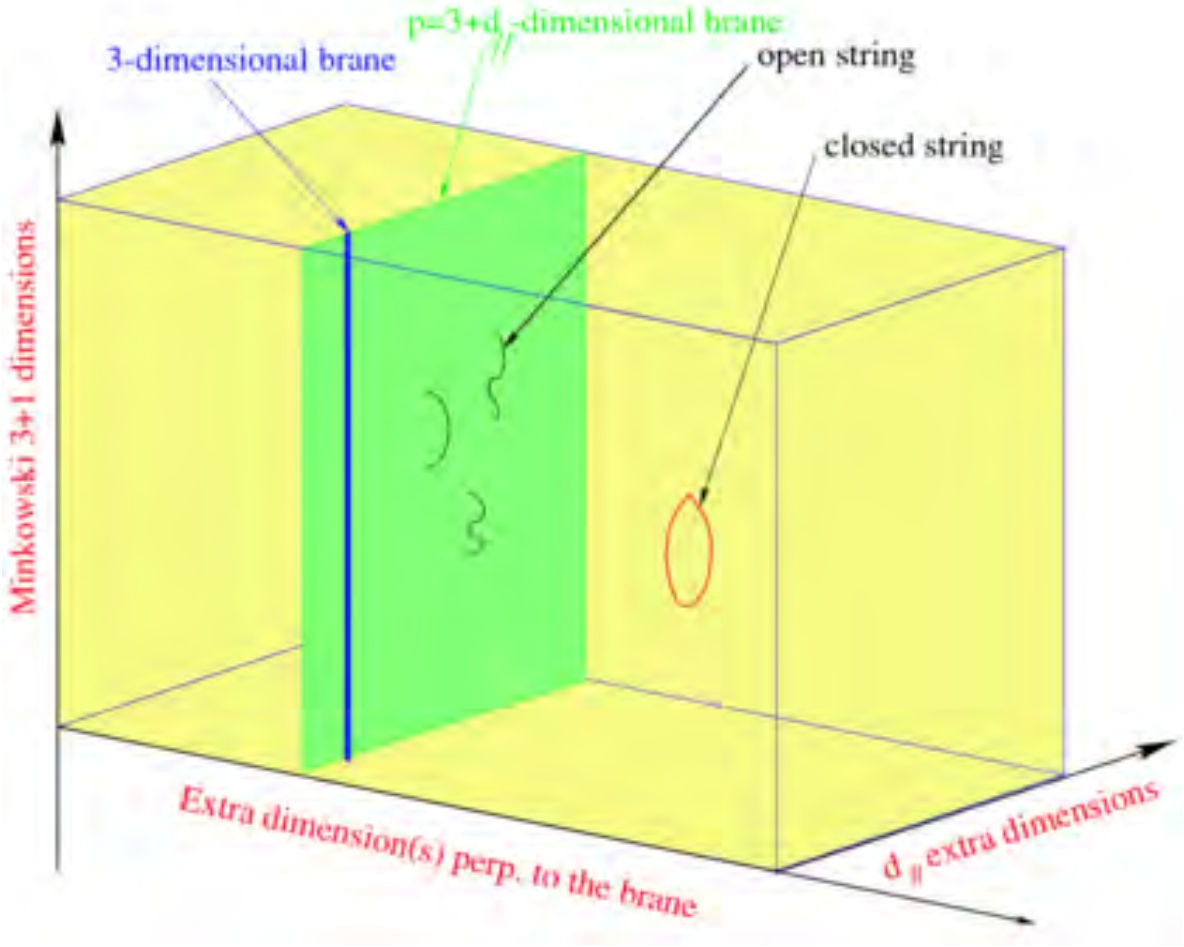

Figure 1.2: The structure of extra-dimensional MG theories. Additional dimensions are either large, i.e. they form a bulk whose surface boundary is the standard $(3+1)$-dimensional manifold, or they form compact dimensions which have effects only on quantum scales. The additional dimensions can be spatial or temporal, and may be "parallel" or "perpendicular" to the brane. Reproduced from [14].

energy conservation and second-order field equations [63]. For a general manifold $\mathcal{M}$ with $N = 2k$ or $N = 2k+1$ dimensions, one obtains the action:

$$S_{\text{Gauss-Bonnet}} = \int_{\mathcal{M}} a_k \mathcal{L}_k \tag{1.9a}$$

$$\mathcal{L}_k = \bigwedge_{i=1}^{k} R^{A_i B_i} \wedge x_{A_1 B_1 \ldots A_k B_k} \tag{1.9b}$$

$$R^A{}_B = R^A{}_{BCD} x^C \wedge x^D \tag{1.9c}$$

where $R^A{}_{BCD}$ is the Riemann tensor and x^D is the basis. For $k = 0$ the only term is a constant, which can be set to -2Λ; for $k = 2$ we obtain the Ricci scalar R; for $k = 3$ the Gauss-Bonnet term appears (the third term in Theorem 1.2) *etc.*. Of particular interest is the case of $N = 5, 6$, termed Einstein-Gauss-Bonnet gravity, where the resulting equations are precisely those of GR with an additional tensor term [16]:

$$S_D = \frac{1}{16\pi G_D}\int \mathrm{d}^{\,D}x\sqrt{-g}\,(R - 2\Lambda + \alpha\mathcal{G}) + S_M \qquad \text{action} \tag{1.10a}$$

$$T_{AB} = \frac{1}{8\pi G_D}\left[G_{AB} + \Lambda g_{AB} + \alpha H_{AB}\right] \qquad \text{field equation} \tag{1.10b}$$

$$H_{AB} = \begin{bmatrix} 2\left(RR_{AB} + R_{ACDE}R^{C}{}_{B}{}^{DE}\right) \\ -4\left(R_{AC}R^{C}{}_{B} + R_{ABCD}R^{CD}\right) \end{bmatrix} - \frac{1}{2}\alpha\mathcal{G}g_{AB} \qquad \text{Lovelock tensor} \tag{1.10c}$$

where g_{AB}, G_{AB}, T_{AB}, R_{AB}, $R^{A}{}_{BCD}$ have their usual meanings but are now over D dimensions, G_D is the D-dimensional Newton's constant, $\mathcal{G}$ is the Gauss-Bonnet scalar and α is a constant (usually positive). Einstein-Gauss-Bonnet gravity can be interpreted as a string-theory-like generalisation of GR [70].

Kaluza-Klein theories posit that of the $N = 3 + d$ spatial dimensions, only 3 grew to become large, while the other d remained microscopically small. Kaluza noticed that pure 5D gravity can reproduce the Einstein-Maxwell Lagrangian of gravity plus electromagnetism in 4D [41], albeit with certain unpleasant geometric properties. Extensions to this theory remain popular due to the necessity of extra, compact dimensions to properly formulate certain quantum gravity theories such as M-theory and string theory. In the usual $(3 + 1)$ boundary, the cutoff energy scale is $M_{\mathrm{Pl}} \approx 10^{19}\mathrm{GeV}$, with associated length scale $l_{\mathrm{Pl}} \approx 10^{-35}\mathrm{m}$. However, in the bulk, the cutoff is M_s, related to the Planck mass by [14]:

$$M_{\mathrm{Pl}}^2 = \frac{1}{g_s^2}{}^{(4+d)}M_s^{2+N}\,{}^{(1)}R_\perp \cdots {}^{(d)}R_\perp \tag{1.11}$$

where g_s is the string coupling constant and we have added d compact dimensions with characteristic radii ${}^{(d)}R_\perp$. Provided that ${}^{(d)}R_\perp \gg l_{\mathrm{Pl}}$, the new cutoff is $M_s \ll M_{Pl}$, so we expect gravity to weaken (compared to the other fundamental forces). The effect of gravity leaking into the bulk manifests on the brane only on scales shorter than $R_\perp$. Theories with compact additional dimensions are testable both using cosmology and using high-energy collider experiments, which makes them easier to constrain.

Brane cosmologies propagate gravity in all $N = 4+d$ dimensions, but limit the Standard Model to interactions on the $(3 + 1)$ boundary. This aims to explain why gravity is so much weaker than the other three fundamental forces: its intensity is reduced by having to propagate into the additional dimensions of the bulk. The usual route is to embed the manifold with FLRW metric (Section 1.3.1) in a higher-dimensional space with Minkowski metric (thus empty by definition) [70]. Then the complete action has

both a bulk term and a brane term [14]:

$$S_{\rm EH} = \left[\begin{array}{l} {}^{(d)}M^{2+N} \int_{\mathcal{M}} \mathrm{d}^{\,4}x\, \mathrm{d}^{\,d}y \sqrt{{}^{(d)}g}\, {}^{(d)}R \\ +\ {}^{(4)}M_{\rm Pl}^2 \int_{\partial\mathcal{M}} \mathrm{d}^{\,4}x \sqrt{{}^{(4)}g}\, {}^{(4)}R \end{array} \right] \text{where } {}^{(4)}M_{\rm Pl}^2 = r_c^{N\,(d)}M^{2+N} \tag{1.12}$$

The Planck masses in the bulk and the brane are related by a characteristic radius r_c, so that on large scales we see the effects of the bulk, but not below them. Theories such as DGP and RS models produce cosmologically testable deviations from ΛCDM. However (by definition!) it is only possible to test these theories via gravitational means.

In Chapter 2 we shall examine the 5D braneworld cosmology of DGP in more detail.

1.2.3 Modified gravity vs dark energy

In closing, we make the distinction between a theory of MG and a theory of DE. There are several competing definitions, amongst which are:

1. [16] The extra fields (or effective fields from geometric terms) in MG theory do couple non-minimally to matter fields, whereas in a DE theory the coupling is minimal.

2. [127] A DE theory does not violate the strong equivalence principle, whereas an MG theory does.

It should be noted that there is some degeneracy between the two definitions. Many types of MG theory can be effectively described by the addition of extra DE fields, simply because one can always move additional terms from the left to the right hand side of the Einstein equation and vice-versa. This is explored in more detail in Chapter 2
.

1.2.4 Progress towards a quantum theory of GR

We briefly mention the lack of a fully quantum understanding of GR and how this affects the development of MG theories.

1.3 Cosmology in GR

GR provided the first quantitative framework to challenge the Newtonian cosmology of a static, infinite universe. In this section we shall see how GR leads to the ΛCDM cosmology which is our current "best-fit" description of the Universe to date. First we will summarise how the cosmological principle leads to the FLRW metric and the expansion history of the Universe. Then we shall use cosmological perturbation theory to approximate the Universe on linear scales. On non-linear scales the Universe can be approximated by a halo model which is a cornerstone of this thesis. Finally we shall illustrate how observational evidence on all of these scales leads to ΛCDM.

1.3.1 The FLRW metric

Application of GR to the cosmological principle results in the FLRW metric, which describes the spacetime of the Universe on the largest scales. The cosmological principle Definition 1.3 is an axiom which needs to be verified by observations.

Definition 1.3 (Cosmological Principle [221])**.** The Cosmological Principle consists of three statements:

1. **(Statistical Isotropy)** Apart from anisotropies of local origin, the distribution of light in the Universe is statistically isotropic.
2. **(Statistical Homogeneity)** The spatial distribution of matter in the Universe is statistically homogeneous on scales larger than a certain homogeneity scale.
3. **(Cosmological Principle)** All physical quantities measured by a co-moving observer are spatially homogeneous and isotropic.

□

The first can be verified by examination of the isotropy of the CMB, while the second can be inferred from the CMB weak lensing map or from large galaxy surveys such as BOSS (we discuss cosmological probes in Section 1.3.4). If we assume that we are typical observers, i.e. that our observations of isotropy and homogeneity are not a result of some privileged location, then the third statement follows.

If we assume the validity of the cosmological principle, then we must treat spacetime as a foliation of maximally symmetric 3-surfaces orthogonal to a time like dimension. This ensures that each hypersurface is both homogeneous and isotropic. The metric which

admits this geometry is known as the FLRW metric. Its line element is [118]:

$$\mathrm{d}\,s^2 = a^2(\eta)\left[-\,\mathrm{d}\,\eta^2 + \frac{\mathrm{d}\,r^2}{1-kr^2} + r^2\left(\mathrm{d}\,\theta^2 + \sin^2\theta\,\mathrm{d}\,\phi^2\right)\right] \tag{1.13}$$

We have introduced the scale factor a, the conformal time co-ordinate η and the metric of the 3-surface (determined by the value of k). Although in theory this may be any of the spherical ($k = +1$), Euclidean ($k = 0$) or hyperbolic ($k = -1$) 3-surfaces, observations show that the Universe is flat to a higher degree of certainty [200]. Therefore we assume flatness for the remainder of this thesis.

As we have already seen in Section 1.1, by specifying the metric, we can use Einstein's equation to infer the contents of the Universe. The diagonality of $\mathbf{G}$ demands that $\mathbf{T}$ consists only of perfect fluids.

Definition 1.4 (Perfect fluid)**.** A **perfect fluid** is a fluid which lacks particle-particle interactions, viscosity and heat conduction, [118, 223] i.e.:

$$T^{\alpha\beta} = \mathrm{diag}\left((\rho + p)\,u^\alpha u^\beta + p g^{\alpha\beta}\right) \tag{1.14}$$

This is equivalent to the requirement that a perfect fluid is isotropic in its rest frame. □

Therefore we have shown that the assumption of the cosmological principle dictates that the Universe can be approximated by a perfect fluid in a time-varying Euclidean geometry.

The background evolution of the Universe is determined by the Friedmann equations. Due to isotropy, the only non-trivial terms of the Einstein equation and the energy-momentum balance equation become [41, 118, 223]:

Definition 1.5 (Friedmann equations)**.** The conformal Hubble factor $H \equiv \partial_\eta a/a$ and its conformal time derivative $H^{'} = \partial_\eta H$ are related to the scale factor a, total energy density ρ and energy pressure $p = w\rho$ of the Universe via:

$$\frac{\partial_0 \rho}{\rho} = -3(1+w)\frac{\partial_0 a}{a} \qquad \left(\nabla_\alpha T^{\alpha 0} = 0\right) \tag{1.15a}$$

$$H^2 = \frac{\kappa}{3}\rho \qquad \left(G^{00} = T^{00}\right) \tag{1.15b}$$

$$H' = \frac{-\kappa}{6}\rho a^2\,(1+3w) \qquad \left(G^{ii} = T^{ii}\right) \tag{1.15c}$$

□

These equations encapsulate the constituents and evolution of the FLRW universe.

1.3.2 The metric on linear scales

It is clear that the cosmological principle cannot be valid on all scales in the Universe. However, we may treat it as a zeroth-order approximation to the full relativistic description. Based upon the work of the previous section, we will now apply linear perturbations to both the metric and the perfect fluid description of the Universe.

Rearranging the energy-momentum balance equation $\nabla_\alpha T^{\alpha\beta} = \nabla_\alpha G^{\alpha\beta} = 0$ gives the relativistic Euler equation:

$$\dot{u}_\beta = -\mu^{-1}\left\{u_\beta\left(\dot{\mu} + \mu\theta\right) + \nabla^\alpha\left(\mu\pi_{\alpha\beta}\right) + \partial_\beta p\right\} \tag{1.16}$$

and via the relations $\dot{u}_\beta u^\beta = 0$ and $u_\beta u^\beta = -1$ we contract to obtain $\dot{\mu} = \dot{\rho} + \dot{p}$ whence arises the relativistic continuity equation:

$$\dot{\rho} = -\mu\left(\theta + u^\beta \nabla^\alpha \pi_{\alpha\beta}\right) \tag{1.17}$$

We have introduced $\mu \equiv \rho + p$ and the velocity four-divergence $\theta \equiv \nabla_\alpha u^\alpha$ in these equations. Now we shall use these equations in addition to the Einstein equation to derive the equivalents to the Friedmann equations at linear order.

Even on linear scales, we can simplify the stress-energy tensor. For simplicity, we choose a reference frame such that $\mathbf{u}$ is the kinematical four-velocity of the fluid and assume that the kinematical and dynamical four-velocities are equal. Then $\mathbf{q}$ vanishes, equivalent to an adiabatic process [97]. Furthermore we can neglect adiabatic stress, so $\boldsymbol{\pi}$ vanishes also. Then Eq. (A.10) simplifies to:

$$T^{\alpha\beta} = \mu u^\alpha u^\beta + p g^{\alpha\beta} \tag{1.18}$$

On linear scales, the scalar, vector and tensor terms decouple (because terms can be at most linear in the perturbations). Hence we can restrict ourselves to scalar perturbations. Then we can define the overdensity δ and the velocity perturbation v^i as the linearised components of:

$$\rho = \bar{\rho}\left(1 + \delta\right) \quad \text{and} \quad u^\alpha u_\alpha = -1 \tag{1.19}$$

By convention we define the perturbations on $\mathbb{R}^3$, not on the actual manifold, so that their indices can be raised and lowered without taking into account deviations from Euclidean geometry [180]. This has the disadvantage that they do not transform as tensors. Fortunately, in GR we obtain only one extra degree of freedom,—the metric potential Φ; equivalently the density perturbation δ—because all the other perturbations vanish [29].

Now we turn to the equations governing the evolution of perturbations. After substantial algebra, Eqs. (1.5), (1.16) and (1.17) become [29]:

$$\nabla^2\Phi = 4\pi G_N a^2 \bar{\rho}\Delta \tag{1.20a}$$

$$\Phi'' + 3H\Phi' + \left(2H' + H^2\right)\Phi = 4\pi G_N a^2 w\delta \tag{1.20b}$$

$$(1+w)\left[3\Phi'' + 3H\left(1-3w\right)\Phi' + \nabla^2\Phi\right] = \delta'' + H\left(1-3w\right)\delta' - w\nabla^2\delta \tag{1.20c}$$

Since we are only concerned with matter perturbations (i.e. we neglect radiation and assume that the cosmological constant does not clump), then we need not sum over all types of matter and can instead set $w = 0$. Then we need only find solutions to the evolution of the gravitational potential Φ, which can be substituted to find the evolution of dark matter.

In Section 1.3 we shall turn to observations in order to characterise the contents of the Universe and to determine at what (physical) scales our perturbative approach breaks down. Beyond these scales, we shall rely on the halo model to describe non-linear structure formation. We describe this in the next section.

1.3.3 GR on non-linear scales

The dynamics of structure formation on non-linear scales cannot be effectively treated by extending perturbation theory beyond second order. Instead, we use the halo model to describe the non-linear collapse of density perturbations into LSS. Locally, we can describe the collapse of an individual over density as a top-hat in real space surrounded by an empty FLRW Universe. As we have seen, Birkhoff's theorem is not valid in some theories of MG so this approach is not always possible. [70]

The halo model aims to predict the statistics of the dark matter halo distribution without following the complex dynamics of the formation of the individual halos. Under the assumption that at early times, the density fluctuations in the Universe follow a Gaussian random field, we can use the initial power spectrum to completely describe the overdensity field. Subsequently, the Euler and continuity equations describe the (non-linear) evolution of the density field, which introduces additional correlations. In order to compute the statistics of the virialised haloes at late times, we require [73]:

1. The growing mode $G(z)$ to the linear density perturbation equations:

$$G(z) = \frac{H(z)}{H_0}\int_z^0 \mathrm{d}\,\bar{z}(1+\bar{z})\left[\frac{H_0}{H(\bar{z})}\right]^3 \tag{1.21}$$

2. A window function $W(kR)$ to relate the power spectrum to the halo mass M via

the fluctuation variance $\sigma = \sqrt{S}$:

$$S(M) \equiv \frac{1}{2\pi^2} \int_0^\infty dk\, k^2\, P(k, z=0)\, |W(kR)|^2. \tag{1.22}$$

3. The transfer function (numerically computed) relating the linear power spectrum at primordial times to its value after matter-radiation equality.

It remains to relate the statistical behaviour of the density field to the non-linear collapse of a single halo. The collapse is given by a non-linear ODE, which we study in Chapters 5 and 6. The relation is given by the excursion set theorem, which we examine in detail in Chapter 5. In summary, we can relate the fraction of collapsed haloes above a certain mass $F(> M)$ to the fraction of Markovian trajectories exceeding a critical density δ_c at resolution S. The analytical solution to this problem is the well-known Press-Schechter mass function [202]:

$$F(> M) = 2 \int_{\delta_c}^\infty P(\delta(S))\, d\delta = \mathrm{erfc}\left(\frac{\nu_h}{\sqrt{2}}\right) \quad \text{where} \quad \nu_h \equiv \delta_c/\sqrt{S} \tag{1.23}$$

Nowadays the appropriate functional forms are computed numerically. The accuracy of this model can be tested by comparison to N-body simulations.

The statistics of the large-scale distribution of the matter density field can also be derived from this very simple picture. If the halo density profile is indeed universal (e.g. the Navarro-Frenk-White profile of [185, 186]) then our halo model (designed for the linear regime) can also provide the statistics of the matter density field on non-linear scales (for collapsed structures). Consequently, we have a prediction for the number density of halos of a given mass without following the complex dynamics of the formation of the individual halos.

Moreover, the baryonic density field can be extrapolated from the halo model. Based upon the formalism of Rees and White [253], different types of galaxies are produced by the potentials of different dark matter haloes, ensuring a correlation between the (detectable) galaxy population and the underlying dark matter halo distribution. These semi-analytic models become especially important when considering the bias between the galaxy and dark matter distributions.

In Chapter 6 we shall go beyond the simple halo model to study the geometry of partially- and fully-collapsed structures in LSS. This replaces the model of a distribution of universal dark matter haloes with baryonic cores as the only objects in an otherwise homogeneous Universe. Instead, considering the density, prolateness and ellipticity of Gaussian density fluctuations leads to a cosmic web. We can classify structures in the LSS according to the number of axes along which they have collapsed. This permits an

analytic treatment of the rich landscape of non-linear structures in the Universe.

1.3.4 Observational evidence for ΛCDM

This section summarises the major observational tool which we can use to discern both the dynamics and the contents of the Universe. Cosmological probes can be divided into early Universe and late Universe types. Each probe produces (often degenerate) constraints on a subset of the cosmological parameters of ΛCDM. First we list the main sources of cosmological data. We shall expand upon these in Section 1.4 when they are applied to MG rather than ΛCDM. Then we describe the evidence at zeroth order for both ingredients of the ΛCDM model. Next we show that at first order there is no evidence for any additional constituents. Finally we summarise the success of ΛCDM, which must be preserved by an observationally-viable MG theory.

At early times, cosmology is tested using the cosmic microwave background. The Planck 2015 results [200] agree with the predictions of concordance cosmology (i.e. 6-parameter, best-fit ΛCDM) temperature and E-mode polarisation (TT, TE and EE spectra); the lensing power spectrum (to 2.5%); flatness ($\Omega_k = 5 \times 10^{-3}$ at 95% confidence); and the number of relativistic particle species ($N_{\rm eff} = 3.046$ to 10%). Moreover, the Planck 2013 results [4] were self-consistent (between lensing and the power spectrum) and both the 2013 and 2015 primordial power spectra favour the purely adiabatic, tilted, otherwise-featureless spectrum predicted by the concordance cosmology (more precisely, $r < 0.11$ at 95% confidence is consistent with the $r = 0.0$ prediction). Thus we have no compelling evidence for a modification to our currently-accepted cosmology at early times.

At late times, a variety of probes exist: baryon acoustic oscillations (BAO; [84]), large-scale structure (LSS, [80, 208]), redshift-space distortions ([130, 176]), Type Ia supernovae [8, 210, 233], weak lensing [138, 154]. So far ΛCDM has passed individual tests provided by observations of LSS, with anomalies limited to $\lesssim 2 - 2.5\sigma$ [55]. Thus at late times there is little to suggest tension between theory and observation.

What do these observations tell us about the geometry of the Universe? Recall that at zeroth order, this is described by the Friedmann equations Definition 1.5. For cosmological purposes, it is useful to re-express the first Friedmann equation as:

$$1 = \Omega_{m0} + \Omega_{\Lambda 0} + \Omega_{k0} \quad \text{where} \quad \Omega_{i0} \equiv \frac{\rho_i(z=0)}{\rho_{\rm crit,0}} = \frac{\rho_{i0}}{3H_0/8\pi G_N} \tag{1.24}$$

This equation constrains the (present-day) proportions of each component of the perfect fluid. The second and third Friedmann equations (Definition 1.5) dictate how the (time-

varying) energy density of each component affects the expansion history of the Universe. Having discarded negligible contributions from neutrinos, radiation, and baryons, the SCDM model contains only a geometric (Ω_{k0}) and a dark matter (Ω_{m0}) component. Peebles was the first to show that the SCDM model plus the flatness constraint from inflation was incompatible with data, instead proposing $\Omega_{m0} = 0.2 \pm 0.1$ [195]. Over the next decade a variety of observations showed that inflation plus a flat SCDM model could not describe the expansion of the Universe [55]. However, it was not until the SNe observations of [196, 210] that the Friedmann equations derived from observations ruled out competing theories such as an open CDM cosmology that ΛCDM became experimentally favoured.

On scales smaller than the homogeneity scale we can compare the predictions of perturbation theory from the previous section with the observations of large scale structure. These are provided by galaxy surveys such as [81, 111, 212, 213] which map the distribution of visible matter in the Universe; from redshift-space distortions, which measure local tidal affects; from galaxy lensing surveys, which measure the distribution of dark matter. Recently, these have been supplemented by the first lensing results of the CMB by LSS [200]. These observations have two main caveats. Firstly they operate on a wide variety of scales, from linear scales $\gtrsim$ 30Mpc to the non-linear regime $\lesssim$ 1Mpc [55]. Secondly, the bias which relates the distribution of luminous matter to the underlying structure of dark matter cannot be predicted from theory. Therefore predictions from cosmological perturbation theory can only be reliably tested on scales where both the matter perturbations and the galaxy bias are linear.

It would seem that ΛCDM manages to predict much of the cosmological properties which we infer from observations. We shall discuss the failures of the ΛCDM model, and plausible alternatives to it in the next section.

1.4 Cosmology in MG

There are three possible viewpoints which encourage modifications to GR. First there are theoretical considerations which disfavour the existence of the Λ in ΛCDM which are collectively known as the cosmological constant problem. Second, there are observational inconsistencies between the various cosmological probes used to justify ΛCDM. Third (provided we do not subscribe to Occam's Razor) we have no *a priori* reason to discard a theory until it has been ruled out either from theoretical considerations or by observational evidence. In Section 1.4.1 we illustrate the motivation for MG theories. In Section 1.4.2 we expand upon the cosmological probes discussed in the previous section in the context of testing MG. The next three sections are devoted to the three

main methods of generating predictions from MG theories: analytic, the quasi-static approximation and N-body codes.

1.4.1 Motivation for MG

If ΛCDM is to provide an accurate description of our Universe, then it must be self-consistent on all scales and at all times. There is some observational evidence that the latest cosmological probes are in tension with one another. Although this problem may be resolved with a better understanding of baryonic physics, we cannot rule out the alternative that we need to change our underlying theory of gravity.

Although ΛCDM has produced predictions which are compatible observations from a wide array of cosmological probes, the best-fit ΛCDM parameters do not necessarily agree between surveys. While the Planck measurements agree well with the expansion history derived from the BAO scale [81, 212, 213], the linear scale clustering signal, and the matter power spectrum [11, 208], tension arises from a variety of other sources. In particular, Planck 2015 favours a higher σ_8 value compared to weak lensing and cluster number counts; the $\sigma_8 - \Omega_m$ plane exhibits tension with CFHTLens and the value of $f\sigma_8$ with that from RSDs to $\sim 1.9\sigma$. Additionally, the value of H_0 disagrees with that from Lyman-α BAO measurements at 2.5σ [84]. We require larger surveys (Table 1.6; so-called "Stage-IV" experiments e.g. Euclid, BigBOSS) to clarify whether these discrepancies are serious enough to cast doubt over ΛCDM as our best-fit cosmology. In the long run, for ΛCDM to be a viable cosmology, different tests need to give consistent results, and the source of the present discrepancy is unknown.

Given that GR is theoretically motivated, it is important to consider objections which derive from either thought experiments or the Standard Model of high energy physics. Collectively, these suggest that the simplicity of the cosmological constant, despite its initial appeal, is in fact a serious flaw. The three parts of the cosmological constant problem (CCP) are:

1. The "old" naturalness problem (that $\Lambda \approx 0$),
2. The "new" dark energy problem (that $\Lambda \neq 0$),
3. The "coincidence" problem (that $\Omega_{\Lambda 0} \sim \Omega_{m0}$).

We will treat the first two simultaneously. This fine-tuning problem can be illustrated as follows. Recall that the left hand side of the Einstein equation admits a geometric cosmological constant term, while the right hand side admits a perfect fluid with $w = -1$. If we model this perfect fluid as the quantum energy density of the vacuum, then

[58]:

$$\rho_\Lambda = \frac{\Lambda_{\text{energy}}}{8\pi G_N/c^2} \sim M_{\text{Pl}}^4 \approx \left(10^{18}\text{GeV}\right)^4 \tag{1.25}$$

The difference between the geometric Λ and the energy Λ corresponds to the effective Λ which is that referred to in ΛCDM [58]:

$$\rho_\Lambda = \rho_{\text{crit},0}\left(1 - \Omega_{m0}\right) \approx 0.7\frac{3H_0^2}{8\pi G_N/c^2} \approx \left(10^{-12}\text{GeV}\right)^4 \tag{1.26}$$

Thus we see that the geometric term and the energy term cancel each other out to over 120 orders of magnitude, yet leave a non-zero residual. We cannot explain this fine tuning problem because the geometric term from GR should be completely independent of the vacuum energy from QFT.

The coincidence problem asserts that the value of the effective Λ is also at odds with the cosmological principle. The temporal corollary of the cosmological principle Definition 1.3 is that we cannot be privileged observers alive at some special epoch of the Universe. However, we have seen in the second Friedmann equation Definition 1.5 that the time during which the energy densities of matter and Λ are equal, corresponds to a very short period of the Universe. Just as we can apply a different cut-off energy scale to lessen the severity of the new CCP we can appeal to the anthropic principle to mediate the coincidence CCP. As we have already seen this only reduces the problem rather than removing it altogether. The very simplicity of Λ which makes it appealing means that we struggle to find physically motivated explanations for its observed behaviour.

We are left with two choices: replacing either Λ by a more complex form of dark energy or GR with a more complex description of gravity. In the next section we shall outline the observational techniques which allow us to distinguish both of these options from ΛCDM.

1.4.2 Observational tests of MG

There are five key tools for testing gravity, all of which operate on different scales. We address each one separately in this section: the CMB in Section 1.4.2.1, BAO in Section 1.4.2.2, redshift-space distortions in Section 1.4.2.3, gravitational lensing in Section 1.4.2.4 and supernovae in Section 1.4.2.5. Because each of these probes tests a subset of the cosmological parameters, they must often be used in conjunction with one another in order to break the degeneracy between parameters.

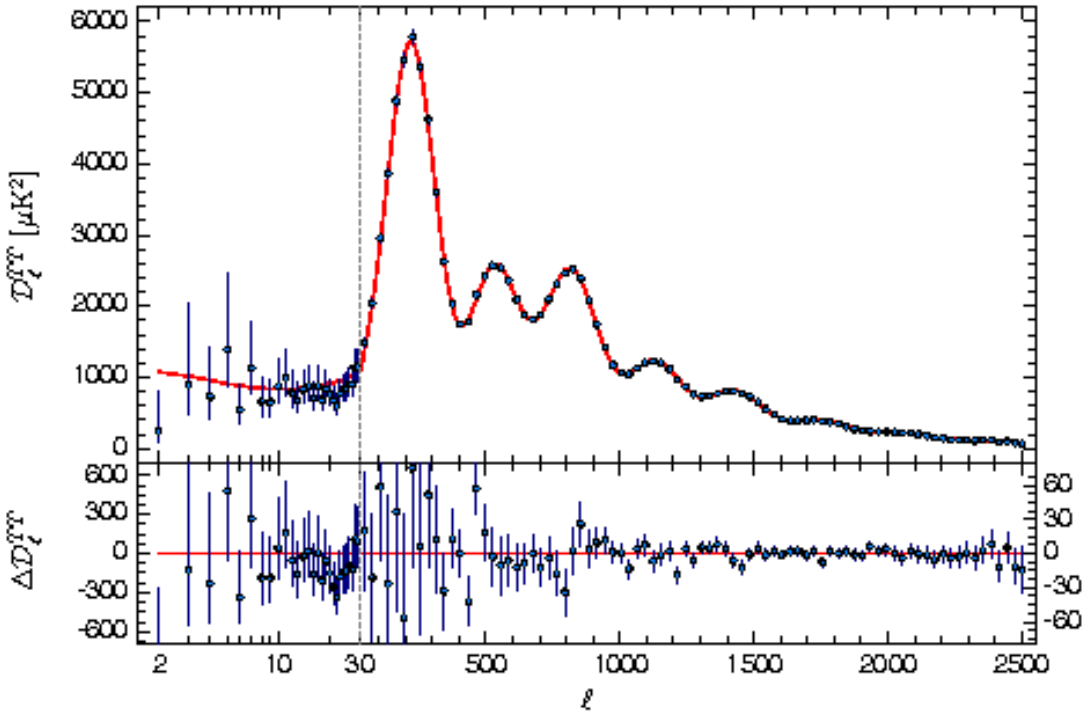

Figure 1.3: The Planck 2015 TT power spectrum, plotted as $\mathcal{D}_\ell = \ell(\ell+1)C_\ell/(2\pi)$ compared with the ΛCDM fit (red). Reproduced from [200]

1.4.2.1 The cosmic microwave background

The cosmic microwave background is a measure of the temperature (and now polarisation) fluctuations of photons emitted at the surface of last scattering. From this we can infer early-time modifications to gravity, zeroth order modifications via the expansion history and first order modifications via the potential wells of large scale structure. There is also a further possibility, namely gravitational lensing of the CMB but we defer this to Section 1.4.2.4.

MG theories which produce early time modifications can only be ruled out by the power spectrum of the CMB. The successful predictions of the temperature power spectrum (Fig. 1.3) using only thermodynamics, the standard model, cold dark matter and GR motivates most MG theories to reduce to GR at redshifts of $z < 1\,000$ [16]. Some MG theories which do not produce this behaviour, e.g. the cubic Galileon model have already been ruled out in this manner [28]. However the ease with which GR reproduces the CMB power spectra does not imply that all MG theories with early time modification should be ruled out *a priori*.

There are three stages in relating the CMB power spectrum produced by a given cosmology to the anisotropies observed on the sky [16].

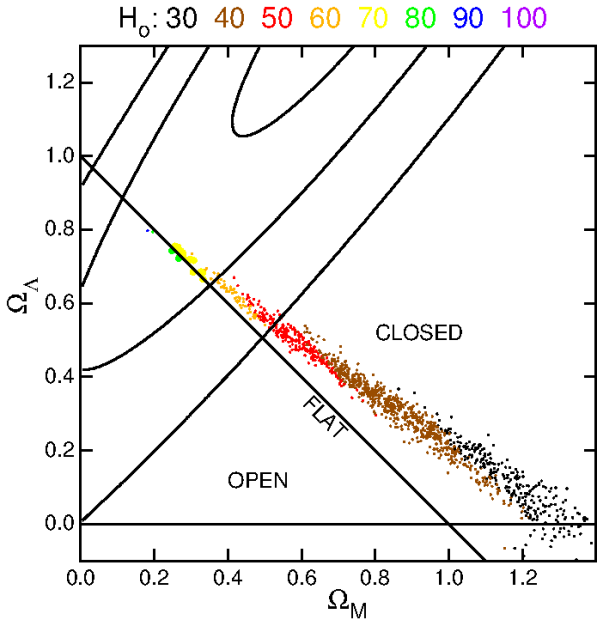

Figure 1.4: Constraints in the Ω_{m0}-Ω_Λ plane from SNe data ($1, 2, 3-\sigma$ contours), combined with values allowed by CMB data from WMAP (dots). Each value is colour-coded according to the value of H_0 (top), so that the straight line indicates the geometric degeneracy between H_0 and $\Omega_K = 1 - \Omega_{m0} - \omega_\Lambda$. Reproduced from [191].

1. Numerical solution of the coupled system of linearised Einstein equations, continuity and Euler equations for matter and the Boltzmann equations for photons and neutrinos.

2. Given the solution for the photon multiple moments at the redshifts of last scattering, calculation of how they are propagated to zero redshift.

3. Conversion of the photon temperatures into observable quantities.

The second stage of this process imparts information about the cosmological parameters. Late-time modifications produce anisotropies via the Sachs-Wolfe effect, the integrated Sachs-Wolfe effect (ISW) and the (thermal and kinetic) Sunyaev-Zel'dovich effect [127]. The probe of most interest in MG is the ISW, which is caused by the change in energy of the CMB photons as they traverse the evolving potential wells formed by LSS. If the potential wells were static over the photon-crossing time, then the blueshift from entering the potential well and the redshift from exiting it would precisely cancel. However, the clusters become more compact (and voids expand) and the potential wells deepen while the photons are still inside, so there is a net blueshift (or redshift) at the angular scales corresponding to large-scale over- (or under-)densities [16]. Quantitatively, this effect manifests in the temperature fluctuations as [228]:

$$\frac{\Delta T}{T} = -\int \mathrm{d}\,\eta\,[\Psi' + \Phi'] \tag{1.27}$$

(where a prime is differentiation with respect to conformal time). In the matter-

dominated regime of GR, the two potentials are equal, whereas in MG they are expected to differ. Unfortunately, the ISW effect is largest on large scales where we can make a limited number of independent measurements of the CMB angular power spectrum, so cosmic variance limits the constraints we can place on MG theories using this technique.

As is clear from Fig. 1.4, the CMB alone neither provides evidence neither for nor against ΛCDM. This is the geometric degeneracy: that the CMB provides constraint contours in the $\Omega_{m0} - \Omega_\Lambda$ plane but not between H_0 and Ω_K. It is only when we use additional cosmological probes that we rule out an open Universe without a cosmological constant.

1.4.2.2 Baryon acoustic oscillations

The Baryon Acoustic Oscillations (BAO) form a spectrum of standard cosmological rulers. Just as the first peak of the CMB represents the horizon scale at the time of photon-electron decoupling so does the first BAO peak measure the horizon scale at the time of baryon-photon decoupling [16]. Since we understand the physics which contribute to the physical size of the BAO upon creation, the angular size of this feature upon observation tells us the angular diameter distance to the peak. This allows us to infer the density budget of the stress-energy tensor.

The BAO was generated by the decoupling of electrons, photons and baryons during the era of recombination. Prior to recombination, all three species formed a plasma, in which electrons were coupled to photons via Compton scattering and to baryons via the Coulomb interaction [16]. While neutral atoms were formed from free electrons and ions, the Hubble expansion rate exceeded the Compton scattering rate, which caused photons to be causally decoupled from electrons. Subsequently, the high energy distribution of photons decreased so that electrons were also decoupled from protons. During this drag epoch at $z_{\rm drag}$, photons also decoupled from baryons because they were only linked via electrons. At this time of decoupling, the characteristic scale of fluctuations $r_s(z_{\rm drag})$ in the now non-existent plasma became imprinted on the distribution of baryons. In the late Universe this corresponds to an imprint on the distribution of galaxies which can be detected as an enhancement to the galaxy power spectrum [127]. The scale at which this enhancement occurs is known as the BAO scale.

Measurement of the BAO scale provides independent constraints on the angular diameter distance (Eq. (1.28a)) and the Hubble factor at the redshift of the drag epoch. This arises from the potential to measure the BAO feature in both radial (Eq. (1.28c)) and

transverse (Eq. (1.28b)) directions [16, 120]:

$$d_A(z) = \frac{c}{H_0(1+z)} \int_0^z \mathrm{d}\,\bar{z} \frac{1}{\sqrt{\Omega_{m0}(1+\bar{z})^3 + \Omega_{k0}(1+\bar{z})^2 + \Omega_{\Lambda 0}}} \tag{1.28a}$$

$$\theta_{\mathrm{BAO}}(z) = r_s(z_{\mathrm{drag}}) \frac{1}{(1+z)d_A(z)} \tag{1.28b}$$

$$\delta z_{\mathrm{BAO}}(z) = r_s(z_{\mathrm{drag}}) \frac{H(z)}{c} \tag{1.28c}$$

Recently the BOSS and WiggleZ galaxy surveys found results consistent with ΛCDM [55]. Despite this, we require surveys which extend to higher redshifts in order to distinguish ΛCDM from MG (rather than ΛCDM from SCDM). Thus the BAO spectrum is a useful probe on the equation of state at late times.

1.4.2.3 Redshift-space distortions

Redshift-space distortions are the major probe for testing linear perturbations generated by MG theories. The growth of large scale structure can be encapsulated by the growth rate f and its index γ [86]:

$$f(k,z) \equiv \frac{\mathrm{d}\,\Delta(k,z)}{\mathrm{d}\,\ln a(z)} = \Omega_m(z)^{\gamma(k,z)} \quad \text{where} \quad \gamma_{\mathrm{GR}} \approx 6/11 \tag{1.29}$$

This is a "smoking gun" for evidence of MG: for in GR the growth rate index is a constant and the growth rate depends only upon redshift. In contrast, most MG theories produce a scale-dependent growth rate [16]. For some MG models γ can be reasonably modelled by a constant which differs from GR ([87] e.g. $\gamma \approx 0.68$ for DGP, $\gamma \approx 0.4$ for $f(\mathcal{R})$). Parametrising the growth rate index enables a better distinction to be drawn between DE cosmologies, which typically have a slowly-evolving γ, whereas MG models have stronger variation [87]. We need to measure γ to far better than an uncertainty of 0.1 to distinguish between currently-plausible theories [198].

Measuring the growth rate in practice entails several difficulties. This is because we can only measure the redshift to luminous galaxies, which do not reflect the underlying distribution of dark matter. Thus we require a detailed understanding of galaxy bias, which is further exacerbated by the present need to probe the growth rate on non-linear scales. (On linear scales, one could use the relation that RSDs measure f/b while the galaxy auto-correlation function measures $\zeta_{\mathrm{mass}} b^2$ to eliminate the linear bias b via constraining $f\sigma_8$ [198].) Our aim is to measure the redshift-space galaxy power spectrum, which (aside from the desired f) also depends upon the velocity field v, normalised to $\mathsf{u} \equiv \mathsf{v}/(faH)$, its component and derivative along the line-of-sight (denoted by $||$)

[198]:

$$P^s(k,\mu) = \int \frac{\mathrm{d}^3\mathsf{r}}{(2\pi)^3} \exp\left(-i\mathsf{r}\cdot\mathsf{k}\right) \langle \exp\left(-ik\mu f u(\mathsf{r})\right) \cdot \left[\delta(\mathsf{x}) + f\partial_{||}u_{||}(\mathsf{r})\right] \left[\delta(\bar{\mathsf{x}}) + f\partial_{||}u_{||}(\mathsf{r})\right] \rangle \tag{1.30}$$

using the shorthand $f(\mathsf{r}) = f(\mathsf{x} - \bar{\mathsf{x}})$. The redshift-space distortion indicates the deviation in this power spectrum from the cosmological redshift obtained purely from background expansion (i.e. the effect of the local potential). The distortion is caused by the peculiar velocity of the galaxy during its in-fall to the bottom of the cluster potential, so it has different effects depending upon the scale under examination. A variety of approximations to Eq. (1.30) exists, which attempt to approximate the kinetic behaviour of the galaxies which are produced in the "Fingers of God" effect shown in Fig. 1.5. Briefly, on large scales (of order 10Mpc) the motion of neighbouring galaxies will be correlated, part of an overall flow towards the bottom of the potential; whereas on halo scales ($\sim$ 1Mpc) the galaxy motions are randomly dispersed; thus we find in the correlation function $\xi(r_p, \pi)$ an increased radial dispersion (along π) at small scales and an increased transverse dispersion (along r_s) on larger ones [198].

Observation of the growth rate is currently at a boundary between "trigger" and "model" surveys. Whereas recent surveys (results shown in Fig. 1.6) can only provide evidence for ΛCDM at a certain confidence level, upcoming surveys have the potential to distinguish between the growth rate from competing MG theories [55].

1.4.2.4 Gravitational lensing

Gravitational lensing (GL) provided the first experimental test of GR. It is well known that Eddington's solar eclipse measurement of gravitational lensing provided the first observation capable of distinguishing GR from Newtonian gravity. A century later, GL provides five different tests of GR [16]:

1. Solar gravitational lensing of the positions of stars during an eclipse;
2. Microlensing of galactic sources, which induce pulsar time delays and temporary magnification of galactic stars;
3. Lensing of high redshift sources by intervening galaxies;
4. Lensing of galaxy distributions by large scale structure;
5. Lensing of the CMB by large scale structure.

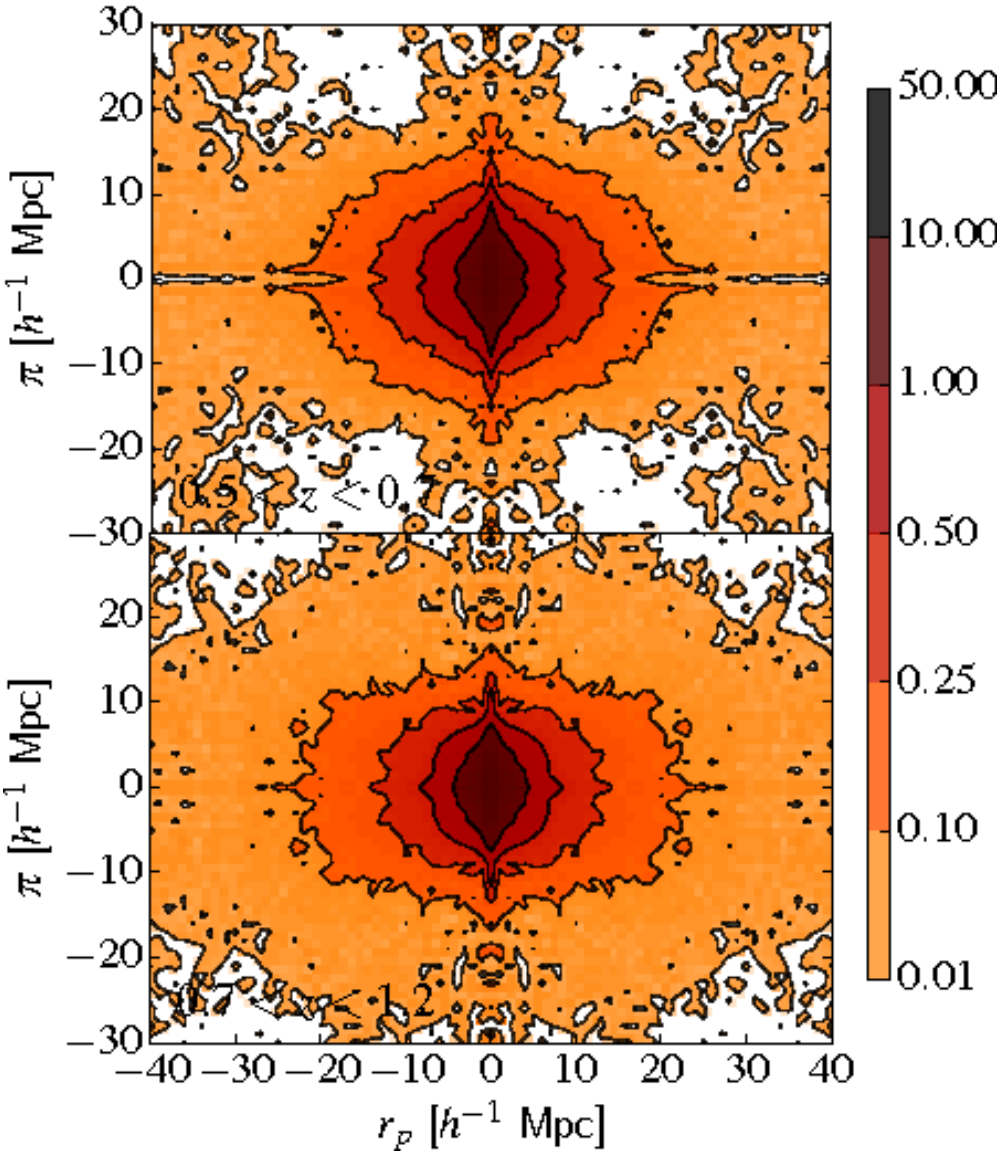

Figure 1.5: Final measurements of the anisotropic redshift-space correlation function, $\xi(r_p, \pi)$ at $z = 0.5$ from the final data of the VIPERS survey. Solid contours correspond to iso-correlation levels of 0.01, 0.1, 0.25, 0.5, 1 [242].

The first three effects are examples of strong lensing, where the source is magnified by the gravitational effects of the lens [220]. The last two are examples of weak lensing in which the effect of the lens is to shear rather than magnify [27]. While the last three effects are potential cosmological probes, only cosmic shear and CMB lensing have been observed to date.

Gravitational lensing has the advantage that it probes the stress-energy tensor of the lens, rather than relying on only the luminous component [220]. If we take the lens to be the intervening large scale structure between the source and observer, then we can model this in terms of the co-moving distance throughout the structure and the linear metric potentials. We have already seen in Section 1.3.2 that at linear-order scalar, vector and tensor perturbations decouple. Consequently, the scalar potentials can be

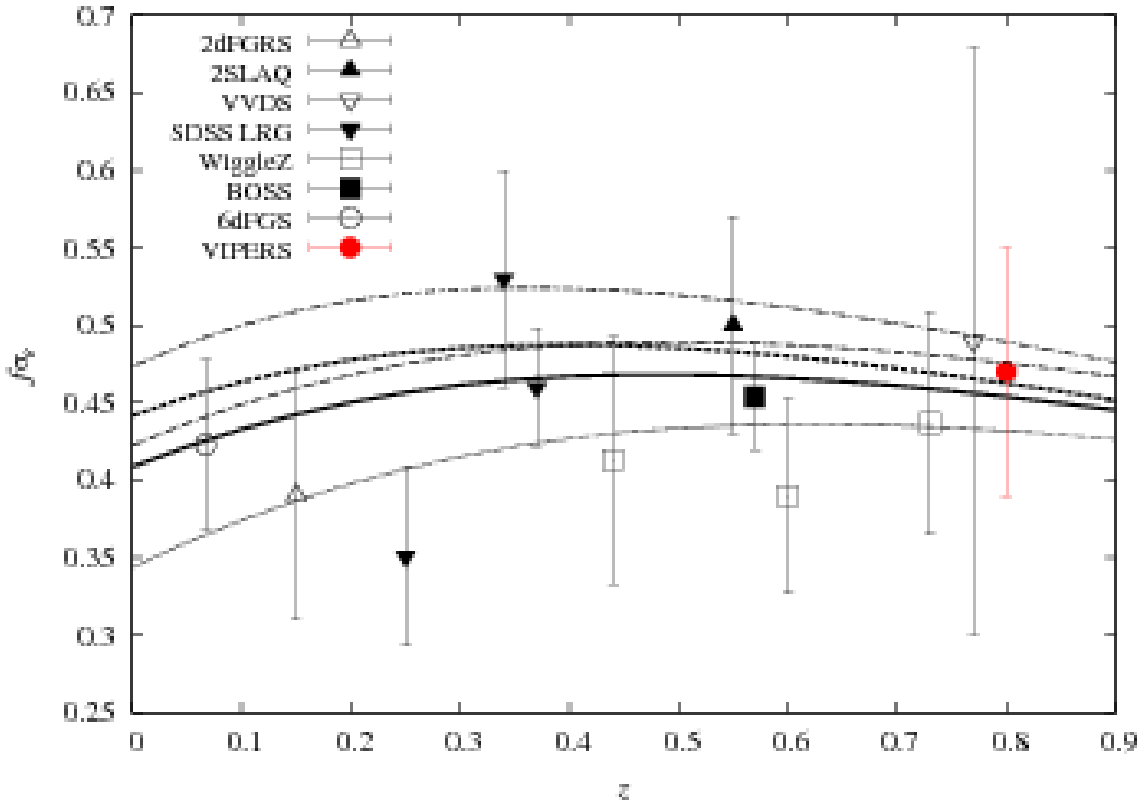

Figure 1.6: Predictions of $f\sigma_8$ from various gravity theories (lines) compared to data from recent RSD surveys (points). The thick solid (dashed) curve corresponds to the prediction for General Relativity in a ΛCDM model with WMAP9 (Planck) parameters, while the remainder are DGP (dotted), coupled DE (dot-dashed), and $f(\mathcal{R})$ (dot-dot-dashed) respectively. Reproduced from [241].

inferred from the TT power spectrum and the galaxy power spectrum, whereas the vector and tensor perturbations require knowledge of the EE and BB power spectra of the CMB. (In practice this is difficult.)

In galaxy weak lensing surveys, we use the cosmological principle to extract cosmic shear from the statistical ellipticity of distant galaxies. Recall that, if we are not privileged observers, then the elliptical galaxies surrounding us must be randomly oriented. While this is approximately true, the presence of the cosmic web produces an obscuring factor called intrinsic alignment, which will become increasingly important in future surveys [220]. Neglecting intrinsic alignment, the lensing transformation between the true (unobserved; θ) and lensed (observed; β) angular positions is entirely given by the local potential ψ [27]:

$$\frac{\partial\beta}{\partial\theta} = \delta_{ij} - \frac{\partial^2\Psi}{\partial_i\partial_j\theta} = \begin{pmatrix} 1-\kappa-\gamma_1 & -\gamma_2 \\ -\gamma_2 & 1-\kappa+\gamma_1 \end{pmatrix} \tag{1.31}$$

Since we cannot observe the unlensed galaxy we must rely on the aforementioned randomness of the galaxy distribution. Any correlations in the convergence term κ and the

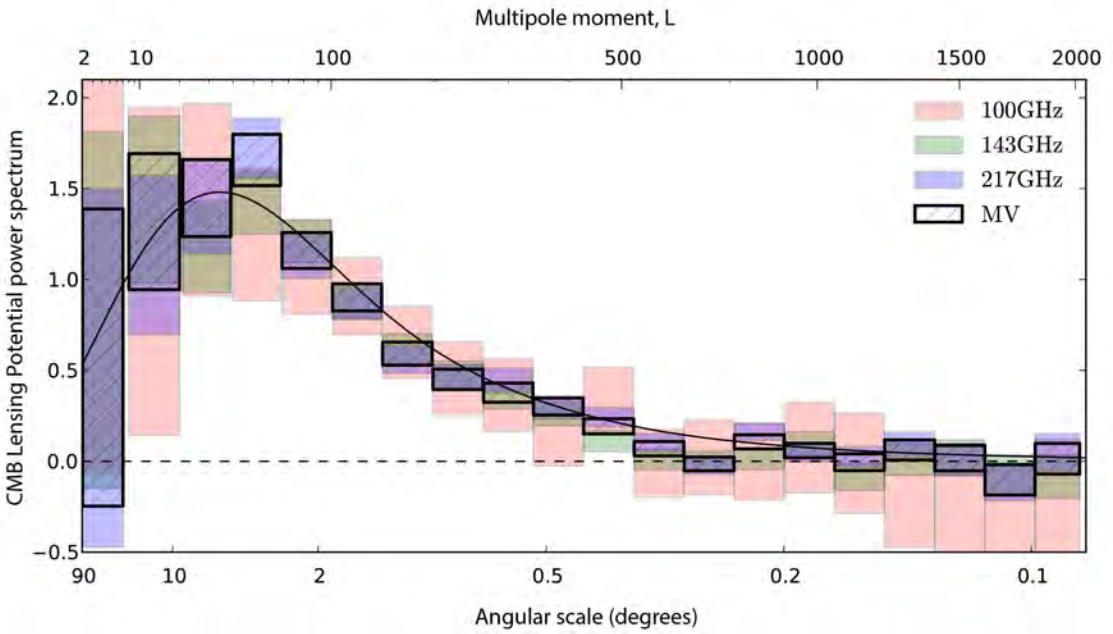

Figure 1.7: The lensing power spectrum as a function of angular scale from [200], at different frequencies (shaded) and the minimum variance combination of these (hatched).

complex shear term $\gamma = \gamma_1 + i\gamma_2$ must be due to the gravitational potentials $\psi \approx \Psi + \Phi$ [27]. While some work has been done on measuring cosmic convergence, the bulk of galaxy weak lensing has been concerned with estimating the shear term. Due to the statistical uncertainties involved, weak lensing must be much better calibrated before it is a useful probe of MG.

Analogous to the weak lensing of distant galaxies is that of the CMB. This permits the CMB to act as a probe of both high redshift and low-redshift regimes. Consequently, the CMB does not need to be combined with late Universe probes to break the geometric degeneracy [235]. The three major CMB telescopes—ACT, SPT and Planck—have all detected CMB lensing. Fig. 1.7 shows the latest results from Planck (2015) for the lensing power spectrum. Qualitatively the amplitude of the lensing power spectrum is increased when LSS forms with deeper potential wells. For example, in the presence of a cosmological constant or a fifth-force structures will grow more slowly and so the photons of the CMB will travel through shallower potential wells. Comparing the equation of state of ΛCDM to MG allows us to generate predictions for the power spectrum.

1.4.2.5 Type Ia supernovae

Type Ia supernovae (SNe) provided the first inescapable evidence that the expansion of the Universe was due to dark energy rather than geometric curvature [196, 210].

Standard candles provide a fixed luminosity with varying redshift. Consequently the apparent magnitude of a standard candle depends only upon the luminosity distance D_L, which can be converted to a redshift via a cosmological model. In ΛCDM:

$$D_L \equiv \sqrt{\frac{L}{4\pi S}} = (1+z)\frac{c}{H_0}\int_0^z \mathrm{d}\,\bar{z}\frac{1}{\sqrt{\Omega_{m0}(1+\bar{z})^3+\Omega_{k0}(1+\bar{z})^2+\Omega_{\Lambda 0}}} \tag{1.32}$$

where L is the bolometric[1] luminosity and S is bolometric flux [120]. Directly related to D_L is the distance modulus μ [120]:

$$\mu(z) \equiv 5\log\frac{D_L}{10pc} = m(z) - M = -5\log h + 42.38 + \kappa\,(z) + A(z) + 5\log D_L(z) \tag{1.33}$$

In practice a variety of effects complicates calculation of apparent magnitude $m(z)$, which in the second equality are [162]:

1. M (absolute magnitude) the object's brightness if it were 10 pc distant
2. $h(z)$ (Hubble parameter) $H_0/(100\text{km s}^{-1}\text{Mpc}^{-1})$,
3. $\kappa(z)$ (k-correction) adjustment for measuring m and M at different wavelengths
4. $A(z)$ (absorption) adjustment for the absorption of light by the interstellar medium

Thus we can convert the distribution of observed supernovae (apparent) magnitudes at an observed redshift to a constraint on the underlying expansion of the Universe.

The specific nature of the Type Ia SN strongly indicates that it is a standard candle. It is commonly held that Type Ia SNe are the thermodynamic explosion of white dwarves [115]. Thus its peak luminosity is independent of the surrounding conditions because it depends on the white dwarf reaching a fixed mass limit. Large-scale studies such as [110] have released a common spectral evolution for SNe Ia and support this by proposing a common physical mechanism explaining the small dispersion in spectra. In particular, there is currently no evidence that Ia SN evolve with redshift [163]. Despite this, a number of studies (e.g. [227]) suggest that the standard candle model for calculating M is only partially correct and that additional parameters need to be added. The general consensus is that more high-z data is required for any conclusive evidence. The use of SNe as cosmological probes has played a vital role in breaking the degeneracy between results from Sne, BAO and the CMB.

[1]This refers to a quantity measured over all wavelengths. A bolometer is a hypothetical device capable of doing so.

1.4.3 The quasi-static regime

On non-linear and weakly linear scales, many approximations can be used to render MG analytically tractable. The most important of these is the quasi-static approximation (QSA). Broadly speaking, this simplifies the equations of motion of the matter fields in the stress energy tensor and also the evolution of metric perturbations in the Einstein tensor. This often reduces complex PDEs into ODEs or algebraic equations in Fourier space. These simplifications are necessary not only in the context of perturbation theory but also in the programming of numerical simulations. In this section we summarise the QSA and outline the extent to which it has been studied in MG. It will be a key aim of this thesis to determine the scales at which QSA provides an accurate approximation.

Let us briefly summarise what exactly the quasi-static approximation entails. In essence it contains two separate assumptions as discussed e.g. in [226]: (a) The relative suppression of time derivatives of metric/field perturbations compared with their spatial derivatives $|\nabla^2 X| \gg \left|\dot{X}\right|$. (b) A sub-horizon approximation $k \gg aH$ or, in Euclidean rather than Fourier space $|\nabla^2 X| \gg \mathcal{H}^2 |X|$. In ΛCDM-like models, the evolution time scale for perturbations is set by the Hubble rate: $\mathcal{H}|X| \geq \left|\dot{X}\right|$; equivalently $\mathcal{H}\left|\dot{X}\right| \leq \mathcal{H}^2|X|$. Now on sub-horizon scales $\mathcal{H}^2|X| \ll |\nabla^2 X|$ by definition. Combining these inequalities, we see that time derivatives are small compared to spatial ones as required. Consequently assumption (b) entails (a). This is not necessarily the case in MG—we shall see the importance of this in Chapter 3.

The usefulness of the quasi-static approximation and consequently its wide-spread use (consider for example the N-body codes [158, 167, 204]) stem from the fact that evaluating the full (un-approximated) evolution equations in N-body simulations is a task which is often computationally expensive. An illustrative example are chameleon scenarios where evaluating the full evolution equations quickly leads to computations requiring $\sim \mathcal{O}(10^7)$ more time steps than their quasi-static counterparts or more [51]. In $f(\mathcal{R})$ models N-body simulations implementing the quasi-static approximation have been carried out e.g. by [102, 126, 146, 150, 190, 216][2], see especially [190] for a numerical check of the quasi-static approximation in this context. For related chameleon models [134] also see [52, 170]. Non-linear structure formation in braneworld-inspired DGP models [92] has been probed by [62, 136, 146, 152, 216, 217, 218], where [217] concludes that the quasi-static approximation is a self-consistent approach on sub-horizon scales in this setup. Linear [23] and non-linear [24, 25, 160] structure formation for galileon models [187] have also been probed. Interestingly there the quasi-static approximation may break down particularly in low density regimes. In the linearised

[2]Interestingly the recent work of [3] outlines a different simulation strategy not explicitly relying on quasi-static behaviour and which should be applicable to models with relativistic scalars in the future.

regime, however, it generically performs well on sub-horizon scales [23].

While the quasi-static approximation therefore appears to do reasonably well in a number of model-specific contexts and there are very good arguments for its general 'reasonableness' in known observationally viable modified gravity models [226], there are also known cases where it explicitly breaks down even on sub-horizon scales [77, 166]. Note, however, that it is not quite clear whether any of those known non-quasi-static scenarios have clear observational signatures in allowed regions of parameter space. In this context also especially note the work of [77], which links the applicability of the quasi-static approximation on sub-horizon scales in $f(\mathcal{R})$ models to the proximity of the background evolution to ΛCDM[3] and also [121] who also probe linear growth in $f(\mathcal{R})$ theories in the quasi-static approximation. The quasi-static approximation is also extended to Jordan-Brans-Dicke theories in [61] and to $f(R,T)$ models in [7][4], where the inclusion of an $f(T)$ term causes scale-dependent behaviour of the density oscillations (in both the unapproximated equations and the quasi-static limit), resulting in inaccurate quasi-static behaviour. In general, and particularly for non-linear structure formation, however, the de facto necessity of the approximation in numerical modelling makes it inherently difficult to precisely determine its range of validity.

One of the key consequences of the quasi-static approximation is that it corresponds to the regime in which MG can be treated as a fifth force. Under these conditions we can model the dynamical effects of MG as an additional multiplicative factor to G_N. This acts as an additional repulsive force to counteract gravitational attraction. Although we can often tune the expansion history of an MG theory to mimic that of ΛCDM, it is far more difficult to mimic the growth of structure in the quasi-static regime.

1.4.4 N-body simulations

We have already seen that the halo model (Section 1.3.3) predicts the abundance of haloes and the statistics of their distribution on linear scales. On weakly-linear scales (if we require a high degree of precision) and on non-linear scales, we must turn to a fully numerical treatment. Collisionless N-body simulations are sufficient to describe the dynamics of dark matter on cosmological scales. Collisionful simulations containing both dark matter and baryons are necessary on cluster and galactic scales. Although most simulations employ Newtonian equations, in recent years there has been some

[3]More precisely, the condition is $|\partial_{\mathcal{R}} f(\mathcal{R})| \ll 1$ at all times. The present-day value of $\partial_R f(\mathcal{R})$ is abbreviated $f_{\mathcal{R}0}$. In particular this means that large classes of observationally viable $f(\mathcal{R})$ theories, i.e. those falling within the constraint $|f_{\mathcal{R}0}| \leq 10^{-6}$ imposed by a combination of solar-system and galaxy-halo tests [124], should satisfy a number of constraints [77, 121] guaranteeing good quasi-static behaviour.

[4]The scalars R and T are the Ricci scalar and the trace of the stress-energy tensor respectively

Name	Code	L_{box}(Mpc/h)	$N_p \times 10^9$	$m_p(M_\odot/h)$	Ref.
DEUS FUR	Ramses-Deus	21000	550	1.2×10^{12}	[5]
Horizon Run 3	Gotpm	10815	370	2.5×10^{11}	[137]
Millennium-XXL	Gadget-3	3000	300	6.2×10^9	[12]
Horizon-4Π	Ramses	2000	69	7.8×10^9	[237]
Millennium	Gadget-2	500	10	8.6×10^8	[229]
Millennium-II	Gadget-3	100	10	6.9×10^6	[43]
MultiDark Run1	Art	1000	8.6	8.7×10^9	[201]
Bolshoi	Art	250	8.6	1.4×10^8	[139]
Phoenix A-1	Gadget-3	41.2	4.1	6.4×10^5	[106]
Aquarius A-1	Gadget-3	5.9	4.3	1.7×10^3	[230]
GHalo	Pkdgrav2	3.89	2.1	1.0×10^3	[232]
Via Lactea II	Pkdgrav2	4.86	1.0	4.1×10^3	[88]

Table 1.2: Current state of the art in DM-only simulations on cosmic, cluster, and galactic scale. Summarised from [147].

Simulation	core-hours ($\times 10^6$)	N_{cores}	memory (TB)	disk space (TB)
DEUS FUR	10	38016	230	3000
Horizon Run 3	4	8240	21	400
Millennium-XXL	2.86	12288	28.5	100
Horizon-4Π	8	6144	14.7	300
Millennium	0.35	512	1	20
Millennium-II	1.4	2048	8	35
MultiDark Run1	0.4	4000	8	20
Bolshoi	6	13900	12	100
Phoenix A-1	1.9	1024	3	15
Aquarius A-1	3.5	1024	3	45
GHalo	2	1000	1	60
Via Lactea II	1.5	3000	0.3	20

Table 1.4: Supercomputers and computational resources utilized for each simulation. Summarised from [147].

progress towards relativistic N-body simulations. While the difference between Newtonian and relativistic simulations is negligible for GR, this may not be the case for MG. Nonetheless, MG simulations are currently performed in Newtonian conditions. In the next few sub-sections we shall discuss each of these points in turn.

Current and future observational surveys (Table 1.6) aim to probe the Universe up to non-linear scales of $k = 1$ across a large angular fraction (or indeed the entirety) of the sky. The cosmological data extracted from these surveys must be compared to theoretical predictions of corresponding complexity (and size). This involves the numerical modelling of highly non-linear equations and the super position of the dynamics of

degenerate or interacting fields. Over the last five decades, the computational power available to N-body simulations has increased to the point that they have become the pre-eminent tool for making theoretical predictions on cosmological scales. Therefore they are an essential link between theory and observation.

The growth of N-body simulations has closely followed Moore's law when measured by the total number of simulation particles. It is well known that for N greater than 2 there is no analytical solution to describe their gravitational interaction. While the first N-body experiment by Holmberg in 1941 used light bulbs to achieve $N = 100$, the first computational simulations in 1960 had only $N = 16$ [83]. As of 2011, the state of the art is $N = 10^6$ for collisionful simulations and $N = 10^9$ for collisionless ones (Fig. 1.8. This indicates the relative difficulty in incorporating baryons into cosmological simulations. Nonetheless N-body simulations have already played an important part in replacing SCDM with ΛCDM as the concordance cosmology. Comparison of the galaxy correlation function from the APM galaxy survey [177] with the dark matter correlation function from the N-body simulation of [254] showed that the observations were incompatible with a dark-matter–dominated Universe [147]. Efstathiou *et al.* resolved this discrepancy by reducing Ω_{m0} to 0.2 and adding a cosmological constant with $\Omega_\Lambda = 0.8$ [95]. As the observational consequences of competing cosmologies become increasingly similar it is all the more important to understand and quantify the approximations made in N-body simulations.

For the last few decades a large amount of effort has been expended in the improvement of N-body codes for ΛCDM. This has improved the efficiency and scalability of a variety of algorithms, which can be principally divided into grid-based and particle-based codes. A recent selection is shown in Table 1.2. It has become important to verify the consistency of these codes and between the codes which extract halos and sub-halos, voids, galaxies and merger histories from the simulations [140, 141, 219]. This minimises the systematics inherent in the complex task of extracting structure formation. This agreement between codes is vital in the construction of theoretical predictions to percent-level accuracy, out to scales of $k = 1$.

The development of N-body simulations which include either dark energy or modified gravity is a much more recent phenomenon. This is because a simulation must not only solve the Vlasov and Poisson equations of weak-field GR, but also the equation of motion of the dark energy field or its MG equivalent [260]. The non-linearity of the equations necessitates the use of the quasi-static approximation as a simplifying factor. A wide variety of codes exist (e.g. generic codes [159, 165, 203]; other codes for specific forms of MG are discussed in Chapter 2) and there has already been considerable effort taken to compare the results of these codes. The discrepancy in MG codes is approximately 1% for both the matter and the velocity power spectrum at $z = 0$, but at the 10% level for

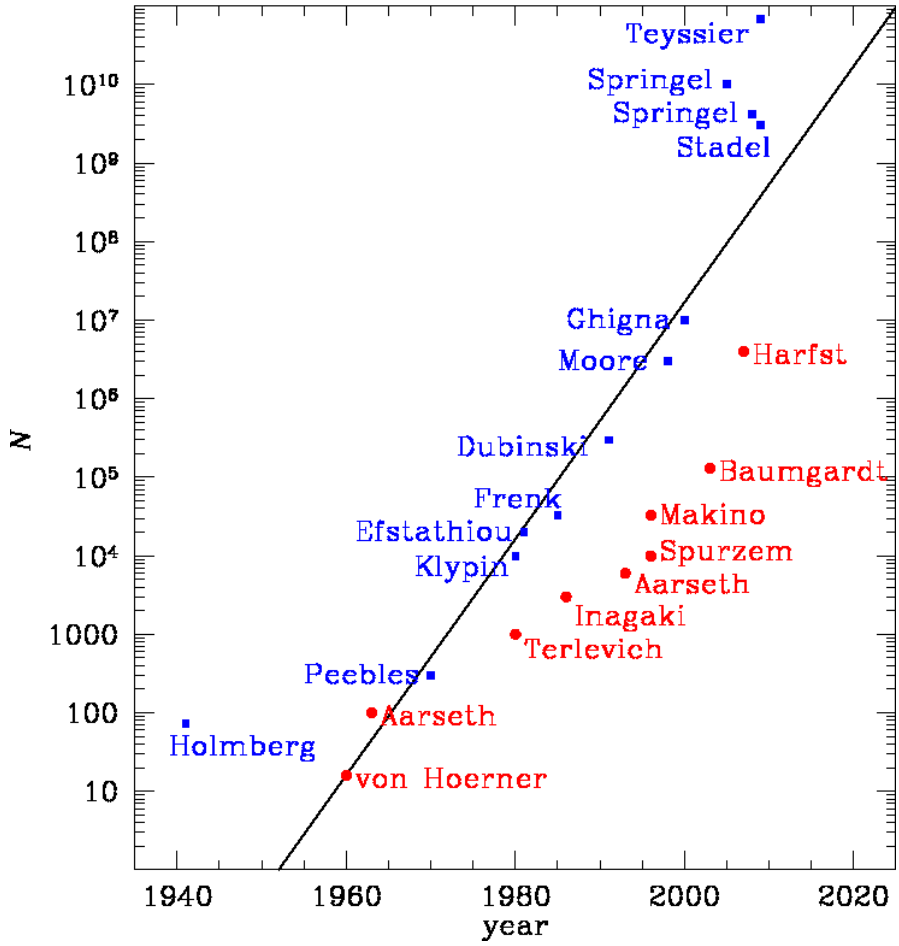

Figure 1.8: Number of particles in a variety of collisional (red) and collisionless (blue) N-body simulations by year. Reproduced from [17].

the halo mass function and there is excellent agreement for the dark matter halo profiles [260]. This strongly suggests that MG N-body codes will provide robust hypotheses which will be observationally testable by the next generation of surveys.

Simulating MG on cosmological scales necessitates dark matter-only simulations. Thanks to the collisionless nature of dark matter, the virial theorem holds [83]

$$\sum_i \{2T_i + W_i\} = 0 \quad \text{where} \quad T_i \equiv \frac{1}{2} m_i \dot{\mathsf{x}}^2 \quad \text{and} \quad W_i \equiv m_i \mathsf{x}_i \ddot{\mathsf{x}}_i \tag{1.34}$$

(as usual, $\dot{\mathsf{x}} \equiv \frac{\mathrm{d}\mathsf{x}_i}{\mathrm{d}t}$ *etc.*) which defines a virialised structure by virtue of having reached a state of equilibrium [109], in which kinetic and potential energy are balanced. The underlying aim is to treat the dark matter particles as a continuous fluid and to solve the resulting collisionless Boltzmann equation [96]:

$$0 = \frac{\mathrm{d}f}{\mathrm{d}t} = \frac{\partial f}{\partial t} + \dot{\mathsf{x}} \frac{\partial f}{\partial \mathsf{x}} - \frac{\partial \Phi}{\partial \mathsf{x}} \frac{\partial f}{\partial \dot{\mathsf{x}}} \tag{1.35}$$

where the spatial density and gravitational potential Φ are defined by integrating over

the phase-space distribution function $f(t, \mathsf{x}, \dot{\mathsf{x}})$. A solution can be found if the system is in equilibrium according to Jeans theorem [83, 96]. However, most LSS formation does not occur in or near equilibrium by definition. Because it is impractical to solve the CBE directly, we instead model the distribution using discrete points which form the N-body simulation. Thanks to linear perturbation theory, we have a Hamiltonian for each particle, which can be solved to find the local Newtonian potential, whence we obtain the Newtonian geodesic equation which governs the motion of each particle [83]. This illustrates that the main challenge in N-body simulations is calculation of the local force (or potential) throughout the box. This problem must be addressed through the use of novel numerical techniques if we are to generate many high-resolution, large-volume simulations required to distinguish between MG theories.

We also require collisionful N-body simulations in order to characterise baryonic effects. This is especially important if we are to accurately model the bias between luminous matter and dark matter, for we have already seen that on weakly-linear scales we cannot neglect baryonic physics if we are to measure the matter power spectrum to the percent level [219]. In collisionful systems, the relevant Hamiltonian and equations of motion are generally solved by brute force [83]. The corresponding phase space grows from six dimensions (for collisionless simulations) to $6N$ dimensions, so the force calculation scales as $\mathcal{O}(N^2)$. The dominant problem in these simulations is the ensuring the accuracy of temporal evolution, especially because the dynamical time for interactions is much less than the relaxation time of the two body interactions [83]. Given these difficulties, it is not surprising that baryonic simulations have only been performed in ΛCDM [17].

It is possible that the Newtonian approximation used in most N-body codes is insufficient. Recent work by [1, 2, 3] has focussed on the development of GR N-body simulations. These simulations are DM-only, but use all six degrees of freedom in the metric perturbations and do not apply the quasi-static approximation. They assume that metric perturbations are small, but place no constraints on the size of energy perturbations, nor on the gradients of the perturbations [2]. However, the prevailing consensus is that the relativistic approach does not produce large discrepancies from the Newtonian approach [2, 112]. Provided that metric perturbations are small, changes exist at the percent level, which are attributed to frame dragging [2]. Despite this, the relativistic approach may be especially useful in MG scenarios, where relativistic corrections may contribute a non-negligible departure from GR predictions.

Dates	Survey	Location	Probe						Area	Depth
			BAO	CMB	GPR	GSR	SN	WL	(deg.^{2})	(z)
2003–2011	CFHTLens	Hawaii			×			×	170	0.7
2006–2011	WiggleZ	Australia	×			×			10 000	$0.2 < z < 1.0$
2009–2011	Planck	space		×					30 000	1 100
2009–2014	Boss	New Mexico	×			×			10 000	0.5, 2.5
2010–2014	pan-starrs-1	Hawaii			×		×	×	30 000	0.5
2012–2015	hetdex	Texas	×			×			420	$1.9 < z < 3.5$
2012–2016	pan-starrs-2a	Hawaii			×		×	×	30 000	0.7
2012–2017	des	Chile			×		×	×	5 000	0.7
2012–2017	subaru	Hawaii			×			×	2 000	$0.6 < z < 1.2$
2012–2017	vst-kidsb	Chile			×			×	1 500	0.6
2014–2015	halo	balloon						×	1000	0.9
2014–2024	LSST	Chile			×			×	20 000	0.9
2017–2022	bigboss	Arizona	×			×			14 000	$0.2 < z < 1.7$
2018–2023	Euclid	space			×	×		×	15 000	0.9
2022–2027	wfirst	space			×			×	30 000	1

Table 1.6: A range of existing and proposed surveys capable of testing gravity. The probes are: BAO, baryonic acoustic oscillations; CMB, cosmic microwave background; GPR, galaxy photometric redshifts; GSR, galaxy spectroscopic redshifts; SN, supernova; WL, weak lensing. [Based on Table 1 from [30]].

1.5 Problems addressed in this thesis

Having outlined the motivation for this thesis and placed it in context, we now summarise its aims.

Chapter 2 describes the MG models which are studied in detail in this thesis.

In Chapter 3 we are interested in the domain of validity of the quasi-static approximation. We investigate this using a chameleon scalar field which serves as an approximation to the scalar field component of the stress-energy tensor produced by families of scalar-MG theories. For cosmologically sensible behaviour of the scalar field, i.e. satisfaction of the slow-roll condition, we find that the quasi-static approximation is valid into the weekly-linear and sometimes the non-linear regime.

Chapter 4 explains how the halo mass function is calculated in both GR and MG. It outlines the excursion set mechanism for providing a theoretical approximation to the HMF. We also summarise the cosmic web formalism, which also accounts for the geometry of the environment as well as its density. Then the various ways of marginalising over the environment "nuisance parameters" are discussed. More prosaically, we summarise fitting functions for the HMF and demonstrate how to extend these from GR to MG. We present the results of the varying methods proposed to incorporate screened MG into the HMF and assess their efficacy.

In Chapter 5 we study the universality of the halo mass function in a variety of screened MG theories. In particular, we address the question of whether HMF's which are derived and calibrated using ΛCDM simulations can be suitably recalibrated to retain their accuracy in MG. We investigate whether evidence for MG can be mistaken for changes in the mass function generated from ΛCDM. We also quantify the invariance of the HMF to modifications of gravity and discuss whether additional gravitational degrees of freedom necessitate additional free parameters in the HMF.

In Chapter 6 we examine semi-analytic predictions for $f(\mathcal{R})$ gravity in more detail. Using the cosmic web, we develop a semi-analytical approximation to the HMF in different geometric structures of LSS. We also show the dependence (or lack thereof) of various halo properties on the geometry of the local environment.

We conclude in Chapter 7, which summarises the key results of this thesis and discusses avenues for further work.

Chapter 2

Screened gravity theories

Screened gravity theories exhibit a fifth-force contribution to gravity which is spatially dependent, thus enabling it to evade local tests of gravity but remain effective on larger scales [257]. In Section 2.1 we demonstrate how the various theories arise from the addition of a scalar field term to the Einstein-Hilbert Lagrangian, which results in an effective gravitational constant $G_{\rm eff} = (1 + F_{\rm eff})G_N$ in the weak-field limit. We classify the theories according to the circumstances in which they are screened. The remaining sections apply the results of Section 2.1 to each of the MG models used throughout the rest of this thesis: $f(\mathcal{R})$ in Section 2.2, Symmetron in Section 2.3 and DGP in Section 2.4. Our parameter values are tabulated in Table 2.2.

MG model	Ref.	$A(X,\phi)$	$B(X,\phi)$	$V(\phi)$	F_{eff}	Parameter values
$f(R)$	[124]	Eq. (2.7)	0	Eq. (2.9)	Eq. (2.14)	$\lvert f_{R0}\rvert = 10^{-5}, 10^{-6}$ $n_{f(R)} = 1$
Symmetron	[116]	Eq. (2.16)	0	Eq. (2.16)	Eq. (2.18)	$\lambda = 1$ Mpc$/h$ $\beta_0 = 1$ $a_{\text{SSB}} = 0.33, 0.5$
normal DGP	[91]	0	1	0	Eq. (2.26)	$r_c = 1.2, 5.6$ c/H$_0$

Table 2.2: The various gravity models used in this thesis, described in Sections 2.2 to 2.4.

2.1 Types of screening

The MG theories studied in this thesis share a common trait to ensure that the successes of GR are unaffected by any modifications. The **screening mechanism** is a technique whereby fifth-force modifications to GR are "screened away" in regions where the theory must mimic GR in order to be experimentally viable. A range of such techniques exists, so we limit ourselves to scalar fields (although [33] suggest a mechanism for vector fields). Currently, there are three[1] types of screening possible with a scalar field, namely: **chameleon** [135], **symmetron** [116, 117] and **Vainshtein** [246]. We explore these categories of screening by selecting one theory from each family, namely: Hu & Sawicki $f(\mathcal{R})$ in Section 2.2 (chameleon), Hinterbichler-Khoury in Section 2.3 (symmetron) and Dvali-Gabadadze-Porrati in Section 2.4 (Vainshtein). Beforehand, this section unifies the mechanisms by showing how they can be derived from the one action, then sets the background expansion in terms of an effective dark energy, before the effects on the halo model manifest as an effective modification to G_N.

First we introduce the notion of a conformal reference frame (Definition 2.1). Recall that the equivalence principles in Definition A.4 introduced the concept of the frame of reference. Now we generalise this to MG theories, in which the strong equivalence

[1]There are various ways of classifying screening theories, e.g. [128] group theories by the order of derivatives of the scalar field. In this work we have absorbed dilaton models [78] into the symmetron class (both reliant on weak coupling) and kinetic models [15] into the Vainshtein class (both reliant on the inertia of the scalar field).

principle does not hold [256]. As a result, two reference frames (which would otherwise be locally inertial in GR) may be mathematically equivalent (i.e. quantities are conformally related, preserving the geometry of the manifold) but not physically equivalent (i.e. measuring a quantity may give differing results depending upon what is being observed [231]; or may give the same result but lead to a different interpretation [89]). Since this equivalence is a point of some contention, we give more concrete examples below.

Definition 2.1 (Conformal reference frame [118, 223])**.** Given a manifold $\mathcal{M}$ of dimension D with co-ordinate chart x^α, we can define the metrics $\mathbf{g}$ and $\widetilde{\mathbf{g}}$ to be conformally related if (and only if):

$$\widetilde{\mathbf{g}} = \Omega^2 \left(x^\alpha\right) \mathbf{g} \tag{2.1a}$$

where Ω is nowhere vanishing, everywhere invertible and smooth. This is not a co-ordinate change, but a geometric rescaling of the metric, such that angles are preserved [118].

Corollary: The affine connection and Ricci scalar transform between these frames as:

$$\widetilde{\Gamma}^\alpha{}_{\beta\gamma} = \Gamma^\alpha{}_{\beta\gamma} + \frac{1}{\Omega}\left[\delta^\alpha{}_\gamma \partial_\beta \Omega + \delta^\alpha{}_\beta \partial_\gamma \Omega - g_{\beta\gamma} g^{\alpha\epsilon} \partial_\epsilon \Omega\right] \tag{2.1b}$$

$$\widetilde{R} = \frac{1}{\Omega^2}\left[R - (D-1)\left(2\frac{\nabla_\mu \nabla_\nu \Omega}{\Omega} - (D-4) g^{\mu\nu} \frac{\nabla_\mu \Omega \nabla_\nu \Omega}{\Omega^2}\right)\right] \tag{2.1c}$$

and see [118] for the Ricci tensor and [118, 223] for the Riemann tensor. □

For now we are interested in the Jordan frame and the Einstein frame (as two of the potentially infinite choices of conformal frame). The **Jordan frame** is defined to be the unique frame in which the additional terms are minimally-coupled to matter [89, 205, 231]. In this frame the scalar field contributes additional terms to the geometry via non-minimal couplings with curvature terms [89]. In this case, the matter fields remain unaffected, so the energy-momentum balance equation Eq. (1.6) still holds as in GR. Moreover, massive particles fall along time-like geodesics (null geodesics remain null under the conformal transformation), because the additional terms are absorbed into the Christoffel symbols [231]. The **Einstein frame** is defined to be the frame in which the Einstein tensor reduces to that of GR. Consequently, the extra degrees of freedom must be non-minimally coupled to matter, so there is never a true vacuum due to the presence of the scalar field as an effective matter component. Then neither the balance equation[2] nor the geodesic equation hold; however the Poisson equation does hold [231]. We shall define our MG theories in the Jordan frame and transform to the

[2]The matter component of $T_{\alpha\beta}$ is no longer covariantly conserved because it cannot be traceless, so $\nabla_\alpha T^{\alpha\beta} = 0 \implies \widetilde{\nabla}_\alpha \widetilde{T}^{\alpha\beta} = 0$ [100].

Einstein frame.

This indicates that one must be careful in deciding which (if any) is the "physical" frame. Faraoni and Nadeau assert that both frames are physical, provided that one takes into account that dimensionful quantities in the Einstein frame have additional powers of Ω arising from the rescaling of the metric. Consider $\mathrm{d}\,t \to \Omega\,\mathrm{d}\,t$, so $[\mathsf{T}] \to \Omega^{-1}[\mathsf{T}]$ generates the transformation between conformal η and physical t time $\mathrm{d}\,\eta = \mathrm{d}\,t/a(t)$, where $a(t)$ is the conformal factor. Similarly [89] suggest that redshift will have the same physical effect in both frames, but can be interpreted differently. Using the same example of conformal time, in the usual FLRW metric the redshift is attributed to expansion of physical lengths by $(1+z)$ over time; whereas the conformally flat FLRW metric is static, so the redshift is interpreted as a rescaling of fermion mass (or energy levels) by $(1+z)^{-1}$ over time. Since we are largely concerned with the fifth-force as an effective modification to the Poisson equation, we shall observe physical quantities in the Einstein frame.

Now we generalise the conformal scaling to a **disformal** one, so that we can obtain a Lagrangian which encompasses all of our screening mechanisms. Then we have the following metric relation between the Jordan and Einstein frames [188]:

Definition 2.2 (Disformal transformation [188])**.** The most general metric transformation $\widetilde{\mathbf{g}} = \widetilde{\mathbf{g}}\,(\mathbf{g}, \phi, \partial\phi)$ which produces equations of motion of at most second order is defined by:

$$\widetilde{g}_{\mu\nu} = A^2\,(\phi, X)\,g_{\mu\nu} + B^2\,(\phi, X)\,(\partial_\mu\phi)\,(\partial_\nu\phi) \text{ where } X \equiv -\frac{1}{2}\,(\partial^\alpha\phi)\,(\partial_\alpha\phi)$$

The conformal factor A and disformal factor B must be functions of co-ordinate invariants, hence the kinetic term X. □

Let us separate the action into a part containing all contribution from ϕ minimally-coupled to the metric $\mathbf{g}$ and a part containing all matter fields Φ_i which are not ϕ, non-minimally coupled to the metric $\widetilde{\mathbf{g}}$:

$$S = \int \partial^4 x \sqrt{-g}\;\mathcal{L}_E + \int \partial^4 x \sqrt{-\widetilde{g}}\;\mathcal{L}_{\text{matter}}\left[\widetilde{g}, \Phi_i\right] \tag{2.2a}$$

$$\mathcal{L}_E = \frac{R}{16\pi G_N} + X - V(\phi) \tag{2.2b}$$

$$\widetilde{T}_{\mu\nu} = \frac{2}{\sqrt{-\widetilde{g}}}\frac{\delta\mathcal{L}_{\text{matter}}}{\delta\widetilde{g}_{\mu\nu}} \tag{2.2c}$$

Then we can vary the action with respect to the scalar field (using the Euler-Lagrange operator Eq. (A.8)) with respect to ϕ to obtain the field equations of motion and with respect to $\widetilde{g_{\mu\nu}}$ to obtain the Einstein equations. A particular choice of A, B and V

corresponds to a particular screened MG theory. Then we can proceed as for GR, but with an additional degree of freedom.

It remains to show that the effect of the scalar field in the halo model is just a redefinition of the Poisson equation. Let us define the most general scalar field Lagrangian in the Jordan frame, which will encompass all our screening mechanisms. This was already treated in Eq. (1.8). We transform to the Einstein frame at the level of the action and define the field equations as per GR. In the conformal FLRW metric Eq. (1.13) this reduces to varying with respect to the scale factor $a(t)$ and lapse function $N(t)$ [41]. The equation of motion for ϕ is obtained as above. Then we apply the weak-field, quasi-static limit to the perturbed equations: after copious algebra [82] show that this relates the metric perturbations Φ, Ψ to the perturbed field χ and gauge-invariant matter density δ. (We shall perform this for chameleon screening in Chapter 3.) More algebraic manipulation allows us to recast this as a Poisson equation (for details see [82]). Thus we obtain our effective multiplication of $G_{\text{eff}} = (1 + F_{\text{eff}})G_N$. For brevity we treat each MG theory separately in the following sections.

Finally, let us characterise the various types of screening used in this thesis. Screening mechanisms add new terms to the GR action, which are designed to suppress the non-GR modifications under certain conditions. By construction, this suppression of the fifth-force modification happens on non-linear regimes. The conditions required for screening divide the mechanism into three groups: chameleon, symmetron and Vainshtein. The different screening methods correspond to different behaviours of the Lagrangian, which we can classify by expanding about some value ϕ_0 by an infinitesimal value $(\delta\phi)$ [36]:

$$\mathcal{L} = \frac{1}{2}\mathcal{R}M_{\text{Pl}}^2 + \partial_\mu\left(\delta\phi\right)\partial_\nu\left(\delta\phi\right)Z^{\mu\nu}\left(\phi_0\right) + \left(\delta\phi\right)m^2\left(\phi_0\right) + \frac{\rho_m}{M_{\text{Pl}}}\beta\left(\phi_0\right) \tag{2.3}$$

In low density regions the scalar field takes a value $\phi_0 = \phi_{\text{low}}$, for which:

$$\gamma \equiv \left|\frac{\vec{F}_\phi}{\vec{F}_N}\right| \propto \beta^2\left(\phi_{\text{low}}\right) \sim 1 \tag{2.4}$$

and we see that the contribution of the fifth force $|\vec{F}_\phi|$ is non-negligible compared to the Newtonian value $|\vec{F}_N|$. Compare this to the high-density value $\phi_0 = \phi_{\text{high}}$, for which:

$$\gamma \ll 1 \qquad \text{by definition} \tag{2.5a}$$

which can only be produced by:

$$\beta\left(\phi_{\rm high}\right) \ll \beta\left(\phi_{\rm low}\right) \qquad \text{matter coupling suppressed} \qquad \text{(symmetron)} \qquad (2.5b)$$

$$m\left(\phi_{\rm high}\right) \gg m\left(\phi_{\rm low}\right) \qquad \text{large local mass} \qquad \text{(chameleon)} \qquad (2.5c)$$

$$Z^{\mu\nu}\left(\phi_{\rm high}\right) \gg Z^{\mu\nu}\left(\phi_{\rm low}\right) \qquad \text{weakened matter source} \qquad \text{(Vainshtein)} \qquad (2.5d)$$

This permits us to classify a screened MG theory not by abstract considerations (*i.e.* which conditions are relaxed in Lovelock's Theorem) but rather by the practicalities of the mechanism by which it evades local tests of gravity.

2.2 $f(\mathcal{R})$ gravity

Definition 2.3 ($f(\mathcal{R})$ gravity)**.** An $f(\mathcal{R})$ theory can be defined in the Jordan frame via the action:

$$S_J = \int d^4x\sqrt{-g}\,\frac{1}{2}\left[\mathcal{R} + f(\mathcal{R})\right] + \mathcal{L}_{\rm m}\left[\Phi_i, g_{\mu\nu}\right] \qquad (2.6)$$

where we have (temporarily) chosen units such that $8\pi G = 1$, the function $f(\mathcal{R})$ is a general function of the Ricci scalar $\mathcal{R}$ and Φ_i denotes all matter fields. □

The $f(\mathcal{R})$ modification in the Jordan frame translates to a scalar-tensor theory of gravity in the Einstein frame where the scalar field ϕ is coupled to matter. Via a series of field redefinitions and a conformal transformation [26, 31, 64, 179]:

$$A\left(\phi\right) = \exp\left(\frac{\phi}{\sqrt{6}}\right) \implies \beta\left(\phi\right) = \frac{1}{\sqrt{6}} \qquad (2.7)$$

we can turn the Jordan frame action into an equivalent Einstein frame one

$$\begin{aligned} S_E &= \frac{1}{2}\int d^4x\sqrt{-\widetilde{g}}\,\widetilde{R} \\ &+ \int d^4x\sqrt{-\widetilde{g}}\left[-\frac{1}{2}\widetilde{g}^{\mu\nu}\widetilde{\nabla}_\mu\phi\widetilde{\nabla}_\nu\phi - V(\phi)\right] \\ &+ S_{\rm matter}[\Phi_i, e^{-\beta\phi}\widetilde{g}_{\mu\nu}] \end{aligned} \qquad (2.8)$$

where a tilde denotes Einstein frame quantities and the corresponding potential is:

$$V(\phi) = \frac{1}{2}\frac{\mathcal{R}f_{\mathcal{R}}(\mathcal{R}) - f(\mathcal{R})}{\left(1 + f_{\mathcal{R}}(\mathcal{R})\right)^2} \quad \text{where } f_{\mathcal{R}} \equiv df(\mathcal{R})/d\mathcal{R} \qquad (2.9)$$

The fact that we have this conformal transformation is the essential ingredient behind the mapping between $f(\mathcal{R})$ and chameleon-screened theories [134]: we will return to

this point in Chapters 3 and 6.

The $f(\mathcal{R})$ modification in the Jordan frame translates to a scalar-tensor theory of gravity in the Einstein frame where the scalar field ϕ is coupled to matter. In this formulation we can see that this model behaves as standard general relativity with the inclusion of a fifth-force mediated by the scalar field with coupling strength 1/3, *i.e.* in the unscreened limit, the gravitational force can be enhanced by a factor of up to 4/3. In the fully screened limit the gravitational force is not enhanced, *i.e.* this modification does not manifest itself in dense environments or on small scales [234]. In order to exhibit this behaviour, the scalar field self-interaction potential must satisfy a number of constraints (*viz.* [189]), which again translates into constraints on the functional form of $f(\mathcal{R})$ (equivalently $V(\phi)$) [10]. At this point one may wonder whether any particular fiducial form suggests itself for the potential. For an arbitrary polynomial of positive powers of R in four dimensions of the form $\sum_{n=1}^{k} a_n R^n$, such a potential will asymptotically approach an exponential potential as $\phi \to \infty$. This is the fiducial potential chosen by [31, 103] and will be the potential we work with throughout most of Chapter 3. However, we will return to the Hu & Sawicki model in the context of the chameleon Section 3.6, where we will also find that an exponential potential qualitatively is a good proxy for this model in several regions of parameter space. We shall also use this model for Chapters 5 and 6.

The explicit $f(\mathcal{R})$ model which we apply here is the Hu-Sawicki model of [124]. This is a well studied model known to exhibit chameleon screening [131]. It is defined by:

$$f(\mathcal{R}) = -H_0^2 \Omega_m \frac{\left(c_1 \left(\frac{\mathcal{R}}{m^2}\right)^{n_{f(\mathcal{R})}}\right)}{1 + c_2 \left(\frac{\mathcal{R}}{m^2}\right)^{n_{f(\mathcal{R})}}} \qquad \text{free parameters } n_{f(\mathcal{R})}, c_2, \text{ and } c_1 = \frac{6\Omega_\Lambda}{\Omega_m} c_2 \tag{2.10}$$

We now reparametrise in more meaningful free parameters. Using the constraint in Eq. (2.10) between c_1 and c_2 we can express $|c_1|/{c_2}^2$ in terms of $|f_{\mathcal{R}0}|$, the value of $f(\mathcal{R})$ in the cosmological background evaluated at $z = 0$:

$$|f_{\mathcal{R}0}| = n_{f(\mathcal{R})} \frac{|c_1|}{c_2^2} \left(\frac{\Omega_m}{3(\Omega_m + 4\Omega_\Lambda)}\right)^{1+n_{f(\mathcal{R})}} \tag{2.11}$$

The value of $|f_{\mathcal{R}0}|$ determines the magnitude of variations from ΛCDM. The value of $n_{f(\mathcal{R})}$ dictates how late the $f(\mathcal{R})$ modification switches on [123]: larger values delay the deviation from the ΛCDM expansion history. While [124] suggest methods to constrain $|f_{\mathcal{R}0}|$ on various scales, [60] find an upper bound of $\log_{10}|f_{\mathcal{R}0}| < -4.79$ for $n_{f(\mathcal{R})} = 1$ by combining cluster data with CMB probes.[3] Larger $n_{f(\mathcal{R})}$ would permit larger $|f_{\mathcal{R}0}|$: [57] note that $n_{f(\mathcal{R})} > 1$ models are not well-constrained. Throughout this thesis we set $n_{f(\mathcal{R})} = 1$ and will only consider $|f_{\mathcal{R}0}| = 10^{-5}$ and $|f_{\mathcal{R}0}| = 10^{-6}$.

[3] After this thesis was submitted, [57] proposed that $\log_{10}|f_{\mathcal{R}0}| \lesssim -7$ for $n_{f(\mathcal{R})} = 1$.

The evolution of the background in an $f(\mathcal{R})$ model is governed by [31]

$$\begin{aligned}\widetilde{H}^2 &= \frac{1}{3}\left(\frac{\dot{\phi}^2}{2} + \widetilde{a}^2 V(\phi) + \widetilde{a}^2\widetilde{\rho}_m\right) \\ \ddot{\phi} &+ 2\widetilde{H}\dot{\phi} + \widetilde{a}^2 V_\phi = \frac{1}{2}\beta\widetilde{a}^2\widetilde{\rho}_m \\ \widetilde{\rho}_m &\equiv \frac{\widetilde{\rho}_m^{*0}}{\widetilde{a}^3}\exp\left(-\frac{\beta\phi}{2}\right).\end{aligned} \tag{2.12}$$

The background cosmology of this model is always very close to ΛCDM as long as $|f_{\mathcal{R}0}| \ll 1$ (which is required to satisfy local gravity constraints). The deviation of $w_{\rm eff}$ from $w_\Lambda = -1$ is of order $f(\mathcal{R})$ [123], which is negligible for the values considered here. Thus we follow [170] in adopting an ΛCDM expansion history in Chapters 5 and 6—but we will use the full expansion history in Chapter 3.

To see how screening works, let us consider a top-hat overdensity of radius $R_{\rm TH}$ and mass $M_{\rm TH}$. The Newtonian potential of the overdensity is $\Phi_N = \frac{GM_{\rm TH}}{R_{\rm TH}}$ at the surface of the overdensity. As shown in [45] the gravitational force on a test-mass of mass m outside the top-hat is approximately given by

$$F = \frac{GM_{\rm TH}m}{r^2}\left[1 + \frac{1}{3}F_{\rm eff}\right] \tag{2.13}$$

where

$$F_{\rm eff}(a, R_{\rm TH}, \rho_{\rm TH}, \rho_{\rm env}) = \frac{1}{3}\left[3\left(\frac{\Delta R}{R_{\rm TH}}\right) - 3\left(\frac{\Delta R}{R_{\rm TH}}\right)^2 + \left(\frac{\Delta R}{R_{\rm TH}}\right)^3\right] \tag{2.14a}$$

$$\frac{\Delta R}{R_{\rm TH}} = \min\left\{\frac{3|f_{\mathcal{R}}^{\rm TH} - f_{\mathcal{R}}^{\rm env}|}{2\Phi_N}, 1\right\} \tag{2.14b}$$

and $f_{\mathcal{R}}^{\rm TH} = f_{\mathcal{R}}(\rho_{\rm TH})$ and $f_{\mathcal{R}}^{\rm env} = f_{\mathcal{R}}(\rho_{\rm env})$ are the scalar field values inside and outside the body respectively. For the Hu-Sawicki model the scalar field value in a region density ρ_m and time (scale-factor) a can be estimated to be

$$f_{\mathcal{R}}(\rho_m) = f_{\mathcal{R}0}\left(\frac{1 + \frac{4\Omega_{\Lambda 0}}{\Omega_{m0}}}{\frac{\rho_m}{\rho_{m0}} + \frac{4\Omega_{\Lambda 0}}{\Omega_{m0}}}\right)^{n_{f(\mathcal{R})}+1} \tag{2.15}$$

where $\rho_{m0} = 3\Omega_{m0}H_0^2 M_{\rm Pl}^2$ is the average matter density in our Universe at the present time. When the overdensity is massive ($\frac{1}{\Phi_N}$ is very small) or is located in a very dense environment ($|f_{\mathcal{R}}^{\rm TH} - f_{\mathcal{R}}^{\rm env}|$ is very small) then $\frac{\Delta R}{R_{\rm TH}} \ll 1$ and the fifth-force is screened. In contrast, when the overdensity is not massive (so $\frac{1}{\Phi_N}$ is very large) then $\frac{\Delta R}{R_{\rm TH}} \approx 1$ and the force is 4/3 the value of the Newtonian prediction. Thus we see that the modification to gravity is sensitive to both the halo mass and the environment density. We have three regimes: on cosmological scales, the background solution mimics ΛCDM; on local

scales in high-density regions, the modification is screened in order to evade tight, Solar System constraints; on local scales in low-density regions the modifications of gravity are in full effect. This completes our discussion of $f(\mathcal{R})$.

2.3 Symmetron gravity

The symmetron mechanism is distinct from both the chameleon (Section 2.2) and Vainshtein (Section 2.4) mechanisms of screening. This model adds to ΛCDM a scalar field with an artificially-imposed $\mathbb{Z}_2$ symmetry and a coupling to matter [116, 199, 234]. The breaking of this symmetry occurs when the environmental density drops below a critical value, which causes the matter-scalar coupling to become non-zero [234].

Definition 2.4 (Symmetron gravity [116])**.** The symmetron model adds a scalar field ϕ with symmetry $\phi \to -\phi$, such that the coupling to matter depends on density. The Einstein-frame Lagrangian is:

$$S = \int \mathrm{d}^4x\sqrt{-g}\,\frac{\mathcal{R}}{2\kappa} - \frac{1}{2}\left(\partial\phi\right)^2 - V\left(\phi^2\right) + \mathcal{L}_m\left[A^2\left(\phi^2\right)g_{\mu\nu}\right]$$

In our specific model V and A are given by Eq. (2.16). □

The modification imposed in the Einstein frame encodes all of the non-gravitational couplings between the scalar field and the matter fields via the conformal function [199]. Various forms of A and V exist ([44] for constraints on the functional form of V). The model [117] used in the N-body code is the simplest such model:

$$\left.\begin{aligned} A\left(\phi\right) &= 1 + \frac{1}{2}\left(\frac{\phi}{M_0}\right)^2 \\ V\left(\phi\right) &= -\frac{1}{2}\mu^2\phi^2 + \frac{1}{2}\lambda\phi^4 + \frac{\mu^4}{3\sqrt{\lambda}} \end{aligned}\right\} \quad \text{free parameters } \mu, \lambda, M \tag{2.16}$$

We re-express the free parameters for each model via [258]:

1. The range of the field at which $\rho = 0$ in Mpc/h : $\lambda_0 = \frac{1}{\mu\sqrt{2}}$
2. A dimensionless coupling constant $\beta_0 = \phi_0\frac{M_{Pl}}{M_0} = \frac{\mu}{\sqrt{\lambda}}\frac{M_{Pl}}{M_0}$
3. The scale factor at which the background density takes the value required for symmetry breaking in the cosmological background $a_{SSB} = \frac{\rho_0}{\mu^2 M_0^2}$

Although the symmetron model should be well-constrained by atomic and astrophysical tests, there is a "desert" in constraints on M_0 and λ for fixed values of μ, caused by

a lack of translating experimental results into bounds on symmetron parameters (*q.v.* Figure 10 of [57]). We can fix a_{SSB} to any time in the matter-dominated regime, so we "switch on" the symmetron modification relatively late; by appropriate use of units λ_0 and β_0 should be of order unity. Thus we set $\lambda_0 = 1$, $\beta_0 = 1$ and $a_{SSB} = 0.33$, 0.5 in our simulations.

The effective gravitational potential can be expressed similarly to that of $f(\mathcal{R})$. For a top-hat of (physical) radius R_{TH} the Newtonian potential is:

$$\Phi_N = \frac{\Omega_{m0}}{2ay}\left(\frac{H_0 R_{\mathrm{TH}}}{c}\right)^2 \tag{2.17}$$

The scalar field value in the cosmological background and inside the halo are:

$$F_{\mathrm{env}} = \sqrt{1 - \left(\frac{a_{\mathrm{SSB}}}{a}\right)^3} \tag{2.18a}$$

$$F_h = \sqrt{1 - (1+\delta)\, a_{\mathrm{SSB}}^3} \tag{2.18b}$$

and the corresponding conformal function is:

$$\beta = \beta_0 F_{\mathrm{env}} \tag{2.18c}$$

which leads to a thin-shell factor

$$\frac{\Delta R}{R_{\mathrm{TH}}} = \frac{\Omega_{m0}}{a_{\mathrm{SSB}}^3}\frac{\lambda_0^2}{\Phi_N}\frac{|F_h - F_{\mathrm{env}}|}{F_{\mathrm{env}}} \tag{2.18d}$$

and as per $f(\mathcal{R})$ the effective factor is:

$$F_{\mathrm{eff}} = 2\beta^2 \mathrm{min}\left\{3\frac{\Delta R}{R_{\mathrm{TH}}}, 1\right\} \tag{2.18e}$$

Let us consider what sort of screening this produces. Again consider a top-hat[4] of radius R and homogeneous mass density ρ which satisfy $M_0 R \ll 1$ and $\rho \gg \mu^2 M_0^2$ (*caveat lector:* this is not the top-hat mass, but the free parameter). The profile of the scalar field has an interior and exterior solution:

$$\phi_{\mathrm{in}}(r) \simeq C\frac{R}{r}\sinh\left(r\frac{\sqrt{\rho}}{M_0}\right) \qquad (r < R) \tag{2.19a}$$

$$\phi_{\mathrm{out}}(r) \simeq D\frac{R}{r}\exp\left(-m_0(r-R)\right) + \phi_0 \qquad (r > R) \tag{2.19b}$$

By matching ϕ and derivatives at the boundary we can find the values of the coefficients

[4]More generally, any static, pressureless, spherically-symmetric source obeys this condition [117].

C, D in terms of a thin-shell factor

$$\frac{\Delta R}{R} \equiv \frac{M_0^2}{\rho R^2} = \frac{\phi_0}{6gM_{Pl}\Phi} \quad \text{where } \Phi = \frac{\rho R^2}{6M_{Pl}^2} \tag{2.20}$$

We quantify the effect on a test particle at r where $R \ll r \ll m_0^{-1}$ depending on the value of the thin-shell factor. The fifth-force effect is:

$$\gamma \equiv \left|\frac{\vec{F}_\phi}{\vec{F}_N}\right| = -\frac{g}{M_{Pl}}\frac{1}{\left|\vec{F}_N\right|}\frac{\mathrm{d}\,\phi}{\mathrm{d}\,r} \simeq \begin{cases} 6g^2\,(\Delta R/R) & \text{(screened: } (\Delta R/R) \ll 1) \\ 2g^2 & \text{(unscreened: } (\Delta R/R) \gg 1) \end{cases} \tag{2.21}$$

By analogy with the chameleon potential in Section 2.2, the modification falls into an unscreened regime where $\phi_{\text{in}} \approx \phi_0$ and the scalar field cannot relax to the value at the effective minimum of the potential $V(\phi)$; and a screened regime where ϕ_{in} is suppressed exponentially compared to ϕ_0. Thus, we see that despite the different mechanism by which screening occurs, the result is very similar for both the chameleon screening in $f(\mathcal{R})$ gravity and symmetron gravity.

2.4 DGP gravity

Dvali-Gabadadze-Porrati (DGP) gravity is a braneworld model, in which the usual $(3+1)$ foliated hypersurfaces are a brane embedded in a(n otherwise empty) higher-dimensional spacetime known as the bulk. While the Standard Model interactions are limited to the brane, gravitational interactions extend into the bulk. The DGP model employs Vainshtein screening to remain observationally viable.

Definition 2.5 (Dvali-Gabadadze-Porrati gravity)**.** Dvali-Gabadadze-Porrati gravity embeds the FLRW manifold into a 5D Minkowski manifold, via the following action [145]:

$$S = \int \mathrm{d}^{\,5}x\ \sqrt{-{}^{(5\mathrm{D})}g}\,\frac{{}^{(5\mathrm{D})}R}{2^{(5\mathrm{D})}\kappa} + \int \mathrm{d}^{\,4}x\ \sqrt{-{}^{(4\mathrm{D})}g}\,\left[\frac{{}^{(4\mathrm{D})}R + 2^{(4\mathrm{D})}K}{2^{(4\mathrm{D})}\kappa} + \mathcal{L}_{\text{matter}}\right]$$

where we have made explicit the bulk (5D) and brane (4D) terms and $K = K^{\mu\nu}K_{\mu\nu}$ is the trace of the extrinsic curvature tensor. The value of κ is defined in 5D by the free parameter of the crossover scale:

$$r_c \equiv \frac{{}^{(5\mathrm{D})}\kappa}{2^{(4\mathrm{D})}\kappa} \quad \text{where } {}^{(4\mathrm{D})}\kappa = (8\pi G_N) \text{ as usual} \tag{2.22}$$

□

When integrated onto the boundary, the DGP action in the bulk can be described by

a boundary-effective action on the brane [70]: In the decoupling limit only scalar self-interactions remain in the brane-bending Lagrangian [70]. Then DGP is equivalent to a purely disformal relation between Jordan and Einstein frames (Definition 2.2) with $B(X, \phi)$ equal to unity [188].

There are two solution branches: a self-accelerating branch and a normal one. While the former is inherently useful because it produces the expansion of the brane without requiring dark energy, fluctuations about the self-accelerating vacuum produce ghost-like instabilities [70]. The latter, which has fewer theoretical problems, is similar to massive gravity, with the usual field of finite mass replaced by a resonance of finite width. This encapsulates the free parameter r_c in Definition 2.5 [165]. On scales $r \gg r_c$, the dynamics are affected by the width of the resonance and the 5D effects are unscreened, whereas on scales $r \ll r_c$, the brane is unaffected by the presence of the bulk and the dynamics are screened [69]. Constraints on the crossover scale from observations are scarce: [169] suggest $r_c > 2.23c/H_0$ for the normal branch, based upon WMAP3 CMB measurements combined with galaxy-ISW correlations in a flat universe. We will only examine the normal branch from now on with $r_c = 1.2,\ 5.6c/H_0$.

The expansion history in the normal branch can be made to mimic ΛCDM [243]:

$$E(a) \equiv \frac{H(a)}{H_0} = \sqrt{\left(\Omega_{m0}a^{-3}\right)^2 + \Omega_{\text{eff},0}} \tag{2.23}$$

Thus we see that the presence of the scalar field ϕ affects the metric only at linear order.

The DGP potentials are related to the GR result $\Phi^{\text{GR}} = \Psi^{\text{GR}}$ by [260]

$$\Psi^{\text{DGP}} = \Phi^{\text{GR}} - \frac{1}{2}\phi \qquad\qquad \Phi^{\text{DGP}} = \Phi^{\text{GR}} + \frac{1}{2}\phi \tag{2.24}$$

In the weak-field, quasi-static limit, the equation of motion for the scalar field is [260]:

$$\frac{8\pi G_N a^2}{3\beta(a)}\delta\rho_m = \vec{\nabla}^2\phi + \frac{r_c^2}{3a^2\beta(a)}\left[\left(\vec{\nabla}^2\phi\right)^2 - \left(\nabla_i\nabla_j\phi\right)\left(\nabla^i\nabla^j\phi\right)\right] \tag{2.25a}$$

where we define

$$\beta(\phi) \equiv 1 + 2r_c H(a)\left(1 + \frac{\dot{H}(a)}{3H^2(a)}\right) \tag{2.25b}$$

Combining Eqs. (2.24) and (2.25), we obtain a modified Poisson equation with:

$$F_{\text{eff}}(r, a) = \frac{2}{3\beta(a)}\frac{\sqrt{1 + x^{-3}} - 1}{x^{-3}} \quad \text{where } x(r, a) \equiv \frac{r}{R_*} \tag{2.26}$$

where R_* in the Vainshtein radius for the mass $M(r)$ enclosed inside the radius r:

$$R_*(r,a) = \left(r_c^2 \frac{16c^2 G_N \delta M(r)}{9\beta^2(a)} \right)^{\frac{1}{3}} \tag{2.27}$$

We can understand the Vainshtein radius using a top-hat of radius R_{TH}. At a distance r outside the top-hat, the scalar field is:

$$\frac{1}{2}\frac{\mathrm{d}\,\phi}{\mathrm{d}\,r} = \frac{1}{3\beta(a)}\frac{G_N}{r^2}\left(\frac{4}{3}\pi R_{TH}^3\right) \qquad (r \gg R_*) \tag{2.28a}$$

$$\frac{1}{2}\frac{\mathrm{d}\,\phi}{\mathrm{d}\,r} \approx 0 \qquad (R_* \gg r) \tag{2.28b}$$

and so is unscreened outside the Vainshtein radius and screened within it. This completes our discussion of DGP gravity.

2.5 Quintessence-like MG

Finally we outline a "dark energy equivalent" model to $f(\mathcal{R})$ gravity. This behaves analogously to the quintessence DE model (described in the next paragraph). We shall use this in Chapter 3 to determine the effect of the coupling to matter on the accuracy of the quasi-static approximation.

Quintessence usually refers to a family of dark energy models wherein a scalar field ϕ with potential $V(\phi)$ is **not** coupled to matter. (Contrast this with the matter couplings in our MG theories.) The equation of state determines the ratio between the scalar fluid pressure and density:

$$w(t) \equiv \frac{P_\phi(t)}{\rho_\phi(t)} = \left[\frac{1}{2}\frac{\mathrm{d}\,\phi}{\mathrm{d}\,t} - V(\phi)\right] \Big/ \left[\frac{1}{2}\frac{\mathrm{d}\,\phi}{\mathrm{d}\,t} + V(\phi)\right] \tag{2.29}$$

(here t is proper time). This divides the possible models into two families depending upon the evolution of w [244]:

- Thawing models: the field has $w \sim -1$ until the mass drops below H, then only evolves at late times
- Freezing models: the field evolves quickly from $w = 0$ towards $w \sim -1$ until the evolution slows at late times

For our choice of potential, we have a freezing model. At early times, either we are in the fast-roll regime $\dot{\phi} \gg V$, in which case $w \approx 1$, or we are in the slow-roll regime $\dot{\phi} \ll V$, in which case $w \approx -1$. In the matter-dominated regime, the scalar field tracks

the condition $\Omega_\phi \propto \Omega_m$ until $\Omega_\phi = 3(1+w)/\lambda^2$ is constant [244]. This resolves the coincidence problem for Λ in Section 1.4.1.

In assessing the accuracy of the QSA in $f(\mathcal{R})$ models we will find it useful to compare them with analogous Quintessence-like solutions, i.e. models with no non-minimal coupling to matter as present in the case of $f(\mathcal{R})$. This corresponds to setting $\beta = 0$ in the action Section 2.2. Consequently, the background evolution equations now are

$$\begin{aligned} \widetilde{H}^2 &= \frac{1}{3}\left(\frac{\dot{\phi}^2}{2} + \widetilde{a}^2 V(\phi) + \widetilde{a}^2\widetilde{\rho}_m\right) \\ 0 &= \ddot{\phi} + 2\widetilde{H}\dot{\phi} + \widetilde{a}^2 V_\phi \qquad (2.30) \\ \widetilde{\rho}_m &\equiv \frac{\widetilde{\rho}_m^{*0}}{\widetilde{a}^3}, \qquad (2.31) \end{aligned}$$

The scalar field obeys the relativistic Klein-Gordon equation:

$$\nabla^\mu \nabla_\mu \phi = -\frac{\mathrm{d}\, V}{\mathrm{d}\, \phi} \qquad (2.32)$$

The decoupling removes any difference between the scalar field potential V and the effective one: we are left with a runaway potential (since $V'(\phi) < 0$ for all ϕ), which should have substantially different behaviour from the $f(\mathcal{R})$ case. This is summarised in Fig. 3.5. The features of our quintessence-like model are summarised in Definition 2.6.

Definition 2.6 (Quintessence-like $f(\mathcal{R})$ [189])**.** Quintessence-like $f(\mathcal{R})$ (henceforth "quintessence") entails a scalar field ϕ minimally coupled to the metric, but not coupled to matter. The action in the Einstein frame is:

$$S_E = \frac{1}{2}\int \mathrm{d}^4x\sqrt{-\widetilde{g}}\left[\frac{\mathcal{R}}{\kappa} - \widetilde{g}^{\mu\nu}\widetilde{\nabla}_\mu\phi\widetilde{\nabla}_\nu\phi - 2V(\phi)\right] + S_{\text{matter}}\left[\Phi_i, \widetilde{g}_{\mu\nu}\right] \qquad (2.33)$$

We choose a potential $V \sim \exp\left(-|\lambda|\,\phi\right)$ with $\lambda = 1.5$. □

This completes our summary of the various MG theories used in this thesis. We shall use the effective fifth-force contribution to G to find the density required for collapse of a spherical top-hat in each MG theory in Section 4.1. We now turn our attention to applications of these theories in the next three Chapters.

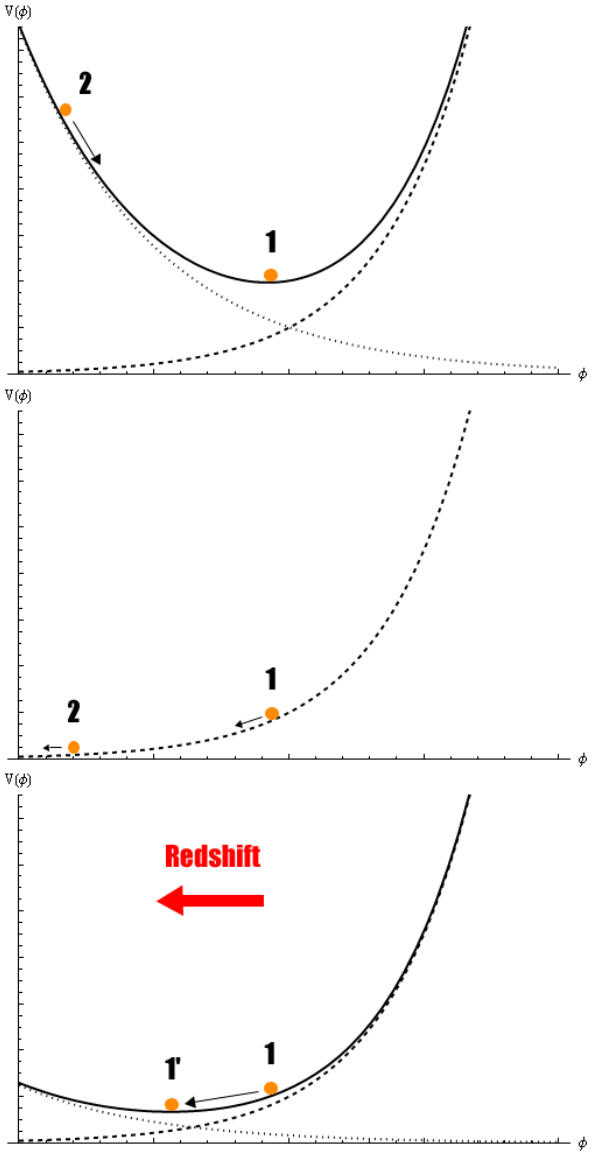

Figure 2.1: Here we show the effective chameleon potential and its evolution. 1 and 2 label the two initial conditions for the field ϕ considered in the main text.
Top: The effective chameleon potential $V_{\rm eff}$ showing the contributions from the original potential $V(\phi)$ (dashed) and from the non-minimal coupling to matter (dotted).
Centre: The corresponding Quintessence potential, which only possesses the contribution from $V(\phi)$ (dashed) since matter is coupled minimally to gravity.
Bottom: Plot showing how the minimum of the effective chameleon potential changes due to the redshifting of the matter-dependent contribution (dotted).

Chapter 3

Relativistic scalar fields and the quasi-static approximation in theories of modified gravity

This chapter discusses the role of the quasi-static approximation in MG compared to GR. As we have already seen in Section 1.2.2, relativistic scalar fields are ubiquitous in modified theories of gravity. An important tool in understanding their impact on structure formation, especially in the context of N-body simulations, is the quasi-static approximation in which the time evolution of perturbations in the scalar fields is discarded.

We show that this approximation must be used with some care by studying linearly perturbed scalar field cosmologies and quantifying the errors that arise from taking the quasi-static limit. We focus on $f(\mathcal{R})$ and chameleon models and link the accuracy of the quasi-static approximation to the fast/slow-roll behaviour of the background and its proximity to ΛCDM. Investigating a large range of scales, from super- to sub-horizon, we find that slow-rolling (ΛCDM-like) backgrounds generically result in good quasi-static behaviour, even on (super-)horizon scales. We also discuss how the approximation might affect studying the non-linear growth of structure in numerical N-body simulations.

3.1 Introduction

While relativistic scalar fields are hard-wired into our current theories of the very early universe, they are also at the heart of our modern understanding of the evolution of the

universe at late times [74]. They are often invoked as the source of dark energy as well as being instrumental in attempts at modifying general relativity [70]. As such, their presence should be felt and have a significant impact on the formation of structure.

The role that relativistic scalar fields play in linear cosmological perturbations of homogeneous universes is well-developed and understood. From coherent perturbations as one finds in a wide range of Quintessence [103, 122, 197] models to incoherent perturbations as emerge in axion and axion-like theories [9, 181, 182, 245] , it is now possible to calculate cosmological observables in the linear regime with almost arbitrarily high precision. Furthermore, a range of phenomenological approaches exist which can be applied to understand the effects of the scalar field in different ways.

The same cannot be said on small scales where non-linear effects come into play. There, the method of choice is to use N-body simulations to study how non-linear evolution will lead to the formation of galaxies, clusters and, more generally, the cosmic web that is such a rich source of dynamical information. N-body simulations are inherently *non-relativistic* — for they simulate a system which interacts under Newtonian gravity — and as such should not, in principle, capture the essential relativistic nature of the scalar field. While there have been attempts at inserting scalar fields into N-body simulations, in general they have been at the expense of taking the equivalent Newtonian limit of the scalar field equation of motion [51, 190]. Broadly speaking this means converting a dynamical, sourced, Klein-Gordon equation into a Poisson-like equation: the *quasi-static* approximation (we will explain this approximation more thoroughly later).

Our approach is to explore the validity of the quasi-static approximation on both large and small scales by using the apparatus of linear perturbation theory. In order to do so, we perform a detailed comparison between quasi-static and full, not approximated evolutions. The models which we consider are representative $f(\mathcal{R})$ and chameleon models of modified gravity, which alternatively may be interpreted as $f(\mathcal{R})$ models without and with screening. Doing so we aim to extend previous work by analytically and quantitatively understanding on which scales and subject to what conditions exactly the quasi-static approximation is a valid approximation for both $f(\mathcal{R})$ and chameleon models.

We explore and quantify these models in enough detail that we can use our results as a guide on how to tackle and better understand the evolution of non-linear perturbations in N-body simulations in the future. In doing so we identify the regimes where the quasi-static approximation can and cannot be trusted.

In Section 3.2 we lay out the pared-down formalism of cosmological perturbations which we will use throughout this chapter and in Section 3.3 we use it to understand the Newtonian limit, the quasi-static approximation and the miracle of N-body simulations

with non-relativistic matter, which does not extend to relativistic scalar fields.

In Section 3.4 we then apply the quasi-static approximation to $f(\mathcal{R})$ models with an exponential potential and compare it to the full evolution of perturbations without the quasi-static approximation. Providing explicit examples, in Section 3.5 we map out the regime of validity of the quasi-static approximation and how it relates to the fast- and slow-rolling nature of the background scalar degree of freedom as well as its proximity to ΛCDM-like behaviour. This analysis is extended to specific $f(\mathcal{R})$ models with screening, namely chameleons, in Section 3.6. Finally, in Section 3.7 we discuss our findings and conclude.

3.2 Cosmological perturbations

Throughout this chapter we will use linear, cosmological perturbation theory to gain insight into structure formation in modified gravity.

To do so, we need to perturb the metric and the energy content of the universe around a homogeneous and isotropic background. Depending upon one's educational background (see [175] for a thorough discussion), one tends to pick one of two gauges: synchronous or conformal Newtonian. In the *synchronous* gauge one chooses a foliation of space-time such that surfaces of equal time correspond to those of equal density — consequently the coordinates are those of a freely falling observer — and the metric can be written

$$ds^2 = a^2(\tau)\left[-d\tau^2 + (\gamma_{ij} + h_{ij})dx^i dx^j\right] \tag{3.1}$$

where τ is conformal time, $a(\tau)$ is the scale factor, γ_{ij} is the conformal 3-space metric of constant Gaussian curvature and h_{ij} its perturbation (from the Fourier-space parametrisation of the scalar modes we have $h_{ij} = h\delta_{ij}/3 + (h + 6\eta)(\hat{k}_i\hat{k}_j - \delta_{ij}/3)$ where $\hat{k}_i$ is the unit vector in the direction of the wave vector $\vec{k}$). Alternatively in the *conformal Newtonian* gauge, the metric is diagonal such that

$$ds^2 = a^2(\tau)\left[-(1 + 2\Psi)d\tau^2 + (1 - 2\Phi)\gamma_{ij}dx^i dx^j\right] \tag{3.2}$$

where Φ and Ψ map directly onto the Newtonian potential field in the non-relativistic limit. In this chapter we will primarily work with the synchronous gauge, although we will resort to the conformal gauge to make a few key points.

The content of the universe must also be suitably perturbed so that key tensors retain a gauge-invariant structure. For example, the stress energy of a perfect fluid has for its

$(0, \mu)$ components:

$$\begin{aligned} T^0_{\ 0} &= -\rho(1+\delta) \\ ik^j T^0_{\ j} &= (\rho + P)\theta \end{aligned}$$

where ρ and P are the background energy density and pressure, δ and θ are the density contrast and the momentum (the divergence of the 3-velocity perturbation) and we have transformed to Fourier space assuming the convention of [174]. While the structure of the perturbed energy momentum tensor is identical in both gauges, the perturbation variables δ and θ behave differently in both gauges. So for example, in synchronous gauge, the evolution of δ and θ for a pressure-less fluid is given by

$$\begin{aligned} \dot{\delta} &= -\theta - \frac{\dot{h}}{2} \\ \dot{\theta} &= -H\theta \end{aligned}$$

while in conformal Newtonian gauge we have

$$\begin{aligned} \dot{\delta} &= -\theta - 3\dot{\Phi} \\ \dot{\theta} &= -H\theta + k^2\Psi \end{aligned}$$

where we have used the conformal Hubble factor, $H = \frac{\dot{a}}{a}$ and $\dot{a} = \frac{da}{d\tau}$.

To determine the perturbed metric (and close the system of equations), one needs to consider the perturbed Einstein field equations, $\delta G^\alpha_{\ \beta} = 8\pi G \delta T^\alpha_{\ \beta}$ where $\delta G^\alpha_{\ \beta}$ and $\delta T^\alpha_{\ \beta}$ are the perturbed Einstein and energy-momentum tensor. In the conformal Newtonian gauge, we can combine the (0,β) components to construct the relativistic Newton-Poisson equation:

$$-k^2\Phi = 4\pi G a^2 \left(\delta T^0_{\ 0} - 3\frac{H}{k^2} ik^i \delta T^0_{\ i} \right) \tag{3.3}$$

In the synchronous gauge we have that the metric is found by solving:

$$\begin{aligned} k^2\eta - \frac{1}{2}H\dot{h} &= -4\pi G a^2 \delta T^0_{\ 0} \\ \ddot{h} + 2H\dot{h} - 2k^2\eta &= -8\pi G a^2 \delta T^i_{\ i} \end{aligned}$$

Specialising to the case of a shear-free fluid, we have

$$\delta T^i_{\ j} = \delta P \delta^i_{\ j}$$

Finally, it makes sense to reduce the contents of the universe to a scalar field and dust,

where the dust mimics dark matter and the scalar field is the 'modified gravity/dark energy degree of freedom'[1]. We now consider the evolution and effect of a scalar field, the archetypal relativistic source in modern cosmology. We will consider models with more complicated matter-scalar field couplings later on, but for the moment it is instructive to focus on a simple example of a Quintessence-like model where matter and the scalar are minimally coupled to gravity without any direct coupling to one another [103]. Typically a scalar field φ obeys a relativistic Klein-Gordon equation

$$\nabla^{\mu}\nabla_{\mu}\varphi = -\frac{dV}{d\varphi}$$

The scalar field can be divided into homogeneous and inhomogeneous components $\varphi = \phi + \chi$ which satisfy

$$\ddot{\phi} + 2H\dot{\phi} + a^2V' = 0 \tag{3.4}$$

where $V' = dV/d\phi$ and

$$\ddot{\chi} + 2H\dot{\chi} + k^2\chi + a^2V''(\phi)\chi = \mathcal{S} \tag{3.5}$$

where $\mathcal{S} = -\frac{1}{2}\dot{\phi}\dot{h}$ in the synchronous gauge and $\mathcal{S} = 4\dot{\phi}\dot{\Phi} - 2a^2V'\Phi$ in conformal Newtonian gauge. The perturbed stress energy components for a scalar field are now

$$\begin{aligned} \delta T^0_{\ 0} &= -a^{-2}\dot{\phi}\dot{\chi} - V'(\phi)\chi \\ ik^i\delta T^0_{\ i} &= a^{-2}\dot{\phi}k^2\chi \\ \delta T^i_{\ i} &= a^{-2}\dot{\phi}\dot{\chi} - V'(\phi)\chi \end{aligned}$$

We can combine these equations to obtain a coupled set of 2^{nd} order ordinary differential equations in Fourier space:

$$\begin{aligned} \ddot{\delta} + H\dot{\delta} - \frac{3}{2}H^2\Omega_m\delta - 2\dot{\phi}\dot{\chi} + a^2V'\chi &= 0 \\ \ddot{\chi} + 2H\dot{\chi} + k^2\chi + a^2m_\phi^2\chi - \dot{\phi}\dot{\delta} &= 0 \end{aligned} \tag{3.6}$$

where $m_\phi^2 = d^2V/d\phi^2$. In what follows, we will make use of these equations in exploring the evolution of cosmological perturbations in the linear regime and also re-encounter them in the context of $f(\mathcal{R})$. The initial conditions chosen are: $\phi_i = 5, \dot{\phi}_i = 0, a_i = 1, \tau_i = 10^{-3}$ in all cases: for the potential (specified later) we set $\lambda = 1.5$. The initial overdensity δ_i can be related to $\widetilde{\rho}_m^{*0}$, which we will change between $f(\mathcal{R})$ and Quint., so that $\Omega_{\phi,i}$ is identical for the two gravity models. The value of $\Omega_{\phi,i}$ is set to $\sim 10^{-4}$ in the fast-roll and ~ 0.2 in the slow-roll scenarios.

[1]Note that in effect this means we will be considering accelerating models that start in a matter-dominated regime and transition into one dominated by the scalar. We ignore radiation throughout.

3.3 The quasi-static approximation and relativistic scalar fields

In this section we discuss a few aspects of cosmological perturbation theory and how we can use it as a guide to understanding N-body simulations of structure formation and the quasi-static approximation. Let us first focus on Section 3.2 and consider the case of a generic, perfect fluid with equation of state $w \equiv P/\rho$. The Poisson equation in Fourier space is now

$$-k^2\Phi = 4\pi G a^2 \rho \delta_{gi} \tag{3.7}$$

where we have defined the gauge-invariant density contrast

$$\delta_{gi} \equiv \delta + \frac{3(1+w)H}{k^2}\theta$$

This is an interesting expression for a number of reasons. For a start, it differs from the non-relativistic Newtonian equation although in the limit where $H/k \to 0$, namely on sub-horizon scales, they agree. Hence, in the Newtonian gauge, one expects relativistic corrections once one looks at sufficiently large scales. But more relevant is the fact that δ_{gi} is a gauge-invariant quantity and the relativistic Newton-Poisson equation we present above is gauge-invariant. The standard gauge-invariant Newtonian potentials map (by construction) directly onto the conformal Newtonian potentials and, if accordingly we calculate δ and θ in any gauge, we can combine them to find δ_{gi}.

It turns out that this form of relativistic Newton-Poisson equation is at the heart of why N-body simulations can accurately calculate the evolution of the Universe from super-horizon down to sub-horizon scales, even though they, in principle, use the non-relativistic Newton-Poisson equation [38]. To understand why this is so, let us briefly sketch the algorithm for an N-body code. The idea is that one follows the motion of a set of N-particles (labelled by $a = 1, \cdots N$) with positions $\vec{x}_a$. These particles obey the non-relativistic geodesic equation

$$\frac{d^2\vec{x}_a}{d\tau^2} + H\frac{d\vec{x}_a}{d\tau} = -\nabla\Phi(\vec{x}_a)$$

while Φ is calculated (using a variety of integral techniques) from the non-relativistic equation:

$$-k^2\Phi = 4\pi G a^2 \rho \delta \tag{3.8}$$

Given that, naïvely, $\delta_{gi} \neq \delta$, one would expect that this equation is not applicable on

scales of order the horizon or greater. Yet, it turns out that the δ as calculated in N-body simulations is in the frame of freely falling observers and hence in the synchronous gauge. If we now take the evolution equation for θ in that gauge, we see that it is solved by $\theta \propto a^{-1}$. Any initial perturbation in θ set up at early times will have completely died away and cannot be sourced at the linear level. This means that, in the synchronous gauge, $\delta_{gi} = \delta$. Given that Φ maps directly onto the gauge-invariant Newtonian potential, for a pressure-less fluid, Section 3.3 is therefore applicable on all scales.

There are two major caveats in our explanation of why conventional N-body algorithms are applicable on cosmological scales (see also [66] for the importance of getting the initial value constraint correct). For a start, we have used linear theory while the whole point of N-body simulations is to understand non-linear gravitational collapse; yet we are trying to understand gravitational collapse on the scale of the horizon and there we expect the evolution of gravitational collapse to be accurately described in the linear regime. But more importantly, we have focused on the case of pressure-less matter which fairly represents the dark matter that one is simulating. If the fluid is not pressure-less and non-relativistic, this argument breaks down. The evolution equations for δ and θ for a shear-free perfect fluid in synchronous gauge are now (*cf.* [67])

$$\begin{aligned} \dot{\delta} &= -(1+w)(\theta + \frac{\dot{h}}{2}) - 3H(c_s^2 - w)\delta \\ \dot{\theta} &= -H(1-3w)\theta + \frac{c_s^2}{1+w}k^2\delta \end{aligned}$$

while in the conformal Newtonian gauge they are

$$\begin{aligned} \dot{\delta} &= -(1+w)(\theta - \dot{\Phi}) - 3H(c_s^2 - w)\delta \\ \dot{\theta} &= -H(1-3w)\theta + \frac{c_s^2}{1+w}k^2\delta \end{aligned}$$

where c_s^2 is the sound speed of the fluid. Note that the Laplacian term will play an important role if $c_s k/H \geq 1$. Furthermore if $w \geq 1/3$, θ will not decay, at least at the linear level, and may play a significant role in δ_{gi}. Hence, the non-relativistic Newton-Poisson equations should not be applied on the scale of the horizon or greater.

A notable example is that of the relativistic scalar field introduced in the previous section. The relativistic Newton-Poisson equation is now

$$-k^2\Phi = 4\pi G a^2 \rho \delta_{gi} + 4\pi G \left[\dot{\phi}\dot{\chi} + V'\chi + 3H\dot{\phi}\chi\right] \tag{3.9}$$

where the last term is the relativistic correction. In fact, we can see from Sections 3.2 to 3.3 that this system is fundamentally relativistic (Quintessence-like models have $c_s =$

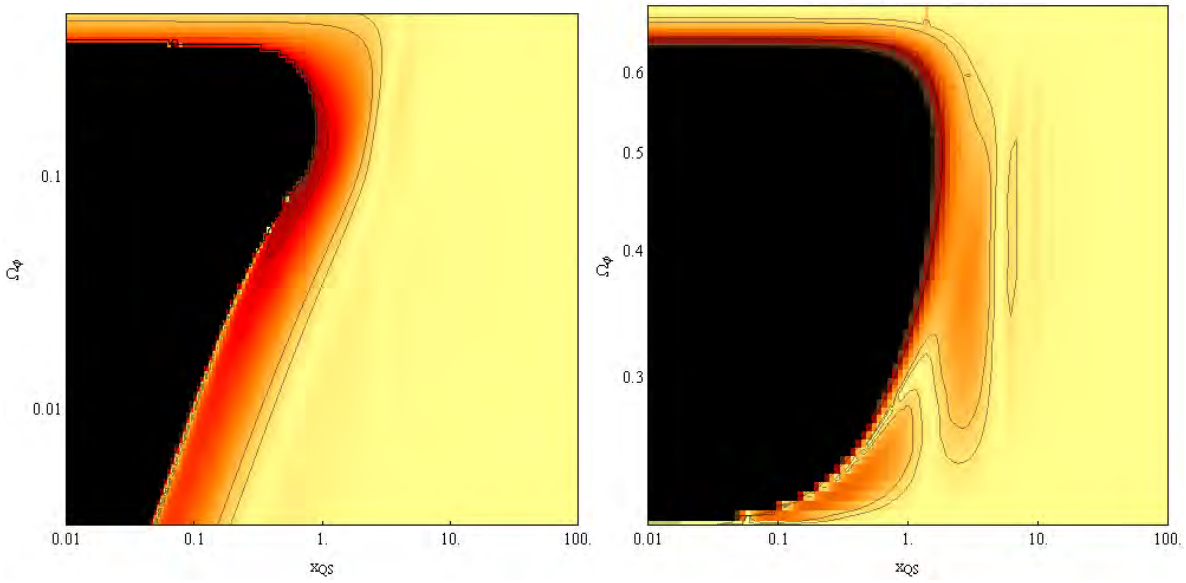

(a) A fast-roll $f(\mathcal{R})$ scenario, where the initial value of Ω_ϕ is small and the field quickly starts evolving.

(b) A slow-roll $f(\mathcal{R})$ setup with a large initial Ω_ϕ, where the field remains frozen-in ('slow-rolling') for a significant amount of time.

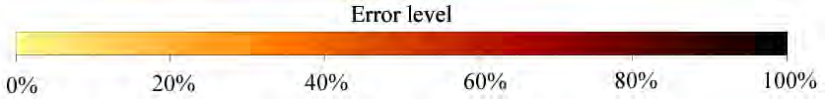

Figure 3.1: Here we show the relative error $\delta_{QS}/\delta_{\rm full} - 1$ resulting from the QSA in $f(\mathcal{R})$ for an accelerating, non-scaling regime ($\lambda = 1.5$ for this plot). The x-axis denotes the value of $x_{QS} = k\tau_{QS}$, and the y-axis denotes the value of $\Omega_\phi(\tau_{QS})$. The evolution is stopped and errors are computed once we reach $\Omega_{\phi,(\rm final)} = 0.7$. Note that the maximum value of the relative error increases with $\Omega_{\phi,(\rm final)}$. Contours denote $5, 10$ and 50% errors from right to left and the black region corresponds to $> 100\%$ error. The oscillatory features mildly visible in the slow-roll case on (sub-)horizon scales are a consequence of the oscillating behaviour of χ on those scales, *cf.* Fig. 3.4.

1). It seems, therefore that to accurately simulate a universe with the usual cosmological fluids and a relativistic scalar field it is necessary to evolve the full relativistic set of equations. This means that for an N-body simulation, not only is it necessary to solve the Newton-Poisson equation and the non-relativistic geodesic equation but also the second order evolution equations for ϕ and χ. This is especially true if one wants to follow the evolution of modes that start off outside the cosmological horizon.

There is a growing interest in simulating N-body systems in the presence of relativistic scalar fields and, as discussed in the introduction, the strategy in the overwhelming majority of cases has been to use the quasi-static approximation when evolving perturbations, where one assumes that[2]

$$\left|\nabla^2 X\right| \gg H^2 \left|X\right| \quad \text{and} \quad \left|\dot{X}\right| \leq H \left|X\right|, \tag{3.10}$$

[2]Our notation follows that of [35] here.

where e.g. $X = \chi, \dot{\chi}, h, \eta, \ldots$ in synchronous gauge. This approximation should be valid on sufficiently small (i.e. sub-horizon) scales: indeed, it is remarkably efficient for evolving cosmological systems without actually having to follow the detailed evolution of the scalar field. It is the purpose of this chapter to explore how accurate this approximation actually is for a range of models which include a relativistic scalar field. Let us reiterate what the QSA entails in more detail than Section 1.4.3:

Definition 3.1 (Quasi-static approximation [226])**.** The quasi-static approximation assumes that the following two conditions are fulfilled:

The relative suppression of time derivatives of metric/field perturbations compared with their spatial derivatives.

$$\left|\dot{X}\right| \leq \mathcal{H}\,|X| \tag{3.11}$$

In principle scalar field (as well as matter and metric) perturbations can follow an evolution with non-negligible time-derivatives, e.g. by displaying highly oscillatory behaviour. However, typically these are heavily constrained. For example, in the case of $f(\mathcal{R})$ gravity $\leftrightarrow$ chameleon models it has been argued that the relative suppression of such derivatives, effectively a slow-roll condition for $\dot{\phi}$, is required by solar system constraints (in order to have a successful screening of fifth forces) [48, 124, 134]. One should keep in mind, however, that this is a model-dependent statement - see e.g. [166] for a symmetron model with collapsing domain walls; a feature absent if a 'static' simulation is employed.

A sub-horizon approximation $k^2 \gg H^2$ or, when written in the same formalism as above

$$\left|\nabla^2 X\right| \gg H^2\,|X|\,, \tag{3.12}$$

This assumption is typically required, since ignoring time-derivatives amounts to neglecting any slow-varying changes to χ as well, which is only justified on sub-horizon scales, where χ has decayed away sufficiently, so that its evolution is no longer important.[3] □

In ΛCDM-like models, the evolution time scale for perturbations is set by the Hubble rate and consequently the sub-horizon assumption is a sufficient condition for the vanishing of time derivatives. However, this is not the case for MG. Here we will solely be concerned with testing the validity of the quasi-static approximation as applied to scalar field fluctuations, so $X = \chi, \dot{\chi}$. Having characterised the quasi-static approximation and how it is used in N-body simulations, we now proceed to explore a few

[3]The oscillatory features visible on (sub-)horizon scales in the contour plots Figs. 3.1 and 3.6 are a result of the intermediate phase where χ is displaying an oscillatory decay, but is still relevant. As a result these features vanish as x_{QS} becomes large, i.e. as the field χ decays away.

representative models. In doing so, we identify the key qualitative features which make the quasi-static approximation a useful and and accurate tool.

3.4 $f(\mathcal{R})$ gravity

In this section and the next we will compare the exact evolution of linearised perturbations in different types of $f(\mathcal{R})$ models with its quasi-static and hence approximate counterpart. The aim is to assess in what regimes the quasi-static approximation is a well-behaved approximation and in particular whether its naïve range of validity (good on subhorizon scales, bad on super-horizon scales) can be extended. We have already defined the $f(\mathcal{R})$ model in Section 2.2.

Recall that in $f(\mathcal{R})$ the equivalent chameleon potential $V(\phi)$ is determined entirely by the original Jordan frame action and is given by

$$V(\phi) = \frac{1}{2}\frac{Rf_{\mathcal{R}} - f}{(1+f_{\mathcal{R}})^2}. \tag{3.13}$$

At this point one may wonder whether any particular fiducial form suggests itself for the potential. For an arbitrary polynomial of positive powers of $\mathcal{R}$ in four dimensions of the form $\sum_{n=1}^{k} a_n R^n$, such a potential will asymptotically approach an exponential potential as $\phi \to \infty$. This is the fiducial potential chosen by [31, 103] and will be the potential we work with throughout most of this chapter too. However, one may wonder what the relevant potential looks like for other motivated potentials of interest, e.g. the Hu & Sawicki model [124], where we have

$$f(\mathcal{R}) = R - m^2 \frac{\left(c_1 \left(\frac{R}{m^2}\right)^n\right)}{1 + c_2 \left(\frac{R}{m^2}\right)^n}, \tag{3.14}$$

where c_1, c_2, n are arbitrary constants. We will return to the Hu & Sawicki model in the context of the chameleon section 3.6, where we will also find that an exponential potential qualitatively is a good proxy for this model in several regions of parameter space. But for the time being we will continue to work in as much generality as possible without specifying a concrete potential.

The evolution of the background in an $f(\mathcal{R})$ model is given in Section 3.4, namely

(tildes indicate that we are in the Einstein frame):

$$\begin{aligned}
\widetilde{H}^2 &= \frac{1}{3}\left(\frac{\dot{\phi}^2}{2} + \widetilde{a}^2 V(\phi) + \widetilde{a}^2\widetilde{\rho}_m\right) \\
\ddot{\phi} &+ 2\widetilde{H}\dot{\phi} + \widetilde{a}^2 V_\phi = \frac{1}{2}\beta\widetilde{a}^2\widetilde{\rho}_m \\
\widetilde{\rho}_m &\equiv \frac{\widetilde{\rho}_m^{*0}}{\widetilde{a}^3}\exp\left(-\frac{\beta\phi}{2}\right).
\end{aligned} \tag{3.15}$$

In synchronous gauge the perturbation equations are given by[4]

$$\ddot{\widetilde{\delta}} + \widetilde{H}\dot{\widetilde{\delta}} - \frac{3}{2}\widetilde{H}^2\widetilde{\Omega}_m(\widetilde{\delta} - \frac{\beta\chi}{2}) - 2\dot{\phi}\dot{\chi} + \widetilde{a}^2 V_\phi\chi = 0 \tag{3.16}$$

$$\begin{aligned}
\ddot{\chi} + 2\widetilde{H}\dot{\chi} + k^2\chi + \widetilde{a}^2 V_{,\phi\phi}\,\chi - \dot{\phi}\dot{\widetilde{\delta}} \\
- \frac{3\beta}{2}\,\widetilde{H}^2\widetilde{\Omega}_m\,(\widetilde{\delta} - \frac{1}{2}\beta\chi) = 0
\end{aligned} \tag{3.17}$$

In the quasi-static approximation, the second perturbation equation can be used to solve for χ, so that we now solve

$$\begin{aligned}
\ddot{\widetilde{\delta}} + \widetilde{H}\dot{\widetilde{\delta}} - \frac{3}{2}\widetilde{H}^2\widetilde{\Omega}_m(\widetilde{\delta} - \frac{\beta\chi}{2}) - 2\dot{\phi}\dot{\chi} + \widetilde{a}^2 V_\phi\chi &= 0 \\
k^2\chi + \widetilde{a}^2 V_{,\phi\phi}\,\chi - \dot{\phi}\dot{\widetilde{\delta}} - \frac{3\beta}{2}\widetilde{H}^2\widetilde{\Omega}_m(\widetilde{\delta} - \frac{1}{2}\beta\chi) &= 0.
\end{aligned} \tag{3.18}$$

Application of the QSA eliminates $\dot{\chi}$, $\ddot{\chi}$ in Eq. (3.17), but not $\dot{\chi}$ in Eq. (3.16), where there is no $k^2\chi$ term relative to which $\dot{\chi}$ is suppressed. Note that, in the evolution equation for χ, several terms survive the QSA. We have both a mass term as well as extra contributions dependent on $\dot{\phi}$ and δ.

In assessing the accuracy of the QSA in $f(\mathcal{R})$ models we will find it useful to compare them with analogous Quintessence-like solutions, i.e. models with no non-minimal coupling to matter as present in the case of $f(\mathcal{R})$. As we saw in Section 2.5, this corresponds to setting $\beta = 0$ in the action Section 2.2. The corresponding background evolution is given in Section 2.5. The perturbations (in the Einstein frame) are governed by

$$\ddot{\widetilde{\delta}} + \widetilde{H}\dot{\widetilde{\delta}} - \frac{3}{2}\widetilde{H}^2\widetilde{\Omega}_m\widetilde{\delta} - 2\dot{\phi}\dot{\chi} + \widetilde{a}^2 V_\phi\chi = 0 \tag{3.19}$$

$$\ddot{\chi} + 2\widetilde{H}\dot{\chi} + k^2\chi + \widetilde{a}^2 V_{,\phi\phi}\,\chi - \dot{\phi}\dot{\widetilde{\delta}} = 0 \tag{3.20}$$

[4]The careful reader will have observed that there are two sign differences between Eq. (3.17) and the analogous equation presented in [31] - the version here corrects these typos.

and the quasi-static approximation reduces this to

$$\ddot{\widetilde{\delta}} + \widetilde{H}\dot{\widetilde{\delta}} - \frac{3}{2}\widetilde{H}^2\widetilde{\Omega}_m\widetilde{\delta} - 2\dot{\phi}\dot{\chi} + \widetilde{a}^2 V_\phi \chi = 0$$
$$k^2\chi + \widetilde{a}^2 V_{,\phi\phi}\,\chi - \dot{\phi}\dot{\widetilde{\delta}} = 0. \tag{3.21}$$

Note how, by taking the limit $\beta \to 0$, Eqs. (3.19) and (3.20) have exactly reproduced the evolution equations for the simple Quintessence-like model in Section 3.2.

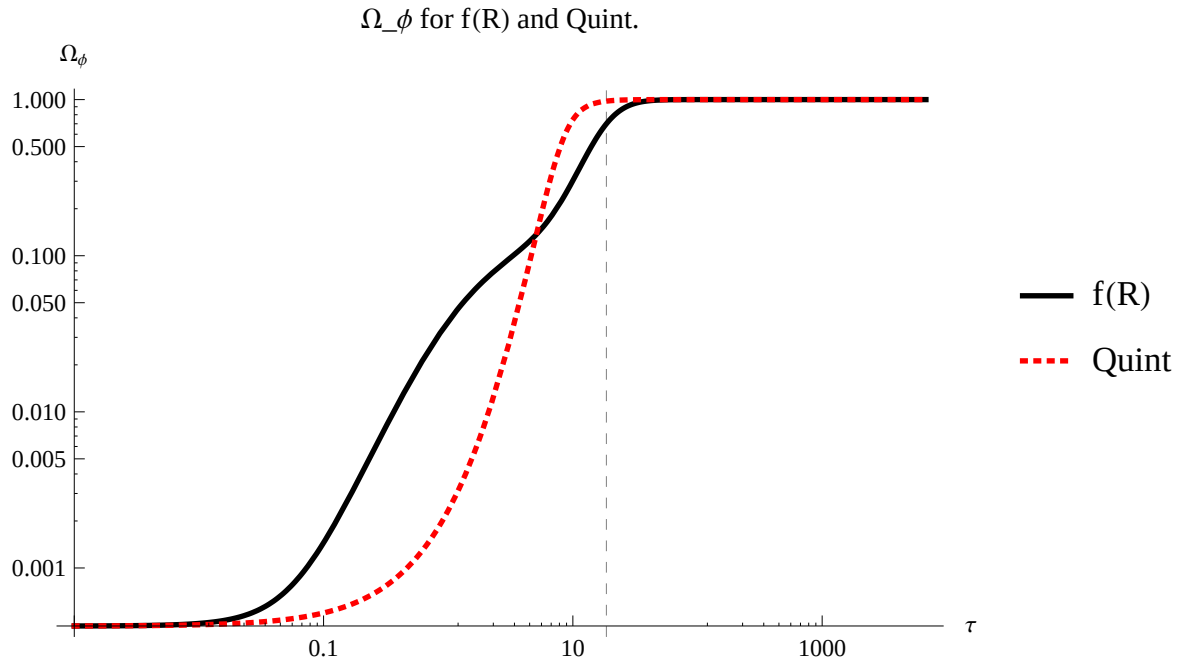

(a) Fast-roll $f(\mathcal{R})$ and corresponding Quint. evolutions starting with an initial $\Omega_{\phi,i} \sim 10^{-4}$ that quickly starts evolving in the $f(\mathcal{R})$ case.

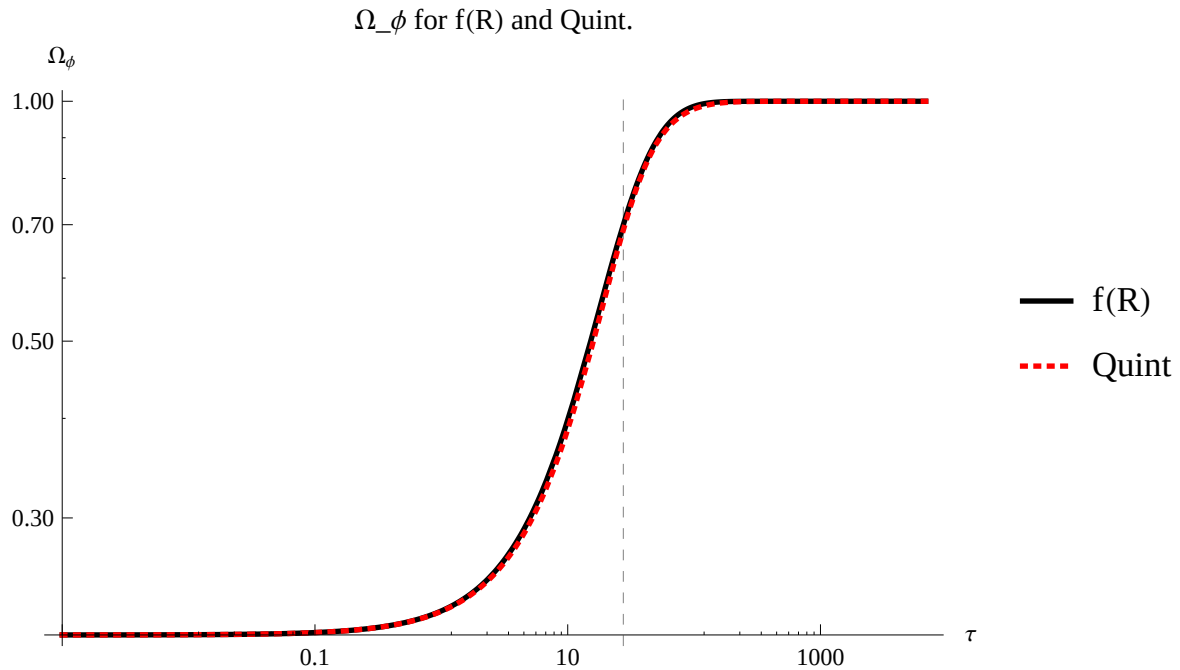

(b) Slow-roll $f(\mathcal{R})$ and corresponding Quint. evolutions starting with an initial $\Omega_{\phi,i} \sim 0.21$ that initially stays frozen in and only later starts evolving. $f(\mathcal{R})$ and Quint. evolutions are nearly indistinguishable in this case.

Figure 3.2: The two different background evolutions in terms of Ω_ϕ considered in this section. Note that the vertical dashed lines indicates when $\Omega_\phi = 0.7$ in the $f(\mathcal{R})$ model considered and that the y-axis has a different range in the two plots.

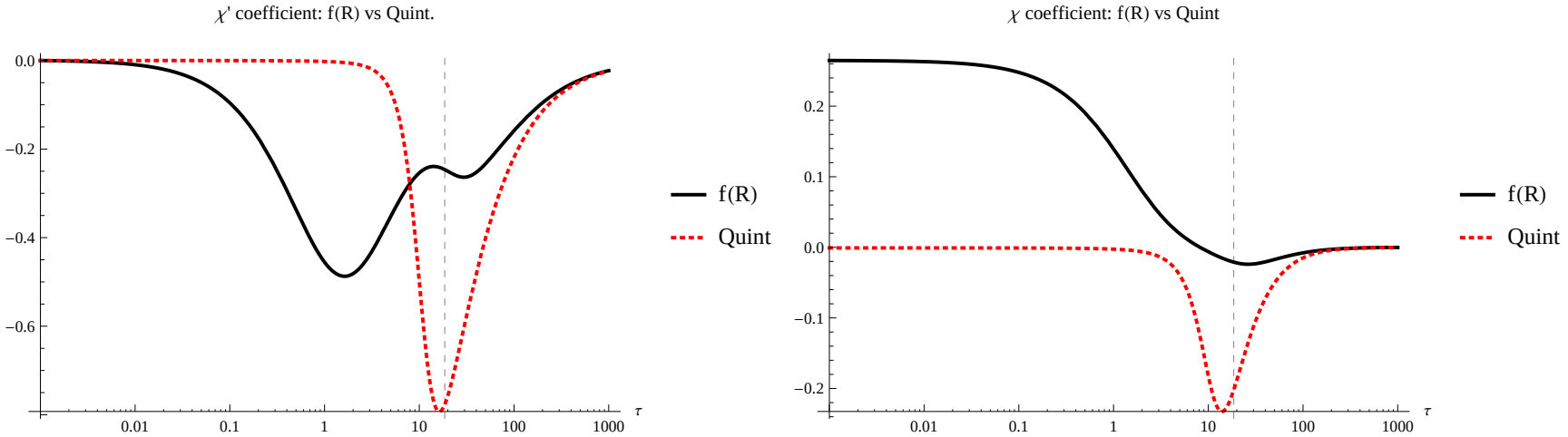

(a) Fast-roll cases: both coefficients are very small at early times when modes of interest are on (super-)horizon scales for Quint., while this is not the case for $f(\mathcal{R})$.

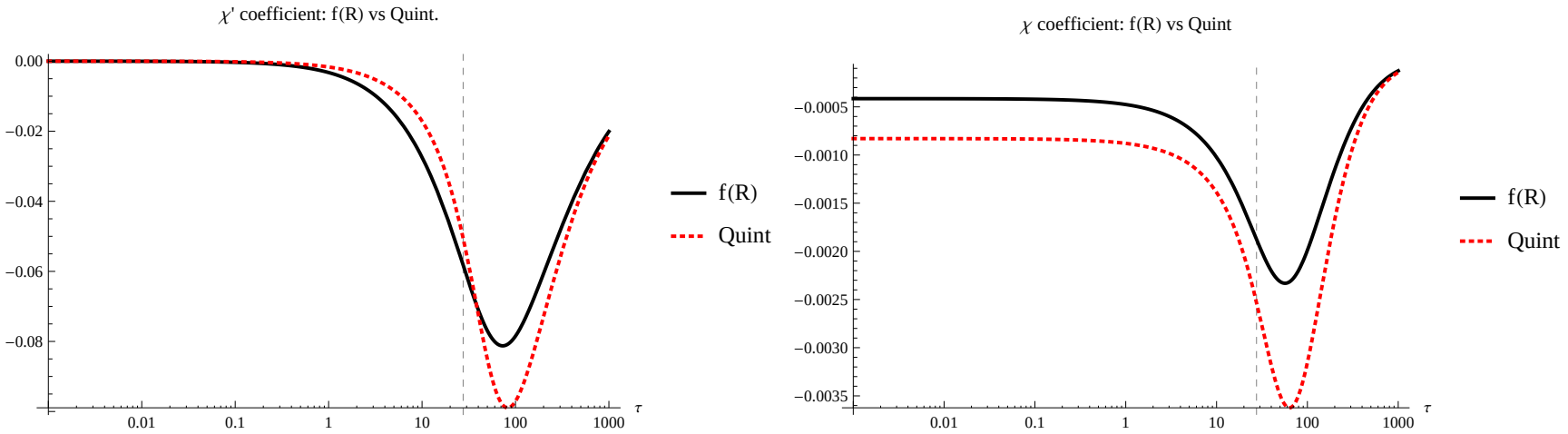

(b) Slow-roll cases: coefficients are small for both $f(\mathcal{R})$ and Quint. leading to a suppression of the QSA error propagation.

Figure 3.3: Plots showing the evolution of the coefficients of χ (left) and $\dot{\chi}$ (right) for $f(\mathcal{R})$ and Quint. in the QSA evolution Eq. (3.25) as discussed in Section 3.4. Once again the vertical dashed lines indicate when $\Omega_\phi = 0.7$ in the $f(\mathcal{R})$ models considered and hence the point at which errors are evaluated in the contour graphs Fig. 3.1.

3.5 The fast and slow roll regime of $f(\mathcal{R})$

It should already be obvious that there are some fundamental differences at the perturbative level between a Quintessence-like model (henceforth Quint.) and an $f(\mathcal{R})$ model as described in the previous section. To understand this difference, in particular in the context of the QSA, consider the solutions to the quasi-static evolution equations:

$$\begin{aligned} \chi_{QSA}^{Quint} &= \frac{\dot{\phi}\dot{\delta}}{k^2 + a^2 V_{,\phi\phi}}, \\ \chi_{QSA}^{f(\mathcal{R})} &= \frac{\dot{\phi}\dot{\delta} + \frac{3}{2}\beta H^2 \Omega_m \delta}{k^2 + a^2 V_{,\phi\phi} + \frac{3}{4}\beta^2 H^2 \Omega_m} \end{aligned} \tag{3.22}$$

Our primary interest is the evolution of δ and errors introduced into this evolution by the QSA. These errors come from the fact that, in the QSA, we simplify the χ evolution equation and hence obtain an inaccurate solution for χ Eq. (3.22) [5]. This propagates to the evolution equation for δ via its direct dependence on χ as well as a dependence on $\dot{\chi}$ via the $\dot{\phi}\dot{\chi}$ term. How much of this error propagates determines how well the QSA does. However, already at this point it becomes clear that the slow- or fast-roll properties of the background (the size of $\dot{\phi}$) will be important for error propagation in the QSA. It will prove useful to consider two concrete $f(\mathcal{R})$ examples. We emphasize that we treat these examples as toy models in order to understand both qualitatively and quantitatively why and when the QSA does well - for the time being, we will therefore not be concerned with tuning all of the model parameters to match observational constraints, but focus on generic features of such models. We will comment on the observational viability of these toy models in the Section 3.6. For both example cases we will, as discussed in the previous section and following [31, 103], pick an exponential potential of the form $V \sim \exp\left(-|\lambda|\,\phi\right)$, choosing $\lambda = 1.5$ so that we obtain a non-scaling, accelerating background solution in which the scalar field dominates at late times. The difference between the two cases will solely consist in the initial conditions imposed on the scalar field, leading to different background evolutions.

We will parametrise the onset of the QSA by two variables. Firstly $x_{QS} = k\tau_{QS}$, labelling the 'time' when the QSA is switched on, i.e. we switch from using the full equations to the approximated ones. If $x_{QS} > 1$ we are in the sub-horizon regime, whereas $x_{QS} < 1$ indicates the super-horizon regime where we would naïvely expect the QSA to fail. Secondly, we keep track of the value of Ω_ϕ at the corresponding time τ_{QS}. We expect this to be relevant, because for a given matching time x_{QS}, the QSA should do better the less-dominant the scalar field is. This is because inaccuracies in

[5] This inaccuracy mainly appears on (super-)horizon scales. On sub-horizon scales the QSA does well by design (at least for the examples considered in this thesis - for counterexamples see [77, 166]) and the corresponding χ solution is a faithful one.

the evolution of χ introduced by the QSA should be less consequential for the evolution of δ. Even though the QSA is only designed to hold for sub-horizon times $x_{QS} \gg 1$, it may therefore still be possible that it faithfully reproduces the full evolution on larger scales. In general, however, we expect the following broad features: for large Ω_ϕ and small x_{QS} we should generate large errors, whereas for small Ω_ϕ and large x_{QS} the QSA should be an excellent approximation.

A few further remarks are in order before proceeding with the QSA analysis for our $f(\mathcal{R})$ scenarios. For the $f(\mathcal{R})$ case we can define the effective (Einstein frame) potential

$$V_{\text{eff},\phi} = V_{,\phi} - \frac{1}{2}\beta\widetilde{\rho}_m \tag{3.23}$$

in terms of which we can also look at the effective equation of state for the scalar degree of freedom

$$w_{\text{eff}} = \frac{1/2\dot{\phi}^2 - V_{\text{eff}}}{1/2\dot{\phi}^2 + V_{\text{eff}}}. \tag{3.24}$$

A slow-rolling model with $\dot{\phi}^2 \ll V_{\text{eff}}$ therefore automatically means the scalar field mimics a ΛCDM evolution with $w \sim -1$ very well. Fast-rolling solutions will tend to take the background away from ΛCDM-like behaviour. We may now recall that [77] found ΛCDM-like background behaviour to coincide with good quasi-static behaviour in $f(\mathcal{R})$ models on sub-horizon scales. We are now in a position to better understand and quantify why this is the case and also to understand how/whether this statement can be extended to super-horizon scales at all.

The coefficients of χ and $\dot{\chi}$ in Section 3.4, that determine how much of the QSA error is propagated to the δ equation respectively are:

$$\mathcal{C}_\chi = \frac{3\beta}{4}\widetilde{\mathcal{H}}^2\widetilde{\Omega}_m + \widetilde{a}^2 V_{,\phi}, \tag{3.25a}$$

$$\mathcal{C}_{\dot{\chi}} = -2\dot{\phi} \tag{3.25b}$$

The second coefficient is clearly suppressed in the ΛCDM-like slow-roll case when $\dot{\phi} \ll 1$. The first coefficient can be re-expressed as

$$\mathcal{C}_\chi = \frac{3\beta}{4}\widetilde{\mathcal{H}}^2\widetilde{\Omega}_m + \widetilde{a}^2 V_{,\phi} = \frac{\beta}{4}\widetilde{a}^2\widetilde{\rho}_m + \widetilde{a}^2 V_{,\phi} \tag{3.25c}$$

It is less obvious how this coefficient will be related to fast- and slow-roll behaviour, so we will investigate this in more detail below.

Above we have already specified that we will use a fiducial potential $V \sim \exp\left(-|\lambda|\,\phi\right)$ as studied by [31, 103]. From our expression for the effective potential Eq. (3.23) we can see that this always has a negative gradient and consequently is a runaway

effective potential without a minimum. In the next section we will discuss what happens when the effective potential displays a minimum (the chameleon case). But for now it suffices to notice that with a choice of potential $V \sim \exp(-|\lambda|\,\phi)$, both V and the β-dependent contribution to the effective potential display runaway behaviour in the same direction

$$V_{\text{eff},\phi} = -|\lambda| V - \frac{\beta}{2}\widetilde{\rho}_m. \tag{3.26}$$

As a direct consequence the $f(\mathcal{R})$ case ($\beta = \sqrt{2/3}$) will have a steeper potential than the corresponding ($\beta = 0$) Quintessence model. This makes slow-roll solutions harder to come by in this particular $f(\mathcal{R})$ model.

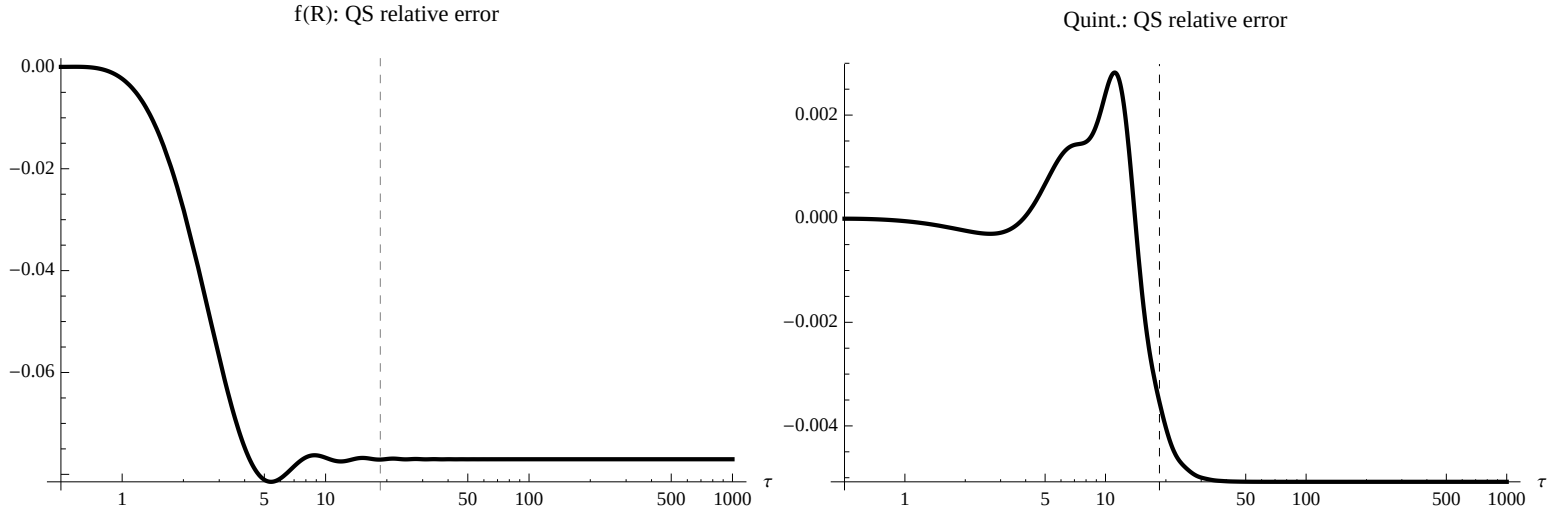

(a) Fast-roll cases: $x_{QS} = 0.5$ and $\Omega_\phi(\tau_{QS}) \sim 0.016$

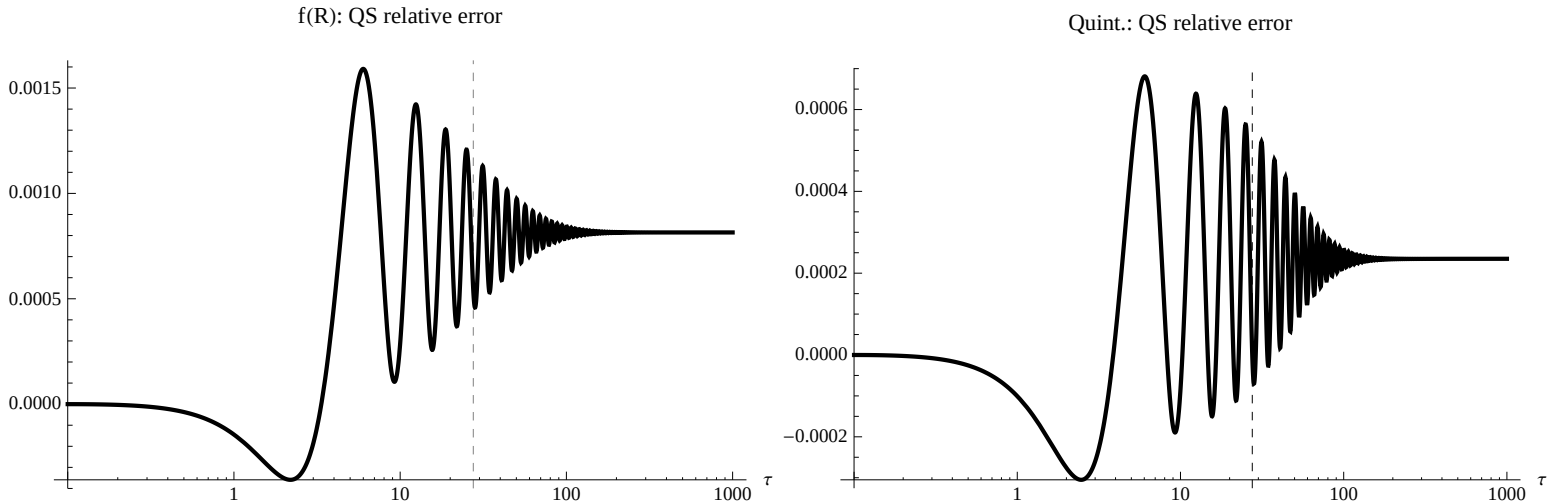

(b) Slow-roll cases: $x_{QS} = 0.1$ and $\Omega_\phi(\tau_{QS}) \sim 0.21$

Figure 3.4: Plots showing the relative error in δ (i.e. $\delta_{QS}/\delta_{\text{full}} - 1$) again for $f(\mathcal{R})$ (top) and for Quint. (bottom). Note that we have chosen units such that $k = 1$ here, so that $\tau = 1$ corresponds to horizon-crossing and these plots essentially correspond to zooming in on a particular pixel in Fig. 3.1. The oscillatory features clearly visible in the slow-roll case are a direct consequence of χ displaying decaying oscillatory behaviour on sub-horizon scales, which are not present in the quasi-static solutions.

3.5.1 Fast Roll

First we consider an evolution where $\dot{\phi}$ swiftly becomes non-negligible, i.e. the field is rolling quickly[6]. The evolution of Ω_ϕ is shown in the left graph of Fig. 3.2. We compare it to a corresponding non-scaling (Quint) Quintessence model (i.e. same potential with $\beta = 0$), where the initial condition ϕ_i has been chosen so that $\Omega_\phi(\tau_{\text{initial}})$ is identical for both cases. The QSA contour plot for this case is shown in the left graph of Fig. 3.1. We plot the relative error $\delta_{QS}/\delta_{\text{full}} - 1$ to show how well the QSA does in comparison with the full linearised solution. We cut off the evolution and evaluate errors when $\Omega_\phi = 0.7$, i.e. our model resembles the state of the universe today[7]. As explained above we plot the final relative error in the parameter space specified by $x_{QS} = k\tau_{QS}$, the 'time' when the QSA was switched on, and the value of Ω_ϕ at τ_{QS}.

A notable feature of Fig. 3.1 is that the error eventually decreases for large values of Ω_ϕ. Note that this is an artefact of cutting off the evolution of the error as soon as an $\Omega_{\phi,\,\text{final}} = 0.7$ is reached. Consequently, if the quasi-static approximation is only switched on at a time when, say, $\Omega_\phi = 0.5$, then even though the QSA will get the evolution of δ very wrong for super-horizon scales, there is just not very much time left until $\Omega_{\phi,\,\text{final}} = 0.7$ is reached, so there is very little time for the error to grow. If a different cutoff at an asymptotic value of $\Omega_{\phi,\,\text{final}} \to 1$ was chosen, and we proceeded to make the analogous contour plot, the error would no longer eventually decreases for large values of Ω_ϕ. Also note that, since Ω_ϕ is still evolving significantly towards its asymptote $\Omega_\phi \to 1$ when the snapshot that leads to Fig. 3.1 is taken (i.e. when $\Omega_\phi = 0.7$), this means the error can also still be evolving. This is demonstrated by comparing Figures 3.2,3.3 and 3.4. The overall error-levels plotted in Fig. 3.1 can therefore continue to grow if a larger $\Omega_{\phi,\,\text{final}}$ is chosen.

The behaviour of the quasi-static approximation for the fast-roll case matches our naïve hypothesis. On sub-horizon scales it performs well irrespective of the initial conditions or the model considered, whereas on super-horizon scales the $f(\mathcal{R})$ model does significantly worse than its Quint. counterpart. To see why, we recall that errors in the QSA for δ stem from propagating an incorrect solution for χ. So we need to investigate how this error propagates to the evolution equation for δ - in other words, check the coefficients of both χ as well as $\dot{\chi}$ in the δ evolution equation. These are purely *background quantities*. They are shown in the two left graphs of Fig. 3.3 and one can immediately read off the reason why the Quint. model performs significantly better in the QSA than the corresponding $f(\mathcal{R})$ setup. We can see that the dependence on both χ and $\dot{\chi}$ is

[6]The initial conditions chosen are: $\phi_i = 5, \dot{\phi}_i = 0, a_i = 1, \lambda = 1.5, \tau_i = 10^{-3}$ and $\widetilde{\rho}_m^{*0} \simeq 10$ for $f(\mathcal{R})$ while $\rho_i = \widetilde{\rho}_m^{*0} e^{-\beta/2\chi_i}$ for Quint., so that $\Omega_{\phi,i}$ is identical for the $f(\mathcal{R})$ and Quintessence models. The initial conditions result in a very small ($\sim 10^{-4}$) initial Ω_ϕ.

[7]In an explicit N-body context one may want to refine this to only extend to the time where a given scale of interest starts to display non-linear behaviour.

highly suppressed at early times (i.e. when relevant modes can still be on super-horizon scales) in the Quint. model, explaining why the error in those quantities does not propagate very much at all to the evolution of δ on those scales. The coefficients plotted in the left graphs of Fig. 3.3 only become relevant for Quint. at late times, when modes of interest are on sub-horizon scales and where the associated χ is very well described by its QSA solution. Note that Ω_ϕ also starts evolving later in the Quint. case (as shown in the left graph of Fig. 3.2), since $\dot{\phi} \ll 1$ for longer here.

For the $f(\mathcal{R})$ case, on the other hand, we can discern two effects. Firstly the new β-dependent terms in the evolution equations result in a significant χ-dependence at early times, when ρ_m is still relevant. Secondly, $\dot{\phi}$ (the coefficient of $\dot{\chi}$) now also evolves at early times, creating yet another source for the propagation of errors in χ on super-horizon scales for modes of interest.

The left hand graphs in Fig. 3.4 finally confirm the intuition gained from the previous plots in this section. Here we zoom in on a particular case, setting $k = 1$, $x_{QS} = 0.5$. This corresponds to a single pixel in the left graph in Fig. 3.1, namely the pixel at $x_{QS} = 0.5$ and $\Omega_\phi(\tau_{QS}) \sim 0.016$ at the very bottom of the graph: i.e. this is a point for which the QSA does fairly well. We find that the relative error for the fast-rolling $f(\mathcal{R})$ setup here is approximately an order of magnitude larger than that for the corresponding Quint. model. Finally it may be worth stressing that, while in the fast-roll case the QSA performs badly on scales close to or above the horizon scale, it still performs well on sub-horizon scales as witnessed by Fig. 3.1, despite having a background evolution that does not closely resemble ΛCDM (*cf.* Fig. 3.2).

3.5.2 Slow Roll

Let us now consider a setup with a long initial slow-rolling phase for ϕ, i.e. $\dot{\phi} \ll 1$[8]. The evolution of Ω_ϕ in this case is shown in the right graph of Fig. 3.2 and we can immediately spot that the Quint. and $f(\mathcal{R})$ cases behave almost identically. The QSA contour plot for this case is shown in the right graph of Fig. 3.1 and indeed the plot mostly agrees with the corresponding (large Ω_ϕ) section of the fast-roll contour plot. However, there is a crucial difference: In the contour plot we show the performance of modes where the QSA is switched on at rescaled time x_{QS} and the background quantity Ω_ϕ is at a given value. But from Fig. 3.2 we know that, due to the initial slow-rolling phase, many modes cross the horizon when Ω_ϕ is still near its initial value. What at

[8]The initial conditions chosen this time are: $\phi_i = 5, \dot{\phi}_i = 0, a_i = 1, \lambda = 1.5, \tau_i = 10^{-3}$ and $\widetilde{\rho}_m^{*0} \simeq 0.016$ for $f(\mathcal{R})$ while $\rho_i = \widetilde{\rho}_m^{*0} e^{-\beta/2\chi_i}$ for Quint., so that $\Omega_{\phi,i}$ is identical for the $f(\mathcal{R})$ and Quint. models. These initial conditions enforce a relatively large (~ 0.2) initial Ω_ϕ which remains frozen in for a significant amount of time. For contour plots Fig. 3.1 we again evolve forwards until $\Omega_\phi = 0.7$. Recall that tildes show that we are using the Einstein frame.

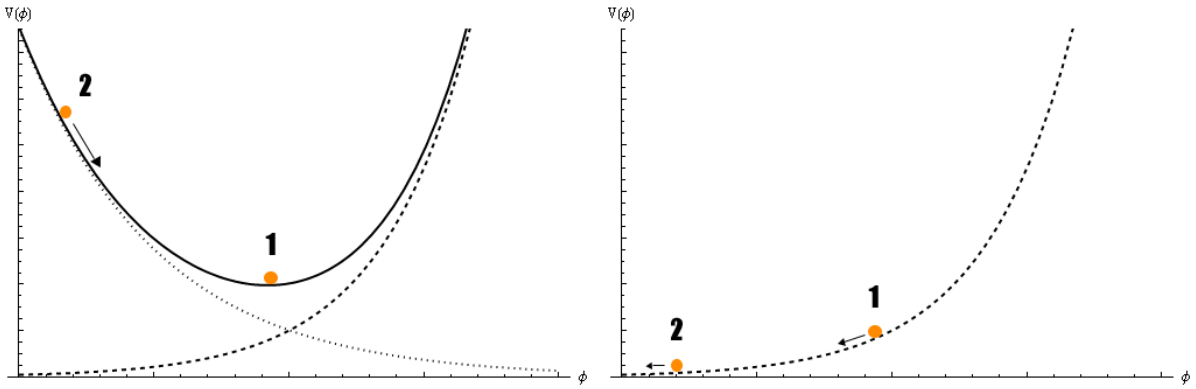

(a) The effective chameleon potential $V_{\rm eff}$ showing the contributions from the original potential $V(\phi)$ (dashed) and from the non-minimal coupling to mat-ter (dotted).

(b) The corresponding Quintessence potential, which only possesses the contribution from $V(\phi)$ since matter is coupled minimally to gravity.

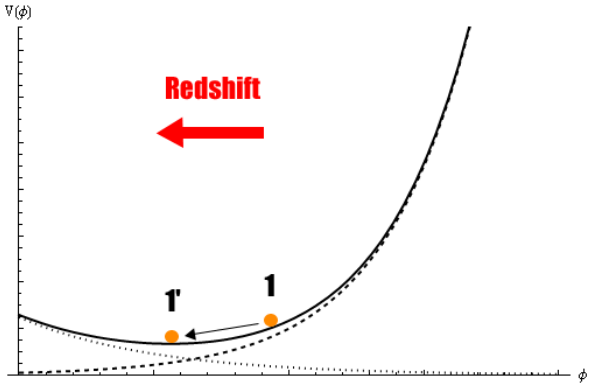

(c) Plot showing how the minimum of the effective chameleon potential changes due to the redshifting of the matter-dependent contribution (dotted).

Figure 3.5: Here we show the effective chameleon potential and its evolution. 1 and 2 label the two initial conditions for the field ϕ considered in the main text.

first sight might appear to be a numerical artefact in the right graph of Fig. 3.1 — the fact that there is a very thin strip directly on top of the x-axis (corresponding to the lowest and initial value of Ω_ϕ which happens to be ~ 0.21 here and which, during the initial phase of the evolution, remains frozen-in as shown in Fig. 3.2) and that the QSA does in fact do very well even for modes crossing the horizon during this initial phase — is a direct consequence of the slow-rolling behaviour of the solution.

This may appear counter-intuitive, since a large Ω_ϕ means the scalar field is relevant to the cosmic evolution and should hence affect δ. By introducing errors into the evolution of χ via the QSA, these should then map onto significant errors for δ. However, we have already seen above that it is in fact other background properties — such as the slow- or fast-rolling nature of $\dot{\phi}$ — that control how much the QSA errors in χ are propagated to the evolution of δ. To make this clear let us once again zoom in on a particular case, setting $k = 1$ and $x_{QS} = 0.1$. This corresponds to a single pixel in the right graph in Fig. 3.1, this time the pixel at $x_{QS} = 0.1$ and $\Omega_\phi = 0.21$ in the thin bright (i.e. low

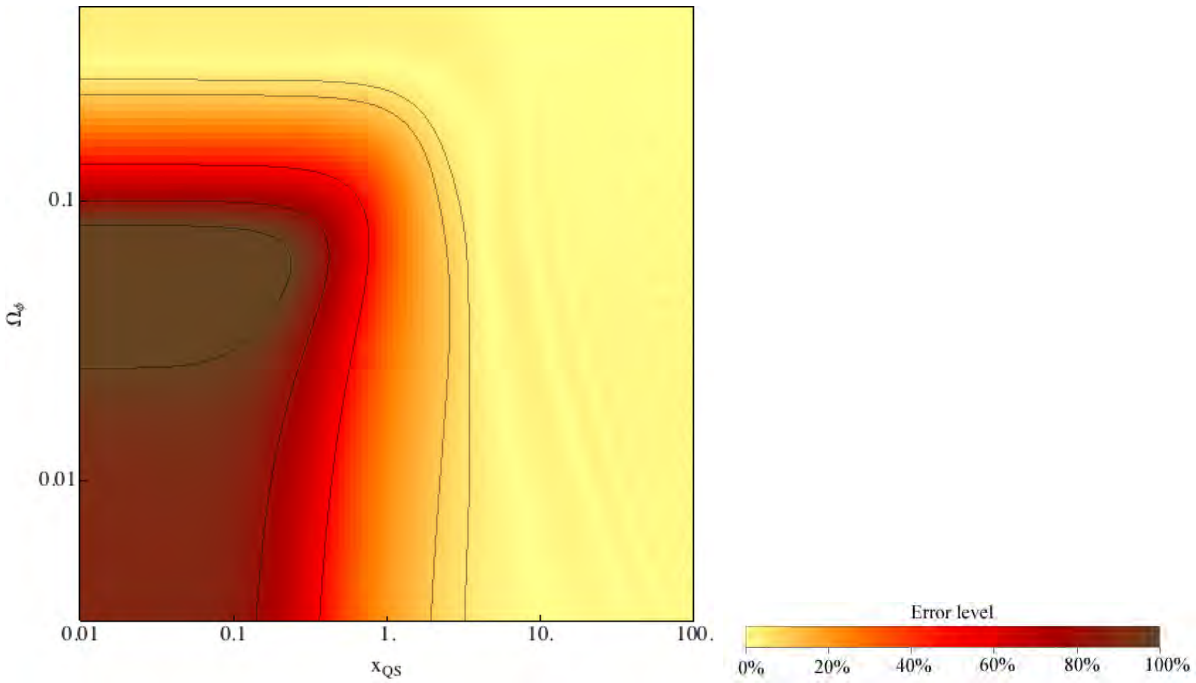

(c) Fast-roll initial condition (case 2) away from the minimum of the effective potential

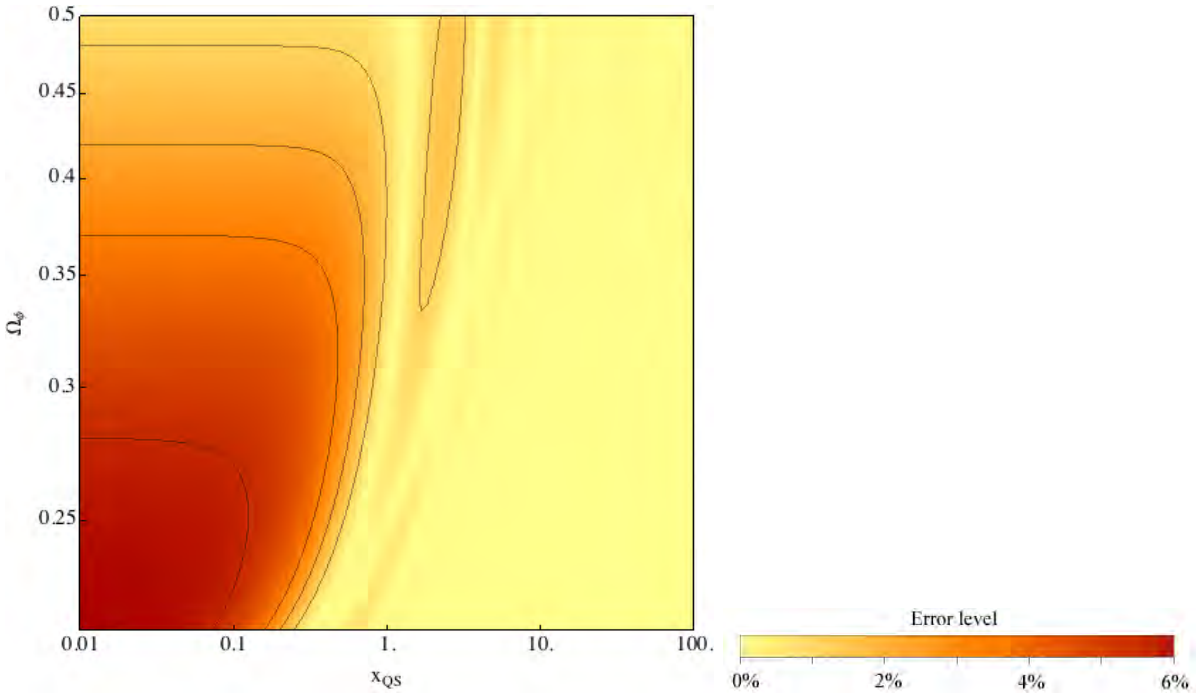

(f) Slow-roll initial condition (case 1) at the minimum of the effective potential

Figure 3.6: Contour plots plotting the relative error $\delta_{QS}/\delta_{\text{full}} - 1$ showing how well the chameleon does in the QSA for the fast-roll and the slow-roll initial condition (*cf.* Fig. 3.5). Note how the slow-rolling nature of the field enforced by case 1 results in a much improved performance of the QSA. Axes are labelled and chosen as in Fig. 3.1 and error contours are $5, 10, 50, 80, 100\%$ and $1, 2, 3, 5\%$ from right to left in the fast- and slow-roll cases respectively. The oscillatory features that are visible on (sub-)horizon scales are a consequence of the oscillating behaviour of χ on those scales, *cf.* Fig. 3.4.

error) strip directly at the bottom of the graph; a point for which the QSA does very well as depicted in Fig. 3.4.

As before, we now need to check whether the error introduced into χ is enhanced or suppressed by the background coefficients in the δ evolution equation. These are shown in the right hand graphs in Fig. 3.3. Comparing with the corresponding Quint. graphs we see that the background behaviour enforces small coefficients $\mathcal{C}_\chi$ and $\mathcal{C}_{\dot{\chi}}$, suppressing the dependence on χ of the evolution equation for δ at early times both for the $f(\mathcal{R})$ and Quint. cases this time. For the modes of interest (subhorizon today) the relevant coefficients only become large after horizon-crossing when the exact and QSA solutions for χ match very well. This is a consequence of the initial slow-rolling phase. The conclusion one draws here is that, once the evolution equations for the perturbations are known, we can understand how well the QSA performs on super-horizon scales in terms of background quantities. In the particular case considered here, even though we started with a large Ω_ϕ, this remained frozen in initially so that $\dot{\phi}$ remained small and the dependence on χ is also suppressed. The right hand graphs in Fig. 3.4 summarise these results, showing that the relative errors for both the $f(\mathcal{R})$ and Quint. setups considered in this section are very small (on the sub 0.1% level).

The key result of this section is that the impact of the QSA can depend crucially on how the evolution equation for the scalar field couples back into that of the density perturbation. Small errors in the QSA for χ can be greatly amplified if the background scalar field evolves substantially. Small values of Ω_ϕ (indicating that the field ϕ only negligibly contributes to the energy density of the universe at the relevant time) may not be enough to prevent the propagation of large errors. In some sense, this is not surprising- it is the *non-static* nature of the background which is pushing the QSA outside its range of validity. And, if the QSA is to be applied in any specific $f(\mathcal{R})$ theory, it is clearly essential to check whether the evolution of the scalar field is such that the approximation is good enough.

3.6 The Chameleon mechanism in $f(\mathcal{R})$

It is well-known [50, 134] that a subset of $f(\mathcal{R})$ models give rise to the so-called chameleon effect, where the non-minimal coupling to matter in the Einstein frame results in an effective potential for ϕ with a minimum, and consequently an effective mass. In chameleon models this is used to screen away any fifth force from ϕ in dense regions, allowing them to evade tight fifth force constraints on solar system scales [134]. Such a screening mechanism is therefore an essential ingredient to construct an observationally viable $f(\mathcal{R})$ model. Screening is an intrinsically non-linear effect and our linearised

analysis is consequently not sensitive to it by default. However, the analysis is sensitive to the form of the potential via the associated mass term[9], so it is worth considering how this impacts our analysis and whether there are any interesting consequences for the QSA.

Let us briefly review the mapping between $f(\mathcal{R})$ theories and chameleons, pointing out some important subtleties between different, typically-used conventions. In order to do so we establish a dictionary between the convention (largely) used in the literature for structure formation in $f(\mathcal{R})$ models (e.g. [31, 124]) and that used in chameleon phenomenology and screening effects (e.g. [121]). The former convention we label I and the latter II: this thesis uses convention I.

Definition 3.2 (Conventions for the chameleon-$f(\mathcal{R})$ mapping)**.** In order to avoid confusion when comparing with other literature, we here explicitly spell out these conventions and the mapping between them.

Convention I: As we saw at the start of this section, the $f(\mathcal{R})$ action can be written (in the Jordan frame) as

$$S_J = \frac{1}{2}\int d^4x\sqrt{-g}\,\left[\mathcal{R}+f(\mathcal{R})\right] + \int d^4x\sqrt{-g}\,\mathcal{L}_{\rm m}[\Phi_i, g_{\mu\nu}]\ , \tag{3.27}$$

which is then mapped into the equivalent Einstein frame scalar-tensor theory

$$\begin{aligned} S_E &= \frac{1}{2}\int d^4x\sqrt{-\widetilde{g}}\,\widetilde{R} \\ &+ \int d^4x\sqrt{-\widetilde{g}}\,\left[-\frac{1}{2}\widetilde{g}^{\mu\nu}\widetilde{\nabla}_\mu\phi\widetilde{\nabla}_\nu\phi - V(\phi)\right] \\ &+ S_{matter}[\Phi_i, e^{-\beta\phi}\widetilde{g}_{\mu\nu}] \end{aligned} \tag{3.28}$$

where we have employed a conformal transformation

$$\widetilde{g}_{\mu\nu} = e^{\beta\phi}g_{\mu\nu}, \tag{3.29}$$

and defined the field ϕ via

$$1 + f_{\mathcal{R}} \;=\; e^{2\phi\beta}. \tag{3.30}$$

β in this convention is $\sqrt{2/3}$. The potential $V(\phi)$ is determined by

$$V(\phi) = \frac{1}{2}\frac{\mathcal{R}f_{\mathcal{R}} - f}{(1+f_{\mathcal{R}})^2}. \tag{3.31}$$

[9]After all, the background field evolution and especially $\dot{\phi}$ are highly sensitive to the form of the potential.

Convention II: The action we start with now is

$$S_J = \frac{1}{2}\int d^4x\sqrt{-g}\ [f(\mathcal{R})] + \int d^4x\sqrt{-g}\,\mathcal{L}_{\rm m}[\Phi_i, g_{\mu\nu}]\ , \tag{3.32}$$

i.e. $f(\mathcal{R})^{(II)} = R + f(\mathcal{R})^{(I)}$ where the Roman index denotes the convention. The metric $\widetilde{g}_{\mu\nu}$ and the field ϕ are now defined via

$$f_{\mathcal{R}}^{(II)} = e^{-2\hat{\beta}\phi}, \tag{3.33}$$

$$\widetilde{g}_{\mu\nu} = e^{-2\hat{\beta}\phi} g_{\mu\nu} = f_{\mathcal{R}}^{(II)} g_{\mu\nu}. \tag{3.34}$$

$\hat{\beta}$ in this convention is $\sqrt{1/6}$. Finally the potential $V(\phi)$ in the second convention is

$$V(\phi)^{(II)} = \frac{1}{2}\frac{R f_{\mathcal{R}}^{(II)} - f^{(II)}}{(f_{\mathcal{R}}^{(II)})^2}. \tag{3.35}$$

The mapping: It is now clear that the difference between the two conventions boils down to a a field redefinition of ϕ, namely

$$\phi_{(I)} \leftrightarrow -\phi_{(II)}. \tag{3.36}$$

This means care has to be taken when considering which potentials have the correct properties to give rise to an effective chameleon.

□

The $f(\mathcal{R})$ model considered in the previous section does not display chameleonic behaviour. This is straightforward to understand from the background evolution equation. Recall this is

$$\ddot{\phi} + 2\widetilde{H}\dot{\phi} + \widetilde{a}^2 V_\phi = \frac{1}{2}\beta\widetilde{a}^2\widetilde{\rho}_m \tag{3.37}$$

for the background scalar ϕ. Now we can write this in terms of an effective potential for ϕ (absorbing the factor $\widetilde{a}^2$ this time)

$$V_{\text{eff},\phi} = \widetilde{a}^2 V_\phi - \frac{1}{2}\beta\widetilde{a}^2\widetilde{\rho}_m. \tag{3.38}$$

However, for the runaway potential $V \sim e^{-|\lambda|\phi}$ both contributions to $V_{\text{eff},\phi}$ are negative, so no minimum exists. Yet, for a chameleon-like model, we require that V_{eff} has a minimum.

Under what conditions does the $f(\mathcal{R})$ potential fulfil the requirements for chameleon behaviour? Adapting the results of [50] to the conventions used throughout this thesis,

we find that the relevant conditions are[10]

$$V_\phi > 0 \qquad\qquad V_{\phi\phi} > 0 \qquad\qquad V_{\phi\phi\phi} > 0. \tag{3.39}$$

We can check that this is indeed the case. Firstly consider a new fiducial chameleon potential $V = \exp(|\lambda|\,\phi)$ trivially satisfying the chameleon conditions above. From Eq. (3.37) this can clearly generate an extremum for the effective potential now. The derivatives of the potential in our convention are now given by

$$V = \frac{\mathcal{R} f_\mathcal{R} - f}{2\left(f_\mathcal{R}+1\right)^2} \tag{3.40}$$

$$V_\phi = \beta \frac{\mathcal{R} + 2f - \mathcal{R} f_\mathcal{R}}{2\left(1+f_\mathcal{R}\right)^2} \tag{3.41}$$

$$V_{\phi\phi} = \frac{\beta^2}{2}\left(\frac{1}{f_{\mathcal{R}\mathcal{R}}} + \frac{\mathcal{R}\left(f_\mathcal{R}-3\right)-4f}{\left(1+f_\mathcal{R}\right)^2}\right) \tag{3.42}$$

$$\begin{aligned} V_{\phi\phi\phi} = &-\beta^3 \frac{f_{\mathcal{R}\mathcal{R}\mathcal{R}}\left(f_\mathcal{R}+1\right)^3 + 3\left(f_\mathcal{R}+1\right)^2 f_{\mathcal{R}\mathcal{R}}^2}{2\left(1+f_\mathcal{R}\right)^2 f_{\mathcal{R}\mathcal{R}}^3} \\ &-\beta^3 \frac{\mathcal{R}\left(f_\mathcal{R}-7\right)-8f}{2\left(1+f_\mathcal{R}\right)^2}. \end{aligned} \tag{3.43}$$

In order for the effective potential $V_{\rm eff}$ to have a minimum in the Jordan frame, the condition

$$\mathcal{R} + 2f - \mathcal{R} f_\mathcal{R} > 0 \tag{3.44}$$

needs to be satisfied [31, 124]. Comparing with our expression for the derivatives of the potential, this shows that $V_\phi > 0$ as expected. As a further check we can cross-check against a model that is known to have consistent chameleon screening, the Hu & Sawicki model [124]. Fig. 3.7 demonstrates that regions of parameter space satisfy the necessary constraints for different choices of parameters in this model. As a corollary we see that the fiducial exponential potential we have chosen here qualitatively is a good proxy for Hu & Sawicki potentials in regions of parameter space that display chameleon screening.

Equipped with the above insights about the nature of the potential, we choose a fiducial chameleon potential $V = e^{|\lambda|\phi}$. The evolution equations for the background, perturbations and perturbations in the QSA laid out in the previous section are still valid. We now contrast two cases. In the first case, we initially place the field at the minimum (this is case 1 shown in the left graph of Fig. 3.5); in this situation we expect the QSA

[10] This may come as a surprise, given the result of [50] who quote the condition: $V_\phi < 0$ $V_{\phi\phi} > 0$ $V_{\phi\phi\phi} < 0$ as required for $f(\mathcal{R})$ models with chameleon screening. This difference is due to two differing conventions used in the literature when mapping a given $f(\mathcal{R})$ model into its scalar-tensor form. We discuss these conventions in Definition 3.2 and describe the field redefinition that maps between them. Also note that we need $V_\phi > 0$, since for a minimum we require $V_{eff,\phi} = 0$, but the contribution from the non-minimal coupling to matter to $V_{eff,\phi}$ is negative.

to do very well and indeed it does as shown in the left graph of Fig. 3.6. This is because, as we saw in the previous section, errors generated by the QSA are propagated via their dependence on $\dot{\phi}$ and $H^2\Omega_m$. If the field is slow-rolling any dependence on χ is highly suppressed; indeed, starting at the minimum should keep ϕ frozen at the minimum. Having said that, since the effective potential will evolve due to the redshifting of matter density, the field will in fact slowly roll tracking the effective minimum, so a small error should still remain. This effect is shown in the right graph in Fig. 3.5, while the middle graph in the same figure shows the corresponding situation in the Quint. setup which lacks any contribution to the effective potential that depends on the cosmological matter density (again we match initial conditions so that the Quint. and chameleon cases start off with the same Ω_ϕ as discussed in the previous section).

The initial condition for starting out at the minimum of the potential is (tildes indicate that we are in the Einstein frame)

$$V_{\text{eff},\phi} = \sqrt{1/6}\widetilde{\rho}_m - \lambda V_0 e^{\lambda\phi} = 0. \tag{3.45}$$

Denoting the initial value of the scalar field by ϕ_i, in terms of an initial condition for the matter energy density $\widetilde{\rho}_m$ this means we require

$$\widetilde{\rho}_{m,\text{ initial}} = \sqrt{6}\lambda e^{\lambda\phi_i}. \tag{3.46}$$

This means that the initial energy density Ω_ϕ, which we may write as

$$\Omega_\phi = \frac{1}{1+\frac{\rho_m}{\rho_\phi}}, \tag{3.47}$$

is fixed once we require the field to start at its minimum and specify λ.

To understand this better let us once again effectively zoom in on a single pixel in the contour plot, setting $k = 100$, $x_{QS} = 0.1$ and $\Omega_\phi(\tau_{QS}) \sim 0.22$. Also setting $\lambda = 1.5$ as for the contour plots we obtain the evolution shown in Fig. 3.8.[11] One sees that the background field ϕ is indeed very slowly rolling. We compare this with a Quintessence-like model that starts out with the same Ω_ϕ. The reason the non-chameleon Quintessence-like model also does relatively well, is that the minimum of the effective potential lies in a region where the curvature of the original ϕ potential is very small (*cf.* the middle graph in Fig. 3.5). Hence the field is slow-rolling in the Quintessence case too, only doing mildly worse in the long run than the chameleonic $f(\mathcal{R})$ setup.

In the second case we start away from the minimum. This is labelled as case 2 for both

[11] Again we emphasize that the parameters (λ, ϕ_i, etc.) chosen for our examples are intended to give rise to toy models providing an understanding of the QSA. An in-detail comparison with observational constraints on the parameter space of such models is beyond the scope of this thesis.

the $f(\mathcal{R})$/chameleon and Quintessence cases in Fig. 3.5. The QSA error introduced now is shown in the left graph in Fig. 3.6 and we see that the QSA does significantly worse than in the the first case, where the field started at the minimum of the effective potential. Zooming in on a pixel with $k = 100$, $x_{QS} = 0.1$ and $\Omega_\phi(\tau_{QS}) \sim 0.0014$, we obtain the evolution shown in Fig. 3.9. As expected the Quintessence-like model is hardly affected by the change from case 1 to case 2. In fact it does slightly better than before since we have effectively moved into the flat, tail end of the original potential for ϕ. However, the ρ_m-dependent term in the effective potential for the chameleon case means the field there is rolling down a very steep slope and hence the QSA error is strongly propagated to the δ evolution equation, resulting in a very bad fit for the QSA (Fig. 3.6).

While the the two cases considered above are extremely useful in understanding what controls the accuracy of the QSA and in particular in stressing the importance of the fast/slow-rolling nature of the background, at this point it is important that an initial condition very close to or identical to case 1 is the observationally motivated case. Firstly note that BBN constraints require the field to have settled into its minimum by the time BBN starts [49]. CMB constraints can also be used to place bounds on the variation of ϕ since recombination, giving [47]

$$\left|\exp\left(\frac{\beta\Delta\phi}{M_{Pl}}\right) - 1\right| < 0.05 \tag{3.48}$$

This ensures that viable chameleon models do well in the QSA in the linearised regime, since as we have seen, the approximation works well if we start close to the minimum of the effective potential (which results in a maximally slow-rolling evolution). This serves as somewhat of an a posteriori justification for the use of the QSA in chameleon models - and we should stress: even on super-horizon scales. Note that this is directly related to the shape of the chameleon potential. Since the field is slow-rolling along with the effective minimum, QSA errors are strongly suppressed. Of course the effective minimum also generates an effective screening mass for ϕ. Nevertheless we should keep in mind that, while the screening properties of chameleon theories are intrinsically non-linear effects, the fact that the QSA does well here solely relies on the slow-rolling nature of the background. One should therefore not convolute explanations for the efficiency of screening and the accuracy of the QSA in this case.

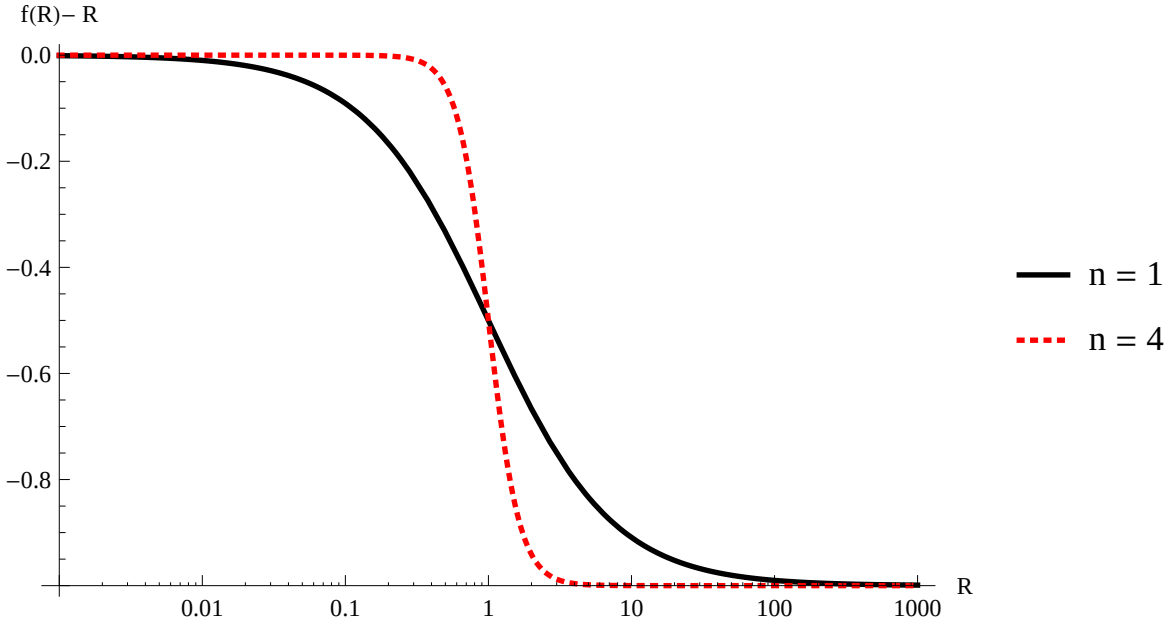

(a) We plot $f(\mathcal{R}) - \mathcal{R}$ vs. $\mathcal{R}$, showing how this model interpolates between different $f(\mathcal{R})$ for large and small curvatures.

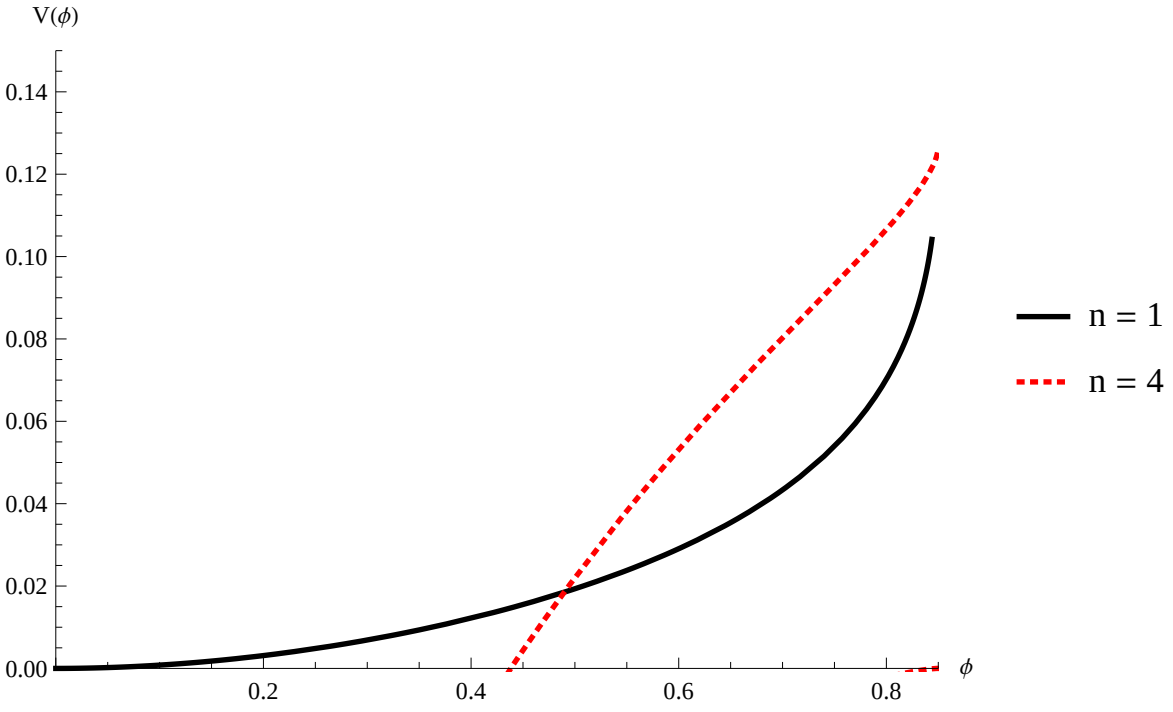

(b) The resulting potential $V(\phi)$.

Figure 3.7: The Hu & Sawicki potential Eq. (3.14) for $m = c_1 = c_2 = 1$. Note how the potential for $n = 1$ satisfies $V_\phi, V_{\phi\phi}, V_{\phi\phi\phi} > 0$ for all $\mathcal{R}$ (and hence always acts as a chameleon), whereas $n = 4$ only satisfies this for large $\phi \sim 0.8$ (which corresponds to large curvature $\mathcal{R}$ here), so chameleon-like behaviour is restricted to the high curvature regime in the second case.

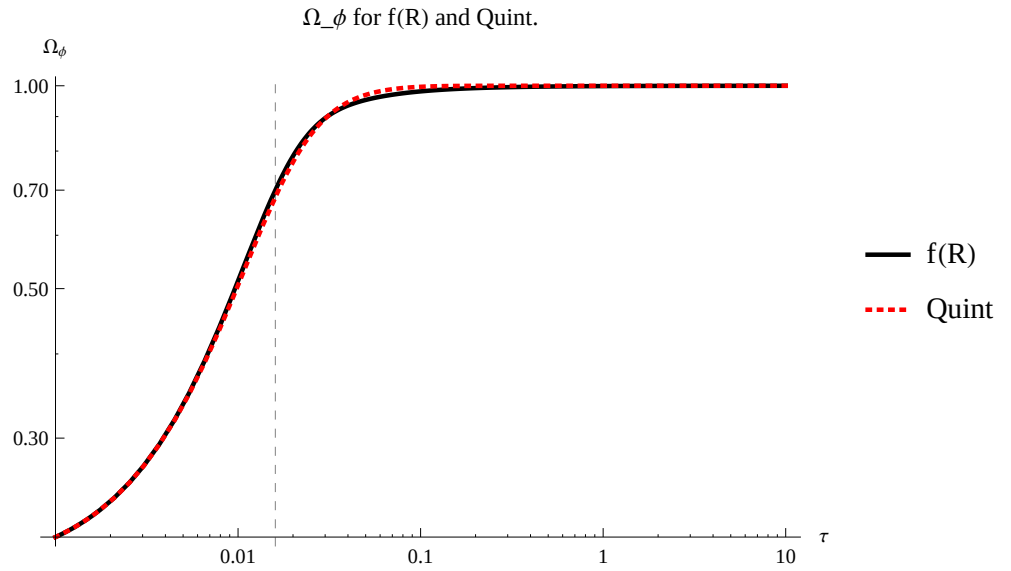

(a) Evolution of Ω_ϕ

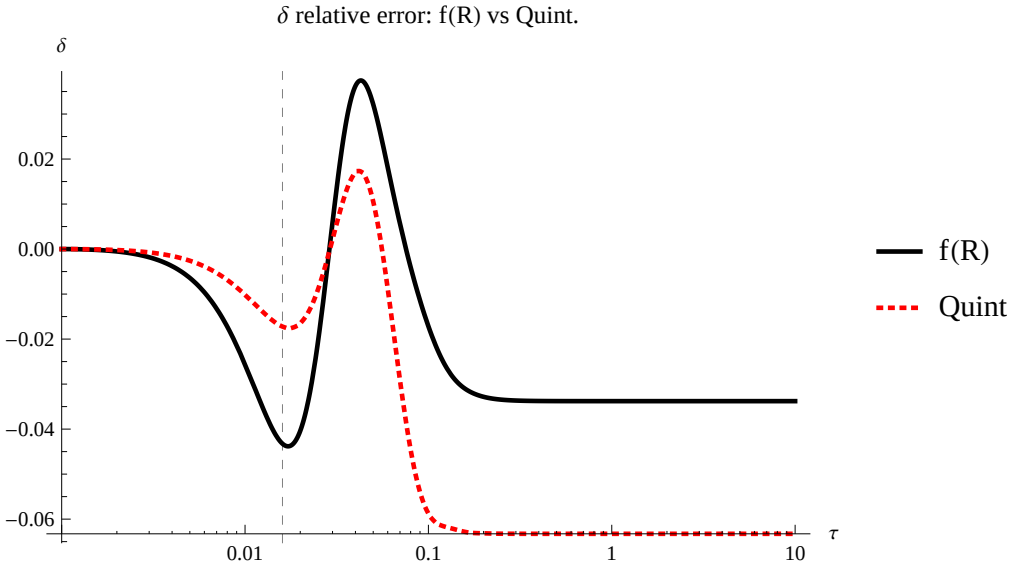

(b) Evolution of $\delta_{QS}/\delta_{\text{full}} - 1$

Figure 3.8: The slow-rolling chameleon (case 1): Initial conditions place the field at the minimum in the effective potential V_{eff}, resulting in a slow-rolling field and small QSA errors. The Quintessence-like case also performs well due to the very flat $V(\phi)$. The dashed vertical line denotes the time when $\Omega_\phi = 0.7$ and the relative error is evaluated in our contour plots. The evolution of Ω_ϕ for a chameleon $f(\mathcal{R})$ and Quint. model starting with identical Ω_ϕ is almost identical. We show the evolution of $\delta_{QS}/\delta_{\text{full}} - 1$ in units where $k = 100$ and choosing $x_{QS} = 0.1$ and $\Omega_\phi(\tau_{QS}) \sim 0.22$ (*cf.* Fig. 3.6). Horizon-crossing therefore takes place at $\tau = 0.01$. The evolution of δ in the $f(\mathcal{R})$ chameleon case and the Quint. case, with full and quasi-static solutions: both agree very well in the slow-roll case shown here. In the evolution of coefficients for $\dot{\chi}$ (left) and χ (right) in Section 3.4 the chameleon $f(\mathcal{R})$ and Quint solution closely follow each other here in comparison to the analogous plots in Fig. 3.9 (up to $\sim 50\%$ vs. $> 1000\%$ difference).

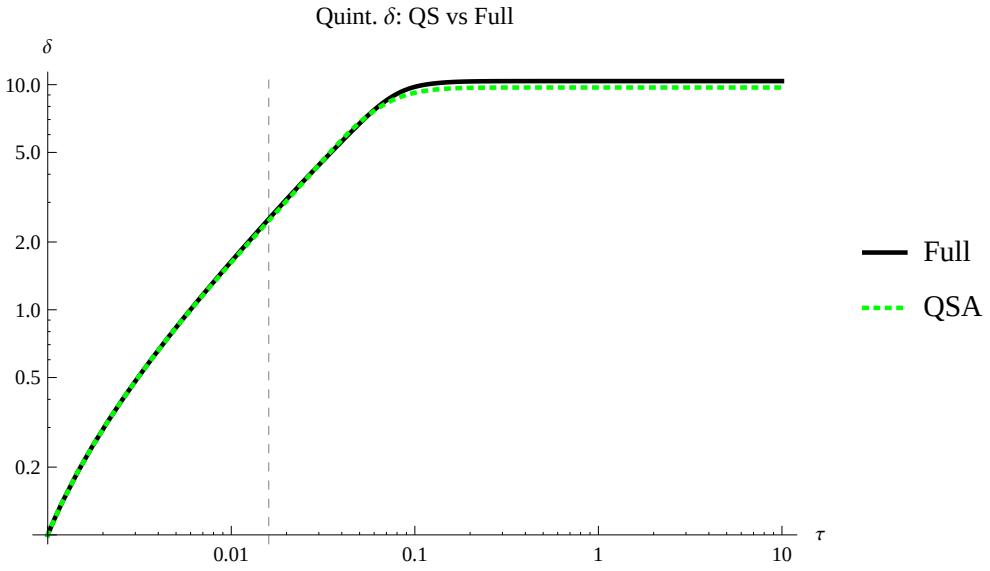

(c) Evolution of δ in Quint.

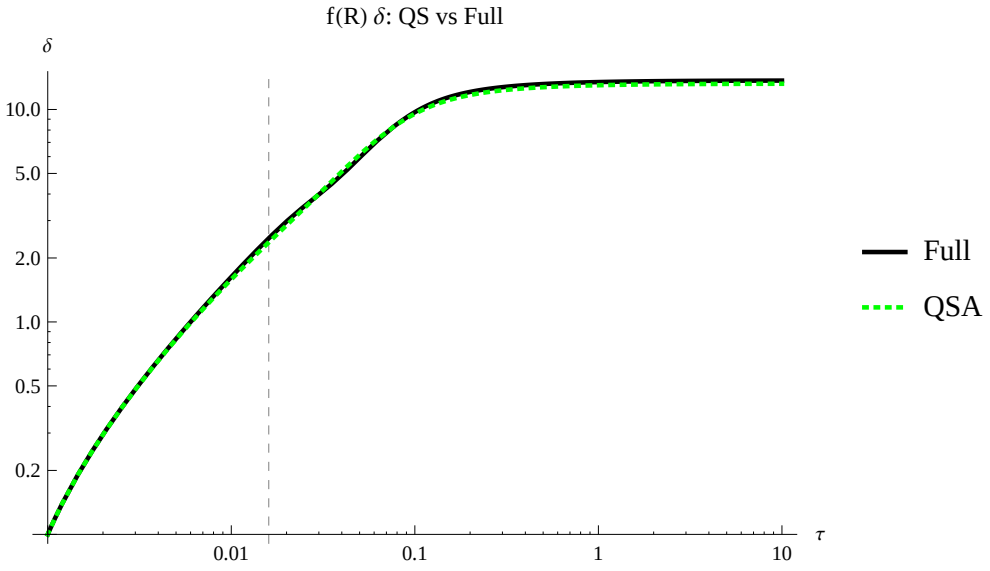

(d) Evolution of δ in $f(\mathcal{R})$

Figure 3.8: The slow-rolling chameleon (case 1): Initial conditions place the field at the minimum in the effective potential V_{eff}, resulting in a slow-rolling field and small QSA errors. The Quintessence-like case also performs well due to the very flat $V(\phi)$. The dashed vertical line denotes the time when $\Omega_\phi = 0.7$ and the relative error is evaluated in our contour plots. The evolution of Ω_ϕ for a chameleon $f(\mathcal{R})$ and Quint. model starting with identical Ω_ϕ is almost identical. We show the evolution of $\delta_{QS}/\delta_{\text{full}} - 1$ in units where $k = 100$ and choosing $x_{QS} = 0.1$ and $\Omega_\phi(\tau_{QS}) \sim 0.22$ (*cf.* Fig. 3.6). Horizon-crossing therefore takes place at $\tau = 0.01$. The evolution of δ in the $f(\mathcal{R})$ chameleon case and the Quint. case, with full and quasi-static solutions: both agree very well in the slow-roll case shown here. In the evolution of coefficients for $\dot{\chi}$ (left) and χ (right) in Section 3.4 the chameleon $f(\mathcal{R})$ and Quint solution closely follow each other here in comparison to the analogous plots in Fig. 3.9 (up to $\sim 50\%$ vs. $> 1000\%$ difference).

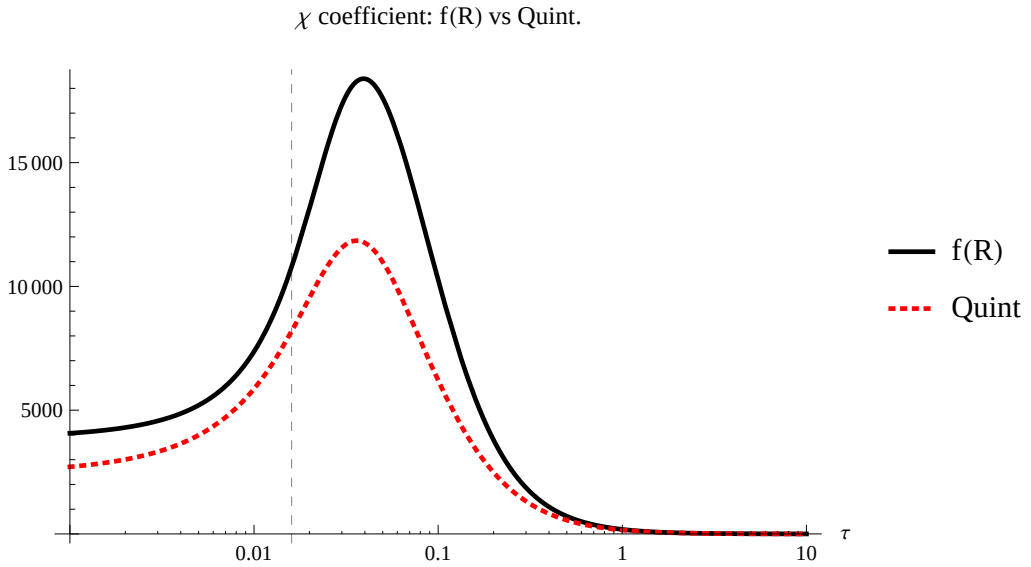

(e) Evolution of coefficients for χ

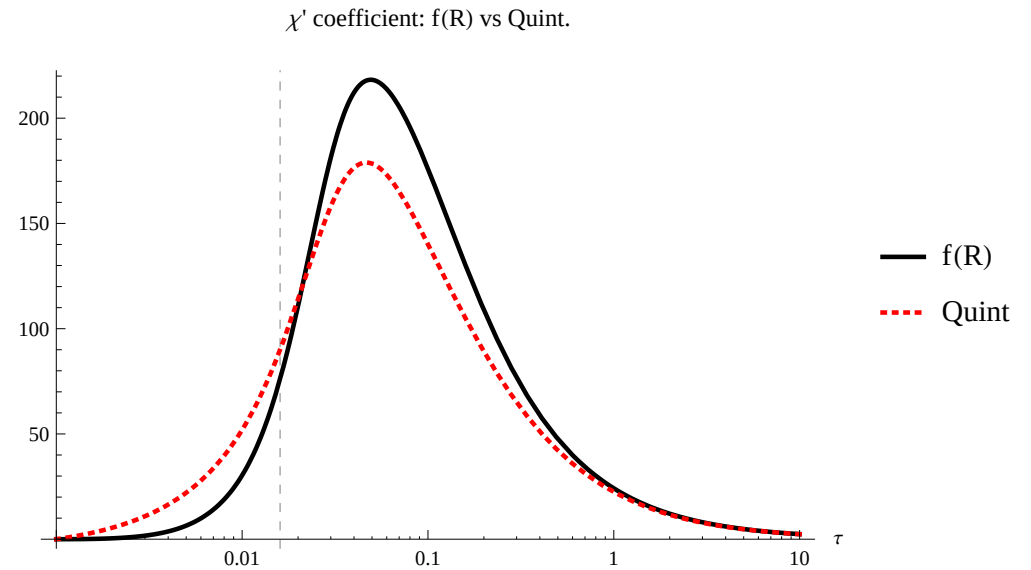

(f) Evolution of coefficients for $\dot{\chi}$

Figure 3.8: The slow-rolling chameleon (case 1): Initial conditions place the field at the minimum in the effective potential V_{eff}, resulting in a slow-rolling field and small QSA errors. The Quintessence-like case also performs well due to the very flat $V(\phi)$. The dashed vertical line denotes the time when $\Omega_\phi = 0.7$ and the relative error is evaluated in our contour plots. The evolution of Ω_ϕ for a chameleon $f(\mathcal{R})$ and Quint. model starting with identical Ω_ϕ is almost identical. We show the evolution of $\delta_{QS}/\delta_{\rm full} - 1$ in units where $k = 100$ and choosing $x_{QS} = 0.1$ and $\Omega_\phi(\tau_{QS}) \sim 0.22$ (*cf.* Fig. 3.6). Horizon-crossing therefore takes place at $\tau = 0.01$. The evolution of δ in the $f(\mathcal{R})$ chameleon case and the Quint. case, with full and quasi-static solutions: both agree very well in the slow-roll case shown here. In the evolution of coefficients for $\dot{\chi}$ (left) and χ (right) in Section 3.4 the chameleon $f(\mathcal{R})$ and Quint solution closely follow each other here in comparison to the analogous plots in Fig. 3.9 (up to $\sim 50\%$ vs. $> 1000\%$ difference).

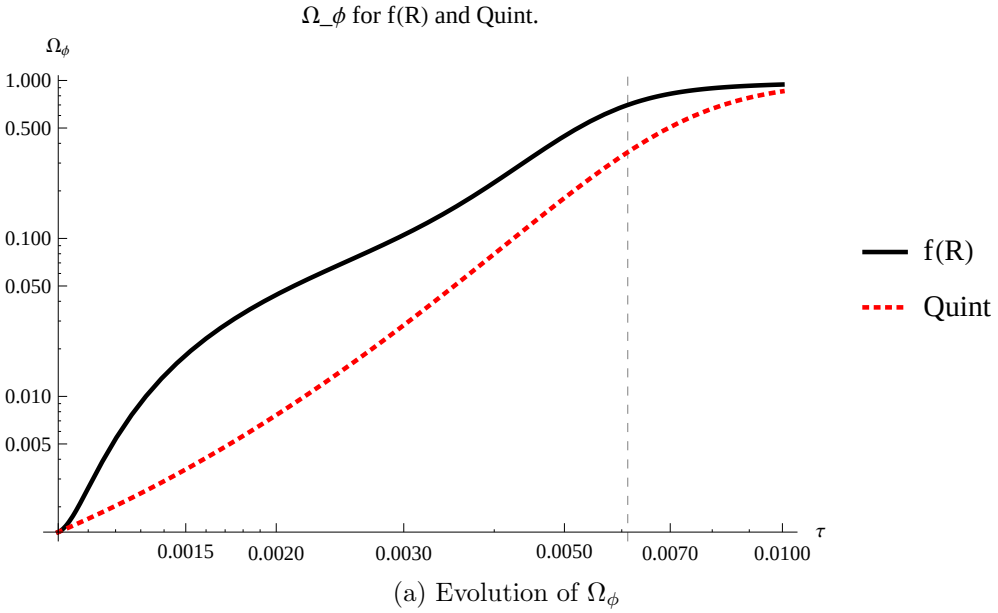

(a) Evolution of Ω_ϕ

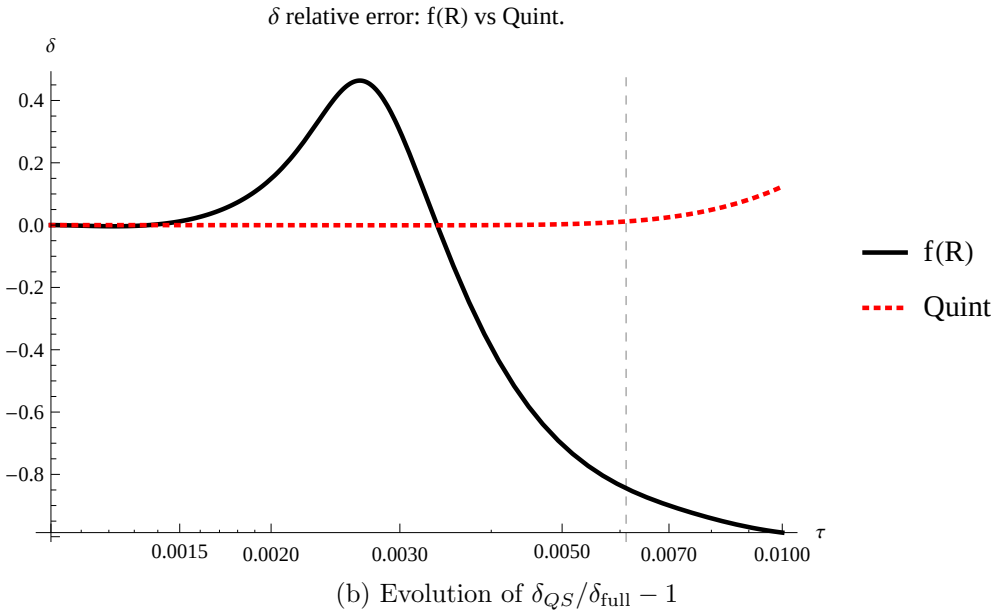

(b) Evolution of $\delta_{QS}/\delta_{\rm full} - 1$

Figure 3.9: The fast-rolling chameleon case (case 2): Initial conditions place the field away from the minimum in the $f(\mathcal{R})$ model, resulting in a fast-rolling field and large QSA errors, markedly different from case 1 shown in Fig. 3.8. The corresponding Quintessence-like performance is hardly changed in comparison with case 1 as expected. The dashed vertical line denotes the time when $\Omega_\phi = 0.7$ and the relative error is evaluated in our contour plots. The evolution of Ω_ϕ for a chameleon $f(\mathcal{R})$ and Quint. model starting with identical Ω_ϕ is visibly different now. We show the evolution of $\delta_{QS}/\delta_{\rm full} - 1$ in units where $k = 100$ and choosing $x_{QS} = 0.1$ and $\Omega_\phi(\tau_{QS}) \sim 0.0014$ (*cf.* Fig. 3.6). Horizon-crossing therefore takes place at $\tau = 0.01$. Evolution of δ also differs in the $f(\mathcal{R})$ chameleon and the Quint. case, showing full and quasi-static solutions . The QSA fails rather catastrophically in the $f(\mathcal{R})$ chameleon here, while the Quint. QSA solution faithfully tracks the full solution. Again this is in stark contrast to the slow-roll case considered before and is a result of fact that in the fast-roll case there is no suppression of the propagation of large quasi-static errors for χ to the evolution of $\widetilde{\delta}$ on super-horizon scales. Evolution of coefficients for $\dot{\chi}$ and χ in Section 3.4 - note that chameleon $f(\mathcal{R})$ and Quint solution are very different now, with the $f(\mathcal{R})$ chameleon displaying much larger coefficients. This explains why the QSA error in evaluating χ is much more strongly propagated into the evolution equation for δ, resulting in the bad QSA fit shown in the middle row. Contrast this with the case shown in Fig. 3.8.

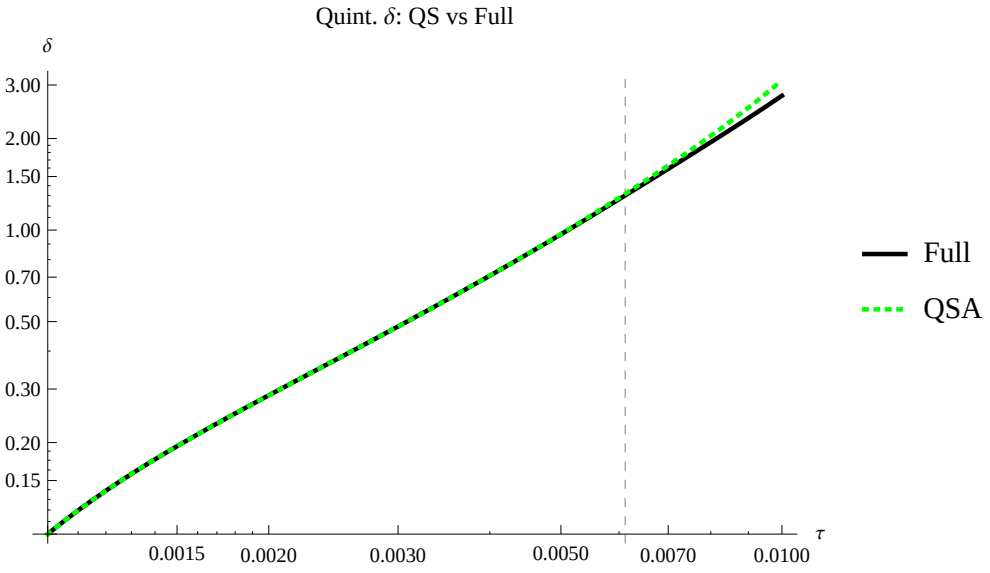

(c) Evolution of δ in Quint.

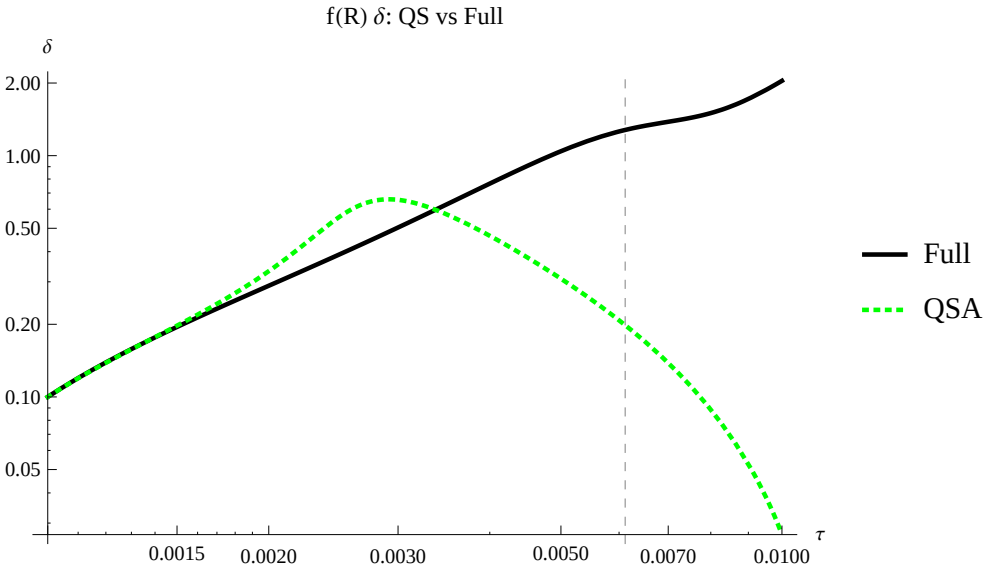

(d) Evolution of δ in $f(\mathcal{R})$

Figure 3.9: The fast-rolling chameleon case (case 2): Initial conditions place the field away from the minimum in the $f(\mathcal{R})$ model, resulting in a fast-rolling field and large QSA errors, markedly different from case 1 shown in Fig. 3.8. The corresponding Quintessence-like performance is hardly changed in comparison with case 1 as expected. The dashed vertical line denotes the time when $\Omega_\phi = 0.7$ and the relative error is evaluated in our contour plots. The evolution of Ω_ϕ for a chameleon $f(\mathcal{R})$ and Quint. model starting with identical Ω_ϕ is visibly different now. We show the evolution of $\delta_{QS}/\delta_{\rm full} - 1$ in units where $k = 100$ and choosing $x_{QS} = 0.1$ and $\Omega_\phi(\tau_{QS}) \sim 0.0014$ (*cf.* Fig. 3.6). Horizon-crossing therefore takes place at $\tau = 0.01$. Evolution of δ also differs in the $f(\mathcal{R})$ chameleon and the Quint. case, showing full and quasi-static solutions . The QSA fails rather catastrophically in the $f(\mathcal{R})$ chameleon here, while the Quint. QSA solution faithfully tracks the full solution. Again this is in stark contrast to the slow-roll case considered before and is a result of fact that in the fast-roll case there is no suppression of the propagation of large quasi-static errors for χ to the evolution of $\widetilde{\delta}$ on super-horizon scales. Evolution of coefficients for $\dot{\chi}$ and χ in Section 3.4 - note that chameleon $f(\mathcal{R})$ and Quint solution are very different now, with the $f(\mathcal{R})$ chameleon displaying much larger coefficients. This explains why the QSA error in evaluating χ is much more strongly propagated into the evolution equation for δ, resulting in the bad QSA fit shown in the middle row. Contrast this with the case shown in Fig. 3.8.

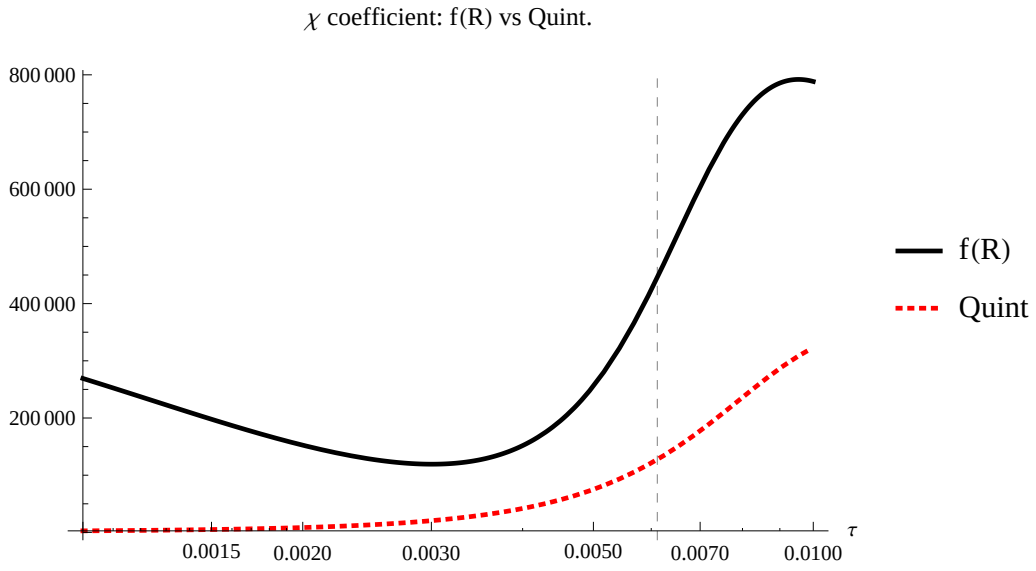

(e) Evolution of coefficients for χ

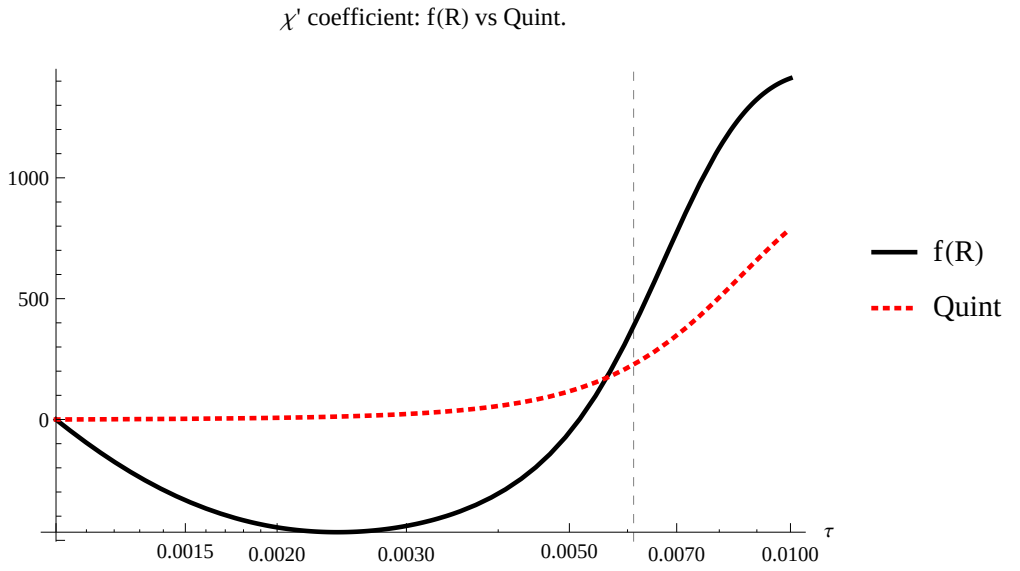

(f) Evolution of coefficients for $\dot{\chi}$

Figure 3.9: The fast-rolling chameleon case (case 2): Initial conditions place the field away from the minimum in the $f(\mathcal{R})$ model, resulting in a fast-rolling field and large QSA errors, markedly different from case 1 shown in Fig. 3.8. The corresponding Quintessence-like performance is hardly changed in comparison with case 1 as expected. The dashed vertical line denotes the time when $\Omega_\phi = 0.7$ and the relative error is evaluated in our contour plots. The evolution of Ω_ϕ for a chameleon $f(\mathcal{R})$ and Quint. model starting with identical Ω_ϕ is visibly different now. We show the evolution of $\delta_{QS}/\delta_{\rm full} - 1$ in units where $k = 100$ and choosing $x_{QS} = 0.1$ and $\Omega_\phi(\tau_{QS}) \sim 0.0014$ (*cf.* Fig. 3.6). Horizon-crossing therefore takes place at $\tau = 0.01$. Evolution of δ also differs in the $f(\mathcal{R})$ chameleon and the Quint. case, showing full and quasi-static solutions . The QSA fails rather catastrophically in the $f(\mathcal{R})$ chameleon here, while the Quint. QSA solution faithfully tracks the full solution. Again this is in stark contrast to the slow-roll case considered before and is a result of fact that in the fast-roll case there is no suppression of the propagation of large quasi-static errors for χ to the evolution of $\widetilde{\delta}$ on super-horizon scales. Evolution of coefficients for $\dot{\chi}$ and χ in Section 3.4 - note that chameleon $f(\mathcal{R})$ and Quint solution are very different now, with the $f(\mathcal{R})$ chameleon displaying much larger coefficients. This explains why the QSA error in evaluating χ is much more strongly propagated into the evolution equation for δ, resulting in the bad QSA fit shown in the middle row. Contrast this with the case shown in Fig. 3.8.

3.7 Discussion

What have we learned from our analysis of the QSA in linearised $f(\mathcal{R})$, chameleon and, *en passant*, in Quintessence models? The key insight of this chapter is that the performance of the perturbative QSA on a given scale in all of these models can be understood in terms of background variables. This allows us to straightforwardly quantify how well a given model does in the QSA and to assess whether this approximation can also be used in super-horizon regimes. In particular the slow- or fast-rolling nature of the background field plays a crucial role in propagating potential quasi-static errors into structure formation, i.e. $\widetilde{\delta}$. Slow-rolling solutions lead to quasi-static solutions which perform well even outside their naïve regimes of validity, i.e. also on super-horizon scales.

Slow-rolling solutions also correspond to ΛCDM-like background evolutions, which [77] found to be linked to good quasi-static evolution on sub-horizon scales. Phrasing this in terms of slow- and fast-rolling solutions and investigating the evolution Eqs. (3.16) and (3.17) and Section 3.4 has allowed us to gain a semi-analytical understanding of why this is the case. We have extended the argument to (super-)horizon scales, where slow-rolling solutions are still accurate within $\sim 5\%$ for the chameleon case considered in Section 3.6. We have also found that on sub-horizon scales the QSA performs well as expected, with $< 1\%$ level errors in $\widetilde{\delta}$. This can even be the case when the field is fast-rolling and the background evolution is consequently distinct from ΛCDM, as the fast-roll examples in Sections 3.4 and 3.6 show[12]. Note that we expect the exact error-levels to be sensitive to the precise nature of the potential, so it will be an interesting task for the future to combine the findings of this chapter with an exhaustive survey of observationally viable chameleon and $f(\mathcal{R})$ models.

Viable $f(\mathcal{R})$ and chameleon models satisfy two conditions. Firstly, they come equipped with a screening mechanism that avoids clashes with tight fifth force constraints. This screening mechanism relies on an effective potential with a minimum. Secondly, BBN and CMB constraints require the field to be very close to this minimum by the time of BBN/recombination and to have the field subsequently slow-rolling together with the evolving minimum (we recall that the minimum evolves due to the redshifting matter density). Here we have shown that the resulting slow-roll condition on the evolution of the background field is precisely what is required for the QSA to perform well even on (super-)horizon scales. It therefore appears that the QSA is well-suited to analyse structure formation in such modified gravity models for a range of scales

[12]Note that we do not expect this to remain true in general, for example in cases where there are still rapid oscillations of scalar field perturbations deep into the sub-horizon regime. An explicit example is provided by the $R^{0.63}$ case discussed in [77], where the QSA fails on sub-horizon scales too. We thank Antonio Maroto for pointing this out to us.

- an encouraging conclusion indeed. This is in agreement with (and an extension of) the conclusions of [77, 121], who discuss sub- and near-horizon scales, and the analysis presented here sheds some light on why the QSA performs so well in these cases.

However, note that a question of precision remains. QSA errors introduced into the evolution of δ can still reach $\sim 5\%$ on super-horizon scales, even in the best cases considered in this chapter, so that the use of the QSA limits the maximal precision that can be reached in any such analysis of structure formation. Such an error is still too large if one targets 1% accuracy for the power spectrum of δ in future experiments.[13] If higher accuracies are desired a more accurate prescription than one employing the QSA will likely be necessary. Also adding a short fast-rolling phase before BBN or maximising the distance the field could have travelled in accordance with constraints would probably worsen the obtained accuracy. This is of crucial importance in the context of N-body simulations, in particular when the QSA is used to set up initial conditions in the linear regime on (super) horizon scales, which is precisely the regime we have probed here.

Much remains to be done. Probing Vainshtein screening in the same quantitative fashion and exploring whether there are viable dark energy models that are not well described by the QSA (along the lines of [166, 226]) are tasks left for future work. For Vainshtein-screened models it could be very interesting to extend the work of [23, 24, 25, 160], exploring the accuracy of the QSA for such models. The fact that the background evolution can be very distinct from ΛCDM in such models might suggest that the QSA will generically perform rather poorly on super-horizon scales there. However, a detailed analysis may uncover interesting exceptions. Finally the analysis in this chapter has focussed on the linear regime relevant to the way initial conditions are set up in N-body simulations and to (super-)horizon scales. An explicit and detailed fully non-linear analysis of the QSA on sub-horizon scales should also result in a better understanding of the applicability of the approximation.

[13] Also note that intrinsic N-body simulation systematics, e.g. due to the discretisation of evolution equations, will introduce further errors. It will be an interesting task for the future to establish precisely at what level these errors contribute. We thank Baojiu Li for raising this point.

Chapter 4

Generalising the halo mass function from GR to MG

The halo mass function $n(M)$ is defined to be the number density of dark matter haloes in a given mass interval at a certain redshift. Using excursion set theory, this can be related to the probability $f(S)$ for a given trajectory in the phase space (δ, S) to be absorbed at resolution S when the overdensity δ reaches the collapse density δ_c. This behaviour amounts to a diffusion equation, where δ and S act as spatial and temporal variables respectively. In turn, $f(S)$ can be expressed in terms of a "universal" fitting function $F(\nu)$, which is invariant under changes in redshift and cosmological parameters.

This chapter explains how the existing frameworks to calculate the halo mass function in GR can be generalised to (screened) MG. In Section 4.1 we show how the barrier density forms the solution to an ODE which can be tailored to each theory of gravity using an effective Newton's constant: the solution to this equation encapsulates the modifications to non-linear collapse from MG. This is utilised when explaining the theoretical approach provided by excursion set theory in Section 4.2.1 (general relativity) and Section 4.2.2 (modified gravity). Then we extend this to dependence on the cosmic web in Section 4.3. The same method can be used for empirical fitting functions (Section 4.4), which are derived from and calibrated using N-body simulations. In particular we focus on the various ways to account for environment dependence—a problem peculiar to chameleon MG theories—and in Section 4.5 we analyse the accuracy of both existing methods and the novel methods which we propose in this chapter.

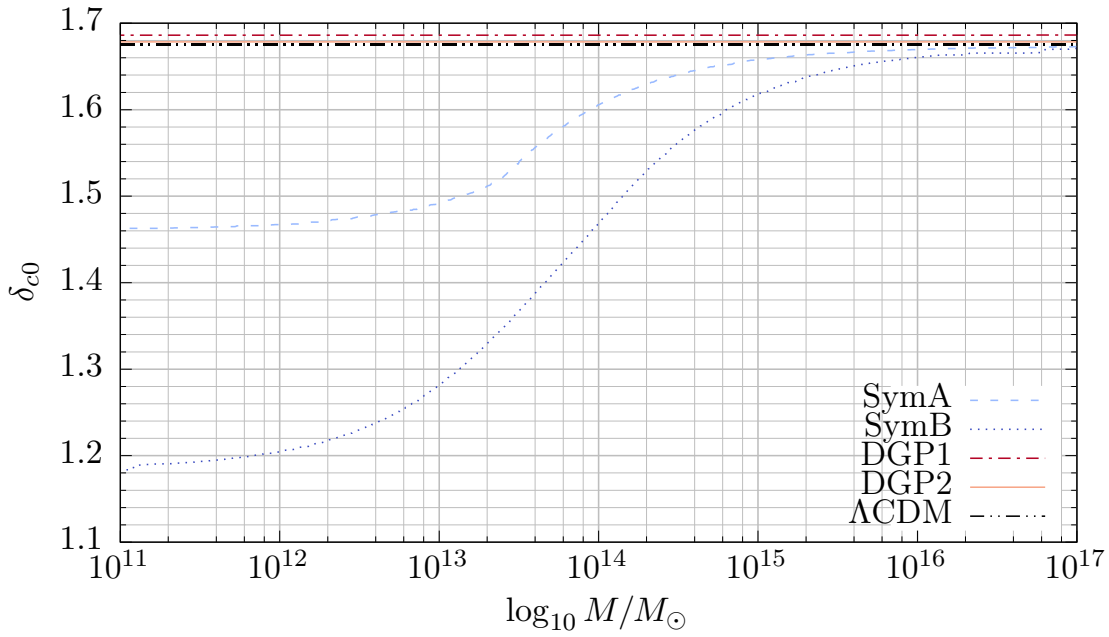

(a) DGP $r_c = 1.2c/H_0$, DGP $r_c = 5.6c/H_0$, Symmetron $a_{\rm SSB} = 0.5$, Symmetron $a_{\rm SSB} = 0.33$

Figure 4.1: The barrier density $\delta_c(M, \delta_{\rm env})$ for each of the MG models in this thesis.

4.1 Spherical collapse in MG

In this section we quantify how screening affects the critical density required for halo collapse in the excursion set formalism. We present a formula for the overdensity required for collapse $\delta_c(M, z, \delta_{\rm env})$ which is sufficiently general for all of our screened MG theories. The main difference in modified gravity is that δ_c depends both on mass and environment density as well as depending on redshift as in ΛCDM.

The density field δ is the linearly-extrapolated over-density at the present epoch.[1] Initially the density field exhibits Gaussian fluctuations on all scales, which we measure according to the fractional overdensity $\rho/\bar{\rho}$ convolved (hence we work in Fourier space) with a window function to obtain the fluctuations over a given scale R, which we expect to have some variance σ, such that $\delta = \nu\sigma(R)$ for any positive constant ν and $\sigma = \sqrt{S}$ defines the resolution S:

$$S \equiv \sigma^2 = \frac{1}{(2\pi)^3}\int \mathrm{d}^3k \left\langle \left|\delta\left(\vec{k}; R\right)\right|\right\rangle = \frac{1}{2\pi}\int_0^\infty \mathrm{d}\ln k\ P(k,z)W(k;R)^2k^3 \tag{4.1}$$

where $P(k, z)$ is the power spectrum which completely describes the original Gaussian density field δ at redshift z.

Now we require a condition for the redshift evolution of the density field: we choose a

[1] Originally [42] denoted this by F to avoid confusion with δ_c and to emphasise that it is not purely $\rho/\bar{\rho}$, the usual cosmological definition of overdensity compared to the background density. However, present convention dictates that δ be used instead.

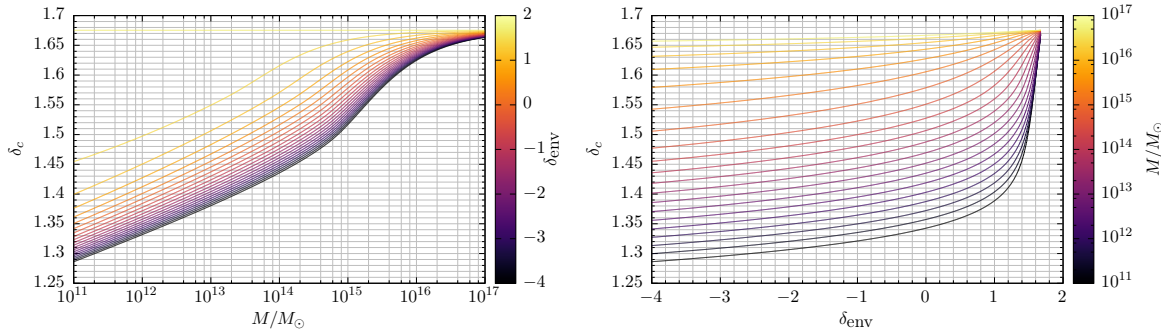

(b) $|f_{\mathcal{R}0}| = 10^{-5}$ (c) $|f_{\mathcal{R}0}| = 10^{-5}$

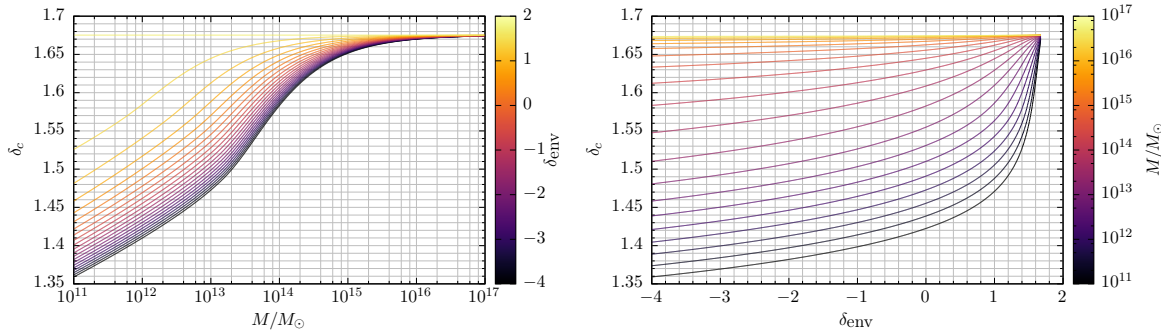

(d) $|f_{\mathcal{R}0}| = 10^{-6}$ (e) $|f_{\mathcal{R}0}| = 10^{-6}$

Figure 4.1: The barrier density $\delta_c(M, \delta_{\rm env})$ for each of the MG models in this thesis.

linear evolution $\delta(k, z; R) = D(z)\delta(k; R)$ where $D(z)$ is the growing mode normalised to unity at the present epoch. Accordingly, we require the linear growing mode $D(z)$ for ΛCDM, which is the solution of the second-order ODE:

$$0 = \frac{\mathrm{d}^2 D}{\mathrm{d}\,\ln a^2} + \left(2 - \frac{3}{2}\Omega_m(\ln a)\right)\frac{\mathrm{d}\,D}{\mathrm{d}\,\ln a} - \left(\frac{3}{2}\Omega_m(\ln a)\right) D(\ln a) \tag{4.2a}$$

$$\Omega_m(\ln a) = \frac{\Omega_{m0}\exp\left(-3\ln a\right)}{\Omega_{m0}\exp\left(-3\ln a\right) + \Omega_{\Lambda 0}} \tag{4.2b}$$

$$\Omega_\Lambda(\ln a) = \frac{\Omega_{\Lambda 0}}{\Omega_{m0}\exp\left(-3\ln a\right) + \Omega_{\Lambda 0}} \tag{4.2c}$$

Let us view the present-day δ as a fixed density field, with a critical overdensity for collapse δ_{c0}: where $\delta > \delta_{c0}/D(z)$, we expect these overdensities to have already collapsed at redshift z; conversely where $\delta < \delta_{c0}$, these parts of the density field have yet to collapse. Our aim is to calculate δ_{c0} for both GR and our screened MG theories.

The collapse of the environment surrounding the halo is equivalent to collapse in general relativity. Let us assume that the initial overdensity is a spherical top-hat in Eulerian space. We can utilise the resulting axisymmetry to simplify the gravitational collapse equation to:

$$0 = \frac{d^2 y}{d\ln a^2} + \left(2 - \frac{3}{2}\Omega_m(a)\right)\frac{dy}{d\ln a} + \frac{1}{2}\Omega_m(a)\left(\frac{1}{y^3} - 1\right) y \tag{4.3}$$

where $y(a)$ is the ratio of the physical radius of the halo $R_{\rm TH}(a)$ to the physical radius of the filter $a(t)R$ [155]. Now we have an expression for the halo density in general relativity and the environment density in modified gravity.

Since all of our MG theories obey a modified Poisson equation in the weak-field limit, we can use the standard equations for collapse of a spherical top-hat overdensity. We need only replace G_N by $G_N(1+F_{\rm eff})$ in the Poisson equation. Following the same steps as for the environment collapse, we obtain:

$$0 = \frac{\mathrm{d}^2 y}{\mathrm{d}\,\ln a^2} + \left(2 - \frac{3}{2}\Omega_m(a)\right)\frac{\mathrm{d}\,y}{\mathrm{d}\,\ln a} + \frac{1}{2}\left(1+F_{\rm eff}\right)\Omega_m(a)\left(\frac{1}{y^3}-1\right)y \tag{4.4}$$

and $F_{\rm eff}$ is the appropriate modification in G_N as tabulated in Table 2.2. Since $F_{\rm eff} \ll 1$ at early times, we can use the same initial conditions as we used for ΛCDM. For Symmetron gravity $F_{\rm eff}$ depends upon the halo overdensity in Eq. (2.18); while in Dvali-Gabadadze-Porrati models $F_{\rm eff}$ depends upon the halo mass and radius in Eq. (2.26). Therefore for Symmetron and Vainshtein screening we need only solve Eq. (4.4). In contrast, the chameleon-screened $f(\mathcal{R})$ theory with $F_{\rm eff}$ in Eq. (2.14) depends both upon the halo density and the environment density: in this case Eq. (4.4) (for the halo collapse) must be coupled to Eq. (4.3) (for the collapse of the surrounding environment). This is the general form for modified gravity collapse of a spherical top-hat.

Finally we set the initial conditions. Mass conservation determines y_i via equating the physical radii of the physical halo and the top-hat window function at the initial time a_i:

$$M = \frac{4}{3}\pi\rho_{m0}a_i^3 R_{\rm TH}^3 = \frac{4}{3}\pi\rho_{m0}\left(1+\delta_i\right)r_i^3 \implies y(a_i) = 1 - \frac{\delta(a_i)}{3} \tag{4.5}$$

At early times we expect the ODE Eqs. (4.3) and (4.4) to be well-approximated by its linearised equivalent. Without loss of generality, we can set the initial redshift of the ODE (we used $z = 500$) to before the modification to GR, hence $F_{\rm eff} = 0$. Substituting the result for y_i gives the corresponding first derivative:

$$\frac{\mathrm{d}\,y(a_i)}{\mathrm{d}\,\ln a} = -\frac{\delta(a_i)}{3} \tag{4.6}$$

An important corollary of Eq. (4.5) is that $\delta = y^{-3} - 1$, which contributes the nonlinearity in the final term of Eqs. (4.3) and (4.4).

Despite the fact that our (coupled) ODEs are in terms of $y(a)$, our aim is to calculate $\delta_c(z_c)$. We define this via the boundary-value problem [143]:

$$\delta_c\left(z_c\right) = \delta_i\left(z_i\right)\frac{D\left(z_c\right)}{D\left(z_i\right)}\,\Big|\; y\left(z_c\right) = 0 \tag{4.7}$$

This condition specifies that y vanish at the boundary z_c. We have one unknown, which

is the value of δ_i controlling both y_i and y_i' at the boundary z_i via Eq. (4.5). We are left with $y'(z_c)$ which is totally unknown. There is no guarantee that this non-linear system of ODEs constrained by boundary values has a solution. We employ a "shooting method" to iteratively find the collapse density which causes the halo to collapse at $z = 0$. An initial estimate for δ_c is scaled to its initial value at z_i and the system of equations is evolved. If the density is too low, the halo will not have collapsed, resulting in $y(z = 0) > 0$, whereas if the density is too high, $y = 0$ will be reached before $z = 0$. These conditions are used to select which branch of the bijection to use for further estimation. The lower limit is $\delta_c > 0$. The upper bound is given by the Einstein-de Sitter result $\delta_{c0} = \frac{3}{20}(12\pi)^{\frac{2}{3}}$ (not the ΛCDM result, because the DGP values exceed this). We now have all the requirements to compute both the present-day collapse density (in fact, the barrier density required for collapse at any redshift).

We checked our results for the collapse density by reproducing the values in [170] for $f(\mathcal{R})$ and [215] for DGP. For the symmetron model only [234] has values for δ_c but their symmetron potential is substantially (algebraically) different from ours, so we verified our results by ensuring that they converged smoothly to ΛCDM as we reduced the modification to gravity.

The collapse densities using our screening parameters are shown in Fig. 4.1. The DGP models produce a flat result with similar values to ΛCDM. This suggests that these results may be indistinguishable from a ΛCDM model with non-standard cosmological parameters. In contrast, the two Symmetron models produce a collapse density which is a function of mass. While it asymptotes to ΛCDM density at high masses, it is substantially lower for small masses and appears to tend to a constant value on sub-cluster scales. As expected, the MG model parameters are correlated with the collapse density divergence from ΛCDM: DGP models recover the ΛCDM collapse density as the cross-over radius tends to infinity, whereas symmetron models do so as the symmetry-breaking scale factor tends to unity.

The $f(\mathcal{R})$ collapse density exhibits a more complex behaviour. We shows its dependence on mass in Figs. 4.1b and 4.1d and environment in Figs. 4.1c and 4.1e. The collapse density is no longer flat: $\delta_c(M, \delta_{\rm env})$ is a monotonically-increasing function of M, and the peak-background split $\delta_c - \delta_{\rm env}$ is a monotonically-decreasing function of $\delta_{\rm env}$. Compared to ΛCDM, we expect haloes to form at higher masses and to have more in low-density regions. Figs. 4.1c and 4.1e demonstrate that the collapse density is always bounded from below by the environment density and from above by the ΛCDM result. We have also marginalised over the environment distribution according to Eqs. (4.14) and (4.15b) as suggested in Section 4.4. The resulting environment-averaged collapse density is shown in Fig. 4.2. This completes our analysis of spherical collapse in MG.

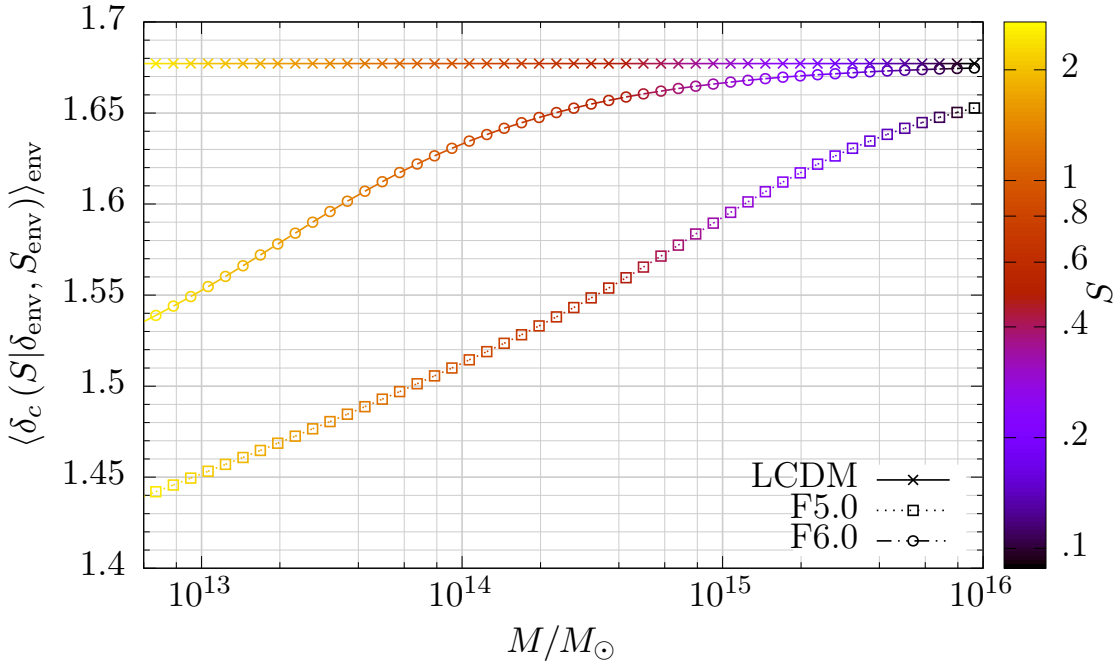

Figure 4.2: The collapse density for ΛCDM, $|f_{\mathcal{R}0}| = 10^{-5}$ and $|f_{\mathcal{R}0}| = 10^{-6}$ averaged over the Eulerian environment distribution Eq. (4.15b) converts the drifting-and-diffusing barrier density to a drifting $\delta_c(S)$.

4.2 Excursion set theory

In this section we derive this relationship between the halo mass function $n(M)$ and the universal fit $F(\nu)$ derived via excursion-set theory, including the scenario in which ν depends upon "nuisance parameters" other than M. We outline the excursion set formalism in general relativity (Section 4.2.1) and then discuss the modifications induced by modified gravity (Section 4.2.2).

4.2.1 The excursion set theory in ΛCDM

The *Ansatz* of the excursion set formalism is the relation of the linear overdensity field in real space collapsing to a halo of mass M to trajectories in the density field being absorbed by a critical density at resolution S. As shown in [42, 148], where they assume top-hat window functions in k-space, this problem reduces to finding the fraction of random walks in the plane (δ, S) that are absorbed by the collapse overdensity δ_c at resolutions earlier than S. These correspond to the cumulative fraction $F(> M)$ of mass contained in haloes above mass M.

We have already seen, albeit *en passant*, the ingredients of the excursion set formalism:

1. The window function $W(kR)$ used to smooth the density field. We utilise a Gaussian filter and a top-hat filter in both real and Fourier space.

2. The overdensity field δ corresponding to the fractional, linearly-evolved overdensity smoothed over a scale R defined by a given Fourier-space window function $W(kR)$.

3. The resolution S, which is related to the linear matter power spectrum $P(k)$ and the halo mass M.

4. The collapse density δ_c which acts as a drifting-and-diffusing barrier in the diffusion equation below.

Following [42], we obtain a diffusion equation for the probability density function $\Pi(S, \delta)$ that a Markovian trajectory which moves randomly in the linearly-extrapolated density field δ and moving linearly forwards in S from the origin will first exceed the barrier density $\delta_c(S)$ at resolution S:

$$\frac{\partial \Pi}{\partial S} = \frac{1}{2}\frac{\partial^2 \Pi}{\partial \delta^2} \quad \text{with boundary conditions} \quad \begin{cases} \Pi(\delta, S) = 0 & \text{at } \delta = \delta_c(S) \\ \Pi(\delta, S) = 0 & \text{at } \delta = 0 \end{cases} \tag{4.8}$$

However, our aim is to express this solely in terms of S—the resulting function $f(S)$ is known as the **first-crossing distribution**—and as the name suggests is the probability of first up-crossing the barrier density at S. In GR the barrier is flat, so we obtain an analytical solution for Π provided that we use a top-hat filter in Fourier space for S. This is given by the Press-Schechter mass function [202]:

$$F(> M) = 2\int_{\delta_c}^{\infty} \mathrm{d}\,\delta\; \Pi(\delta(S)) = \int_0^S \mathrm{d}\,S' f(S') = \mathrm{erfc}\left(\frac{\nu_h}{\sqrt{2}}\right) \tag{4.9}$$

where $\nu_h \equiv \delta_c/\sqrt{S}$. (A more detailed derivation of this result is in [42].)

Excursion set theory can be extended to theories with a non-flat barrier $\delta_c(S, S_{\mathrm{env}}, \delta_{\mathrm{env}})$ which depends upon the starting point of the random walk $(S_{\mathrm{env}}, \delta_{\mathrm{env}})$ and the variance S at which the random walk crosses the barrier. By assuming that trajectories in (δ, S)

are uncorrelated, the diffusion equation admits the solution [192]:

$$f(S|S_{\rm env},\delta_{\rm env}) = g(S) + \int_{S_{\rm env}}^{S} \mathrm{d}\,x\; k(S,x)\, f\left(x \,|\, S_{\rm env},\delta_{\rm env}\right) \tag{4.10a}$$

$$k(S,x) = \left[\frac{\delta_c(S)-\delta_c(x)}{S-x} - 2\frac{\mathrm{d}\,\delta_c(S)}{\mathrm{d}\,S}\right] \frac{1}{\sqrt{2\pi(S-x)}} \exp\left\{-\frac{(\delta_c(S)-\delta_c(x))^2}{2(S-x)}\right\} \tag{4.10b}$$

$$g(S) = \left[\frac{\delta_c(S)-\delta_{\rm env}}{S-S_{\rm env}} - 2\frac{\mathrm{d}\,\delta_c(S)}{\mathrm{d}\,S}\right] \frac{1}{\sqrt{2\pi(S-S_{\rm env})}} \exp\left\{-\frac{(\delta_c(S)-\delta_{\rm env})^2}{2(S-S_{\rm env})}\right\} \tag{4.10c}$$

It is straightforward to show that this has an analytical solution for a linear barrier density [192, 262], including the constant case $\delta_{c0}^{\Lambda} \approx 1.676$ which is the ΛCDM solution:

$$f(S|S_{\rm env},\delta_{\rm env}) = \frac{\delta_c^{\Lambda}-\delta_{\rm env}}{\sqrt{2\pi(S-S_{\rm env})^3}} \exp\left[-\frac{1}{2}\frac{\left(\delta_c^{\Lambda}-\delta_{\rm env}\right)^2}{S-S_{\rm env}}\right] \tag{4.11}$$

We shall refer to this as the (environment-)conditional HMF from now on. We shall require this result in the MG case, having seen in Fig. 4.1 that some of our gravity theories produce flat barriers, others "drifting" barriers $\delta_c(S)$ and other the full "drifting-and-diffusing" barrier $\delta_c(S, S_{\rm env}, \delta_{\rm env})$.

Finally we must marginalise over the environment. We require a probability distribution for $\delta_{\rm env}$, upon which we will expand in Section 4.2.2. Then the unconditional mass functions is simply the conditional one marginalised over the nuisance parameter [155, 156]:

$$f\left(S\right) = \left\langle f\left(S \,|\, S_{\rm env},\delta_{\rm env}\right)\right\rangle_{\rm env} = \int_{-\infty}^{\delta_\Lambda} \mathrm{d}\,\delta_{\rm env}\; p\left(\delta_{\rm env} \,|\, S_{\rm env}\right)\; f\left(S \,|\, S_{\rm env},\delta_{\rm env}\right) \tag{4.12}$$

In ΛCDM we obtain an analytic solution which is precisely the Press-Schechter function:

$$f\left(S\right) = \frac{\delta_c^{\Lambda}}{\sqrt{2\pi S^3}} \exp\left[-\frac{1}{2}\frac{\left(\delta_c^{\Lambda}\right)^2}{S}\right] \tag{4.13}$$

The unconditional HMF Eq. (4.13) has the same functional form as the conditional one Eq. (4.11), albeit with the substitutions $\delta_c \to (\delta_c - \delta_{\rm env})$ and $S \to S - S_{\rm env}$. In Section 4.4 we shall assume that this applies to other fitting functions beyond Press-Schechter.

4.2.2 Excursion set theory in MG

How does screened gravity alter this result? After solving Eqs. (4.3) and (4.4) we can derive values for δ_c in general relativity and modified gravity, and for the starting point of the random walk $\delta_{\rm env}$. We have already seen the integral required to obtain the conditional first-crossing distribution in Eq. (4.10). Now we must account for the environment dependence, which forms nuisance parameters in the unconditional (i.e. environment-averaged) HMF $n(M)$.

Three options are frequently used for the environment density in the literature:

1. Lagrangian distribution from excursion set theory
2. Eulerian equivalent to Item 1
3. Numerical distribution from N-body simulations

Recall that we assume that the environment behaviour is on sufficiently large scales that it is well-approximated by ΛCDM. Then [42] have shown that the environment distribution can be obtained using the same excursion set method by which we have derived the PS mass function. The probability that the trajectory starting from $(0, 0)$ survives to up-cross the environment density $\delta_{\rm env}$ at resolution $S_{\rm env}$ is [42]:

$$p\left(\delta_{\rm env}\right) = \frac{\mathcal{H}\left(\delta_c^\Lambda - \delta_{\rm env}\right)}{\sqrt{2\pi S_{\rm env}}}\left[\exp\left(-\frac{\delta_{\rm env}^2}{2S_{\rm env}}\right) - \exp\left(-\frac{\left(\delta_c^\Lambda - \delta_{\rm env}\right)^2}{2S_{\rm env}}\right)\right] \tag{4.14}$$

where $\delta_c^\Lambda \approx 1.676$ is the barrier density for ΛCDM and $\mathcal{H}$ is the Heaviside step function.

Item 2 can be obtained from Eq. (4.14) by treating the non-linear Eulerian overdensity Δ as the barrier function in the excursion set method:

$$\Delta(S) = \delta_c\left[1 - \left(\frac{R_{\rm env}}{8\ {\rm Mpc}/h}\right)^{3/\delta_c}\left(\frac{S}{\sigma_8^2}\right)^{1/\omega}\right] \tag{4.15a}$$

which produces the distribution[2] for the Eulerian linear density contrast

$$q\left(\delta_{\rm env}\right) = \frac{\beta^{\omega/2}}{\sqrt{2\pi}}\left[1 + (\omega - 1)\,\frac{\delta_{\rm env}}{\delta_c^\Lambda}\right]\left[1 - \frac{\delta_{\rm env}}{\delta_c^\Lambda}\right]^{-(\omega/2+1)}\exp\left[-\frac{\delta_{\rm env}^2}{2}\left(\frac{\beta}{1 - \frac{\delta_{\rm env}}{\delta_c^\Lambda}}\right)^\omega\right] \tag{4.15b}$$

where

$$\omega = -\delta_c \left.\frac{\mathrm{d}\,\ln S}{\mathrm{d}\,\ln M}\right|_{\mathrm{env}} \qquad \text{and} \qquad \beta = \left(\frac{R_{\mathrm{env}}}{8\ \mathrm{Mpc}/h}\right)^{3/\delta_c} \left(\frac{1}{\sigma_8}\right)^{2/\omega}$$

The corresponding Lagrangian and Eulerian probability density functions for $R_{\mathrm{env}} = 10\ \mathrm{Mpc}/h$ are shown in Fig. 4.3. The Lagrangian PDF is quasi-symmetric: whereas the PDF asymptotes smoothly to zero for $\delta_{\mathrm{env}} \leq -\delta_c^\Lambda$, it is artificially set to zero for values $\delta_{\mathrm{env}} \geq \delta_c^\Lambda$ because these environments would already have formed a halo. The Eulerian PDF is asymmetric, with a greater proportion of overdensities (i.e. where $\delta_{\mathrm{env}} \geq 0$) than voids. However, it does not asymptote to zero for negative densities as rapidly as the Lagrangian PDF. We analyse the effect of the choice of PDF on the HMF in Section 4.5.

Whereas both of these are analytic methods, perhaps the most accurate solution is simply to extract the distribution from the N-body simulations. This would isolate the effects of the MG excursion set prediction from those of assuming a theoretical approximation to the δ_{env} distribution. (Implicit in the use of this distribution is the assumption that the environment in the box is an unbiased sub-sampling of the cosmological environment density.) However, each environment probability density function would differ in each simulation, so it would be difficult to disentangle the effects of averaging over a different $p(\delta_{\mathrm{env}})$ from the effects of the gravity model on the conditional HMF. Thus we discard this option.

Throughout this thesis we set $S_{\mathrm{env}} = S(10\ \mathrm{Mpc}/h) \approx 0.1$, i.e. an environment radius of $\approx 14\,\mathrm{Mpc}$. Using a Gaussian window function limits the maximum halo mass to $\lesssim 10^{16} M_\odot$. We confirmed that this is above the maximum halo mass found in our N-body simulations, so that we do not exclude any data by imposing the excursion-set condition $S < S_{\mathrm{env}}$. The values of $\sigma_8 = 0.8$ and $n_s = 0.966,\ 1.0$ for the Eulerian probability density function are set by the simulations (Sections 1.4.4 and 5.2.1).

So far we have neglected the additional complications that the resolution S is sensitive to the MG parameters (e.g. $f(\mathcal{R})$) via the power spectrum and that the collapse density is now a function of S. We address these now.

We have chosen to use the linear $P(k)$ computed in the ΛCDM model in Eq. (4.1) when computing the $f(\mathcal{R})$ gravity predictions. The same approach was taken in [59]. The reason for this choice is that linear theory massively overestimates the clustering in modified gravity theories such as $f(\mathcal{R})$: Fig. 4.4 shows that the ratio of the linear

[2]We correct an error in [170] Equation (49) and [156] Equation (15) by restoring the δ_{env}^2 term in the exponent. Without it, the distribution does not normalise to unity. Furthermore [170] Equation (49) has an error in the definition of β, which is correct in [156] Equation (15).

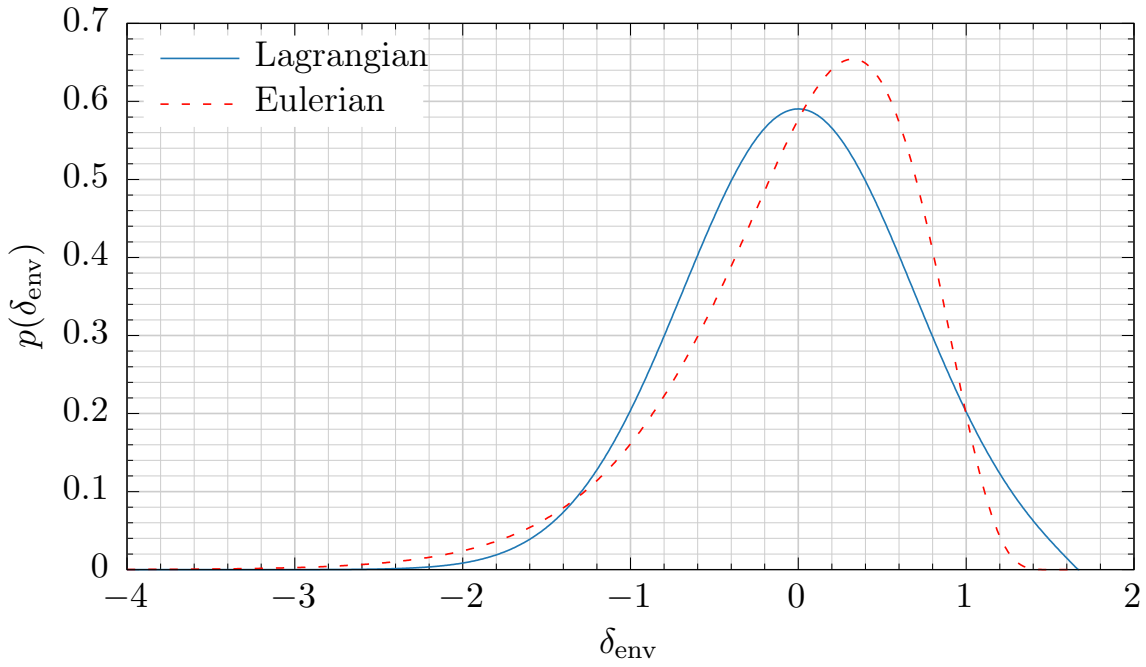

Figure 4.3: The probability density functions for Lagrangian and Eulerian environment density according to Eqs. (4.14) and (4.15b) respectively. This assumes a smoothing scale of 10 Mpc/h for both environments.

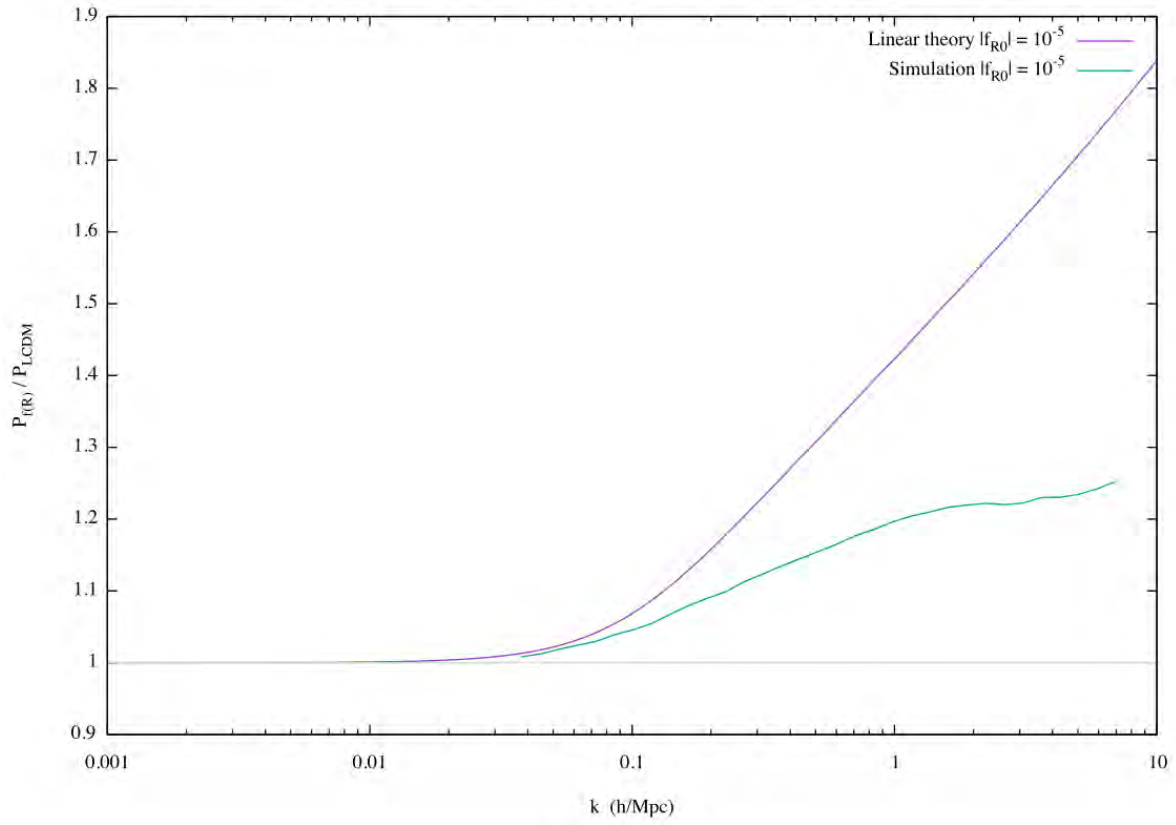

Figure 4.4: The ratio of the $f(R)$ power spectrum to that of ΛCDM for the linear (purple) and non-linear (green) case. The effect of screening is clearly visible at increasingly large k: the non-linear result is suppressed, while the linear result increases rapidly.

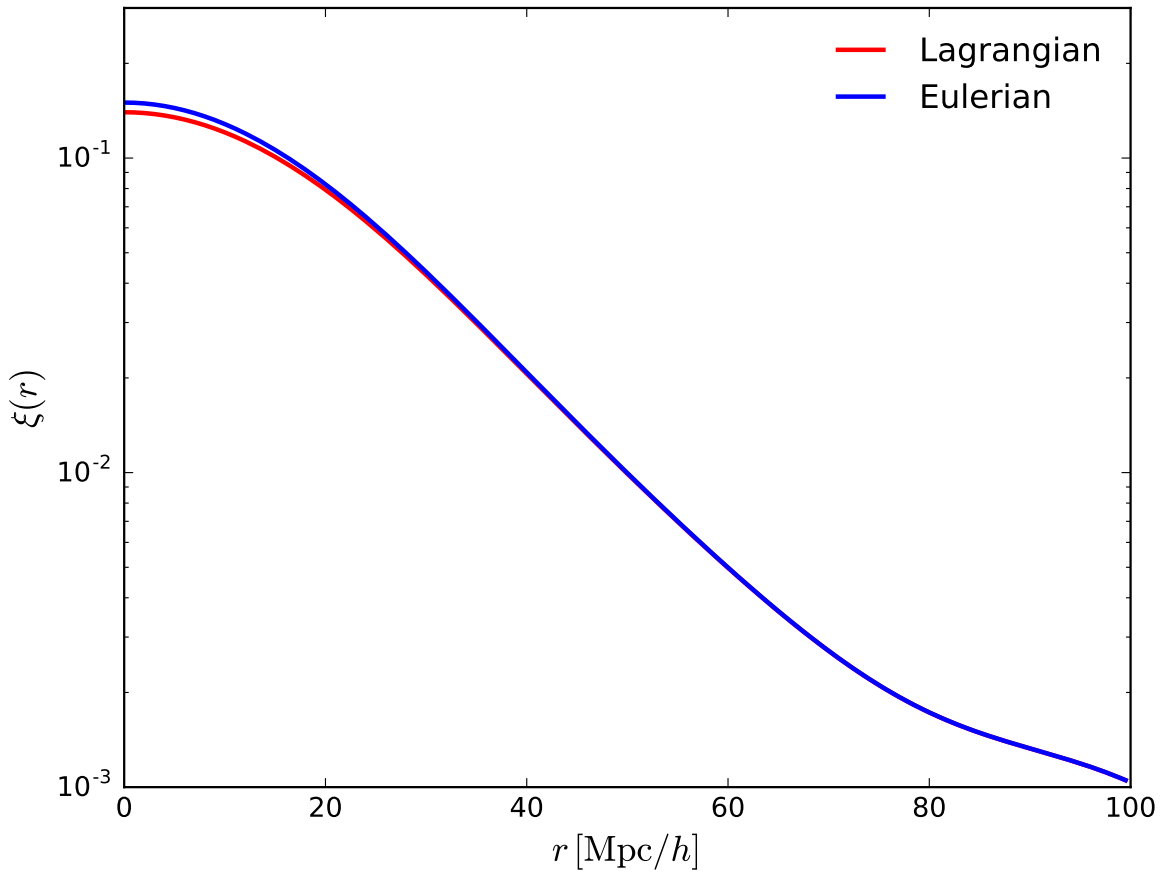

Figure 4.5: Two-point correlation function of the Lagrangian (red) and Eulerian (blue) matter density fields, the latter approximated by a lognormal transformation of the former. The results are shown for a Gaussian smoothing scale $R_{\rm env} = 10\,\mathrm{Mpc}/h$. The relative difference between both curves is smaller than 7% on all scales.

power-spectrum in $|f_{\mathcal{R}0}| = 10^{-5}$ to the linear power-spectrum in ΛCDM shows a much larger deviation than the ratio of the corresponding non-linear power spectra obtained from simulations. The reason is that screening is not present in linear theory. One can easily construct modified gravity models of this type where non-linear results for the power spectrum and the mass function can be arbitrarily close to ΛCDM while at the same time having a linear power-spectrum that deviates significantly from ΛCDM. In such scenarios excursion set theory is not able to give results that agree with simulations if the modified gravity linear power spectrum is used in the calculations. We have checked that this gives results which are in better agreement with simulations by comparing the results using the full linear power-spectrum. An alternative would be to consider a compromise approach where we use the linear ΛCDM power-spectrum corrected with a boost-factor $P_{f(\mathcal{R})}(k)/P_{\Lambda\mathrm{CDM}}(k)$ computed from simulations, however this would require explicit simulations which goes against the appeal of using the excursion set approach—which is to extract observables without having to perform expensive numerical calculations.

We finish this section by noting that, in a strict sense, when relating the excursion-

set predictions to simulated or real data, the scale of the environment $S_{\rm env}$ should correspond to its Lagrangian scale (i.e. in the initial conditions) instead of its Eulerian size, and as pointed out by [149, 156] these effects could be relevant for modified-gravity theories. However, for the environment scales studied in this work ($R_{\rm env} \geq 10\,{\rm Mpc}/h$), we expect these two quantities to be very similar, the evolution of the density field since on such large scales is close to self-similar. We can verify this with a quick test: the effect of the Eulerian evolution can be roughly captured by making a log-normal transformation on the linear (Lagrangian) density field [72]. Then, since the shape of density profile around any point in either the Lagrangian or Eulerian fields is, on average, determined by the correlation function of the field, we can explore the effects of this distinction by studying the correlation function in either case. Under a lognormal transformation, the correlation function of the log-normalized (i.e. Eulerian) field would be given by $\xi_{\rm Eu}(r) = \exp[\xi_{\rm Lag}(r)] - 1$, where $\xi_{\rm Lag}$ is the correlation function of the linearized (i.e. Lagrangian) field. Fig. 4.5 shows both correlation functions for the smallest smoothing scale explored in this work ($R = 10\,{\rm Mpc}/h$), and shows the negligible effect of ignoring the true Eulerian scale of the environment.

4.3 Tidal classification of the cosmic web

So far the halo collapse has only depended upon the variance and overdensity of the local environment. Now we propose a method to include not only these two properties, but also the prolateness and ellipticity of the environment surrounding the halo. This was the main result of [6] in ΛCDM, upon which we built in [248] to find the equivalent in $f(\mathcal{R})$. As done in e.g. [6, 104], we characterise the environment in terms of the properties of the local tidal tensor T_{ij}, defined as the the Hessian of the normalised, Newtonian potential ϕ smoothed with a given kernel of size $R_{\rm env}$

$$\mathsf{T}_{ij} = \frac{\partial_i \partial_j \phi}{4\pi G \bar{\rho}}. \tag{4.16}$$

The environment is then classified into one of four different classes, depending on the values of the three eigenvalues of T, $\lambda_1 \geq \lambda_2 \geq \lambda_3$, in relation to a given eigenvalue threshold. We thus define voids, sheets, filaments and knots as regions in which $\alpha \in \{0, 1, 2, 3\}$ eigenvalues are above the threshold respectively. Since the tidal tensor quantifies the direction and intensity of the local tidal forces, this classification thus informs about the number of dimensions in which extended objects are contracted or stretched. We will call these environment types "elements" of the cosmic web.

For convenience, let $S_{\rm env}$ be the variance of the overdensity field convolved with the

kernel defining the environment, and let us introduce the three useful quantities:

$$\nu_{\rm env} = (\lambda_1 + \lambda_2 + \lambda_3) / \sqrt{S_{\rm env}}, \tag{4.17a}$$

$$\theta = \frac{1}{2} (\lambda_1 - 2\lambda_2 + \lambda_3) / \sqrt{S_{\rm env}}, \tag{4.17b}$$

$$\rho = \frac{1}{2} (\lambda_1 - \lambda_3) / \sqrt{S_{\rm env}}. \tag{4.17c}$$

These diagonalise the covariance matrix of the λ_i in the previous paragraph. The classification scheme outlined above can be re-cast in terms of these quantities as:

$$\nu_{\rm env} - \nu_{\rm th} \in [f_1(\rho, \theta \,|\, \alpha) \;,\; f_2(\rho, \theta \,|\, \alpha)] \quad \text{where } \nu_{\rm th} = 3\frac{\lambda_{\rm th}}{\sqrt{S_{\rm env}}} \tag{4.18a}$$

$$f_1(\rho, \theta \,|\, \alpha) = \begin{cases} -\infty & \alpha = 0 \quad \text{(voids)} \\ -3\rho - \theta & \alpha = 1 \quad \text{(sheets)} \\ 2\theta & \alpha = 2 \quad \text{(filaments)} \\ 3\rho - \theta & \alpha = 3 \quad \text{(knots)} \end{cases} \tag{4.18b}$$

$$f_2(\rho, \theta \,|\, \alpha) = \begin{cases} -3\rho - \theta & \alpha = 0 \quad \text{(voids)} \\ 2\theta & \alpha = 1 \quad \text{(sheets)} \\ 3\rho - \theta & \alpha = 2 \quad \text{(filaments)} \\ \infty & \alpha = 3 \quad \text{(knots)} \end{cases} \tag{4.18c}$$

where $\lambda_{\rm th}$ is the eigenvalue threshold, and α is the number of eigenvalues above it.

The probability distribution for the environmental tidal field in terms of $\nu_{\rm env}$, ρ and θ is given by [6, 248]:

$$p(\rho, \theta, \nu_{\rm env}) = 225\frac{\sqrt{5}}{2\pi}\rho\left(\rho^2 - \theta^2\right)\exp\left[-\frac{1}{2}\left(15\rho^2 + 5\theta^2 + \nu_{\rm env}^2\right)\right] \tag{4.19}$$

after integrating over the irrelevant rotation angles that diagonalize the tidal tensor. Thus we can estimate the volume fractions taken up by each element of the cosmic web:

$$F_{\rm vol} = \int_0^\infty d\rho \int_{-\rho}^{\rho} d\theta \int_{\nu_{\rm th} + f_1(\rho,\theta\,|\,\alpha)}^{\nu_{\rm th} + f_2(\rho,\theta\,|\,\alpha)} d\nu_{\rm env}\; p(\rho, \theta, \nu_{\rm env}). \tag{4.20}$$

Now we use the Gaussian statistics to find the conditional Press-Schechter *Ansatz*. The simplification that we are only interested in spherical collapse has the corollary that the distribution of the overdensity field conditional on environment only depends explicitly

on the value of the environmental overdensity $\delta_{\rm env} = \nu_{\rm env}\sqrt{S_{\rm env}}$:

$$p\left(\delta_h \,|\, \delta_{\rm env}\right) d\delta_h = \frac{d\nu_h}{\sqrt{2\pi\left(1-\epsilon^2\right)}} \exp\left[-\frac{\left(\nu_h - \epsilon\nu_{\rm env}\right)^2}{2\left(1-\epsilon^2\right)}\right] \tag{4.21}$$

where $\nu_h = \delta_h(S, \delta_{\rm env})/\sqrt{S}$ refers to the halo[3], with $\nu_{\rm env} = \delta_{\rm env}/\sqrt{S_{\rm env}}$ the analagous quantity for the environment and $\epsilon^2 = S_{eh}/\left(S_{\rm env}S\right)$ is the correlation coefficient between δ_h and $\delta_{\rm env}$.

We are now in a position to present the key integral of this chapter. First we must take into account that we require $S > S_{\rm env}$ for the excursion set theory to work. This corresponds to the physical requirement that the halo be embedded in the environment and not vice-versa. Under the simplification that the moving barrier δ_c does not affect Eq. (4.21), we find that the conditional collapsed mass fraction is the same as the result in Eq. (6.1), subject to the change of variables from ν to $\nu_{\rm eff}$ (defined below). Thus we find the corollary that the first-crossing distribution becomes:

$$f\left(S \,|\, \alpha\right) = \frac{1}{F_{\rm vol}\left(\alpha\right)} \int_0^\infty d\rho \int_{-\rho}^{\rho} d\theta \int_{\nu_{\rm th}+f_1(\rho,\theta\,|\,\alpha)}^{\nu_{\rm th}+f_2(\rho,\theta\,|\,\alpha)} d\nu_{\rm env}\; p(\rho,\theta,\nu_{\rm env}) g\left(\nu_{\rm eff}\right) \tag{4.22}$$

This effective-ν approach can be used for any fitting function, once we have transformed the independent variable from σ to ν in the unconditional HMF.

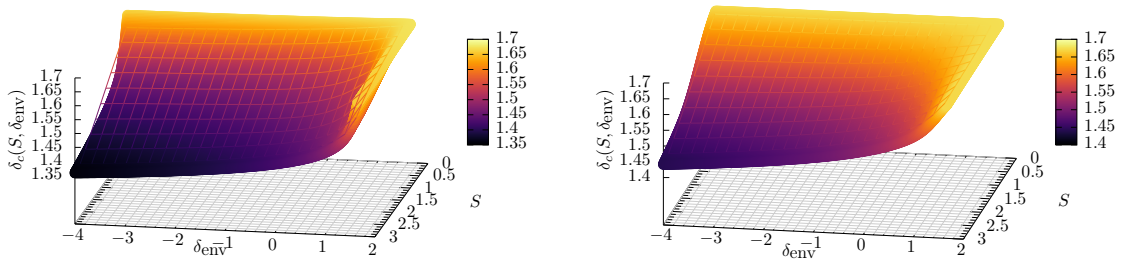

Figure 4.6: The full barrier (surface) and linear approximation (grid) for $f(\mathcal{R})$ models with $|f_{\mathcal{R}0}| = 10^{-5}$ and $|f_{\mathcal{R}0}| = 10^{-6}$. Both the surface and the grid are coloured according to the value of δ_c, so any areas in which the grid is visible indicates a discrepancy between the linear estimate and the true value. This is particularly pronounced for $|f_{\mathcal{R}0}| = 10^{-5}$ compared to $|f_{\mathcal{R}0}| = 10^{-6}$.

4.4 Generalising HMF fitting functions

This section summarises the various halo mass functions used in this thesis. In GR a variety of empirical fits to N-body simulations have been proposed in a "universal" form $f(\nu)$. The aim of these fits is to find a fitting function over a broad range of masses which is independent of redshift and cosmology, and the extent to which each fitting function exhibits this universality is a controversial one even in GR. Nonetheless, we show how to generalise the HMFs proposed in GR to three types of screened MG. Furthermore, we show a variety of methods to include environment dependence in the HMF, as required by chameleon-screened MG. A summary of the functions used in this thesis is in Table 4.1.

Two of the fitting functions used here (*viz.* Press-Schechter and Sheth-Mo-Tormen) can be derived analytically. As we have seen in Section 4.2.2, the Press-Schechter function results from assuming spherical symmetry and a flat (scale-independent) barrier density. That Press-Schechter can be derived analytically in screened MG (e.g. for a chameleon model [155]) via a simple change of variables is the very reason that we can extend the other mass functions in this thesis to MG as well. The Sheth-Mo-Tormen function in [224, 225] was originally a fit to data with the substitution $\delta_c \to \sqrt{a}\delta_c$ made to produce a better fit than Press-Schechter. Later [178] showed that this is equivalent to using excursion set theory with the moving barriers which result from ellipsoidal collapse. To our knowledge, no-one has shown that the assumptions used to construct the Sheth-Tormen function in GR also hold in MG. Nonetheless it is their analyticity in GR which makes these appealing functions for use in MG.

The remaining fitting functions are purely empirical fits, derived from ΛCDM N-body simulations. Having extracted the discrete approximation to the HMF $n(M)$, this can be converted to a discrete first-crossing distribution and a continuous "best-fit" approximation found—either in terms of σ or in terms of ν—which holds for a given redshift (range), mass range and cosmology (or family of cosmologies). The resulting HMF also depends upon the halo finder used to extract the halo masses, as well as any subsequent calibration or corrections. These factors all contribute to the final parameter values adopted by a particular function. This is particularly notable for the Sheth-Mo-Tormen fit, for which several authors[4] [75, 125, 224, 251] have proposed their own "improved" values for the best-fit parameters of this function. This emphasises that while the same functional form can provide a good fit to data in different background cosmologies, the same N-body data and the same fitting function will produce

[3]We use δ_c and δ_h interchangeably: the subscript c when employed as a collapse density equivalent to the excursion set barrier and a subscript h when we wish to emphasise the difference between halo and environment quantities.

[4]This is why Jenkins appears twice in Table 4.1: one instance is their calibration for the SMT function (as with Courtin) and the other is their new fitting function.

different best-fit parameters and varying degrees of invariance depending upon the halo extraction techniques and the theoretical assumptions of the authors. For this reason, we have separated the HMFs into families which share the same functional form. We summarise the HMFs $f(\nu)$ in Table 4.1.

There are four steps involved in generalising the ΛCDM HMFs to MG:

1. Calculating the appropriate barrier density;
2. Selecting the appropriate linearised power spectrum;
3. Converting from σ to ν as the dependent variable;
4. Rescaling the free parameters accordingly.

We discuss Item 1 in Section 4.1.

In Item 2 we must decide whether to keep the ΛCDM power spectrum or to adjust it according to the MG theory. Motivated by Section 4.2.2 we keep the linear $P(k)$ from ΛCDM, in agreement with [59, 248].

Item 3 is concerned with making explicit the dependence on the collapse density. In GR, one is faced with the question of whether the appropriate independent variable for the HMF is ν or S (equivalently any other function of σ). Those in the former camp (*inter alia* [193, 224, 225, 261]) assert that according to excursion set theory the (albeit weak) cosmological and redshift dependence of both δ_c and σ cancel when the first-crossing distribution is expressed in terms of $\nu \equiv \delta_c/\sigma$ in GR cosmologies. Those in the latter camp (*inter alia* [76, 125, 206, 207, 239, 251]) assert that δ_c is a sufficiently weak function of Ω_{m0} and z that this dependence can be ignored; in fact [125] go so far as to say that "taking $\delta_c = 1.686$ in all cosmologies leads to excellent agreement with our numerical data if halos are defined at fixed overdensity". Thus, while the choice of S or ν appears to be mere semantics in GR cosmologies (because this is an invertible mapping if and only if δ_c is assumed to be a constant), this is clearly not the case in our extended gravity theories. This is especially true for $f(\mathcal{R})$, which has both a mass- and $\delta_{\rm env}$-dependence for δ_c.

Item 4 is the consequence of Item 3. All the free parameters in the HMFs[5] need to be converted from $\ln(\sigma^{-1})$ to ν, by absorbing factors of δ_c. This requires paying particular attention to whether the SCDM or ΛCDM collapse density is used in the original papers, as this has implicitly been absorbed into the best-fit parameters.[6] This "updates" the

[5]The "Reed 2007" fit is the 2003-like fit from [207], rather than the one with $n_{\rm eff}(\sigma)$ dependence, which creates ambiguity about which terms to convert to ν. In the fit we use the σ-dependence is clearly only caused by treating δ_c as a constant.

[6]If we were concerned with redshift evolution, we would have to decide whether to absorb δ_{c0} or $\delta_c(z)$. Some authors fix δ_c and allow the free parameters to vary with redshift; others do the opposite.

ΛCDM-calibrated fits to a format which is compatible both with GR and MG.

This is sufficient for MG theories which only have a drifting barrier $\delta_c(S)$, but not for the drifting-and-diffusing barrier $\delta_c(S, \delta_{\rm env}, S_{\rm env})$. We treat this additional generalisation in the next few paragraphs.

The drifting-and-diffusing barrier can be accounted for using a wide variety of methods:

1. Scaling using the Volterra integral solution in Eq. (4.10a)
2. Averaging over the cosmic web (described in [248])
3. Calculating a $\delta_{\rm env}$-averaged collapse density, i.e. converting to a drifting barrier
4. A flat or linear-barrier approximation to the full excursion-set problem

We address each of these in turn.

Technique 1 utilises the fact that we already know how to account for the extra barrier complexity in the excursion set approach: whereas the flat barrier produces the Press-Schechter distribution, the drifting-and-diffusing barrier leads to the solution Eq. (4.10a). So we may calculate the unconditional HMF, i.e. assuming ($\delta_{\rm env} = 0$, $S_{\rm env} = 0$), then accounting for the effects of the drifting and diffusing barrier using excursion set theory. This results in a rescaling of the unconditional HMF:

$$f(S)_{\rm MG} = f(S|S_{\rm env} = 0, \delta_{\rm env} = 0)_{\rm MG} \quad \frac{\text{Volterra solution}}{\text{Press-Schechter}} \tag{4.23}$$

This is efficient, as we only need to solve the Volterra equation once for each drifting-and-diffusing barrier density, rather than re-calculating for each HMF as well.

Technique 2 uses the $\nu_{\rm eff}$ prescription of Section 4.3. This can be substituted directly into the HMF:

$$\nu_{\rm eff} = \max\left\{0, \frac{\nu_h\left(S, \delta_{\rm env}\right) - \epsilon^2\left(S, S_{\rm env}\right)\nu_{\rm env}\left(S_{\rm env}, \delta_{\rm env}\right)}{\sqrt{1-\epsilon^2\left(S, S_{\rm env}\right)}}\right\} \tag{4.24}$$

Since we are not interested in restricting ourselves to a particular environment, we can simplify Eq. (4.22) to:

$$f\left(S\right) = \int_{-\infty}^{\infty} \mathrm{d}\,\nu_{\rm env}\; f\left(\nu_{\rm eff}\right) \int_0^{\infty} \mathrm{d}\,\rho \int_{-\rho}^{\rho} \mathrm{d}\,\theta\; p(\rho, \theta, \nu_{\rm env}) \tag{4.25}$$

We have rearranged the order of integration to highlight that the conditional mass function $f\left(\nu_{\rm eff}\right)$ is independent of ρ and θ.

Technique 3 approximates the drifting-and-diffusing barrier by a drifting-only barrier.

The aim is to integrate over the environment density at the stage of calculating the collapse density:

$$\nu_{\rm eff} = \frac{\langle \delta_c \rangle_{\rm env}}{S} \quad \text{where} \quad \langle \delta_c \rangle_{\rm env} = \int_{-\infty}^{\delta_\Lambda} \mathrm{d}\,\delta_{\rm env}\; p\left(\delta_{\rm env} \,|\, S_{\rm env}\right)\; \delta_c\left(S \,|\, S_{\rm env}, \delta_{\rm env}\right) \tag{4.26}$$

This effective-ν is substituted directly into the unconditional HMF. In contrast to the full barrier solution—where the random walk must upcross δ_c at S having started at $(\delta_{\rm env}, S_{\rm env})$—here there is no accounting for the environment in the excursion set phase space. This method does not account for the absorption of the Markovian trajectories in (δ, S) caused by the drifting-and-diffusing barrier in the excursion set methodology.

Technique 4 approximates the full solution to the Volterra equation in Eq. (4.10a) by a linear barrier. This is motivated by the fact that the Volterra equation with a linear barrier $\delta_c(S) = \omega - \beta S$ is calculable analytically [192]:

$$f\left(S, \delta_c(S) \,|\, S_{\rm env}, \delta_{\rm env}\right) = \frac{\delta_c - \delta_{\rm env}}{\sqrt{2\pi \left(S - S_{\rm env}\right)^3}} \exp\left[-\frac{1}{2}\frac{\left(\delta_c - \delta_{\rm env} - \beta\left(S - S_{\rm env}\right)\right)^2}{S - S_{\rm env}}\right] \tag{4.27}$$

so we can substitute the effective arguments into the fitting function, in the same way as for the cosmic web. However, Fig. 4.6 shows that the $f(\mathcal{R})$ barriers are not linear in S (except when $\delta_{\rm env} \to \delta_c^\Lambda$). The linear approximation is always an overestimate and is particularly poor at approximating the sharp rise at $\delta_{\rm env} \approx \delta_c^\Lambda$. Therefore we discard this approach due to its poor approximation.

A *caveat* for all of these methods is that there is no way to eliminate dependence on $S_{\rm env}$. The excursion set condition $S_{\rm env} < S$ prevents us from marginalising directly. The environment distributions (whether cosmic web or the PDFs for the environment overdensity) in the limit $S_{\rm env} \to 0$ do not have a finite limit. Instead we take a sufficiently large environment radius (e.g. $R_{\rm env} = 10$, $20\mathrm{Mpc}/h$) that $S > S_{\rm env}$ is always obeyed (but not too large, otherwise this is no longer a sufficiently local description of the halo surrounds [156]).

The main result of Section 4.5 is to compare these methods for generating the conditional HMFs for $|f_{\mathcal{R}0}| = 10^{-5}$ and $|f_{\mathcal{R}0}| = 10^{-6}$. For the other MG models, the barriers do not have an environment-dependent component, so their calculation is straightforward.

This updates the ΛCDM-calibrated HMFs to screened MG.

Fitting function $f(\nu)$	Mass calibration	Cosmology	Reference
$\sqrt{\frac{2}{\pi}}\nu \exp\left[-\frac{\nu^2}{2}\right]$	–	EdS	Press-Schechter [202]
$A\sqrt{\frac{2a}{\pi}}\left[1+\left(a\nu^2\right)^{-p}\right]\nu\exp\left[-\frac{a\nu^2}{2}\right]$	$\nu^2 \in [0.5, 10]$	ΛCDM SCDM OCDM	Sheth-Tormen [225]
	$\ln\sigma \in [-0.7, 0.8]$	ΛCDM, OCDM, SCDM, τCDM	Jenkins [125]
	$\ln\sigma \in [-0.7, 0.8]$	ΛCDM SCDM L-ΛCDM LRP-CDM	Courtin [75]
$A\left[\left(\frac{\nu}{\delta_c^\Lambda}\right)^a + b\right]\exp\left[-c\nu^2\right]$	$M \in [10^{10}, 10^{15}]M_\odot$	ΛCDM	Warren [251]
	$M \in [10^{10.5}, 10^{15.5}]M_\odot$	ΛCDM	Crocce [76]
$A\exp\left[-\left\lvert\ln\nu + b\right\rvert^a\right]$	$\ln\sigma \in [-1.05, 1.2]$	ΛCDM OCDM SCDM τCDM	Jenkins [125]
$\frac{\nu^2\exp(-c\nu^2)}{\left(1+a\nu^b\right)^2}\left[ab\nu^{b-1} + c(1+a\nu^b)\right]$	$M \in [10^{10}, 10^{15}]M_\odot$	ΛCDM	Peacock [193]
$A\sqrt{\frac{2a}{\pi}}\nu\exp\left[-\frac{ca\nu^2}{2}\right]$ $\left[1+\left(a\nu^2\right)^{-p} + Q\exp\left[-\frac{1}{2}\left(\frac{\ln\nu - q}{0.6}\right)^2\right]\right]$	$\ln\sigma \in [-0.9, 1.7]$	ΛCDM	Reed 2007 [207]
$A\left[(b\nu)^a + 1\right]\exp\left(-c\nu^2\right)$	$\sigma \in [10^{-0.4}, 10^{0.6}]$	ΛCDM	Tinker 2008 [239]
	$M \in [10^8, 10^{16}]M_\odot$	ΛCDM	Angulo [13]
	$\ln\sigma \in [-1.31, 0.55]$	ΛCDM	Watson [252]

Table 4.1: Details of the HMF fitting functions used in this paper. The various "nCDM" cold dark matter cosmologies are described in Table 4.2. For some fits, we have rewritten the function in terms of ν by substituting for σ and absorbing factors of δ_c into the original free parameters.

Cosmology	Parameters				HMF paper(s)
	Ω_{m0}	$\Omega_{\Lambda 0}$	σ_8	h	
ΛCDM	0.269	0.731	0.80	0.704	This paper
	0.29	0.71	0.90	0.72	WMAP1 (Courtin)
	0.30	0.70	0.90	0.70	WMAP1 (Sheth-Tormen, Jenkins, Tinker, Warren)
	0.24	0.76	0.74	0.73	WMAP3 (Courtin, Reed)
	0.24	0.76	0.75	0.73	WMAP3 (Tinker)
	0.24	0.76	0.8	0.73	WMAP3 (Tinker)
	0.26	0.74	0.79	0.72	WMAP5 (Courtin)
	0.27	0.73	0.80	0.70	WMAP5 (Watson)
	0.28	0.72	0.80	0.70	WMAP5 (Watson)
	0.27	0.73	0.90	0.70	Tinker
	0.27	0.73	0.79	0.70	
	0.26	0.74	0.75	0.71	
	0.23	0.77	0:75	0:73	
	0.20	0.80	0:90	0:70	
	0.25	0.75	0.80	0.70	Crocce
	0.25	0.75	0.80	0.73	Peacock
	0.25	0.75	0.90	0.73	Angulo, Reed
SCDM	1.0	0.0	0.60	0.50	Sheth-Tormen
	1.0	0.0	0.51	0.50	Jenkins
	1.0	0.0	0.79	0.72	Courtin
OCDM	0.30	0.0	0.85	0.70	Sheth-Tormen, Jenkins
τCDM	1.0	0.0	0.51	0.5	Jenkins
	1.0	0.0	0.60	0.50	Sheth-Tormen, Jenkins
L-ΛCDM	0.10	0.90	0.79	0.72	Courtin
LRP-CDM	0.26	0.74	0.79	0.72	Courtin

Table 4.2: Cosmological parameters used to derive each of the HMF fitting functions in GR.

4.5 Accounting for the drifting-and-diffusing barrier in MG

Section 4.5 presents our new results for incorporating MG into ΛCDM-calibrated HMFs.

In Section 4.4 we suggested a variety of different methods to implement the full effects of environment dependence in MG for a fitting function. We compare the data from our $f(\mathcal{R})$ simulations with $|f_{\mathcal{R}0}| = 10^{-5}$ and $|f_{\mathcal{R}0}| = 10^{-6}$ to the theoretical HMF using each method. In the order given by Fig. 4.7 we have:

1. The unconditional HMF using $\langle \delta_c \left(S \,|\, \delta_{\rm env}, S_{\rm env} \right) \rangle_{\rm env}$, the environment-averaged collapse density Eq. (4.26)
2. The conditional HMF marginalised over the Eulerian $\delta_{\rm env}$-distribution Eq. (4.15b)
3. The conditional HMF marginalised over the Lagrangian $\delta_{\rm env}$-distribution Eq. (4.14)
4. The unconditional HMF, i.e. assuming both $\delta_{\rm env}$ and $S_{\rm env}$ vanish
5. The Volterra solution to Eq. (4.10)
6. The unconditional HMF scaled with the Volterra solution using Eq. (4.23)

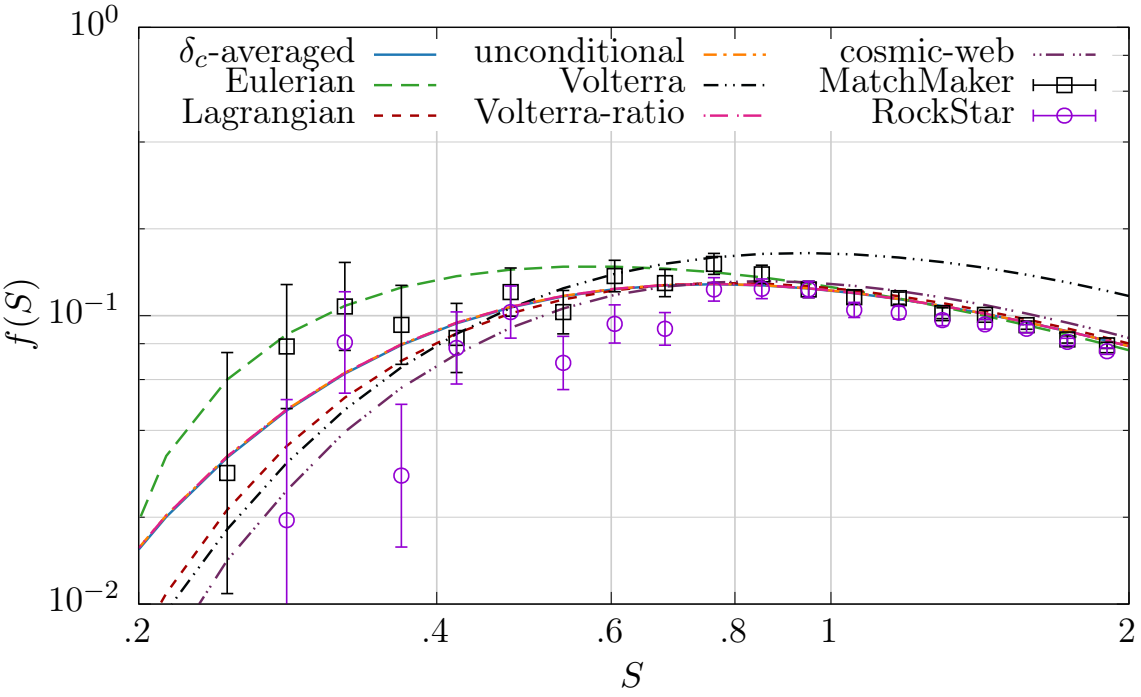

(a) ΛCDM

Figure 4.7: The first-crossing distribution for a drifting-and-diffusing barrier using the variety of methods explored in this thesis are shown as lines. We also plot the $f(\mathcal{R})$ data from the N-body simulations using the two halo finders.

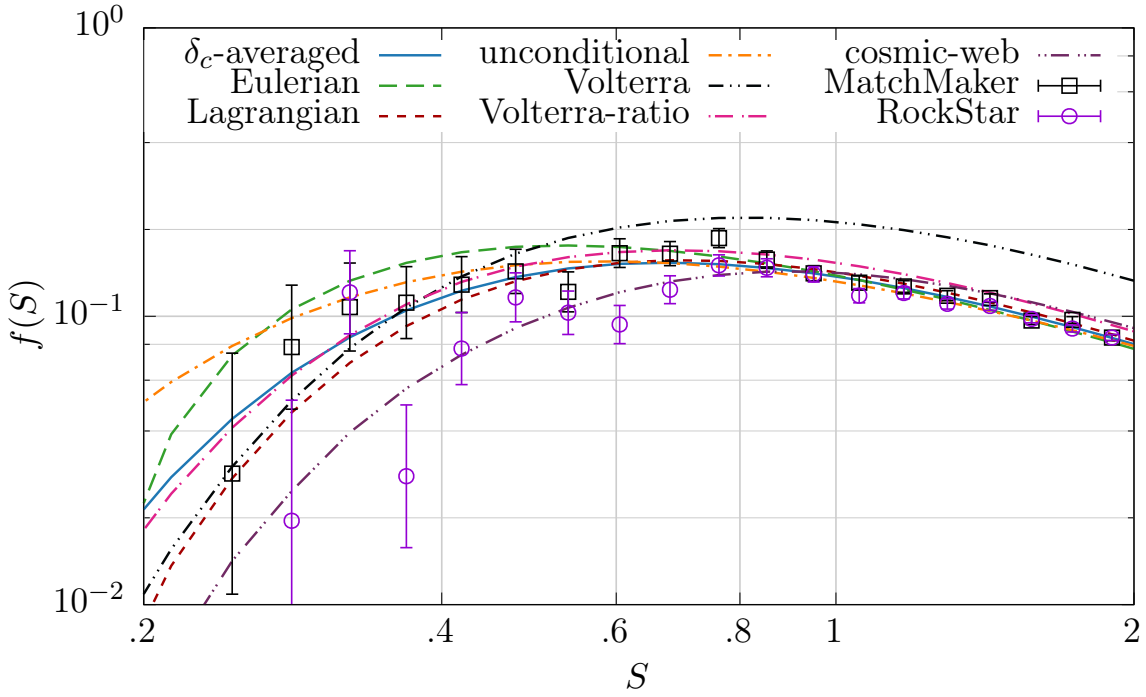

(b) $|f_{\mathcal{R}0}| = 10^{-5}$

Figure 4.7: The first-crossing distribution for a drifting-and-diffusing barrier using the variety of methods explored in this thesis are shown as lines. We also plot the $f(\mathcal{R})$ data from the N-body simulations using the two halo finders.

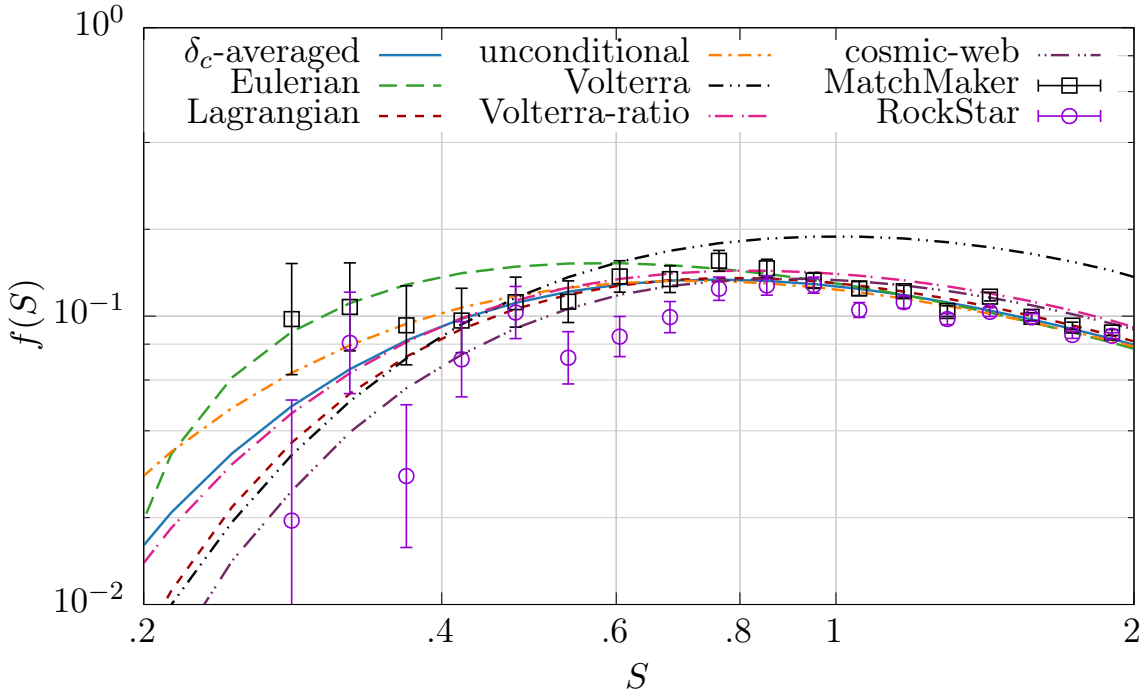

(c) $|f_{\mathcal{R}0}| = 10^{-6}$

Figure 4.7: The first-crossing distribution for a drifting-and-diffusing barrier using the variety of methods explored in this thesis are shown as lines. We also plot the $f(\mathcal{R})$ data from the N-body simulations using the two halo finders.

7. The cosmic web HMF marginalised over the tidal tensor distribution Eq. (4.25)

Fig. 4.7 shows these methods for the Reed-07 fitting function[7] (lines) and the N-body HMFs calculated using the `MatchMaker` and `RockStar` halo finders (points). These simulations and the workings of the two halo finders are described in Section 5.2.1. We examine the ΛCDM results before discussing each method over the next few paragraphs.

The ΛCDM behaviour in Fig. 4.7a is consistent with the excursion-set framework we discussed in Section 4.2.2. The environment-averaged collapse density is δ_c^Λ (because the excursion-set barrier is flat) and the Volterra solution reduces to Press-Schechter. Therefore both of these methods produce the same result as the unconditional HMF. The other four methods all differ. While both the Lagrangian and cosmic web methods do equal the unconditional HMF using Press-Schechter, this is due specifically to the design of this function from excursion set theory. It is the only integrand for which the solution to the integral equation Eq. (4.10a) is merely a rescaling between the conditional and unconditional forms of ν. We have now ensured that the different methods behave as expected in GR, before applying them to $f(\mathcal{R})$.

The first option avoids using excursion set theory altogether, by pre-emptively converting the drifting-and-diffusing barrier to an average density. The drifting barrier $\delta_c(S)$ can be incorporated straightforwardly, just as in the non-chameleon MG models, into the unconditional HMF. Surprisingly, this gives a very good fit, superior to the purely unconditional HMF. Although the peak of Eq. (4.14) is at zero, this result illustrates that we need to use the entire PDF, rather than only using the peak to approximate the average. In this way we can account for the peak-background split, whereby it is easier for haloes to form as $\delta_{\rm env} \to \delta_c$ in dense regions and more difficult in under-dense regions. This method has the advantage that we can compute the barrier density once, rather than re-computing the conditional function at every stage of the MCMC process. We have managed to produce a good fit by considering only the barrier density, rather than accounting for the complex excursion set behaviour of the full drifting-and-diffusing barrier.

The conditional HMFs marginalised over the Lagrangian (Eq. (4.14)) and Eulerian (Eq. (4.15b)) theoretical distributions $p(\delta_{\rm env})$ have appeared in the literature before[8] [170], where they were applied to the Sheth-Tormen HMF. The authors suggested discarding the Lagrangian (density) distribution in favour of the Eulerian, on the basis that a density distribution which better reflects the physical formation of overdensities,

[7] We might have used any of the fitting functions, because our aim is to compare the behaviour of each technique for extending the mass function to MG. The Reed fit produced the closest fit to the data given the default parameters.

[8] [170] only plotted the relative enhancement $n_{\rm MG}(M) - n_{\rm GR}(M)/n_{\rm GR}(M)$, rather than the HMF proper $n(M)$, so we cannot readily compare our results to theirs.

would correspondingly produce a more accurate HMF. This is supported by the findings of [156]. While our results agree using the `MatchMaker` halo finder, the `RockStar` halo finder predicts a systematically lower distribution of haloes, better suited to the Lagrangian model. The question of which PDF to use is somewhat moot considering that neither fit performs particularly well. This is probably due to generating the conditional from the unconditional HMF. The rescaling at the end of Section 4.2.1 which is used in [155, 170] implicitly assumes that a linear function of $\delta_c(S)$ is a good approximation for the actual barrier density. We have already seen in Fig. 4.6 that this is not the case. Therefore we cannot use methods which work for a flat barrier density in ΛCDM to good effect in $f(\mathcal{R})$.

The solution to the integral equation is the MG-equivalent of Press-Schechter. For this reason, we do not expect it to be a good fit to the data. Indeed the $|f_{\mathcal{R}0}| = 10^{-5}$ and $|f_{\mathcal{R}0}| = 10^{-6}$ plots in Figs. 4.7b and 4.7c share the recognised flaws of the Press-Schechter fit in ΛCDM in Fig. 4.7a, namely that it under-predicts at the high-mass end (low-S) and over-predicts at the low-mass end (high-S). Nonetheless, it reproduces the general behaviour of the first-crossing distribution, which is remarkable for such a simple model.

Moreover, we can improve the result from the unconditional HMF by scaling by the ratio of the Volterra solution to Press-Schechter. The two poor results combine to form a decent approximation. At the low-S end, the Volterra solution forms too few haloes because the random walks in excursion set theory are not absorbed early enough by the barrier density, so too many trajectories survive to produce haloes at high-S. In contrast, the unconditional HMF assumes $\delta_{\rm env} = 0$ (and $S_{\rm env} = 0$) so at small values of S the value of $\nu = \delta_c(S)/\sqrt{S}$ is large and vice-versa at high-S. Since the fitting function $f(\nu)$ is monotonically increasing with ν, we have too many haloes at small S and too few at low S. These two behaviours counteract one another to reduce the overall discrepancy of the fit. This is because we have deliberately designed a method to combine different strengths of the analytical and empirical approaches. The unconditional fitting function is designed to produce a good approximation to the ΛCDM data. The Volterra solution captures the excursion set behaviour of the barrier density, which incorporates the main effect of $f(\mathcal{R})$ compared to ΛCDM from a theoretical viewpoint. Thus, we can combine two simple mechanisms to produce a relatively good solution, despite their individual predictions being ineffectual.

The performance of the cosmic web method is discussed in more detail in Chapter 6. In general it under-predicts the HMF at the high-mass end, whereas it works well at the low-mass end. There are two contributing factors, namely the $\nu_{\rm eff}$ approximation substituted into the fitting function and the $p(\rho, \theta, \nu_{\rm env})$ distribution related to the tidal tensor in the cosmic web. The former is not particularly successful even in ΛCDM ([6])

so we ought not expect any better performance in $f(\mathcal{R})$ where the spherical collapse in more complicated due to the fifth force. The latter is the equivalent of the Lagrangian distribution for $\delta_{\rm env}$ applied to all three eigenvalues of the tidal tensor rather than its trace. We have already seen that the Lagrangian-$\delta_{\rm env}$ fit does not produce an accurate fit. This technique is useful for calculating the HMF in individual structures of the cosmic web (e.g. voids, sheets *etc.*), wherein we have no other analytical treatment, but not the overall HMF.

Finally we comment on the distinction between the cosmic web results (Eq. (4.25)) and those of the Lagrangian PDF (combining Eqs. (4.12) and (4.14)). Given that the conditional HMF in the cosmic web doesn't depend upon (ρ, θ), and that the distributions for $p(\nu_{\rm env})$ and $p(\delta_{\rm env})$ have the same dependence on $\delta_{\rm env}$, one may expect that these two methods should produce the same results. Clearly Fig. 4.7 does not agree. This is due to the effect of the window functions in calculating $S(M)$ and $S_{\rm env}(R_{\rm env})$. In cosmic web we use a Gaussian window function for the environment and a (real-space) top-hat for the halo, whereas in the excursion set we used a top-hat window function for both halo and environment. This affects the value of $S_{\rm env}$ obtained from the same environment radius. Additionally, the Lagrangian (and Eulerian) result(s) both assume that the halo-environment correlation is $\epsilon = S_{\rm env}/S$. This is due to the assumption in excursion set theory that our trajectories in (δ, S) are uncorrelated at successive values of S, for which one requires a sharp-k window function, whence comes this expression for ϵ. In the cosmic web method we calculate ϵ numerically for a Gaussian and top-hat window function in the environment and halo respectively. Therefore the same values of $\delta_c(S|\delta_{\rm env}, S_{\rm env})$ map differently onto the argument of the conditional HMF. Once this is established, it does not matter that the marginalisation over the environment is the same in both methods.

What improvements in the numerics are required to decisively exclude some of these methods? In Fig. 4.7, the uncertainty on the HMF is on the same order as the spread of results from the different techniques. There is also considerable spread in the N-body results when extracted using different halo finders at low resolution. This is expected, since at low-S scales the halo finders count high-mass haloes, of which few exist in the simulation box. Unfortunately the halo-rich end at high-S—where constraints are tightest—is the excursion set regime in which all the methods converge because the trajectories which have survived avoiding the drifting-and-diffusing barrier for many steps in the random walk. Therefore we require larger simulations which contain more large-mass haloes, in order to maximise constraints at the low-resolution end. Furthermore, multiple halo finders need to be utilised, in order to better characterise the uncertainty from data reduction. This should permit better analysis of the efficacy of the different theoretical methods against numerical results.

Given the performance of the various techniques for extending the fitting functions to chameleon MG, and the performance factor involved in re-calculating a conditional HMF (and marginalising over it) at every stage of the MCMC procedure, we shall use the Volterra-ratio method to calculate the $f(\mathcal{R})$ HMF in Section 5.4.3. Nevertheless, we have found a broad spectrum of possible methods by means of which we can incorporate MG into fitting functions originally designed for ΛCDM alone. Moreover, we have found that some are more suited to certain applications (e.g. the cosmic web approach) or halo finders (e.g. the two density-marginalised methods) than others. This demonstrates the additional complexity which environment dependence produces in chameleon screening compared to symmetron- and Vainshtein-screened theories. We cannot neglect this and simply substitute the unconditional HMF if we wish to produce a useful empirical function to use in lieu of deriving one from N-body simulations.

Chapter 5

Universality of the HMF in screened MG

5.1 Introduction

The halo mass function (HMF) $n(M)dM$ is the number n of haloes with mass in the range $[M, M + dM]$ per unit volume. It has two remarkable properties which render it a useful probe of extensions to general relativity (GR). On the one hand, it is (nearly-)universal, in the sense that it can be written in a form $f(\nu)$ which is (practically) insensitive to changes in redshift and cosmological parameters [34, 261], where ν is the universal parameter and f is a fitting function with a number of free parameters. On the other hand, the HMF is sensitive to both the expansion history of the universe and the nonlinear behaviour of spherical collapse via the critical density parameter δ_c [40] and the matter power spectrum via the halo resolution $S(M)$ (both of which appear in ν). This presents a number of interesting possibilities for the use of the HMF in "modified gravity", i.e. gravity theories which extend GR, namely:

- How do underlying assumptions in constructing the HMF from simulations affect the success of the fitting functions?
- Should we blindly apply HMFs calibrated using GR (specifically ΛCDM) to other theories of gravity?
- Can evidence for modifications to GR be mistaken for changes in the free parameters in the GR HMF?
- Which HMFs are more universal across (i.e. insensitive to) different gravity the-

ories?

- Do the extra gravitational degrees of freedom necessitate additional parameters in the HMF?

Only after such avenues are investigated can we begin to probe the universality of the HMF in MG theories. We cannot determine whether the kind of universality of the HMF enjoyed in GR also applies to extended gravity theories without understanding its behaviour at a fixed redshift and cosmology. This chapter addresses all of these questions for a comprehensive range of currently-viable HMFs by focusing on a subset of MG theories known as screened gravity.

Modifications to GR are motivated by a number of factors. From a theoretical standpoint, it is interesting to see what extensions to GR are permitted by Lovelock's theorem [70]. Consequently, we have a useful division of theories into families depending upon which condition(s) in Lovelock's theorem is (are) relaxed. From a cosmological viewpoint, the era of precision cosmology now enables us to distinguish between competing models. While the concordance cosmology of ΛCDM has performed remarkably well over the past two decades (see [55] for a summary), there exist theoretical problems (e.g. fine-tuning of Λ, the lack of direct detection of CDM, possible fine-tuning of inflation) [70] and tensions between observations measured at early times (with Planck 2015 [200]) and at late times (e.g. the values of σ_8 from weak lensing and cluster number counts, H_0 from Lyman-α measurements of BAO, $f\sigma_8$ from redshift-space distortions) [55]. Thus it is useful to have a range of possible gravity models which may alleviate these problems. Clearly, these motives give rise to a plethora of theories (see e.g. [70] for a summary), and it is impractical to test them all. Therefore in this chapter we restrict ourselves to a class of theories which exhibit screening, i.e. have the deviations from GR screened away in dense environments such as the Solar System. We are also restricted by the requirement to have a number of N-body simulations available for comparison to our theoretical HMFs. In this chapter we examine $f(R)$, Symmetron and Dvali-Gabadadze-Porrati (DGP) models. This selection represents a range of MG families (and screening mechanisms), while ensuring that each theory is broadly related.

A pre-requisite for using the HMF as a probe of MG is a firm understanding of its behaviour in GR. Superficially this may be obvious: the analytical HMF of Press and Schechter [202] has long been supplanted by a range of fitting functions (see [183] for a summary) whose free parameters are calibrated using N-body simulations. This calibration is valid only for certain cosmological parameters (which were employed in the N-body code) and a certain range in mass and redshift (for which the fit agrees with the simulation bins). It is this fitting function $f(\nu)$ which is universal, rather than the HMF itself $n(M)$. Specifically, the "universality" arises from the fact that $f(\nu)$ can be applied to a range of redshifts and cosmologies [239]. Recently, there has been

disagreement over whether this universality holds [129, 173, 261] or not [206, 207, 251]—and even these papers test only a few of the competing fitting functions. Consequently, one might argue that there is no clear "null hypothesis" against which deviation from GR may be tested. Despite this, once various obscuring factors are addressed, the deviations from non-universality in the calibrated HMFs are of a few percent [239]. In particular, if one uses the correct measurement of halo overdensity [85] and includes z-dependence in the overdensity and the resolution, the best-fit parameter values provide an HMF which applies over several decades of mass and beyond $z = 0$ (sometimes up to $z = 30$; [207]), but only for a fixed cosmology [75]. Thus, we can firmly establish the null result against which to test the effects of modified gravity.

Now we must establish how to derive the HMF in MG compared to GR. The underlying mechanism for generating halo mass functions differs in the MG and GR cases. Usually, N-body simulations are far more expensive to run because of the additional computation time and complexity required (discussed in Section 5.2.1). Consequently, rather than inventing and calibrating fitting functions, one typically uses either the Press-Schechter or the Sheth-Tormen functions (although [248] uses the Peacock function). The advantage of Press-Schechter is that it can be derived in both GR and MG using excursion set theory (Section 4.2.2), whereas Sheth-Tormen provides better agreement with N-body results. For the (quartic and quintic) Galileon HMF, the authors of [22] are forced to adopt the Press-Schechter approach due to the fact that the assumptions used in the Sheth-Tormen model are unlikely to hold, given the Galileon fifth-force modification to GR. In contrast, the DGP mass function in [215] is derived using the Sheth-Tormen approach, on the grounds that the Sheth-Tormen fit is considered satisfactory in the GR simulations. It is worth noting that both of these theories fall into the broader class of Vainshtein mechanism models—so in some sense the modification to gravity is the same—yet there is no agreement on which excursion set model is the appropriate one. The symmetron HMF in [234] uses Sheth-Tormen, following the same logic as [161, 215]. The $f(R)$ mass function is relatively advanced in comparison, with a variety of different approaches in reasonable agreement. These approaches illustrate the additional theoretical complications when applying excursion set theory to MG. In particular, the process also highlights ambiguities in the universal parameter $\nu = \delta_c / \sqrt{S}$ which are not present in GR: do we change only $S(M)$ [161] or only δ_c [248] or both [170], or do we need to evolve the full scalar field equations [143]? Once we have defined ν, what should be done about the parameter values? Usually the ΛCDM values are retained; sometimes the normalisation constant is left free while the other parameters are fixed at ΛCDM values [234] or recalibrated from appropriate MG simulations [20, 21]. Nonetheless, the approach is very different from the empirical, N-body driven approach used in GR.

This chapter seeks to address these issues. We have already outlined the various screened models of MG in Chapter 2. Moreover we have seen the fitting functions used in this chapter in Chapter 4. Therefore we describe the numerical work: Section 5.2 outlines the simulation parameters and algorithms used for the various N-body simulations and the extraction of the HMF from the simulations; Section 5.3 describes the "nested sampling" algorithm used to calculate the best-fit values for the free parameters in the HMFs. The results section discusses the questions raised at the beginning of this chapter: Section 5.4.2 shows how MG manifests in the parameters even when assuming a ΛCDM HMF; Section 5.4.3 recalibrates the fitting functions using the same gravity model in both the N-body simulations and the HMFs; Finally we summarise our method and key results and discuss avenues for further work in Section 5.5.

5.2 Data processing

This section summarises the N-body simulations from which we obtain the halo catalogues which form our simulated data. We also outline the nested sampling technique which we use for parameter estimation. We define the likelihood functions used in this chapter.

5.2.1 N-body simulations

The N-body simulations were run using the `ISIS` [165] and `ECOSMOG` codes [157]. Both of these are a modified gravity modification of the high-resolution N-body code `RAMSES` [236]. These codes belong to the class of adaptive mesh refinement codes, for which the equations Eqs. (5.1) and (5.2) and the fifth-force equations due to the scalar field are solved at multiple points on a grid, where the resolution of the grid adapts to the local density [157]. For details about the implementation and for a comparison of these codes see the modified gravity N-body code comparison project [260].

We ran two sets of simulations with different mass resolution. Simulation set 1 has $N = 512^3$ particles of mass $8.75\times10^9 M_\odot/h$ in a box of $B = 250$ Mpc$/h$. The background cosmology is a flat ΛCDM model with $\Omega_m = 0.269$, $\Omega_\Lambda = 0.732$, $h = 0.704$, $n_s = 0.966$ and $\sigma_8 = 0.8$. These simulations were presented in [260]. Simulation set 2 has $N = 256^3$ particles of mass $3.531 \times 10^{10} M_\odot/h$ in a box of $B = 200$ Mpc$/h$. The background cosmology is a flat ΛCDM model with $\Omega_m = 0.267$, $\Omega_\Lambda = 0.733$, $h = 0.719$, $n_s = 1.0$ and $\sigma_8 = 0.8$. These simulations were presented in [46].

Dark matter N-body simulations are performed by evolving two equations. The first

one is the Poisson equation which gives us the gravitational potential Φ in terms of the particle positions (which determines the density field ρ_m)

$$\nabla_x^2 \Phi = 4\pi G(\rho_m - \overline{\rho}_m) \tag{5.1}$$

and the second is the geodesic equation

$$\ddot{\mathbf{x}} + 2H\dot{\mathbf{x}} = -\nabla_x \Phi \tag{5.2}$$

which determines the evolution of the particles. For the modified gravity simulations we consider here the only change is that we have a fifth force $-\nabla\varphi$ that contributes to the right hand side of Eq. (5.2) and we have to solve a field equation similar to Eq. (5.1), but highly non-linear, to get the fifth-force potential φ. It is this addition which requires the main difference between `ISIS` and `RAMSES`, namely that the linear multigrid solver is replaced by a non-linear one. The equations are discretised and scaled into code units to render them dimensionless, e.g. `ECOSMOG` uses "supercomoving co-ordinates" [157]. This latter step increases numerical stability. The gravitational potential is calculated on the grid and gravitational fields are computed as its spatial derivatives. Matter evolution is determined by discretising the mass distribution into particles and computing their geodesics. (Baryons require an additional Godunov solver because they are collisionful.) Rather than solving the scalar field evolution directly, it is transformed (nonlinearly) to fix its sign and reduce large gradients [165]. The resulting equations of motion are solved on the grid using a variety of methods depending upon whether or not they are in canonical form. The simulations are performed in the quasi-static limit. Fortunately, we have already discussed in Chapter 3 that this is a reliable approximation in cosmologically-viable models. This alleviates the need to use small time steps to quantify the behaviour of the scalar field evolution, which becomes increasingly difficult at higher (spatial) resolutions because the oscillations are largest on small scales [46]. Non-QSA code do exist (e.g. [164]), by which one can quantify the errors due to the QSA for a specific gravitational model. More details about the implementation for the models considered in this chapter are contained in [46, 165, 260]. The results obtained using different MG N-body codes agree to the level of a few percent for the HMF [260], so this is not a sufficiently large error to be concerned with in our study.

We utilised two different halo finders of differing complexity:

1. The friend-of-friend halo-finder `MatchMaker`[1] with linking-length $b = 0.2$.

2. The 6D phase-space friend-of-friend halo-finder `RockStar` [32].

[1]MatchMaker can be found at https://github.com/damonge/MatchMaker

First we describe the Friends-of-Friends (FoF) algorithm developed in [79], since this is an essential part of both halo finders. Particles are formed into connected graphs by drawing an edge between vertex particles if the distance between them is less than some fraction b of the mean inter-particle distance. This is usually taken to be the cube root of the mean inter-particle volume [32]. Each connected graph is defined to be a halo if it is not a subgraph of a larger halo. Decreasing b leads to more tightly-clumped haloes, whereas increasing it links more diffuse particles, leading to more irregular structures. FoF does not account for the time evolution of the haloes.

The `MatchMaker` finder is a parallel 3d-FoF finder. We used the canonical linking length $b = 0.2$. The simulation volume is separated into nodes, each of which has a buffer in the adjacent node. The distance between particles is the usual 3d Euclidean distance:

$$d(\text{particle}_1, \text{particle}_2) = \sqrt{(\mathsf{x}_1 - \mathsf{x}_2)^2} \tag{5.3}$$

Particles can be "friends" with any particle within its own node, and if necessary, within the buffer. In this way the FoF graphs are built within each parallelised cube and then spanning adjacent cubes.

The `RockStar` finder uses a four-stage process. First it uses the normal FoF in 3d Euclidean space (albeit with a longer than usual linking length $b = 0.28$) to identify groups of particles. The remainder of the algorithm is run on each cluster of particles in parallel. Within each group it identifies subgroups by using FoF in the 6d phase space whereby the "distance" between two particles is:

$$d(\text{particle}_1, \text{particle}_2) = \sqrt{\frac{(\mathsf{x}_1 - \mathsf{x}_2)^2}{\sigma_x^2} + \frac{(\mathsf{v}_1 - \mathsf{v}_2)^2}{\sigma_v^2}} \tag{5.4}$$

depending upon their positions x, velocities v and the respective dispersions σ_x, σ_v for each subgroup. These subgroups are converted into subhaloes by forming a seed halo at the most dense subgroups. Successively less dense subgroups have their particles assigned to a halo according to another distance measure:

$$d(\text{halo}_1, \text{particle}_2) = \sqrt{\frac{(\mathsf{x}_1 - \mathsf{x}_2)^2}{r_{\text{vir}}^2} + \frac{(\mathsf{v}_1 - \mathsf{v}_2)^2}{\sigma_v^2}} \tag{5.5}$$

This is similar to the particle-particle distance, with the position dispersion replaced by the virial radius of the halo r_{vir}. In this way, subhaloes are built into parent haloes using the various levels of the 6d-FoF hierarchy. Finally any unbinding of particles from haloes is performed using the halo potentials. (This algorithm is summarised in Figure 1 of [32].)

Subsequently halo properties are extracted. The halo property with which we are

concerned in this chapter is the halo mass of the parent haloes only (i.e. we ignore subhaloes because we are only interested in the largest mass ranges). This is defined to be M_{200}, the total mass of all particles within the overdensity satisfying $\rho \geq 200\rho_{\rm crit}$, where $\rho_{\rm crit}$ is the background critical density (not the matter density) [32].

A comparative analysis of halo finder performance in ΛCDM can be found in [140].

5.2.2 Simulation corrections

Having obtained our halo catalogues we now approximate the continuous HMF using a histogram.

We do not make any corrections to the data. Some authors propose adjusting the values of $\sigma(M)$ in the simulation data. The aim is to correct for the finite box size, which precludes modes with $k \leq 2\pi/L_{\rm box}$ from contributing to the overdensity fluctuations in the halo. This effect can be approximated by the extended Press-Schechter approach (amongst other methods: see [173] for details). We avoid corrections for the mass variance due to our large box size, for which corrections are negligible.

It is necessary to remove simulation artefacts from the low-mass end. We truncate the mass function at a lower bound of 100 particles, where one particle is the mass resolution of the N-body simulations. (This is independent of the minimum number of particles required in the halo identification process.) Compared to the cuts of [173] this is a conservative cut: faced by a relatively small box size, we wish to retain as much of the HMF as possible. However, the cut is sufficient to remove the low-mass "tail" where the mass function—which should be monotonically-decreasing with mass—actually increases with mass. Such a phenomenon arises from the finite (mass) resolution of the simulations. At the lowest masses, there is insufficient resolution to identify all of the bound objects with few particles, so the number density is increasingly suppressed at masses below a characteristic turnover mass. This limitation cannot be alleviated without sub-sampling the simulation box at finer resolution. Slightly higher, at haloes with tens of particles, the uncertainty on the mass values is a significant fraction of the total halo mass. Consequently, the loss or addition of one particle can move the halo between bins. There are two possible ways of accounting for this: either incorporating a mass uncertainty in the likelihood function, or minimising the effect by judicious bin optimisation. We opt for the latter. This low-mass effect is well-known and we do not discuss it further.

At the high mass end our cutoff is artificially imposed by the finite box size. The finite box size curtails the number of large mass haloes found in a finite sub-volume of the horizon (this underestimation is quantified for ΛCDM in [183]). In addition, our

excursion set technique prevents us from calculating the HMF for masses of $S < S_{\rm env}$ (for the excursion-set method) or $\nu_{\rm eff} < 0$ (for the cosmic web). Using a Gaussian window function with a radius of $10\,{\rm Mpc}/h$ this corresponds to a mass of $M \approx 10^{16} M_\odot$. We have confirmed that this does not remove any haloes from our data.

The remaining factor in our simulated HMF is the bin width of the histogram. The aim is to verify that the seemingly arbitrary bin choice (which varies in every HMF chapter) has minimal effect on the calibration of the free parameters. We adopted three constant-width bin methods, explained in the next paragraphs.

The constant bin width method is that most widely adopted in the literature. The haloes are typically binned in constant intervals of $\log_{10} M$ [59], or $\ln \sigma^{-1}$ [125], rather than $\ln \nu$, so the same $f(\nu)$ will produce a different (discrete) HMF in different MG theories. We adopt $\ln M$ to ensure a ready comparison between different gravity theories. A non-arbitrary method for selecting the bin width is to decide upon the maximum Poisson error tolerated and find the bin width ensuring this error in the most massive bin. (Lower-mass bins will have more haloes, hence less Poisson error.) However this produces an impractically small number of bins, of order the number of free parameters $(3-6)$ in the fitting functions. The advice of [251] is to leave the most massive bin variable and set a constant width for the other bins. While this method has the advantage of being directed by the simulation data, rather than arbitrarily selected, it produces relatively few bins. Instead, we applied $N = 10$ and $N = 100$ bins in order to approximate a choice of too few or too many bins. The former has difficulty accurately representing the steep gradient at the high-mass end, whereas the latter has such narrow bins that monotonic behaviour of the HMF is not observed, or even punctuated by zero-occupancy bins. This illustrates two possible dangers of arbitrarily selecting a number of bins.

In order for the bin width to be driven by the data, one can use Bayesian analysis to find an optimal number of bins. There exist a number of ways to find a "best" number of bins from a distribution by minimising the L_2 norm between the data and the underlying (unknown) smooth density function [105, 222, 250]. However, it is possible to minimise the required assumptions using the method of [142], which computes the likelihood that the binned data is drawn from the smooth distribution. The bin width, i.e. amount of discretisation, which maximises this likelihood value is judged to be optimal. The downside of this method is the computational expense of the MCMC calculations required (to ensure that the uncertainty in the posterior mean is much less than half, i.e. we are certain to within a unit of one bin). However, for a one-dimensional histogram computed using ~ 50000 haloes, we found that this required ~ 1 minute per simulation. The results differ according to the gravity model used and the halo finder (as expected, for each has a different HMF). Since we did not wish to

introduce another free parameter, we adopted a value of $N = 30$ bins as an average value across all our data sets.

5.2.3 Uncertainty in the data

Finally we quantify the uncertainty in the HMF.

The uncertainty in the bin occupation is assumed to be Poissonian. The usual uncertainty on bin occupations is taken to be the well-known result[2] that the Poisson standard deviation on a bin containing N haloes is $\sigma = \sqrt{N}$. Various HMF papers (e.g. [173]) use an "improved" Poisson error defined by [113]:

$$\sigma_{\pm} = \sqrt{N + \frac{1}{4}} \pm \frac{1}{2} \tag{5.6}$$

This asymmetric error asymptotes to the usual one for large N but is better-behaved for small N, particularly for empty bins. Fig. 5.1 compares the two methods. While this does not affect the Poisson-based likelihood, it does enter the Gaussian-based likelihood. The reason is straightforward: the number of counts per bin is known precisely, so there is no uncertainty. The Poisson "noise" expresses the uncertainty in the mean of the underlying Poisson probability density function, which is equal to the variance term which does enter into the Gaussian probability density function [238]. Since the error does not enter the likelihood function, we make no cuts when using constant-width bins (explained below). For variable-width bins, we tolerate an error of 10% or less, which is in line with the choice from other papers (e.g. [75]). We must pay attention to combining the asymmetric errors via the method of [19]. The combined variance is:

$$V(x \,|\, \hat{x}) = V_0 + V_1(x - \hat{x}) \quad \text{where} \quad V_0 = \sigma_+\sigma_- \quad \text{and} \quad V_1 = \sigma_+ + \sigma_- \tag{5.7}$$

This method tightens the uncertainty on the low-occupation bins, weighting the likelihood more favourably towards the high-mass end than with symmetric errors.

[2] Eq. (11) in [75] is not true, but is related to the standard deviation as a **fraction** of bin occupation: $\sigma/N = 1/\sqrt{N} \implies \sigma = 1/N$.

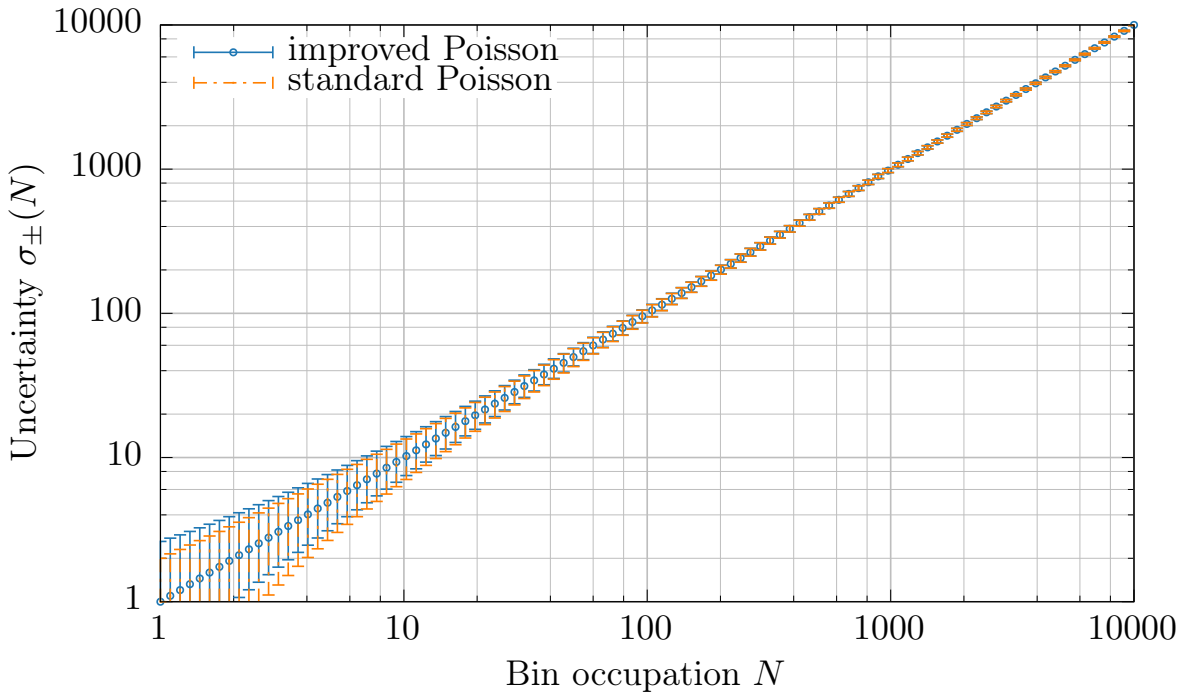

Figure 5.1: Uncertainty due to discretisation of the underlying Poisson distribution, showing the upper and lower error bounds (y-axis) for N haloes per bin (x-axis). Lines are for the standard Poisson errors (solid) and the improved ones (dashed).

5.3 Bayesian inference

The problems of both estimating the best-fit parameters in our fitting function and comparing between functions can be achieved simultaneously using Bayesian inference. First, we outline calculation of the posterior from the data using Bayes theorem. Then we explain the problem of finding the maximum-likelihood values in the parameter space of each model. Next, we use this result to evaluate the relative likelihood of one model compared to another. Finally, we describe the algorithm calibration used in this chapter to ensure accurate posteriors.

5.3.1 Priors

The priors I contain both our assumptions about the likelihood function and our prior distribution for the parameters of the hypothesis. We discuss the former in the next paragraph. The latter we set to uniform priors, i.e. we have no reason to favour any regions of parameter space over another. The lower limit for the priors is zero, because we must avoid an HMF which is negative (if the scaling parameter is $A < 0$), complex (fractional powers of $a\nu$ where $a < 0$), or non–monotonically-decreasing (since ν is an increasing function of mass, ν^p must have $p > 0$). The upper limit is arbitrary. Given that most published values for the parameters lie in $[0, 2]$ (the exception being

Jenkins $a = 3.8$), we used an upper limit of 10 to ensure that the credible regions were well-contained within the prior region.

5.3.2 Choice of likelihood

Our aim is to find the posterior probability distribution $p\,(H \mid D, I)$ for a given hypothesis H when we take into account our prior information I and the data D. In our case, H is either a set of values for the free parameters in our fitting function, or a choice of fitting function overall. We have already examined D, the counts per mass bin from our simulation data in Section 5.2.2.

The choice of likelihood function largely reflects one's probabalistic education. The two schools of thought are typically a Gaussian likelihood based upon the frequentist chi-squared estimator and a Poissonian likelihood based upon maximum-entropy results from Bayes theorem. We characterised the available likelihood functions by testing the results for a known set of parameters. The result which gives the tightest credible regions around the input parameter is the function we used on the runs with simulation data. We choose between:

1. The Poisson likelihood (the last term is zero when n_i is zero):

$$\ln \mathcal{L} = -\sum_i \left(\mu_i - n_i + n_i \ln \frac{n_i}{\mu_i} \right) \tag{5.8}$$

2. The Gaussian likelihood with symmetric errors

$$\ln \mathcal{L} = -\frac{1}{2} \sum_i \left[2\pi V_0 + \frac{(\mu_i - n_i)^2}{V_0} \right] \tag{5.9}$$

3. The Gaussian likelihood with asymmetric errors

$$\ln \mathcal{L} = -\frac{1}{2} \sum_i \left[2\pi \left(V_0 + V_1(\mu_i - n_i) \right) + \frac{(\mu_i - n_i)^2}{V_0 + V_1(\mu_i - n_i)} \right] \tag{5.10}$$

where $\mu_i(\mathbf{q})$ is the number of counts (first-crossing distribution) given by the parameter set $\mathbf{q}$ and n_i is that given by the data in the i-th bin and the choice between counts and first-crossing distribution is determined by the use of the Poisson and Gaussian likelihood respectively. When applied to counts, n is always a positive integer, whereas μ is a positive real number. Bayesian inference implies that Eq. (5.8) will produce the most accurate result, whereas the standard frequentist approach is equivalent to Eq. (5.9). The last approach Eq. (5.10) is no longer equivalent to the frequentist

approach because the errors are asymmetric. We compare the results of Eq. (5.8) and Eq. (5.10) in Section 5.4.1.

The likelihood $\mathcal{L}(H)$ is the probability that the hypothesis H produces the data D. However, we are interested in the probability that the data are consistent with the hypothesis. The complete posterior PDF for our hypothesis H in light of the data D given prior information I is given by:

$$p\left(H \mid D, I\right) = \frac{p\left(H \mid I\right) p\left(D \mid H, I\right)}{p\left(D \mid I\right)} \tag{5.11}$$

For our purposes H is either a choice of parameter values for a given HMF (in which case I includes a choice of fitting function) or a choice of fitting function (in which case I represents our priors alone). We discuss these two cases in more detail in the next two (sub-)sections.

5.3.3 Parameter estimation

Having chosen a particular HMF, we are interested in the universality of the HMF across different MG theories. One way in which to measure this is to see how the best-fit parameter values change depending on the MG model. `MultiNest` gives three different options to define "best-fit": the maximum-likelihood (ML), maximum-a-posteriori (MAP) and posterior mean (PM) values.

The ML value for a given parameter θ is defined to be that which maximises $p\left(D \mid \theta, I\right)$, i.e. the most probable value for the model to give the observed data. In contrast the MAP value maximises the probability $p\left(\theta \mid D, I\right)$. Since we have chosen uniform priors, the MAP value is equal to the ML value via Eq. (5.11). Since the ML value is the fastest to converge to the true value in MultiNest [101], we used this value for our best-fit parameters. We are also interested in the PM value

$$\langle\theta\rangle = \int \mathrm{d}\,\bar{\theta}\; p\left(\bar{\theta} \,\middle|\, D, I\right) \bar{\theta} \tag{5.12}$$

because the 1σ credible regions given by MultiNest are only provided for the posterior mean.

If the full PDF is not well-described by a single value (e.g. the three values above are very different, or the posterior is very flat *etc.*), then we are better off examining the credible region R of credibility C, which is the set:

$$R = \left\{ \boldsymbol{\theta} : \int_{p\left(\bar{\boldsymbol{\theta}} \,\middle|\, D, I\right) > c} d\bar{\boldsymbol{\theta}}\; p\left(\bar{\boldsymbol{\theta}} \,\middle|\, D, I\right) = C \right\} \tag{5.13}$$

where c is the level set forming the boundary ∂R, inside which the probability is greater than c and outside which it is less than c. We refer to the 1σ and 2σ credible regions for $C = 0.68$ and $C = 0.95$ respectively. This is particularly the case in multiple dimensions, e.g. examining correlations between variables. We show our results in Section 5.4.2 assuming the ΛCDM case for all our halo data and in Section 5.4.3 matching the excursion set model to the MG model for each dataset.

5.3.4 Nested sampling calibration

We used the `MultiNest` nested sampling algorithm of [101] to carry out the integrals in the previous subsections. This section describes the calibration process we used to tune the algorithm.

The simulated data in this section was made by generating an HMF with the "default" parameter values for each fitting function,i.e. the values in the original publication. The Poisson error was simulated by scattering each data point by a value in $[-\sqrt{N}\,,\sqrt{N}]$, where N is the number of haloes per bin. The sign of the scatter was selected from a uniform distribution $[-1, 1]$ by rounding away from zero, whereas the magnitude was chosen from a normal distribution in $[0\,,\sqrt{N}]$. We used both 30 and 100 data points, equivalent to binning our halo data into 30 and 100 equal-ln M bins. Recall that the former was the number of bins suggested by the optimisation in Section 5.2.3. We derived the latter by increasing the number of bins by 10 until the maximum-likelihood values returned from `MultiNest` were within 10% fractional error of the default parameters from all our HMF functions using the Poissonian likelihood. The `MultiNest` parameters were selected until both the "Poisson" and "Gaussian" likelihoods returned credible regions which included the original parameter. These regions were calculated automatically by `MultiNest` for the posterior PDF marginalised over all other parameters. We verified these results by comparing with the graphical output from `GetDist`.

The key settings are tabulated in Table 5.1. Importance Nested Sampling was turned off to increase the speed of convergence, which did not impact appreciably on the posteriors. Searching for multi-modal posteriors was switched on to verify that no spurious modes were identified in addition to the correct, single mode. The number of live points controls the density of sampling within the ellipses: too few, and the evidence is incorrectly approximated; too many, and the algorithm cannot discard and re-sample points effectively. Ideally, one would required this to scale with the dimensionality of the parameter space. However, for the sake of efficiency, we capped the number of live points at 10 000. (This was particularly important for the Reed-07 run.) The tolerance determines the maximum contribution to the total evidence from the unsampled points: this was set unusually stringently, in order to ensure smooth posteriors

and profile likelihoods. The calibration process ensured that our MCMC code produced reliable results for the likelihood functions and parameter spaces which were particular to this problem.

We show the results of our calibration in Section 5.4.1. This examines the effect of the number of bins, the likelihood function and the number of live points.

Description	Values tested	Final value
Importance Nested Sampling	True, False	True
Identify multi-modal posteriors	True, False	False
Number of live points	100 200 500 1000	500
Tolerance factor	1d-4, 5d-4, 5d-3, 5d-2, 5d-1	1d-4
Sampling efficiency	3d-1, 5d-1, 8d-1, 1, 2	8d-1

Table 5.1: Calibration parameters used to tune `MultiNest`. The same values were used for both likelihood functions.

5.4 Results and discussion

This section addresses the questions posed in the introduction. Section 5.4.1 confirms that our parameter estimation technique is reliable for the problem at hand. Then in Section 5.4.2 we discuss whether the presence of screened gravity can be mistaken for a change in best-fit parameter values for the ΛCDM HMF. In Section 5.4.3 we apply the procedure used in ΛCDM to calibrate the MG HMF using the full excursion set approach. We compare to existing values from the literature and assess the deviation. In particular we address the universality of the halo mass function,i.e. the invariance of the best fit free parameters to changes in the underlying gravity model.

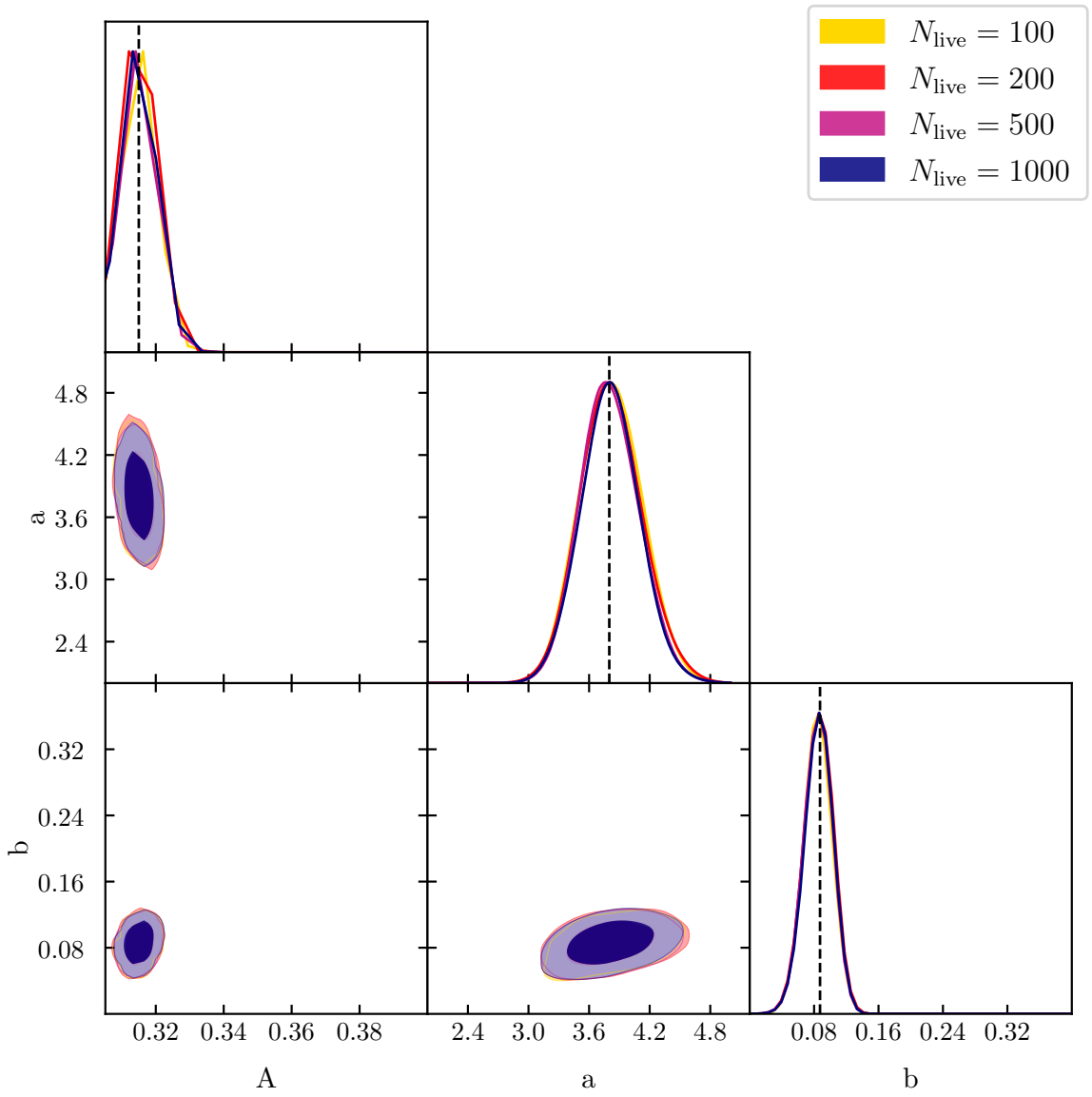

Figure 5.2: Posteriors for the Jenkins HMF using different numbers of live points (coloured). The main diagonal shows the 1-d posteriors marginalised over all other parameters, while the off-diagonal plots show correlations between pairs of parameters via the 2-d $1, 2\sigma$ credible regions. The black dashed lines show the input values, while the coloured lines show the PDF of the values recovered by nested sampling, with 30 bins, assuming a Poissonian likelihood.

5.4.1 Calibration of MultiNest

This section analyses the effect of the bin width, the number of live points and the choice of likelihood function on simulated data. We discussed the simulated data in Section 5.3.3. The calibration process tuned `MultiNest` to ensure that (known) input parameters were recovered within 1σ credible regions of the posterior "best-fit" values.

Having calibrated `MultiNest` as described in Section 5.3.4, the algorithm was used to recover (as best as possible) the input parameter values. The properties which we varied

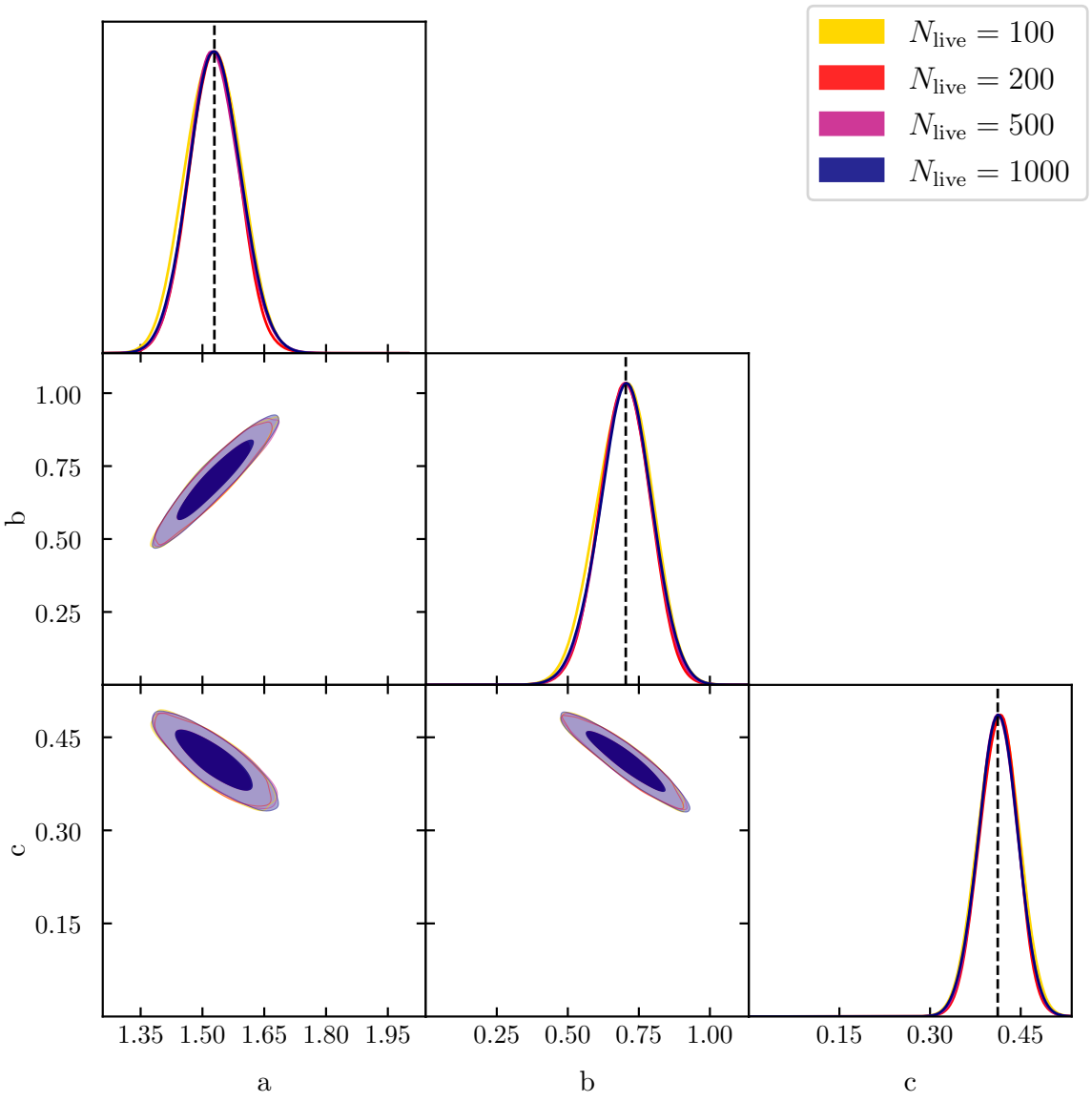

Figure 5.3: Posteriors for the Peacock HMF using different numbers of live points (coloured). The main diagonal shows the 1-d posteriors marginalised over all other parameters, while the off-diagonal plots show correlations between pairs of parameters via the 2-d $1, 2\sigma$ credible regions. The black dashed lines show the input values, while the coloured lines show the PDF of the values recovered by nested sampling, with 30 bins, assuming a Poissonian likelihood.

were:

1. The likelihood function: Gaussian or Poissonian
2. The number of bins: 10, 30 or 100 (equivalently, the bin width)
3. The number of live points

Figs. 5.2 to 5.6 show—for a given HMF—the posteriors produced by the two likelihood functions. The number of live points is indicated by the colour of the credible regions. Where a colour does not appear, `GetDist` did not find that the chains had converged sufficiently to produce unimodal credible regions. In those cases, we confirmed that

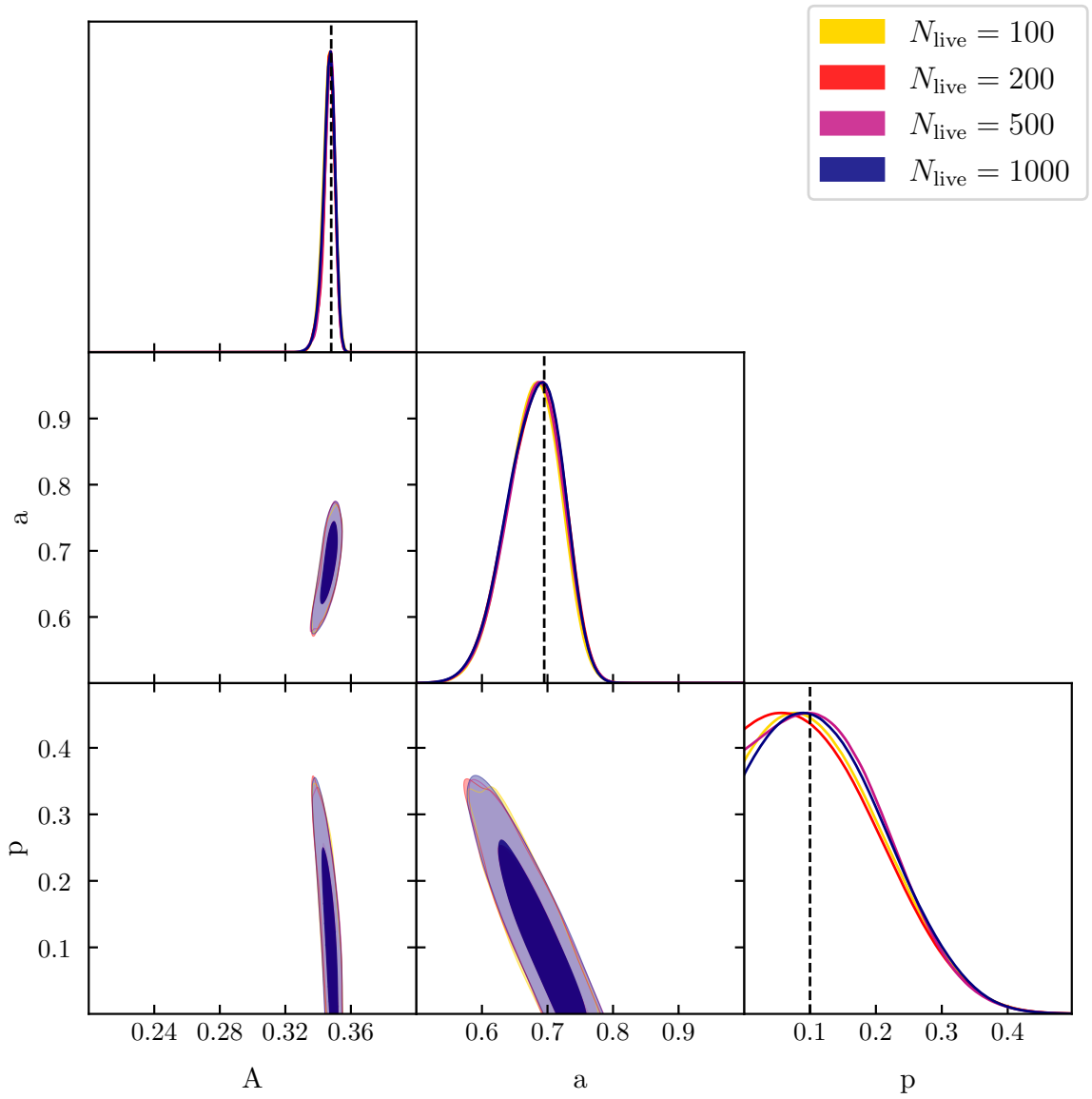

Figure 5.4: Posteriors for the SMT-Courtin HMF using different numbers of live points (coloured). The main diagonal shows the 1-d posteriors marginalised over all other parameters, while the off-diagonal plots show correlations between pairs of parameters via the 2-d $1, 2\sigma$ credible regions. The black dashed lines show the input values, while the coloured lines show the PDF of the values recovered by nested sampling, with 30 bins, assuming a Poissonian likelihood.

the maximum-a-posteriori, maximum-likelihood and input values were all within the 1σ error on the posterior mean directly with the `MultiNest` output. The dashed black line shows the value of the parameter at input.

The choice of likelihood function has a common behaviour across all of the HMFs. The Gaussian data is not shown here. This is because we found that the Gaussian likelihood produces far larger credible regions than the Poissonian one. The posteriors are broad rather than peaked—in fact the 1σ regions occupy most of the parameter space. Expanding the prior volume did not affect this result, which indicates that the

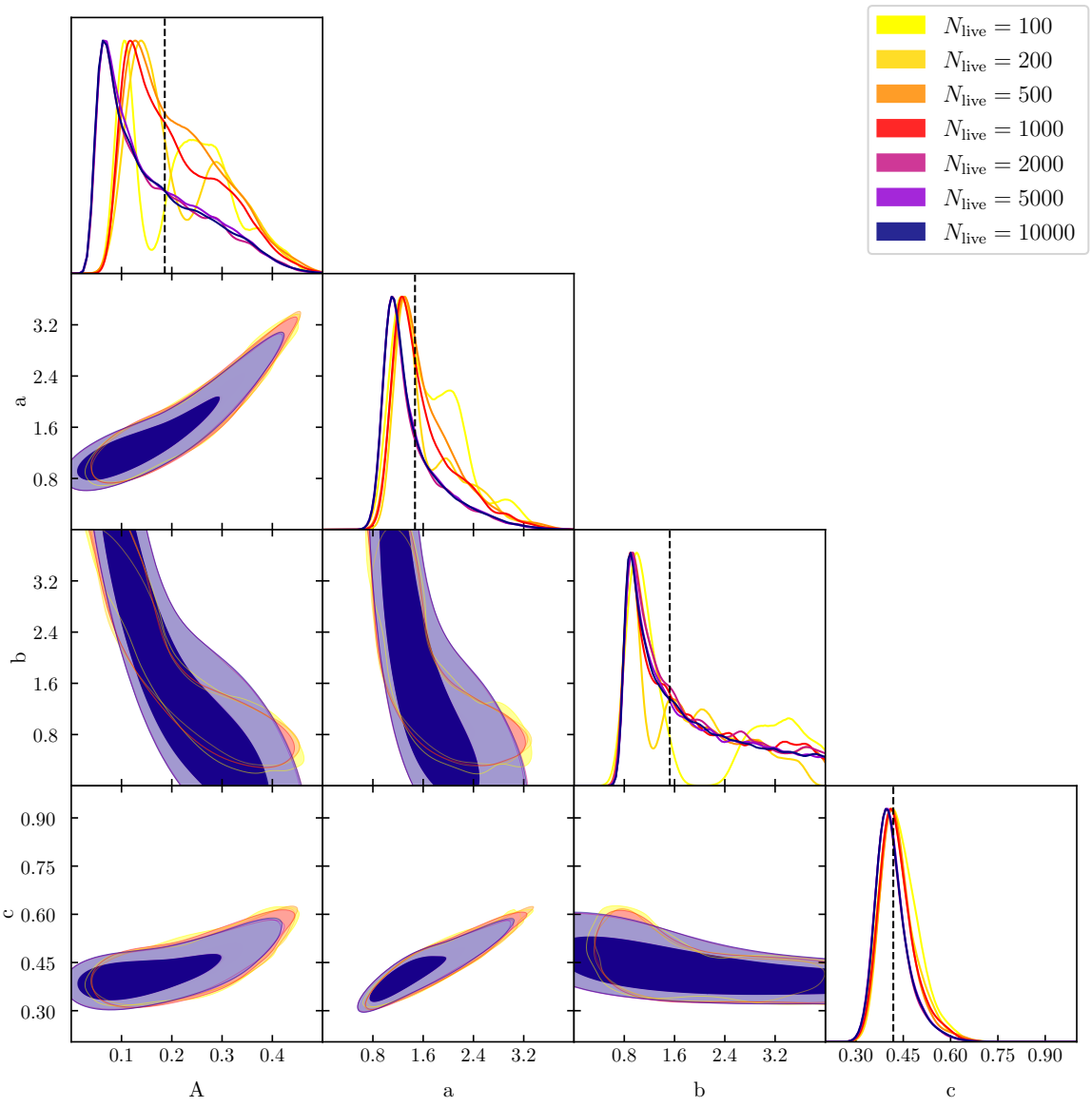

Figure 5.5: Posteriors for the Tinker-Angulo-Watson HMF using different numbers of live points (coloured). The main diagonal shows the 1-d posteriors marginalised over all other parameters, while the off-diagonal plots show correlations between pairs of parameters via the 2-d $1, 2\sigma$ credible regions. The black dashed lines show the input values, while the coloured lines show the PDF of the values recovered by nested sampling, with 30 bins, assuming a Poissonian likelihood.

posteriors are prior driven rather than constrained by the data. The credible regions do not shrink appreciably when the number of live points is dramatically increased (from 10^1 to 10^4), so this is a consequence of the likelihood rather than the algorithm used to calculate it. Moreover, this is not a consequence of the scatter in the data, because the Poisson likelihood *does* produce narrow, peaked posteriors with the same data. The remaining factor is the poor performance of this likelihood function. Consider that the standard deviation is equal to the Poisson error. Substituting into the likelihood, we

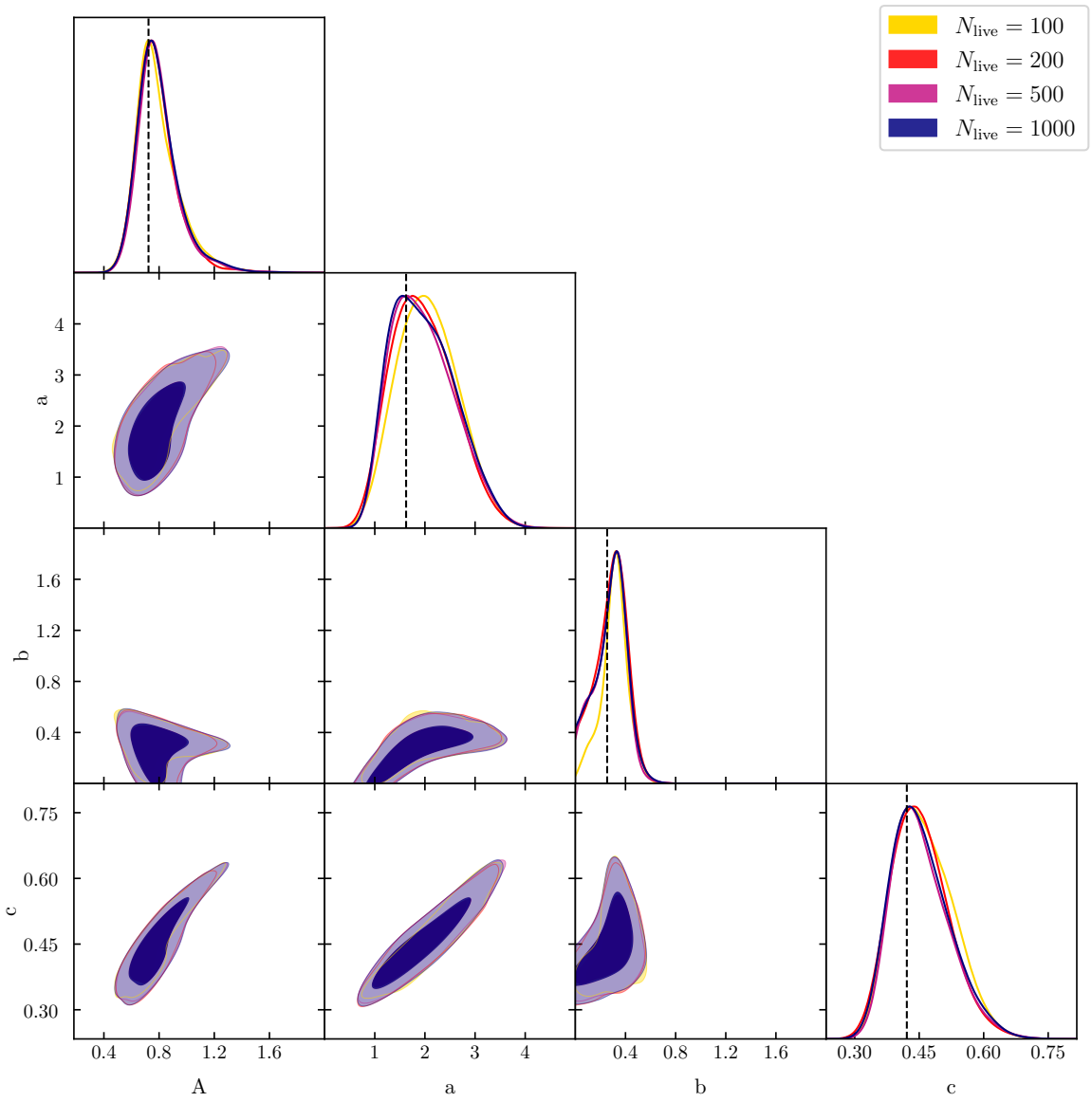

Figure 5.6: Posteriors for the Warren-Crocce HMF using different numbers of live points (coloured). The main diagonal shows the 1-d posteriors marginalised over all other parameters, while the off-diagonal plots show correlations between pairs of parameters via the 2-d $1, 2\sigma$ credible regions. The black dashed lines show the input values, while the coloured lines show the PDF of the values recovered by nested sampling, with 30 bins, assuming a Poissonian likelihood.

have:

$$\ln \mathcal{L} = -\frac{1}{2} \sum_i \left\{ 2\pi N_i + \left(1 - \frac{\mu_i}{N_i} \right)^2 \right\} \tag{5.14}$$

The first term $\sum_i N_i$, which does not depend upon the model, dominates regardless of the value of μ_i in the second term. [119] suggest dropping the first term and only using the exponential, but we found that this also saturated the prior volume. Thus there must be additional problems with this likelihood. Low-mass bins with more counts are weighted by the first term to decrease the likelihood more than high-mass bins with few counts. (In fact when $N_i = 0$ the first term is a maximum.) However, these are

the very bins where the fraction in the second term is small, so this term approaches a maximum. At the low mass end, the bin occupation has tighter uncertainties, but this is the region where all the fitting functions converge to similar values regardless of the choice of free parameters (except perhaps for the scaling factor A). At the high mass end the low-occupation bins cannot provide strong constraints on the parameter values because $\sqrt{N} \to N$ as the bin occupation drops to zero. We can test our assumptions about bin occupation by comparing the 100-bin data with the 30-bin data for a given HMF. We find that these trends are independent of the bin width used. Thus it is the Gaussian shape of the likelihood which prevents us from obtaining narrow credible regions. For this reason, we discard the Gaussian likelihood when using real data. It is difficult for this function to have a sharp peak in the parameter volume because it penalises the most certain bins. The only way to utilise the Gaussian likelihood is to replace the Poisson errors with much smaller ones. For example, [34] run multiple N-body simulations and use jack-knife errors which are much smaller. However, it is impractical to replicate this in the synthesised data. Therefore we do not apply the Gaussian likelihood to our halo data. This illustrates the importance of correctly selecting a likelihood function using maximum entropy principles (i.e. based upon the underlying distribution in the data).

The number of bins is a compromise between the amount of information provided by the data and the scatter in this information. Thinner bins produce more data points with which to constrain the parameter values, so we expect smaller credible regions with 100 than with 30 bins. However, the finite number of haloes in the simulation limit the number of samples drawn from the continuous (underlying) distribution (which would be obtained with an infinite number of haloes as the bin width approached zero). Therefore—particularly at the high-mass end with few haloes—bins may be insufficiently wide to preserve the monotonicity of the HMF, or may be empty altogether. This does not only widen the posteriors, but may also shift the peaks, if the low-mass end does not provide sufficient constraints where the scatter is minimal. In our simulated "data," we have maximised the scatter (to within Poisson errors) to produce a pessimistic scenario. The performance of each HMF is similar, so we only show the Peacock HMF in Fig. 5.7. We find that this produces little to no effect on the location or width of the 1σ credible regions. This behaviour is largely independent of the number of live points as well.

The number of live points is of interest as we need to find a compromise between efficiency and accuracy. The higher the dimensionality of the parameter space, the more live points are typically required to constrain the posterior. However, we find that once the number is increased beyond 10^2, there is usually little difference between the 100, 200, 500 and 1000 posteriors. (`MultiNest` advises using fewer than 1000 live points when the Importance Nested Sampling mode is used, due to memory constraints.)

The credible regions all largely overlap, independent of the number of live points. The marginalised posteriors usually overlap as well (e.g. all parameters in Figs. 5.2 and 5.3; $\{A, a\}$ in Fig. 5.4; $\{A, b, c\}$ in Fig. 5.6). In some cases (p in Fig. 5.4; a in Fig. 5.6) the peaks of the posteriors move further from or closer to the original value. This does not affect the result that in all cases the input parameters lie within the 1-σ credible regions. This illustrates the need to find a minimum number of live points for which the results converge and ensuring that adding more live points does not move the ML and MAP estimates outside the existing credible regions. This demonstrates that our estimates of the posteriors have already converged to an accurate representation of the likelihood with only $\sim 10^2$ live points.

Finally we examine the effect of the number of free parameters. The HMFs with three free parameters—Jenkins, Peacock and SMT-Courtin—can all be reasonably constrained by the available data. Of the two four-parameter fits, Warren-Crocce also recovers the required values whereas Tinker-Angulo-Watson does not produce such an accurate result. Although `MultiNest` did find the ML values to within a few percent of the input values, the posteriors created by `GetDist` showed a broad tail in its credible regions for $\{A, a, b\}$, while c was fine. Although the chains do converge as we increase the number of live points, they converge to the wrong values when examining the peaks in the posterior (as processed by `GetDist`). The nested sampling ellipses exclude the ML value at some point during the sampling, from which point onwards the sample can only be drawn from within the likelihood iso-surface created by the ellipses. (This is hardly surprising given that $A(b\nu)^a$ is automatically degenerate. Such behaviour was also seen in [54].) The Reed 2007 fit has six parameters. In this case the Poissonian likelihood cannot identify the original parameter values used to create the data. Many pairs of parameters in this fitting function are degenerate (Table 4.1). This may be a failure of the data as well: counts must be rounded to an integer value (to correspond with the behaviour in our N-body derived data) and, once scattered, could be negative. Rounding the counts mapped a small portion of the parameter space (used for calculating the first-crossing distribution) to the same counts. The two factors which affect this conversion are the box size and the bin width (larger boxes create more haloes; wider bins include more haloes). The behaviour of the fit agrees with statements in [206, 207] that some of their parameters can only be constrained by masses $M \geq 10^{15} M_{\odot}$, of which we have very few in the halo data. The nested sampling algorithm is not infallible. For this reason, we exclude the Reed and Tinker-Angulo-Watson fits from our halo results in the next two sections.

Having explored the effects of the likelihood function, the number of bins and the number of live points, we have found that the optimal choices are the Poissonian likelihood function with at least 100 live points and that the number of bins is irrelevant. Thus we set 30 bins and 500 live points for our data proper in the next two sections. We

also exclude the Tinker-Angulo-Watson and Reed-07 fits on the basis that we have insufficient data to properly constrain their free parameters.

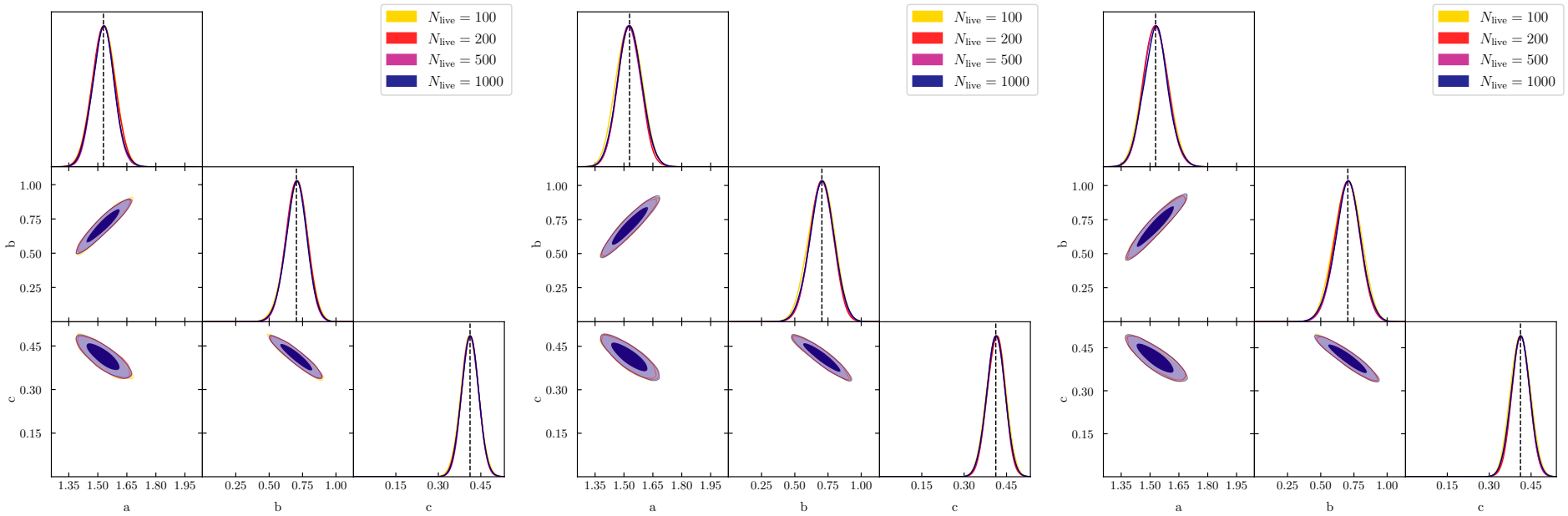

(a) 10 bins (b) 30 bins (c) 100 bins

Figure 5.7: The effect of changing bin width on the Peacock HMF. The triangle plot is the same as Fig. 5.3. The subfigure captions show the number of bins used in calculating the input HMF and discretising the model HMFs proposed by the nested sampling routine.

5.4.2 Assuming concordance cosmology

The first problem is perhaps so obvious as to be invisible: if we do not set out to look for modified gravity, we may be unable to detect it. In other words, having assumed a ΛCDM cosmology *a priori*, does modified gravity present itself *a posteriori* as merely a different (i.e., non-standard) set of best-fit parameters in a ΛCDM halo mass function? In this subsection, we fit the N-body HMFs for each modified gravity model using the ΛCDM mass functions. We used 10^2 and 10^3 live points to ensure that our results had converged, i.e. that our estimate of the posteriors PDFs was accurate. We also examined the effects of both the `MatchMaker` and `RockStar` halo finders, which we expect to differ due to their varying criteria for finding bound objects, which translates into a different halo mass function.

First we define appropriate criteria for a fitting function to produce a well-behaved fit to the data. We define a fit to be "successful" if the credible regions are continuous, smooth and peaked, tending to zero well within the prior parameter range. We do not exclude a fit form being well-behaved if zero is within its 1σ credible region: instead we examine the proximity of the maximum-a-posteriori value, excluding the fit if the probability at zero is close to that of the MAP. (A more quantitative option would be to exclude a fit if zero lies within the full-width-half-maximum of the Gaussian posterior, but we cannot guarantee that our posteriors are Gaussian.) The upper limit is set by the priors, so our main criterion is the breadth of the posterior. If it does not have a clear peak (or peaks), but a flat posterior, then there is too much uncertainty for the fit to be useful: it is not constrained by the data.

The majority of the mass functions are well-behaved for all MG models and both halo finders: Peacock (Fig. 5.9), Jenkins (Fig. 5.8). Initially, SMT-Courtin (Fig. 5.10) appears to not be successful because both halo finders and all MG models have a peak as p approaches zero. However, this lower bound is set by the physical requirement for the parameters to be positive, rather than an indication that we have not explored enough of the parameter space. Moreover, considering that the prior volume of p is in $[0, 10]$, the motion of the maximum-likelihood from 0.1 (Courtin *et al.*'s original value) to 0.0 is only a 1% shift relative to the size of the parameter space. The Warren-Crocce fitting function exhibits slightly different behaviour in Fig. 5.11 for b. Using the `MatchMaker` finder, only LCDM, DGP1 and F5 peak clearly away from $b \approx 0$; whereas using `RockStar` only SymB peaks at $b \approx 0$. The same logic applies as with SMT-Courtin, except that we can be more reassured here because the majority of MG models produce a ML value at the published value (the black dashed line). However, the posteriors are broader and more complicated in shape than the simple peaks for the other HMFs. This is probably due to the corrections made to the mass of each halo when Warren *et al.* derived the function: a halo of N particles was corrected to

$N(1 - N^{-0.6})$, producing a non-linear correction to the resulting $n(M)$. In this way we have found that all of our fitting functions can exhibit a degeneracy between a change in cosmology and a change in the underlying gravity theory.

We can now determine whether some HMFs are more sensitive to the underlying theory of gravity than others. A halo mass function whose parameters have credible regions highly insensitive to the gravity model which generated the N-body halo data is one in which we are unlikely to detect deviations from general relativity inadvertently. Conversely, should the values of (or degeneracies between) parameters change sufficiently between N-body simulation "data", then we have an HMF in which deviations from ΛCDM values may reliably indicate the underlying deviation from an ΛCDM cosmology. Our results lie somewhere between these extremes: we can use a subset of the free parameters to distinguish between different classes of models, but cannot really test the parameters in the MG models themselves.

For example, Jenkins shows a high degree of overlap between all the MG models for a and b, so we must rely on A. Certain MG theories are clearly distinct (F5, SymA and SymB) whereas DGP and LCDM are nearly indistinguishable and F6 has some overlap with the two symmetron models. Thus we can clearly identify whether a result is in one of the DGP-LCDM or Sym-FR "families"but not confidently be more specific.

Similarly, the Peacock model is nearly indistinguishable for b and c, despite showing a broad spread of best-fit values along the parameter space for the remaining parameter A. This spread is slightly different depending upon the halo finder: for `RockStar` the overlap within each of the three "sets" of theories is nearly total, whereas for `MatchMaker` the overlap is less extreme.

The situation is even more problematic for the SMT-Courtin fit, where not only does a have significant overlap, but p peaks to the same value for all MG models. Once again for A we may reasonably expect to separate the DGP and LCDM models (themselves inseparable) from the F5 model, and this from the F6 and Symmetron ones.

The Warren-Crocce model with `MatchMaker` has only three well-behaved MG results, so we can use A to readily distinguish between DGP1, F5 and SymB. Conversely, the `RockStar` result has too much overlap to determine the underlying MG model.

Therefore we find that is it possible for MG to be mis-interpreted as a ΛCDM result for most of the fitting functions, bar Tinker-Angulo-Watson. However, we cannot distinguish between the underlying mechanisms for the deviation from ΛCDM, despite our ability to distinguish these posteriors from the ΛCDM case. The same trends occur: the separation of LCDM and the two DGP models into one group and the $f(\mathcal{R})$ and Symmetron ones into one or more others.

However, we cannot readily use this to test for varying theories of MG because the fitting functions display considerable similarities in their credible regions, so we are forced to rely on one or two parameters where the variation is distinctive. Nonetheless, it is remarkable that MG theories which have not only additional fifth-force interaction governing their spherical collapse, but also more complex excursion set behaviour, can be well-approximated by the HMF functions derived from ΛCDM simulations. Consequently, we do not necessarily have to reproduce the approach of inventing new functions and calibrating them, as was done in GR.

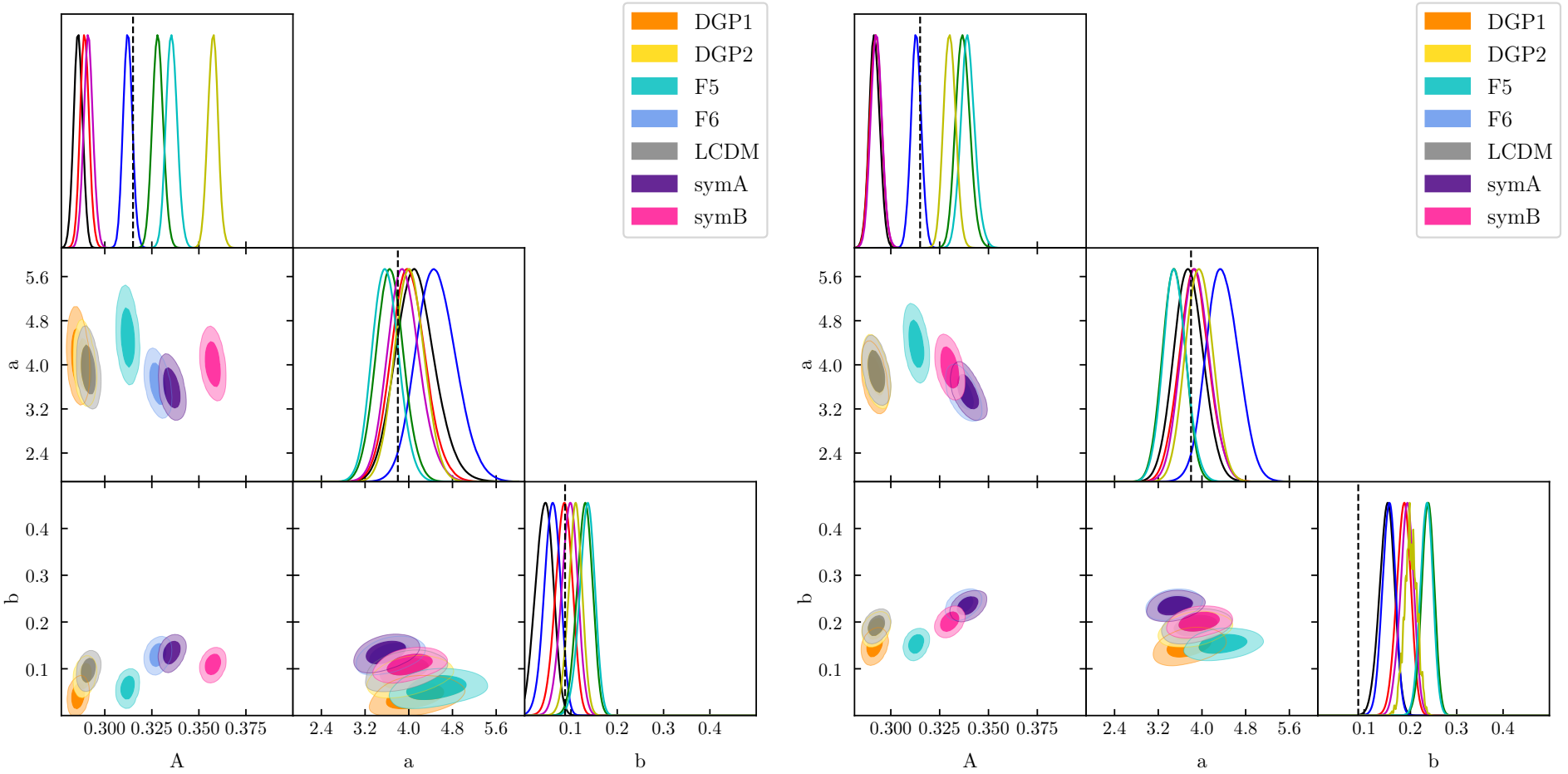

(a) MatchMaker halofinder, 30 bins

(b) RockStar halofinder, 30 bins

Figure 5.8: Posteriors for the Jenkins HMF in ΛCDM for each gravity model. The main diagonal shows the 1-d posteriors marginalised over all other parameters, while the off-diagonal plots show correlations between pairs of parameters via the 2-d $1, 2\sigma$ credible regions. The black dashed lines show the values proposed by [125].

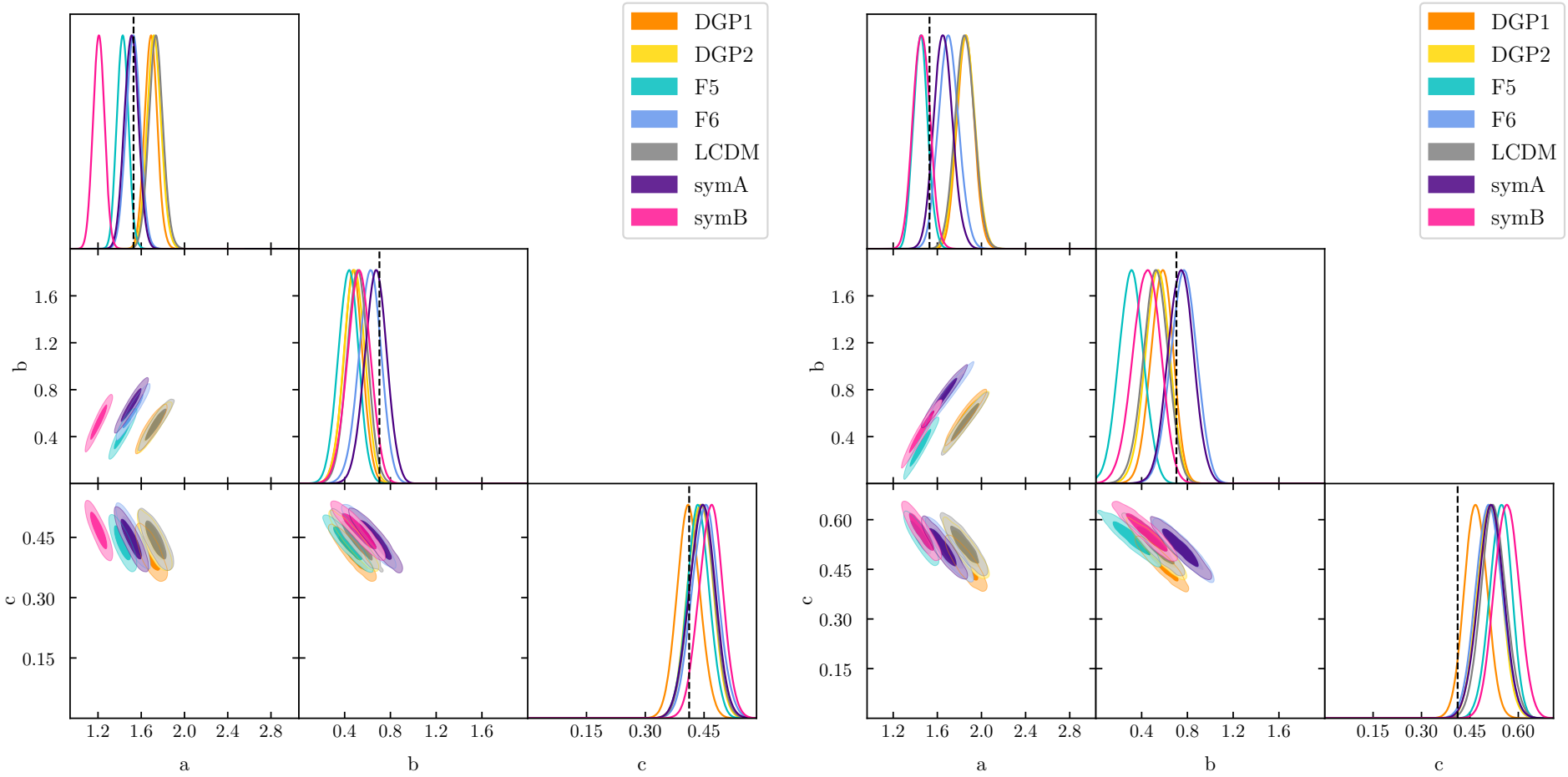

(a) MatchMaker halofinder, 30 bins

(b) RockStar halofinder, 30 bins

Figure 5.9: Posteriors for the Peacock HMF in ΛCDM for each gravity model. The main diagonal shows the 1-d posteriors marginalised over all other parameters, while the off-diagonal plots show correlations between pairs of parameters via the 2-d $1, 2\sigma$ credible regions. The black dashed lines show the values proposed by [193].

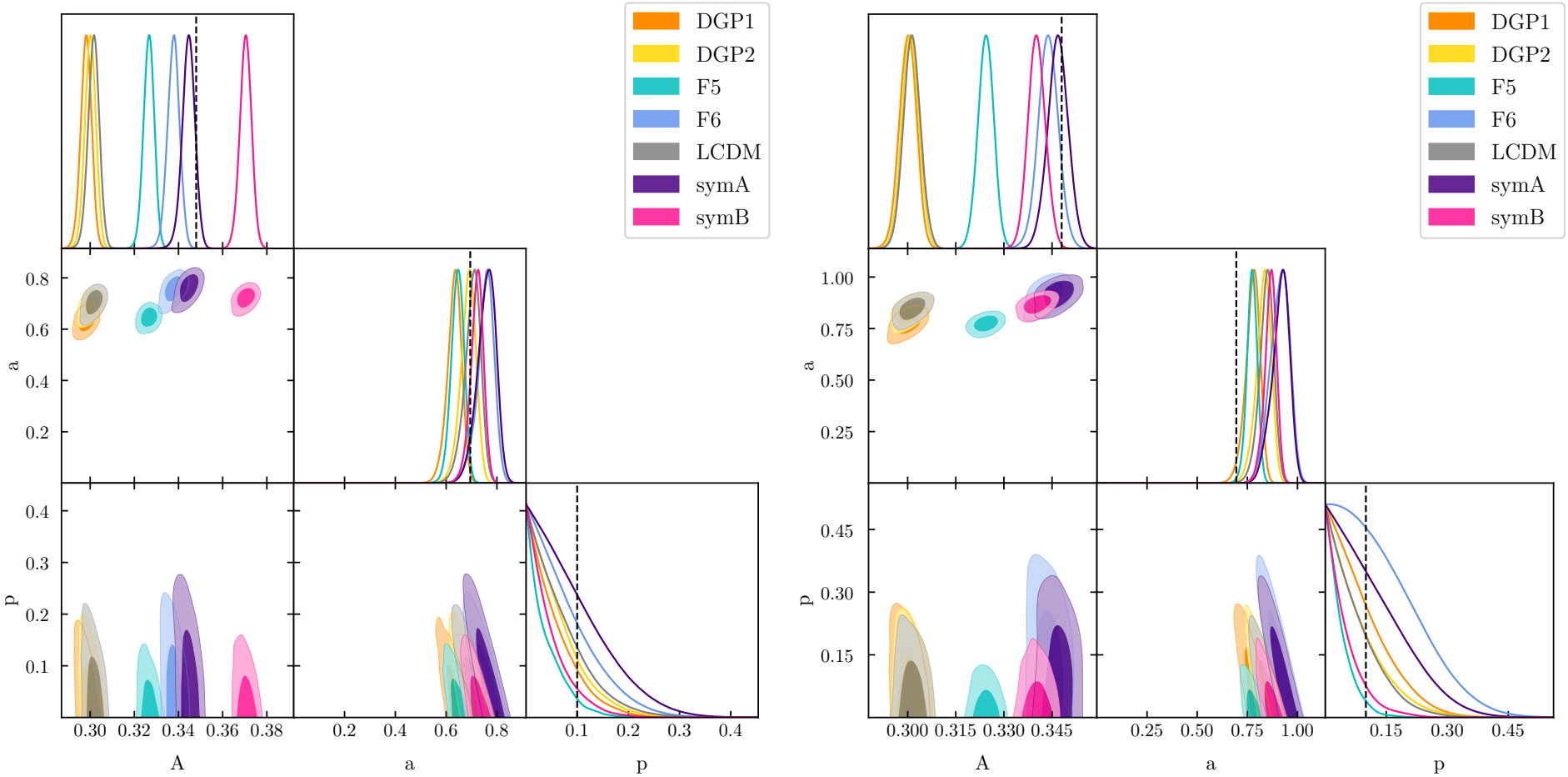

(a) MatchMaker halofinder, 30 bins

(b) RockStar halofinder, 30 bins

Figure 5.10: Posteriors for the SMT-Courtin HMF in ΛCDM for each gravity model. The main diagonal shows the 1-d posteriors marginalised over all other parameters, while the off-diagonal plots show correlations between pairs of parameters via the 2-d $1, 2\sigma$ credible regions. The black dashed lines show the values proposed by [75].

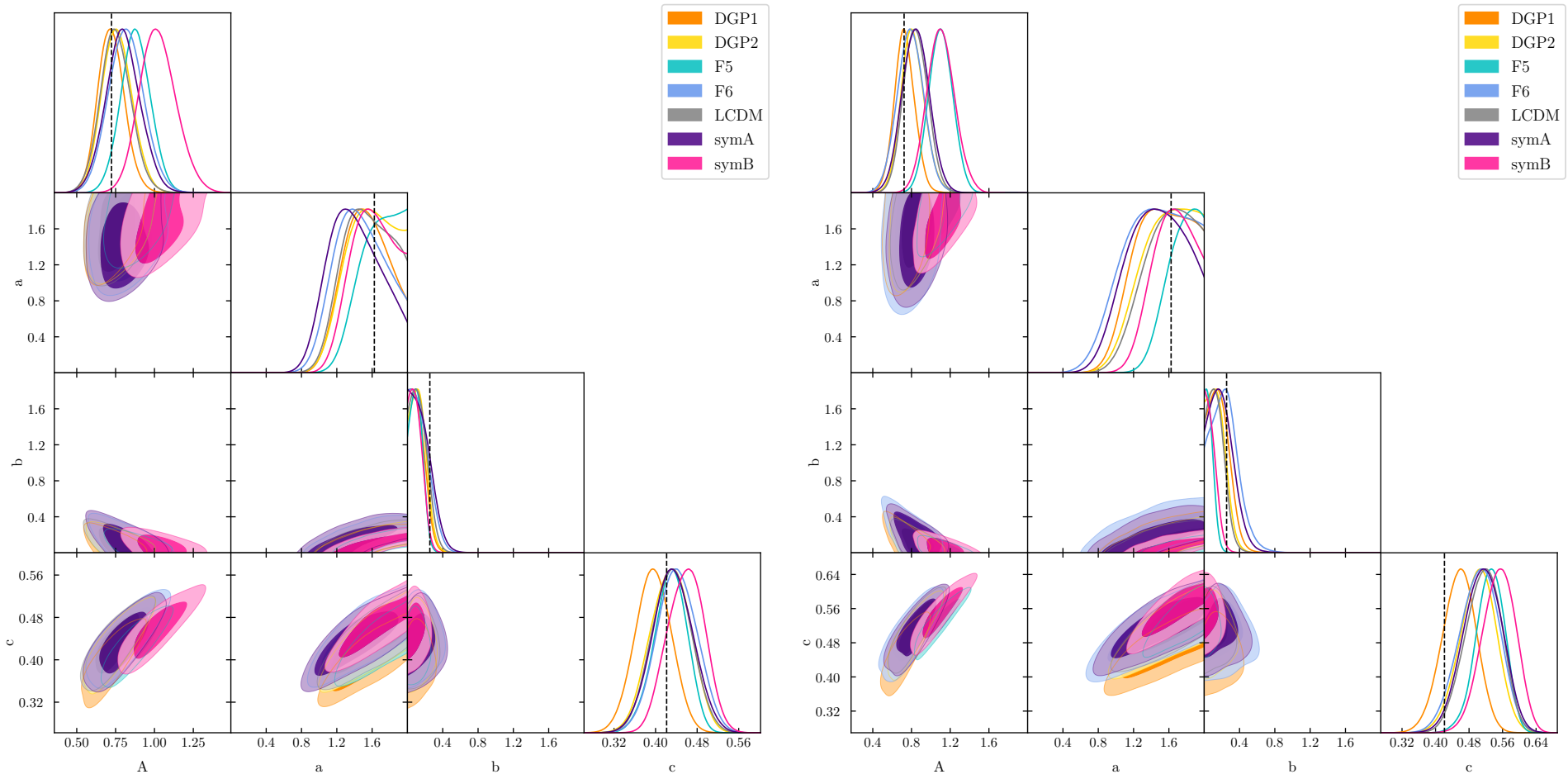

(a) MatchMaker halofinder, 30 bins

(b) RockStar halofinder, 30 bins

Figure 5.11: Posteriors for the Warren-Crocce HMF in ΛCDM for each gravity model. The main diagonal shows the 1-d posteriors marginalised over all other parameters, while the off-diagonal plots show correlations between pairs of parameters via the 2-d $1, 2\sigma$ credible regions. The black dashed lines show the values proposed by [251].

5.4.3 Recalibrating best-fit parameters

Now we explore the opposite question to the previous one, namely: how universal is the halo mass function? In this subsection, we use the same extended gravity model for both the N-body data and the collapse density for the halo mass function. In this way, insensitivity of the credible regions for the fitting function parameters to the gravity model used would indicate that the halo mass function in question is "universal" in a greater sense than that which is currently applied. Not only would it be insensitive to the redshift, but also to the model of gravitational collapse under which the haloes formed. This would vindicate the current practice to derive and calibrate HMF functions in ΛCDM N-body simulations alone—with the advantage that they could then be reliably applied to any scalar theory of MG with the same cosmological parameters.

Figs. 5.12 to 5.15 show the 1,2-σ credible regions for the free parameters in each of the fitting functions which passed our tests in Section 5.4.1. As in the previous subsection, the main diagonal show the 1-d posteriors marginalised over all other parameters, while the off-diagonal plots show correlations between pairs of parameters via the 2-d credible regions at $1, 2$-σ. The black dashed lines show the published values for each HMF, i.e. those proposed by their original authors. (Where it is not visible, the value is outside the range of the plot provided by `GetDist`.) We examined the behaviour of both the `MatchMaker` and `RockStar` halo finders.

Should we expect the LCDM results from our calculations to equal those from the original values of their respective papers? We do not expect to recover these results for a variety of reasons:

- The value of δ_c changes with Ω_{m0} and H_0
- The value of σ depends upon the power spectrum and value of σ_8
- Differing halo finders and settings
- The presence (or absence) of corrections to the N-body halo data

Let us examine each of these in turn.

Table 4.2 summarises the cosmological parameters used for each of the papers which provided "best-fit" parameters for particular fitting functions. The dependence of δ_c^Λ on Ω_{m0} is given in parametric form by [94] as $\delta_c = 1.68/\Omega_{m0}^{0.28}$—we can also see that this parameter enters the collapse ODE Eq. (4.4). Our value is $\delta_c^\Lambda \approx 1.675$. This contrasts with most of the papers (bar [75]). Some [76, 193, 225] use the SCDM value $\delta_c \approx 1.686$ (following Press-Schechter [202]) regardless of the actual cosmology of their simulations. Others [13, 125, 239, 251, 252] absorb the value of δ_c into their free parameters because

they use σ as the independent variable rather than ν, so their choice—which we need to convert back to ν—is ambiguous. In all cases we have assumed the exact SCDM collapse value $\delta_c = 3 \cdot (12\pi)^{2/3}/20$ when converting from σ to ν. Only Courtin et al. vary δ_c according to the solution of the spherical collapse equation for a variety of cosmologies. Thus we have a different numerator for ν. Moreover, it is unlikely that our $P(k)$ is precisely equal to any of those used in the papers. Even if it did match, the normalisation σ_8 differs. The variance σ which forms the denominator of ν therefore also differs from previous publications. Since the independent variable ν (or more precisely, our mapping $\ln M \to \nu$ from counts to first-crossing distribution) differs in this paper (and indeed in all of the others), our free parameters must change to compensate. Even if we had exactly the same numbers of counts and the same bins, and our best-fit HMF had the same $n(M)$ values as a preceding paper, we would see a change in $f(\nu)$. This is a small contribution to the movement of the maximum-likelihood peaks from the published values.

The choice of halo finder further abstracts the problem. All of the published values except Peacock and Watson (both of which are FoF-only) arise from a compromise between the best-fit values for multiple halo finders. For example, Jenkins [125] uses both FoF and SO halo finders to find a fitting function which has a residual of within 20% compared to their N-body HMFs simulated for a range of cosmologies (not just ΛCDM). Even when restricting their data to FoF-only and SO-only (whereby they obtain different best-fit values), the FoF linking length is changed between cosmologies ($b = 0.2$ for τCDM, $b = 0.164$ for ΛCDM), so we cannot disentangle the cosmological effects from the reduction of the N-body "data". As we can see by comparing the results for `MatchMaker` and `RockStar` in Figs. 5.9, 5.12, 5.14 and 5.15, the same distribution of mass within the N-body simulations produces a different HMF according to the halo finder used. [140] discuss this in great detail for ΛCDM and we have no reason to disagree with their findings.

Differing authors also treat the distribution $n(M)$ obtained from their halo finder(s) in a variety of ways. As we briefly covered in Section 6.3, the mass cutoffs are controlled by the simulation box size and the mass resolution. Table 4.1 summarises the mass range used by each paper. This shifts the sampling along a subsection of the actual HMF, changing the influence of each parameter in the likelihood function. An extreme example of this is the Reed 2003 fit, whose parameter c is completely unconstrained by masses $M \leq 10^{15} M_\odot$ [206]. Sometimes the individual halo masses are systematically "corrected", e.g. [34] or (more relevantly here) the Warren correction: a halo of N particles was updated to $N(1 - N^{-0.6})$ to account for perceived flaws in the halo finders. These factors all affect the final first-crossing distribution of the data, against which is compared the first-crossing distribution of the model (converted to counts per bin) which contains the values of the free parameters at a chosen point in the parameter

volume.

Given these factors, it is not surprising that our LCDM values do not always align with the published values. In Figs. 5.9, 5.12, 5.14 and 5.15 the grey lines show our ΛCDM posteriors, while the black dashed lines show the values from one of the relevant papers respectively. (We do not show all of the published values for every fitting function because this would lead to up to five lines on some plots, which would be confusing.) Of particular interest is the variety of best-fit values for the SMT fitting function. Our changes in all HMFs are the same order of magnitude as the changes other authors have found when altering the cosmological parameters, halo finders and data reduction techniques used to derive the HMF. Since we are utilising a single cosmology and separating the effects of our two halo finders, it is not surprising that our values do not reproduce the existing ones.

Despite the fact that we have used the full MG modifications to $\nu\left(S \,|\, \delta_{\rm env}, S_{\rm env}\right)$, the behaviour of the HMFs mirrors that of the previous subsection, in which we assumed $\nu = \delta_c^\Lambda / S$. Some HMFs have precisely the same "good behaviour" (or lack thereof) in both cases. The Jenkins plot has the same flaws with $b \approx 0$ for DGP1 in Fig. 5.12a (*cf.* Fig. 5.8a). The Peacock plot has the same multi-modal tendencies for c in Fig. 5.9a and Fig. 5.13a. Otherwise these HMFs have well-behaved posteriors. SMT-Courtin in Fig. 5.14 is well-behaved for all MG theories and both halo finders. It is notable that the Peacock HMF—an empirically-derived fit to the Watson-FoF HMF accurate to 1% in ΛCDM—does behave well when generalised, whereas the original Watson fit does not. This suggests that the behaviour is not caused by over-simplifying the gravitational collapse, but by the underlying form of the fitting function itself. In contrast, Warren-Crocce shows considerable improvement in terms of the poor behaviour of the posteriors peaking at $b \approx 0$ in both Fig. 5.15 and Fig. 5.11. However for the `MatchMaker` result, both F5,6 models are well-behaved in MG, compared to F5 alone in ΛCDM; moreover `RockStar` behaves (relatively) well for everything apart from SymB. In this case, accounting for the mass dependence of the critical density does improve the behaviour of the HMF. Thus we see that generalising ν from its ΛCDM value (proportional to σ^{-1}) to MG does not affect the overall behaviour of the HMFs, compared to the previous subsection.

We can use the HMFs to examine the universality of ν: specifically, whether accounting for the excursion set behaviour of the MG models is sufficient to render our fitting functions independent of MG. While it is evident from Figs. 5.12 to 5.14 that no single value works for every MG model, we do find clustering between families. The Jenkins posteriors (Fig. 5.12) show that the credible regions for the two symmetron models are quite distinct from the other five models, all of which have overlapping credible regions. The Peacock function shows a higher degree of universality than Jenkins: particularly

in Fig. 5.13a, but slightly less in Fig. 5.13b. In particular, c is practically universal, but there is a spread of overlapping values for the other two parameters. SMT-Courtin (Fig. 5.14) has very similar behaviour to the Jenkins HMF, with the two Symmetron models distinct from each other as well as the clustering–but here it is four of the other five models, with F6 closer to the Symmetron results. Unlike the preceding fitting functions, Warren-Crocce (Fig. 5.15) has posteriors which largely overlap, perhaps with the exception of F6, and more clustering in `MatchMaker` than `RockStar`. This fitting function has no credible regions which are isolated from one other. Thus, the fitting functions display a range of behaviours, but most show that the best-fit parameter values for multiple MG models do overlap.

Where the symmetron models are distinguishable from the others, the differences are driven by the "normalisation[3] factor:" the symmetron models underpredict $n(M)$, requiring a systematic upwards shift by increasing the multiplicative factor A. These models have a drifting barrier $\delta_c(S)$ which includes mass dependence. However, this dependence via the collapse density ODE is not accounting for all of the actual behaviour of the haloes in non-linear collapse. Considering that we use a simple model of a collapsing spherical top-hat, we may be oversimplifying the effect of the symmetron fifth-force.

There is also the issue of the F5 and F6 models exhibiting greater spread (albeit still with overlapping credible regions) than the LCDM and DGP results. This is particularly visible in Warren-Crocce. Recall that here we fully account for the excursion-set barrier density using the Volterra solution. However, we use this to scale the unconditional HMF, so we approximate the integral over the environmental dependence of the HMF via the value at the peak of the environment distribution (which happens to be $\delta_{\rm env} = 0$). Under these circumstances, it is remarkable that our approximation does produce such a universal result.

The two DGP models cluster strongly with ΛCDM in all the HMFs. This is possibly because all of these models use a flat barrier, so there is no additional mass- or environment-dependence to be included in ν, so no additional excursion set behaviour which needs to be approximated by the change in the independent variable.

While we do not find a strong degree of overall universality, we can see that the different screening mechanisms do behave similarly. This is independent of the choice of halo finder, so this clustering is not caused by systematic effects or scatter in the N-body data.

This illustrates the caution which must be employed when using fitting function orig-

[3]While A originally played this role in the SMT-Courtin function [225], we no longer require the cumulative mass fraction to tend to unity.

inally calibrated in ΛCDM in the context of MG. Although the generalisation of the fitting functions from ΛCDM to MG does not produce a completely universal fitting function, there is a degree of universality in the clustering of the credible regions for different screening mechanisms. This is because the effects of the fifth-force are largely encapsulated by the modified Poisson equation which appears in the ODE for gravitational collapse. The resulting δ_c clearly does not contain all of the non-linear collapse information (otherwise we *would* have a universal HMF) but it does incorporate enough into ν that the resulting fitting function depends only on the type of screening, rather than the values of the fifth-force parameters.

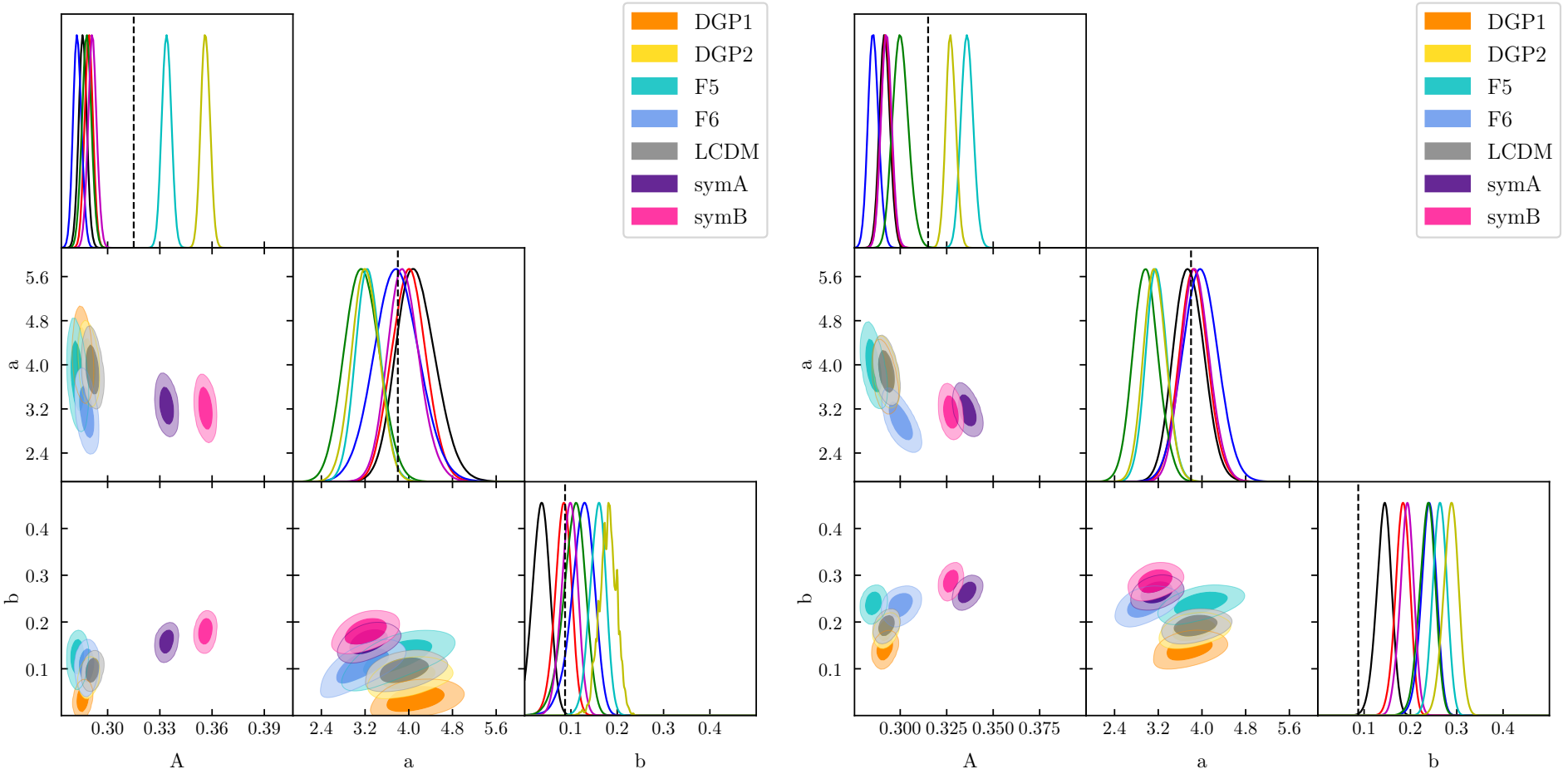

(a) MatchMaker halofinder, 30 bins

(b) RockStar halofinder, 30 bins

Figure 5.12: Posteriors for the Jenkins HMF calculated with the MG extensions for each gravity model. The main diagonal shows the 1-d posteriors marginalised over all other parameters, while the off-diagonal plots show correlations between pairs of parameters via the 2-d $1, 2\sigma$ credible regions. The black dashed lines show the values proposed by [125].

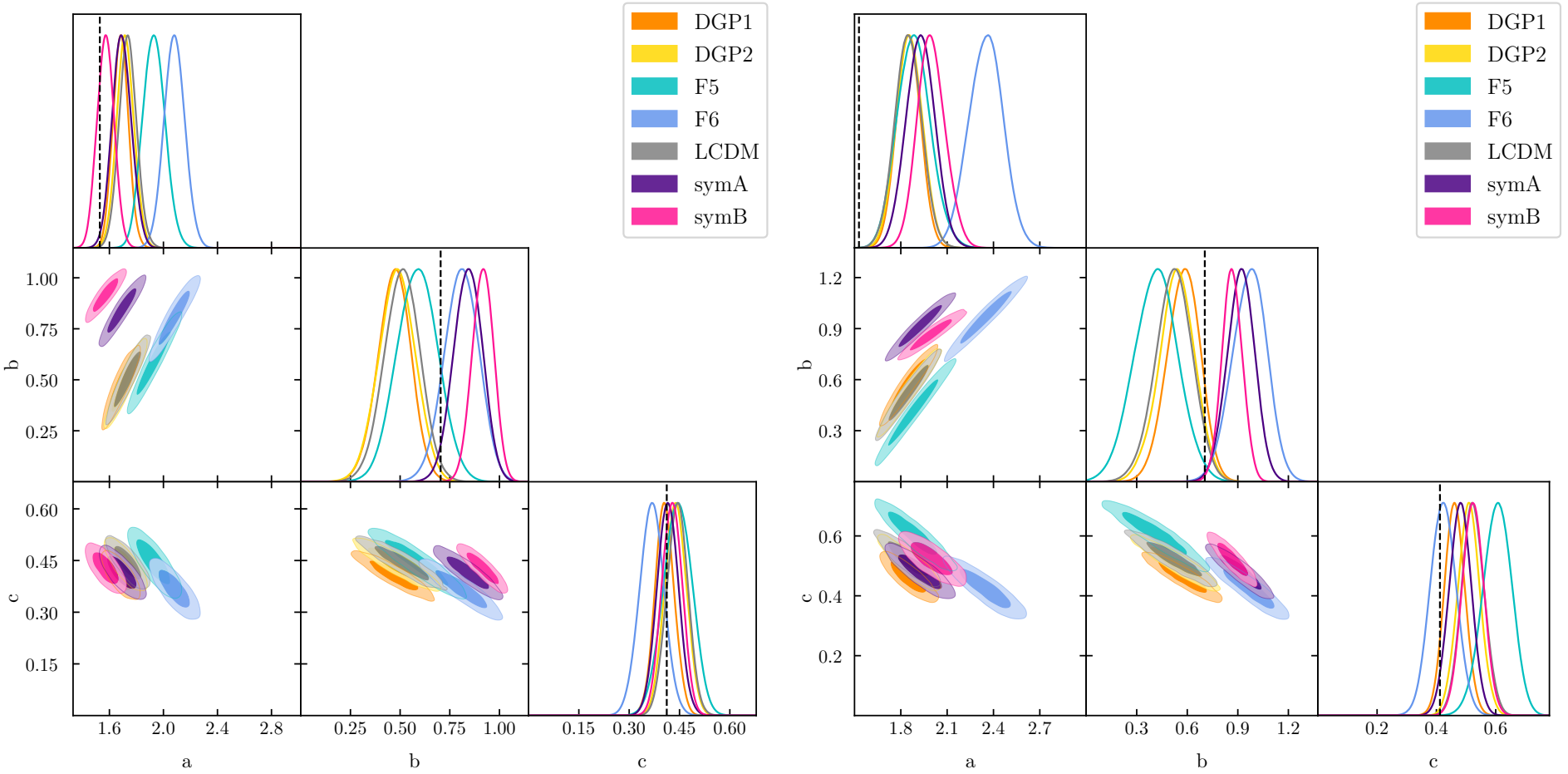

(a) MatchMaker halofinder, 30 bins

(b) RockStar halofinder, 30 bins

Figure 5.13: Posteriors for the Peacock HMF calculated with the MG extensions for each gravity model. The main diagonal shows the 1-d posteriors marginalised over all other parameters, while the off-diagonal plots show correlations between pairs of parameters via the 2-d $1, 2\sigma$ credible regions. The black dashed lines show the values proposed by [193].

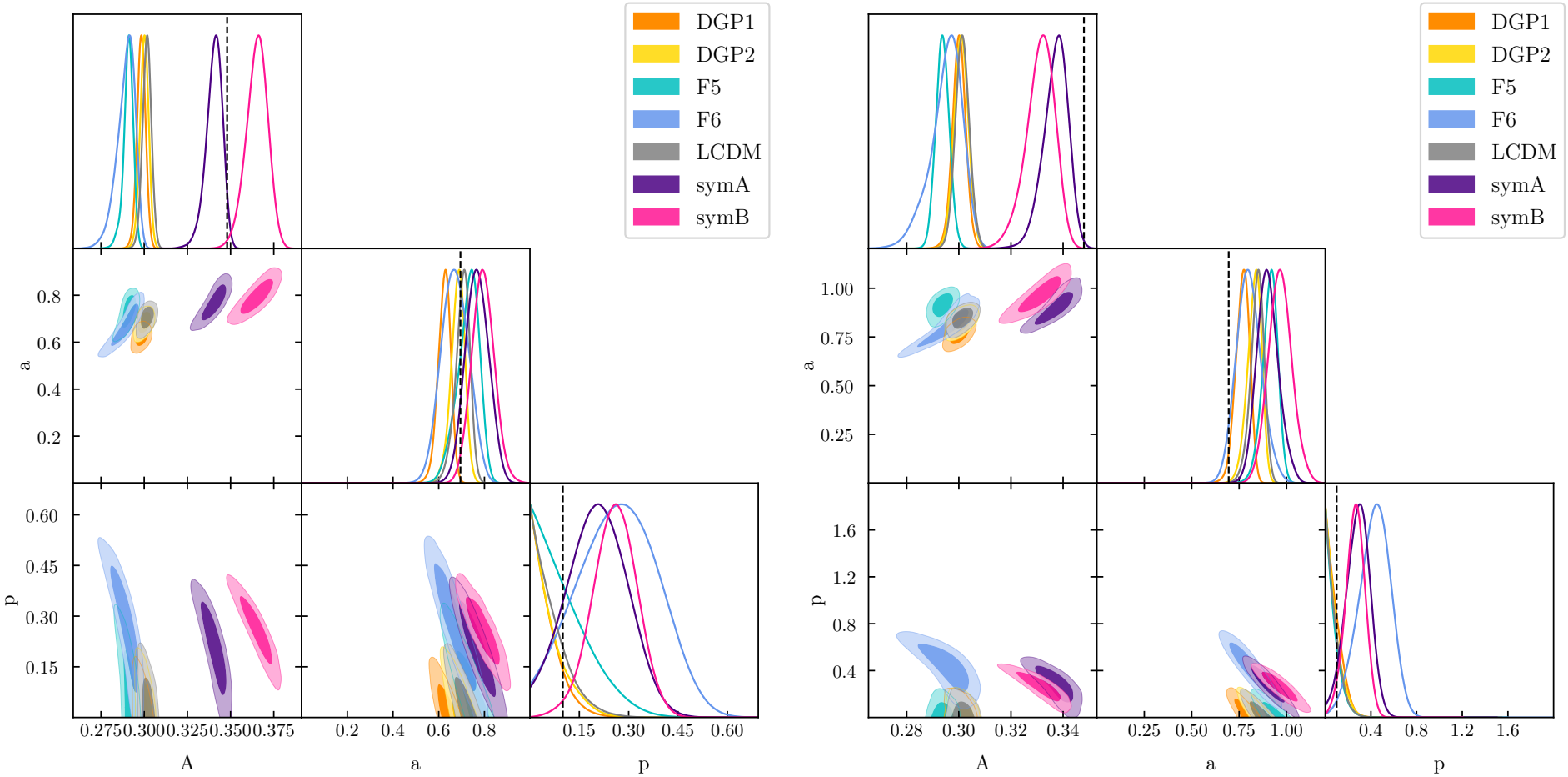

(a) MatchMaker halofinder, 100 bins

(b) RockStar halofinder, 100 bins

Figure 5.14: Posteriors for the SMT-Courtin HMF calculated with the MG extensions for each gravity model. The main diagonal shows the 1-d posteriors marginalised over all other parameters, while the off-diagonal plots show correlations between pairs of parameters via the 2-d $1, 2\sigma$ credible regions. The black dashed lines show the values proposed by [75].

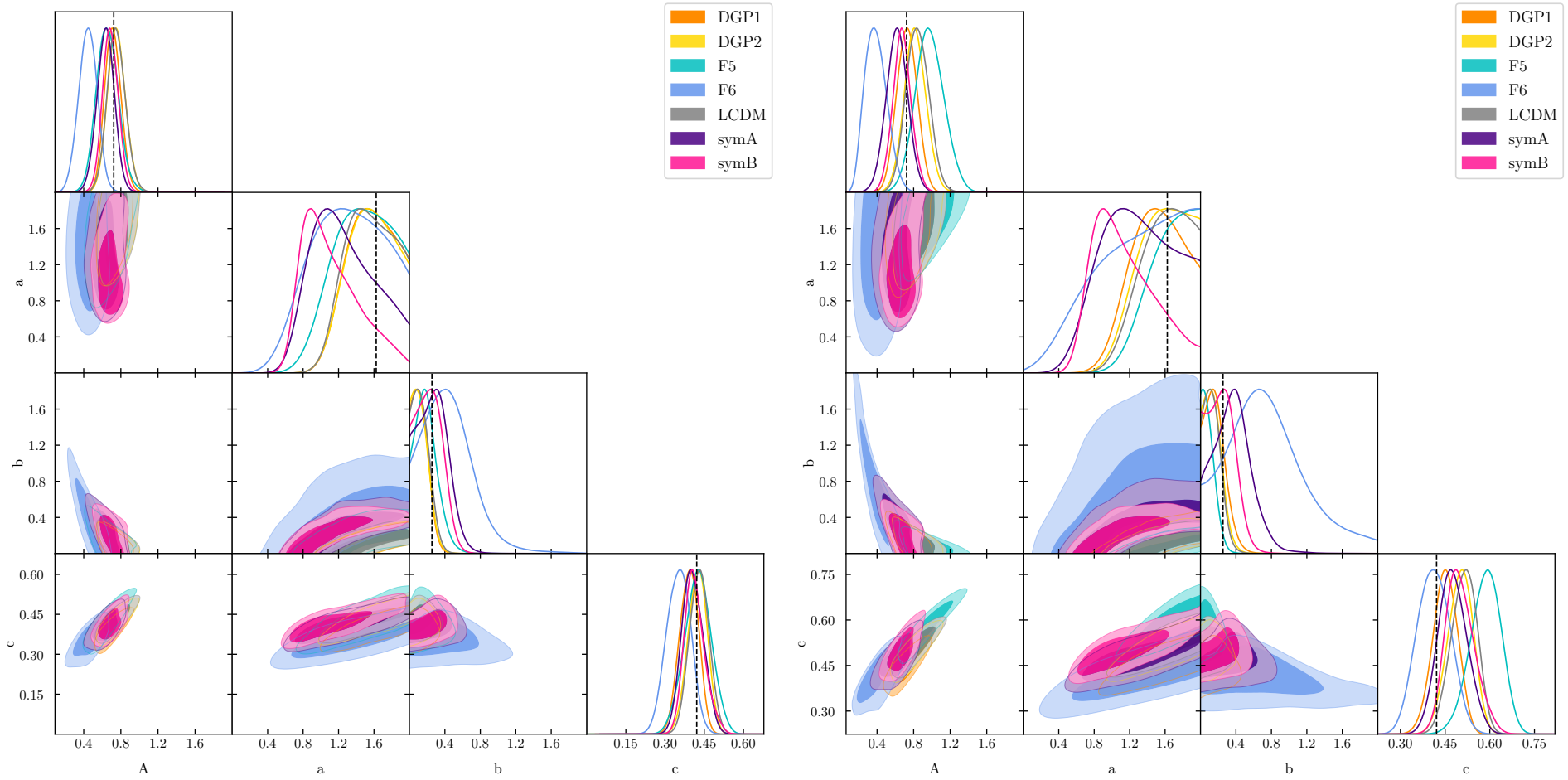

(a) MatchMaker halofinder, 30 bins

(b) RockStar halofinder, 30 bins

Figure 5.15: Posteriors for the Warren-Crocce HMF calculated with the MG extensions for each gravity model. The main diagonal shows the 1-d posteriors marginalised over all other parameters, while the off-diagonal plots show correlations between pairs of parameters via the 2-d $1, 2\sigma$ credible regions. The black dashed lines show the values proposed by [251].

5.5 Conclusions

This section reiterates the salient points of this chapter. We outline the method we have used, before describing avenues for generalisation and other possibilities for further work. We conclude by summarising the key results of this chapter.

5.5.1 Summary

This chapter builds upon the earlier parts of this thesis, in which we explored the use of the halo mass function in screened MG theories. We selected a range of theories which have different screening mechanisms (Sections 2.2 to 2.4) and derived their additional contribution to the spherical collapse equation (Section 4.1). After motivating our transformation between GR and MG via the excursion set theorem (Section 4.2.2), we summarised a variety of HMFs and described the nature of their universality in GR and how to transform this into the equivalent in MG (Section 4.4).

We have illustrated a method to apply the same rigorous calibration techniques used to generate the HMF in GR to various theories of screened MG. The N-body simulations from which we extracted halo catalogues to compare to our empirical fits are described in Section 5.2.1. Similarly, the Bayesian methodology for estimating maximum-likelihood parameters and the relative likelihood of the different models is outlined in Section 5.3. The key steps of our method are:

1. Conversion of the GR HMF from σ to ν (if necessary).
2. Calculation of the effective fifth-force $F_{\rm eff}$ to insert into the spherical collapse ODE.
3. Calculations of the collapse density $\delta_c(S, \delta_{\rm env}, S_{\rm env})$ to incorporate into ν.
4. Use of an appropriate excursion-set technique to account for the barrier density δ_c.
5. MCMC estimation of the best-fit free parameter values and their credible regions.
6. Output of the corresponding best-fit HMF.

Our main results (Section 5.4) are as follows. In our calibration of the `MultiNest` MCMC code, we found that the posteriors are much tighter for the Poissonian than the Gaussian likelihood, due to the large standard deviation in the latter, which is a consequence of the Poisson noise involved in counting the haloes per mass bin. Fortunately, we found that the bin width, which controls the discretisation of the HMF,

does not affect the posteriors when using the Poissonian likelihood. In fact, we are able to recover the input values for all of our fitting functions. This enabled us to fix the likelihood, the bin width and the number of live points for use on our N-body data. We then applied this method to determine whether the ΛCDM HMF can be used as a probe of MG.

We found that the effects of MG can be interpreted as a change in best-fit parameters in the ΛCDM HMF for all of the fitting functions. Alternatively, the relation can be inverted to judge the universality of the HMF, i.e. its independence on the underlying theory of gravity. Although we found no completely universal HMF, the parameter values did cluster according to the type of screening mechanism, with Jenkins, Peacock and SMT-Courtin being the least universal and Warren-Crocce the most. The former group required very different best-fit parameters for the two Symmetron models, whereas in the latter all of the models had overlapping credible regions. The results suggest that a single, best-fit HMF might be used for each type of screening, independent of the parameters in the MG model. This demonstrates that the additional complexity of the gravitational collapse in screened MG theories cannot always be accounted for using the techniques developed in GR. However, it is unnecessary to develop new fitting functions and calibrate them on a case-by-case basis.

We have demonstrated that it is possible to generalise some of the halo mass functions in common use in GR to incorporate MG theories with a variety of screening mechanisms. However, the calibration of these fitting functions has a number of caveats which are not encountered in the ΛCDM framework for which they were initially developed. Nonetheless, it is remarkable that our method can incorporate much of the non-linear collapse behaviour of screened MG in a simple and efficient mechanism. This is in direct contrast to the difficulties encountered in performing N-body simulations in screened MG. Thus we have provided an excursion-set-motivated alternative in MG to the need to replicate the time-consuming development of accurate halo mass functions which took place (and is ongoing) in GR.

5.5.2 Further work

The method presented in this chapter for calculation of the MG halo mass function using the fitting functions derived from ΛCDM has many avenues for generalisation. Most straightforward of these is the application to other fitting functions as they become available, provided that these functions can be expressed in terms of the "universal parameter" ν rather than the variance σ.

The universality of the halo mass function can be further extended to higher redshifts.

The collapse ODE in Section 4.1 has a new stopping condition that $y_h(z_c) = 0$, but the same bijection scheme can be applied to calculate the collapse density $\delta_c(z_c)$. The variance $\sigma(z)$ is obtained from the present-day value via the growth factor $D(z)$. However, to a good approximation, these modifications cancel, leaving ν independent of z [261]. This generalisation is particularly relevant given the ongoing discussion on the z-independence of $f(\nu)$ in ΛCDM. It would be particularly interesting to determine the influence of the fifth-force on the evolution of the HMF.

The calibration techniques are applicable to any MG theory which satisfies a number of constraints:

- Existence of a modified Poisson equation to approximate the gravitational effects of MG
- Well-posedness of the corresponding spherical-collapse ODE
- Background expansion similar to ΛCDM (so that the ΛCDM growth factor can be used and the halo environment treated as ΛCDM in the collapse ODE)

Galileon MG is an example of a screened theory for which this technique may be used. However, it may also be applied to MG theories which do not involve screening, but have some other method of being observationally-viable. It would be interesting to investigate whether the results we have found are unique to screening models, or whether they extend to non-screened theories.

The cosmology-dependence of these results can also be explored. This would be a daunting task, requiring N-body simulations for a grid of cosmological parameters, especially given the additional complexity of incorporating a fifth-force into the simulations. Nonetheless, this would permit comparison with the investigation of the cosmological-dependence of the HMF in GR (e.g. [75]). Moreover, if using changes in the best-fit GR parameters for a given fitting function to suggest a deviation from ΛCDM, it would highlight the potential degeneracy between a change in MG and a change in the GR cosmological parameters. This is important if we are to use the HMF as a probe of MG in future surveys.

The many avenues for generalisation illustrate that the same attention to detail can be applied to the HMF in both ΛCDM and MG. Having illustrated a number of caveats—the choice of fitting function, likelihood and the dependence of the results on both halo finder and bin width—we nonetheless show that three common HMFs can be used and calibrated in both GR and MG. Without applying the same calibration techniques in both theories, we are not making a like-for-like comparison when analysing the behaviour of the HMF, especially when constructing theoretical HMFs to compare to observations.

Chapter 6

The $f(R)$ mass function in the cosmic web

6.1 Introduction

The discovery of the accelerated expansion of the Universe [196, 210] is one of the biggest puzzles in modern cosmology. Having accepted the Einstein equations as the correct description of the interaction between matter and geometry, one is left with no alternative but to modify either side of the equation in order to account for this acceleration. On the one hand, modifying the stress-energy tensor necessitates the presence of an unknown substance dubbed dark energy; on the other, modifying the Einstein tensor requires modifications to relativity at a more fundamental level. This poses the question: should one of these choices be favoured over the other? Dark energy—at its simplest a vacuum energy which acts in the form of an effective cosmological constant—is in excellent agreement with most observations so far, but suffers from some theoretical problems including fine-tuning [70]. Extended gravity theories—at their simplest adding extra complications to the Einstein-Hilbert action—have a secure theoretical motivation, but need to be carefully designed to satisfy observational constraints.

General Relativity has been tested to great precision on Earth and in the Solar System [36, 37, 256]. Thus, if it is modified then some form of screening mechanism [53, 132, 133, 144] is required to hide the effects in these regimes. As we have tested general relativity only in high density regimes (relative to the cosmic mean), this naturally leads to an environmental dependence on the modifications of gravity. In turn this would translate into an environmental dependence on observables [e.g. 214, 259]. Thus

the very screening which modified theories of gravity invoked to evade local, Solar System tests can be harnessed as a detection mechanism by examining different regions of the cosmic web. This can also be used to distinguish it from other dark energy scenarios.

In this chapter we examine a variety of halo properties in the different geometric structures of the cosmic web, namely: the abundance of halos of different masses; the alignment of the halo spins and shapes with the local tidal structure; the halo spin parameter and the concentration-mass relation. We provide an excursion-set-based approximation to the N-body results for the halo mass function. This synthesises two, major existing results: the unconditional mass function in $f(\mathcal{R})$ calculated by [143, 155, 170] and the classification of halo statistics in the cosmic web by e.g. [6, 90, 104]. In the same vein as those chapters, our aim is to build a semi-analytic model which combines an empirically-derived halo mass function in the unconditional case for ΛCDM with a physical model derived using the tools of excursion set theory. Such a model, if sufficiently accurate, can then be used to cheaply compute observables for quantities that otherwise would require expensive numerical simulations.

The structure of the chapter is as follows: we have already encountered the Hu & Sawicki $f(\mathcal{R})$ model of modified gravity in Chapter 2. We reiterate the equations for calculating the HMF conditional on the cosmic web in Section 6.2, where we specifically apply the Peacock fitting function. The N-body simulations against which we benchmark our semi-analytical model are described in Section 6.3. In Section 6.4 we compare the accuracy of our theoretical model to N-body simulations (Sections 6.4.1 and 6.4.2) and we analyse deviations from ΛCDM for each of the halo properties (Sections 6.4.3 and 6.4.4). We suggest possible generalisations and applications of this method in and conclude in Section 6.5.

6.2 The multiplicity function

In this chapter, we adopt the Peacock mass function[1] [193]

$$F(>M) = \frac{\exp\left(-c\nu_h^2\right)}{1 + a\,\nu_h^b} \quad \text{where} \quad \begin{cases} a &= 1.529 \\ b &= 0.704 \\ c &= 0.412 \end{cases} \tag{6.1}$$

[1]This simple functional form matches the Warren et al. fit [251] to the mass function to sub-percent accuracy.

Instead of the collapsed mass fraction (Eq. (6.1)), we will use its differential, known as the multiplicity function[2]:

$$f(M) \equiv \frac{dF(<M)}{d\ln M} = f(S)\left|\frac{dS}{d\ln M}\right| = -\langle f\left(\delta_c(S), S \,|\, \delta_{\rm env}, S_{\rm env}\right)\rangle_{\rm env}\frac{dS}{d\ln M} \tag{6.2}$$

where we have defined the first-crossing distribution $f(S)$, the probability that the random walk will be absorbed by the barrier at resolution S. We have already seen in Section 4.2.2 that this becomes much more important in modified gravity than general relativity.

We have already derived the key integral of this chapter, which incorporates the dependence on the cosmic web (Section 4.3). In this chapter we have singled out the Peacock HMF:

$$f\left(\nu_{\rm eff}\right) = -\frac{\exp\left(c\nu_{\rm eff}^2\right)}{\left(1+a\nu_{\rm eff}^b\right)^2}\left[ab\nu_{\rm eff}^{b-1} + 2c\nu_{\rm eff}\left(1+a\nu_{\rm eff}^b\right)\right]\frac{\partial\nu_{\rm eff}}{\partial S} \tag{6.3a}$$

$$\nu_{\rm eff} = \max\left\{0, \frac{\nu_h\left(S,\delta_{\rm env}\right) - \epsilon^2\left(S,S_{\rm env}\right)\nu_e\left(S_{\rm env},\delta_{\rm env}\right)}{\sqrt{1-\epsilon^2\left(S,S_{\rm env}\right)}}\right\} \tag{6.3b}$$

Eq. (6.3) is the first-crossing distribution which we substitute into Eq. (6.2) to obtain the $f(\mathcal{R})$ multiplicity function conditional to the tidal classification of the environment. In this way, we ensure that our base model is an excellent fit to simulations, while also retaining the semi-analytical nature of the model.

6.3 Simulations and algorithms

The simulations used in this chapter were performed with the `ISIS` code [165], which is a modified gravity modification of the N-body code `RAMSES` [236].

We performed two large-box simulations: one for ΛCDM and one for $|f_{\mathcal{R}0}| = 10^{-5}$ using an approximate method [258] to incorporate the scalar field. We also performed two small-box simulations: one for ΛCDM and one for $|f_{\mathcal{R}0}| = 10^{-5}$ fully solving for the scalar field in the simulation box [260]. The approximate method has previously been shown to produce very good results (accuracy to a few percent) with respect to the matter power spectrum and the halo mass function [258]. The modified gravity simulations were performed using the same initial conditions as the corresponding ΛCDM simulations. This allows us to compare the two models without requiring multiple realisations of the initial conditions. The cosmological parameters are: $\Omega_{m0} = 0.27$, $\Omega_{\Lambda 0} = 0.73$,

[2]Note that some authors define the multiplicity function as the derivative with respect to σ rather than $\ln M$. Moreover, although $f(M)$ and $f(S)$ are related, they do not denote the same functions, despite the same letter being conventionally used for both.

Box size (Mpc/h)	Particles per box	Cosmology	MG algorithm
1024	1024^3	ΛCDM, $\lvert f_{\mathcal{R}0}\rvert = 10^{-5}$	Approximate
256	512^3	ΛCDM, $\lvert f_{\mathcal{R}0}\rvert = 10^{-5}$	Full

Table 6.1: The N-body simulations used in this chapter. The cosmological parameters used to generate initial conditions was: $\Omega_{m0} = 0.27$, $\Omega_{\Lambda 0} = 0.73$, $h = 0.704$, $n_s = 0.966$ and $\sigma_8 = 0.8$.

$h = 0.704$, $n_s = 0.966$ and $\sigma_8 = 0.8$ and the other simulation parameters are listed in Table 6.1.

We located haloes using a Friend-of-Friend algorithm[3] as well as the spherical overdensity halo finder `AHF` (Amiga Halo Finder)[4] [108]. The N-body particles were binned to a $N_{\rm grid} = 512^3$ grid using Cloud-in-Cell interpolation and then smoothed with a Gaussian kernel of widths $R_{\rm env} = 10$ and 20 Mpc/h in this chapter. The local tidal tensor and its eigenvalues were then computed using a public code[5]. The error bars in the plots were computed using jack-knife resampling of the simulation box with 8 samples. To generate error-bars for ratio plots coming from two different simulations, we used:

$$\Delta\left(\frac{a}{b}\right) = \frac{a}{b}\sqrt{\left(\frac{\Delta a}{a}\right)^2 + \left(\frac{\Delta b}{b}\right)^2 - 2\,r\,\frac{\Delta a}{a}\frac{\Delta b}{b}} \tag{6.4}$$

where r is the correlation coefficient. The quantities whose ratios we compute are highly correlated (since they are taken from simulations with the same initial conditions) so for simplicity we have used a fixed value of $r = 0.9$ (or $r = 0$ for cases where we wanted to be conservative) to estimate the error-bars.

6.4 Results

We compare the behaviour of the ΛCDM and $f(\mathcal{R})$ mass functions in various environments. Then we evaluate the accuracy of our semi-analytic model using N-body simulations and describe its limitations and possibles paths to improvement. Finally, we analyse the effect of modified gravity on a number of internal halo properties as a function of tidal environment.

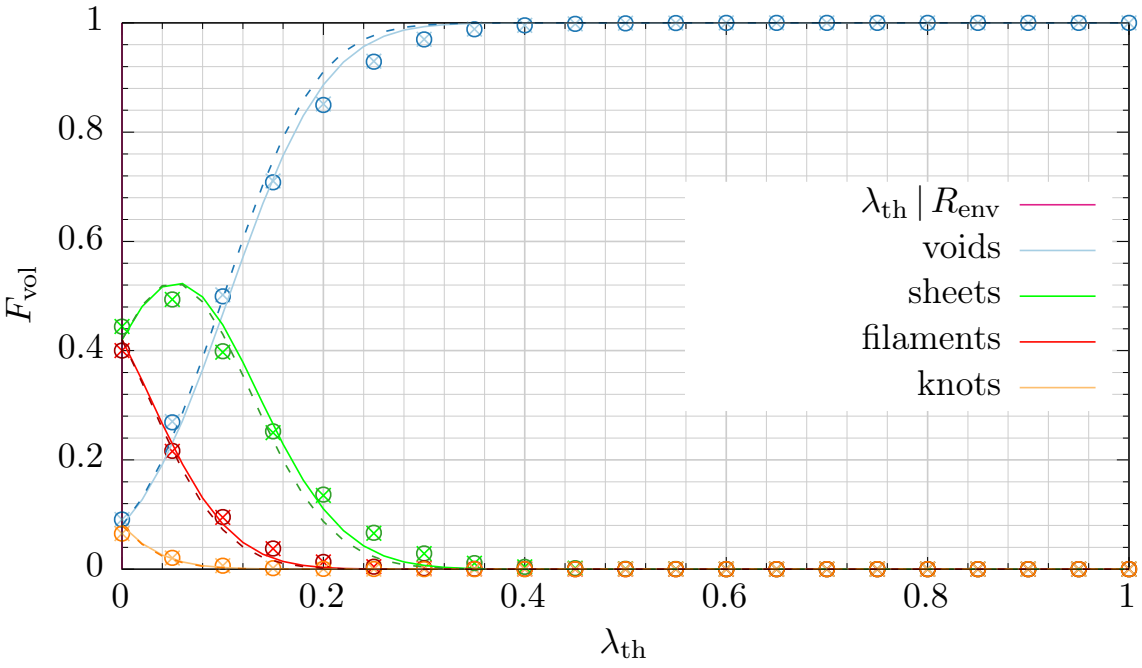

(a) $R_{\rm env} = 20/h$ Mpc

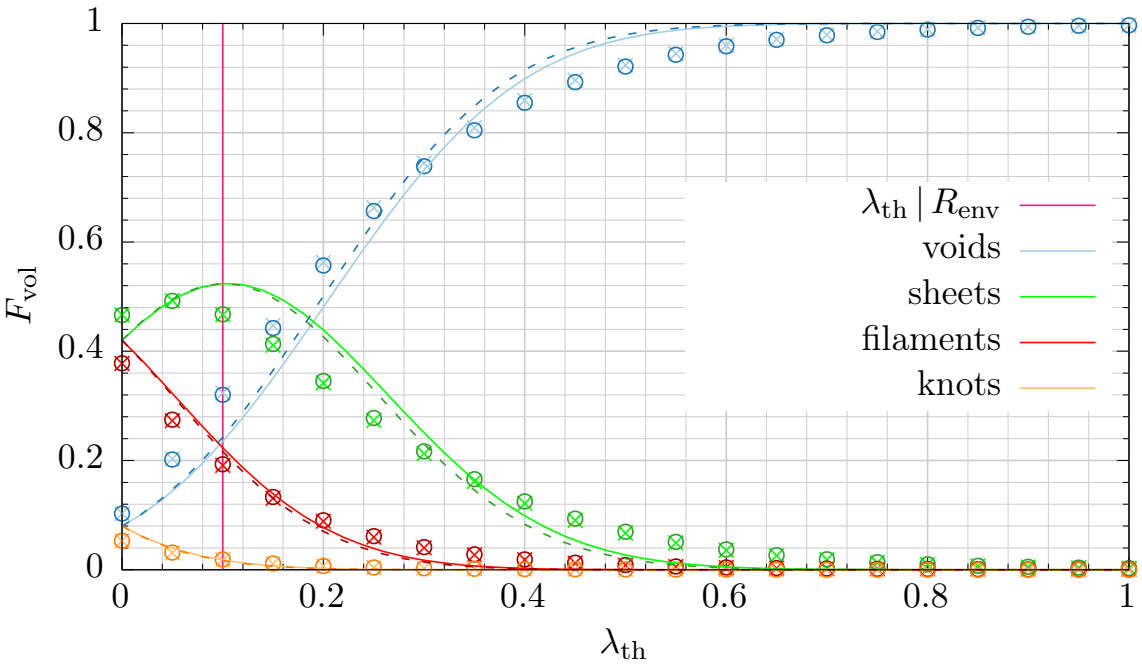

(b) $R_{\rm env} = 10/h$ Mpc

Figure 6.1: Volume fraction according to the Gaussian probability distribution function Eq. (4.19) (lines) and the N-body simulations (points), as a function of the threshold $\lambda_{\rm th}$. Light colours (solid lines; crosses) are for ΛCDM, darker ones (dashed lines; circles) for $|f_{\mathcal{R}0}| = 10^{-5}$. The value of $\lambda_{\rm th}$ chosen for the remainder of this work is shown by the vertical line (at 0.0 for $R_{\rm env} = 20/h$ Mpc and 0.1 for $R_{\rm env} = 10/h$ Mpc).

6.4.1 Volume fractions

We can indirectly measure the accuracy of the Gaussian model for the eigenvalue probability distribution via the volume fractions in different cosmic web elements. In Fig. 6.1 we compare the values from our model to those from the N-body simulations.

The behaviour with $\lambda_{\rm th}$ permits us to select a suitable value for $\nu_{\rm th}$ in Eq. (4.18). We require a value for which there is a (relatively) even distribution between the different morphologies (amongst other requirements discussed in [6]). Thus we select $\lambda_{\rm th} = 0$ for $R_{\rm env} = 20$ Mpc/h and $\lambda_{\rm th} = 0.1$ for $R_{\rm env} = 10$ Mpc/h. We utilise the same threshold for the smoothing in our semi-analytic model and the N-body simulations.

We compare the volume fractions calculated from Eq. (4.20) to the N-body volume fraction in Fig. 6.1. At scales of $R_{\rm env} = 20\,{\rm Mpc}/h$ Eq. (4.19) performs well, whereas at $R_{\rm env} = 10\,{\rm Mpc}/h$ we find that $p(\rho, \theta, \phi)$ is a poor approximation of the real overdensity field. This should not be surprising given the non-linear evolution of the density field on all but the largest scales.

The Gaussian volume fraction in Fig. 6.1 illustrates the large-scale behaviour of the scalar field modification to general relativity. Compared to ΛCDM (solid lines in Fig. 6.1) there is a greater fraction of voids and a smaller fraction in collapsed structures. At larger scales, the change in volume fraction due to modified gravity is more pronounced. This is due to the scalar field leaving the chameleon regime at small scales and moving to the linear regime at large scales (although on cosmological scales it returns to mimic general relativity behaviour). More compact morphologies exhibit a greater deficiency, so that the overall fraction remains at unity. However, the difference between even $|f_{\mathcal{R}0}| = 10^{-5}$ and ΛCDM is dwarfed by the difference between the theoretical volume fraction and the N-body result at all smoothing scales. This provides a quantitative basis for the assertion in [170] that there is insufficient evidence to warrant modelling the environment density using the $f(\mathcal{R})$ equations.

6.4.2 Multiplicity functions in each environment

We compare the behaviour of the ΛCDM mass functions to $f(\mathcal{R})$ with $|f_{\mathcal{R}0}| = 10^{-5}$ in the different structures of the cosmic web and averaged over all environments. Our semi-analytic model performs best at successively larger scales and in lower-density environments, but reproduces the main trend found in the simulations: the $f(\mathcal{R})$ abundances are amplified in underdense environments and at low masses.

[3] `https://github.com/damonge/MatchMaker`
[4] `http://popia.ft.uam.es/AHF/Download.html`
[5] `https://github.com/damonge/DensTools`

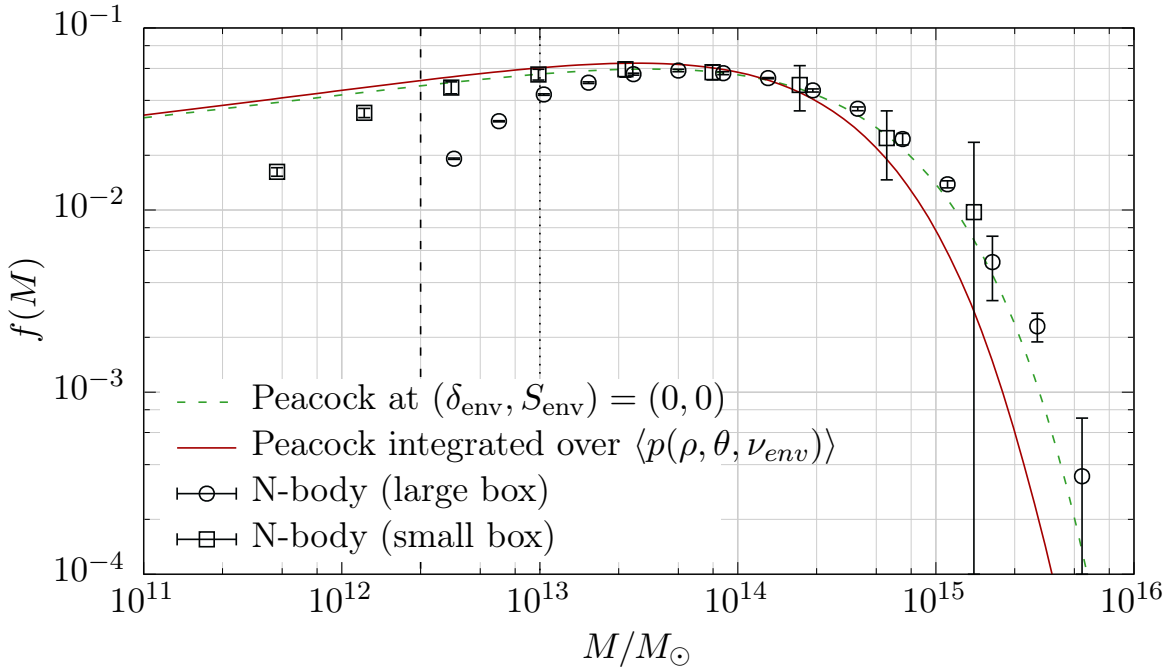

Figure 6.2: Multiplicity function $f(M)$ for each "unconditional" definition at $R_{\rm env} = 10\,{\rm Mpc}/h$. The green dashed line shows the Peacock model for the unconditional multiplicity function, while the solid red line shows our re-scaling method for the conditional mass function applied to the Peacock multiplicity function and then integrated over the environment distribution. Boxes and circles show the data from the large- and small-box N-body simulations. The cut-off below which the mass resolution of the simulations make the results unreliable are shown as dashed (dotted) lines for the small (big) simulations.

The smoothing scale determines the range of masses in which our results are reliable. Recall from Section 4.2.1 that the major shortcoming of the excursion set formalism is that whenever $S < S_{\rm env}$ the process is not well defined, since the condition $S < S_{\rm env}$ implies that the halo has already collapsed at resolution S, before the starting points of its trajectory at $S_{\rm env}$. Therefore care must be taken when interpreting any results for masses with $S \sim S_{\rm env}$. For the filter sizes used in this work, $R = 10\,{\rm Mpc}/h$ and $R = 20\,{\rm Mpc}/h$, the corresponding masses enclosed within them are $M_{10} = 1.67 \cdot 10^{15}\,M_\odot/h$ and $M_{20} = 1.34 \cdot 10^{16}\,M_\odot/h$, which act as upper bounds for the mass range where the excursion set predictions are meaningful.

A desirable property of any model of the mass function that incorporates environmental dependence is that, when marginalised over all possible environments, one should recover the unconditional mass function given by the same model. Currently our model is based on simply substituting the argument of the unconditional mass function from ν_h to $\nu_{\rm eff}$, inspired by the equivalent result found in the excursion-set formalism. However, this rescaling of the mass function is only mathematically consistent, in the sense described above, for the specific form of the Press-Schechter mass function [192]. Thus, most simple attempts at modelling the conditional mass function have only been able

to provide a qualitative description of it, with a poor quantitative performance. This problem is also illustrated in Fig. 6.2, which shows the mass function from our simulations together with the Peacock unconditional mass function and the excursion set prediction after rescaling the Peacock mass function and marginalising it over the environment. Our results agree with [192], who showed that the only solution of Eq. (4.10a) which matches the unconditional case is Press-Schechter with a δ_c linear in S. Thus we do not expect the cosmic-web-sensitive result to match the percent-level fits to N-body which motivated the unconditional form of the Peacock mass function.

The additional dependence of the collapse density in $f(\mathcal{R})$ amplifies this same problem: compare Figs. 6.3a, 6.4a, 6.5a and 6.6a to Figs. 6.3b, 6.4b, 6.5b and 6.6b, which show the multiplicity functions in different environments measured from the simulations together with the predictions of our method for a range of smoothing kernels (with $R_{\rm env} = 10$ and 20 Mpc/h in Figs. 6.5 and 6.6 and Figs. 6.3 and 6.4 respectively, and using Gaussian and sharp-k filters in Figs. 6.3 and 6.5 and Figs. 6.4 and 6.6 respectively). We concur with [170], who state that the environment-averaged result simplifies to the result with the random walk starting at $(\delta_{\rm env} = 0, S_{\rm env} = 0)$ (i.e. to the unconditional mass function) only in ΛCDM and not in $f(\mathcal{R})$. Thus we expect our fits to be less accurate (when compared to N-body results) in $f(\mathcal{R})$ than in ΛCDM, a hypothesis borne out by our results.

The trends with environment smoothing scale and density shown in Figs. 6.3 to 6.6 can be understood in terms of deviations of the non-linear environment distribution with respect to the Gaussian prediction. Having seen in Fig. 6.1 that the $R_{\rm env} = 20\,{\rm Mpc}/h$ volume fraction is well-approximated by the integral of $p(\rho, \theta, \nu_e)$, the density field on such large scales is still evolving linearly from the primordial Gaussian density field. Thus in Figs. 6.3 and 6.4, we find good agreement in both ΛCDM and $f(\mathcal{R})$, regardless of halo mass or the location within the cosmic web. On environment scales of $R_{\rm env} = 10\,{\rm Mpc}/h$, the results in Section 6.4.1 suggest that the density field evolution is weakly-linear. We expect deviations from linear collapse to occur more quickly in increasingly dense environments, where the local structures have already collapsed along one (sheets), two (filaments) or all three (knots) axes. In Figs. 6.5 and 6.6 our predictions lie within the N-body error bars at progressively fewer points for voids, sheets, filaments and knots. These trends occur independent of cosmology, which further reinforces the hypothesis that the Gaussian model for the density is responsible, as we model the large-scale structure according to general relativity in both ΛCDM and modified gravity.

Like [6], we find that the excursion-set prediction for the conditional mass function in ΛCDM becomes a worse model for the N-body data in higher-density environments, underpredicting the number of low-mass halos and over-predicting the abundance in

the high-mass tail at $R_{\rm env} = 10\,{\rm Mpc}/h$ (see Figs. 6.5a and 6.5b), and this is true also for $f(\mathcal{R})$. For a smoothing of $20\,{\rm Mpc}/h$, Figs. 6.3a and 6.3b show that the prediction becomes a much better fit, with a slight deficiency of haloes at high masses in knots.

Despite the shortcomings of the excursion set formalism when making accurate predictions for the conditional mass function, we can still use this framework to understand the differences between the ΛCDM and $f(\mathcal{R})$ predictions. The $f(\mathcal{R})$ mass functions are amplified compared to ΛCDM. The key trends visible in Figs. 6.3c, 6.4c, 6.5c and 6.6c are that the amplification increases with lower environment density. The amplification tends to increase with halo mass in voids and sheets, while there is a maximum enhancement mass in filaments and knots. This behaviour can be explained by the peak-background split. For equivalent values of S, the barrier density is lower for $|f_{\mathcal{R}0}| = 10^{-5}$ than ΛCDM, which makes it more probable for the first-crossing of the excursion set trajectory to occur. This effect is amplified by a larger value of $\delta_c(\delta_{\rm env}, S) - \delta_{\rm env}$, i.e. in voids and sheets, but damped in dense regions where $\delta_c(\delta_{\rm env}, S) - \delta_{\rm env} \to 0$ via screening. Thus, the modified gravity behaviour compared to ΛCDM is driven by screening at all scales.

In order to improve the semi-analytical model for the mass function used here, three problems need to be overcome:

- The Gaussian eigenvalue distribution $p(\rho, \theta, \nu_e)$ is a poor description on small smoothing scales.
- At resolutions smaller than $S_{\rm env}$, the excursion set theory which underpins the first-crossing distribution is undefined.
- The $\nu \to \nu_{\rm eff}$ rescaling is known to be a poor approximation to the conditional mass function even in ΛCDM.

The first issue can be resolved in three ways. Following [6], we could replace the functional form with the distribution of values from the N-body simulations. We find this solution unsatisfactory, due to the requirement to run many realisations to avoid cosmic variance and the dependence upon individual simulation parameters. However, as [6] note, this remains a useful technique to separate the effects of the Gaussian density field from the other approximations. Alternatively, it may be possible to add small-scale corrections to the probability density function, or to replace the Gaussian density field of [18] with the log-normal density field proposed by [72].

The second item appears to be insurmountable. This is because $M(S_{\rm env})$ is completely controlled by our smoothing scale $R_{\rm env}$ via the window function. Fortunately, on mildly non-linear scales and larger, there are so few haloes with $M > M(S_{\rm env})$ that the problem

is only an issue in mass bins which are already uncertain due to small-number statistics and cosmic variance. Resolving these problems will improve the quantitative accuracy of our model beyond the large-scale, low-density regime. [6] found a better fit to the data by using an "effective-universe" approach, where halo abundances in an environment with overdensity $\delta_{\rm env}$ are predicted as the unconditional abundance in a universe with effective cosmological parameters governed by the value of $\delta_{\rm env}$, and the $S_{\rm env}$ mass cut is accounted for in an ad-hoc manner by limiting the Fourier modes available in that effective universe to those smaller than $\sim R_{\rm env}$. While there remain quantitative issues to overcome, our extremely simple model performs well qualitatively on all scales and in all density environments.

The last item is not readily solved, and is a common limitation of the conditional mass function. In order to produce an environment definition more akin to the excursion-set formalism we have also studied cases where the density field is filtered using a sharp-k window function. As shown in Figs. 6.4 and 6.6, this produces a better agreement with the N-body simulations. A possible improvement may be to use an alternative to excursion set, *e.g.* the survival probability approach of [194] or the Markovian Velocity excursion set of [184].

We have seen in the preceding two sections that the model illustrated in this chapter is qualitatively useful but not always quantitatively accurate. At large smoothing scales, where we are in the linear regime, our results agree well with the full N-body calculations. As we move to smaller scales, we encounter the increasing non-Gaussianity of the environment overdensity and the chameleon regime of the $f(\mathcal{R})$ modification. While we can extend our model into this regime in low-density environments, it performs badly in knots, and by non-linear scales we only reproduce qualitative behaviour. Nevertheless, we can attribute the difficulties to certain approximations and assumptions in our model, which in turn suggests avenues for improving our results.

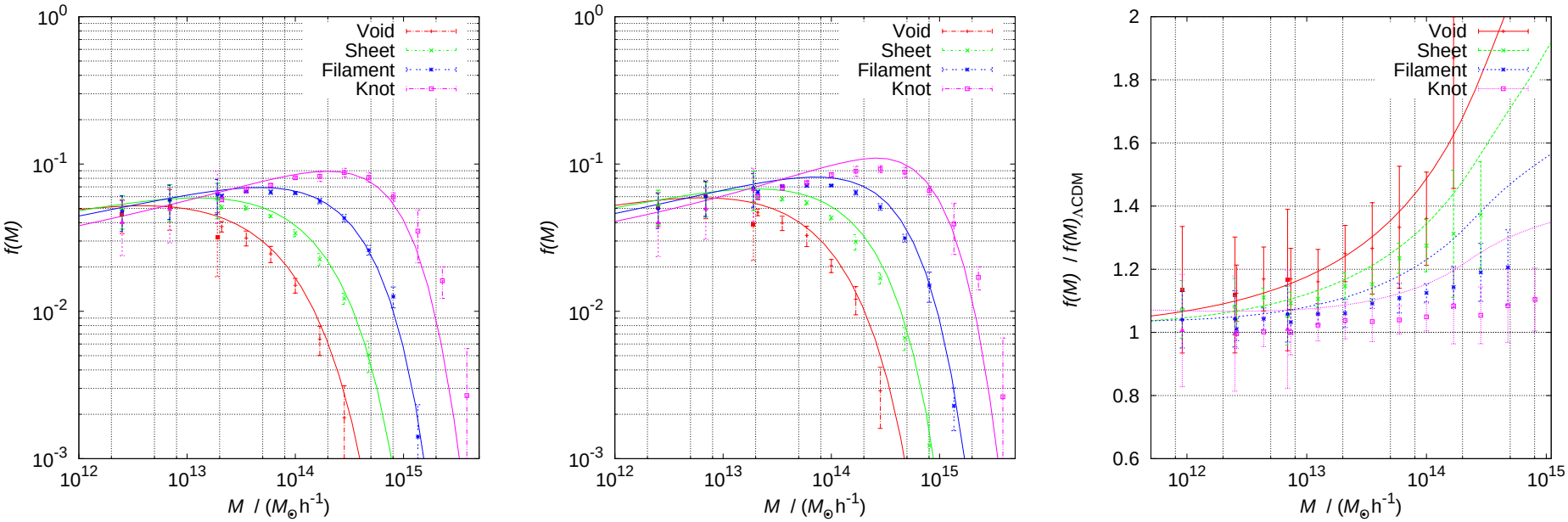

(a) Multiplicity for ΛCDM

(b) Multiplicity for $|f_{\mathcal{R}0}| = 10^{-5}$

(c) Ratio of the $|f_{\mathcal{R}0}| = 10^{-5}$ to ΛCDM results.

Figure 6.3: $f(M)$ for each environment at $R_{\rm env} = 20\,{\rm Mpc}/h$, assuming a Gaussian window function. Lines indicate our model according to Eq. (4.22) and points indicate the N-body results.

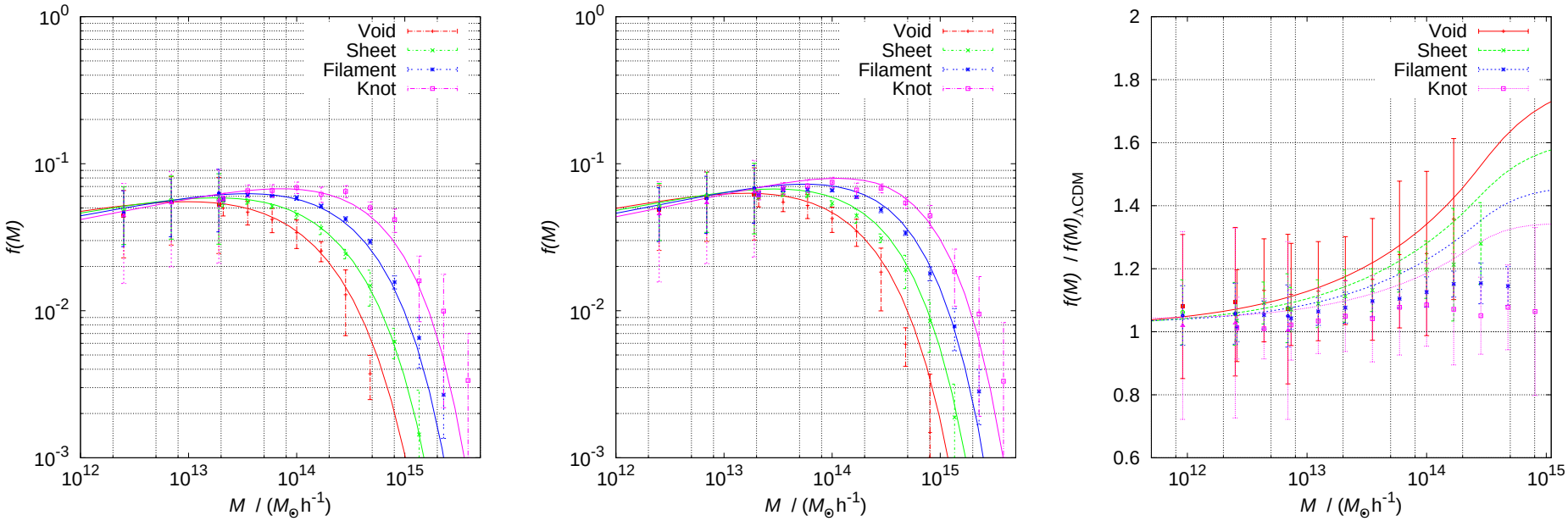

(a) Multiplicity for ΛCDM

(b) Multiplicity for $|f_{\mathcal{R}0}| = 10^{-5}$

(c) Ratio of the $|f_{\mathcal{R}0}| = 10^{-5}$ to ΛCDM results.

Figure 6.4: $f(M)$ for each environment at $R_{\rm env} = 20\,{\rm Mpc}/h$, assuming a sharp-$k$ window function. Lines indicate our model according to Eq. (4.22) and points indicate the N-body results.

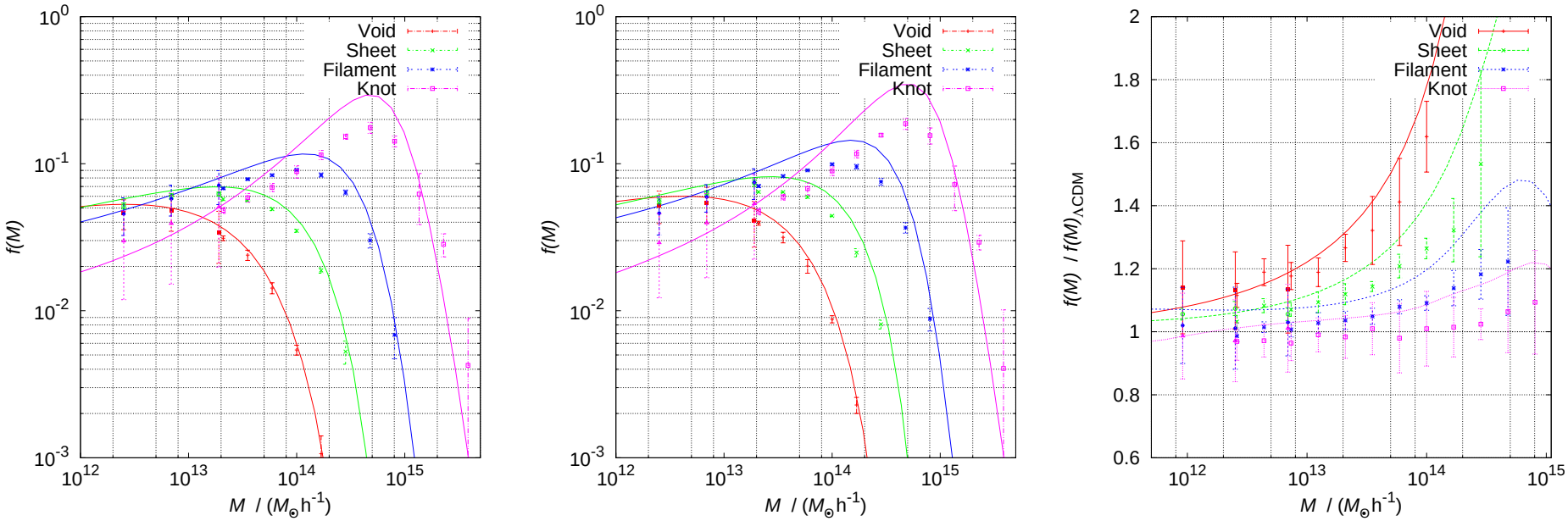

(a) Multiplicity for ΛCDM

(b) Multiplicity for $|f_{\mathcal{R}0}| = 10^{-5}$

(c) Ratio of the $|f_{\mathcal{R}0}| = 10^{-5}$ to ΛCDM results.

Figure 6.5: $f(M)$ for each environment at $R_{\rm env} = 10\,{\rm Mpc}/h$, assuming a Gaussian window function. Lines indicate our model according to Eq. (4.22) and points indicate the N-body results.

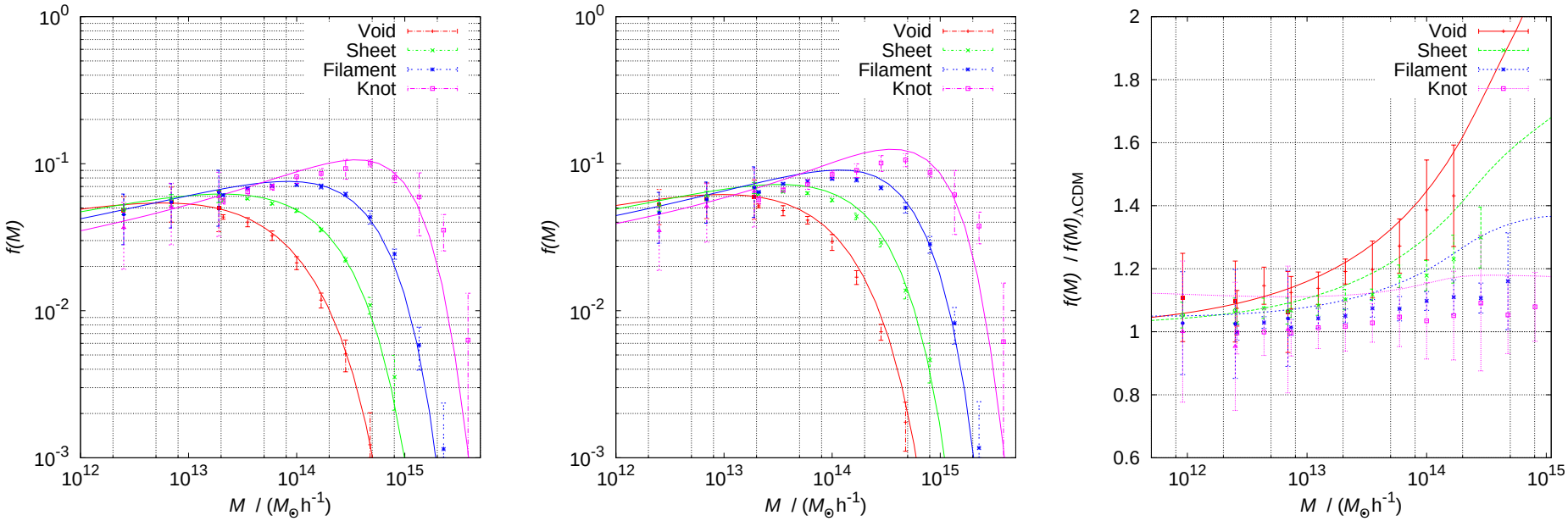

(a) Multiplicity for ΛCDM

(b) Multiplicity for $|f_{\mathcal{R}0}| = 10^{-5}$

(c) Ratio of the $|f_{\mathcal{R}0}| = 10^{-5}$ to ΛCDM results.

Figure 6.6: $f(M)$ for each environment at $R_{\rm env} = 10\,{\rm Mpc}/h$, assuming a sharp-$k$ window function. Lines indicate our model according to Eq. (4.22) and points indicate the N-body results.

6.4.3 Multiplicity functions at fixed environment density

One of the key predictions of the excursion-set formalism in ΛCDM cosmologies with Gaussian initial conditions is that halo abundances only depend on the density of the environment, i.e. not on any other local environmental parameters. In spite of the approximate nature of this formalism, this result was found to be true in [6] in comparison with N-body data. Therefore, it is interesting to explore whether the same is true for modified gravity theories.

Fig. 6.7 shows the conditional mass function for fixed environmental densities in different types of environments defined in terms of the eigenvalues of the tidal tensor. We do not find significant differences between environments in terms of halo abundances. This is also a prediction of our semi-analytic model: we treat the environment as if it were ΛCDM (rather than with a full $f(\mathcal{R})$ treatment) not only in calculating the environment density ODE, an approximation justified in [170]; but also (via the power spectrum) the environment variance. Furthermore, the only change from ΛCDM to $f(\mathcal{R})$ in our model is the barrier density, which itself is only a function of $\delta_{\rm env}$ and not of (ρ, θ). This is an *a priori* simplification which is a corollary of only examining the modified gravity collapse assuming spherical symmetry, instead of the full ellipsoidal collapse. Nevertheless, as in the case of ΛCDM, we find that this phenomenological result is in agreement with the simulated data. It could be that $f(\mathcal{R})$ does modify the ΛCDM result in certain regimes, but $R_{\rm env} = 10/h$ Mpc is a sufficiently large scale that the modifications are negligible, i.e. the $f(\mathcal{R})$ modification is in the cosmological regime where it must mimic the ΛCDM background. Alternatively, perhaps the influence of $f(\mathcal{R})$ is minimal on the structure of the cosmic web (*e.g.* by late times non-linearities in the density field or the merger history of haloes may overwhelm any contribution from modified gravity) so the same physics dominates in both cosmologies. Regardless, the fact that we encounter the same result in both the semi-analytical and the numerical solution is encouraging.

6.4.4 Internal halo properties

The relation of certain internal halo properties with the tidal structure of the environment could also potentially contain relevant signatures for modified gravity models. To this end, we have studied the relative orientation of the halo shapes and halo spins with respect to the eigenvectors of the local tidal tensor, as well as the distribution of the halo spin parameter and the concentration-mass relation as a function of environment type. In order to obtain reliable estimates of these internal properties, we selected a subset of the halo catalogue containing only virialised structures (as done in [165]) with more

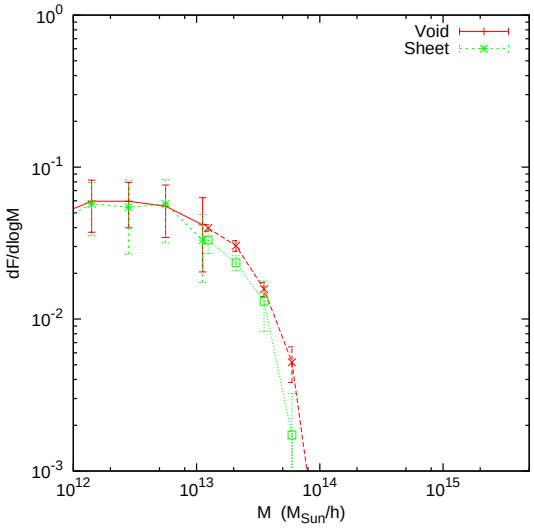

(a) ΛCDM, $\delta_{\rm env} \in [-0.5, -0.3]$

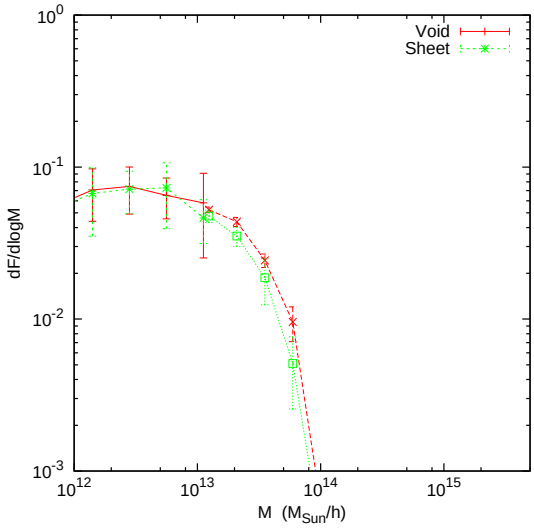

(b) $|f_{\mathcal{R}0}| = 10^{-5}$, $\delta_{\rm env} \in [-0.5, -0.3]$

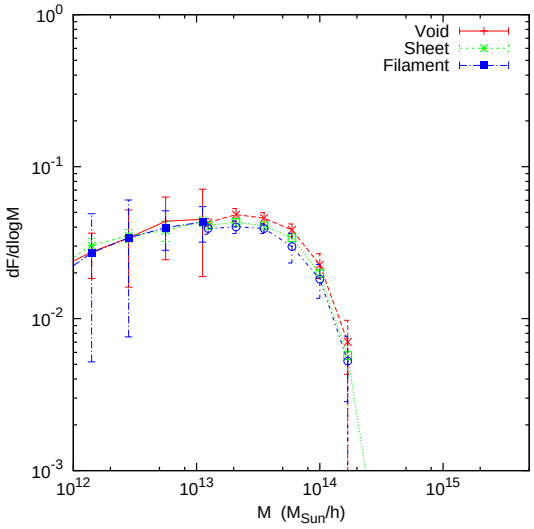

(c) ΛCDM, $\delta_{\rm env} \in [-0.1, 0.1]$

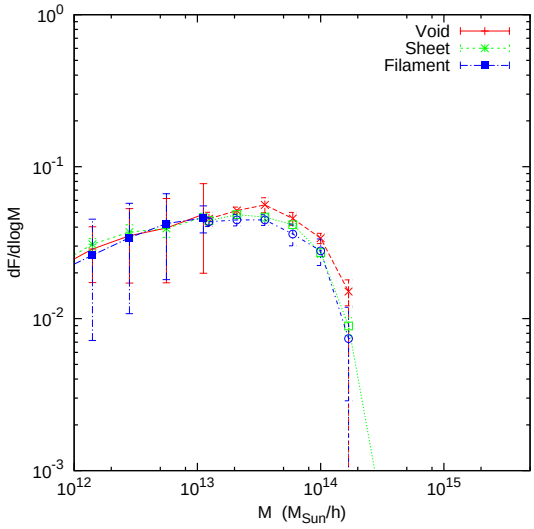

(d) $|f_{\mathcal{R}0}| = 10^{-5}$, $\delta_{\rm env} \in [-0.1, 0.1]$

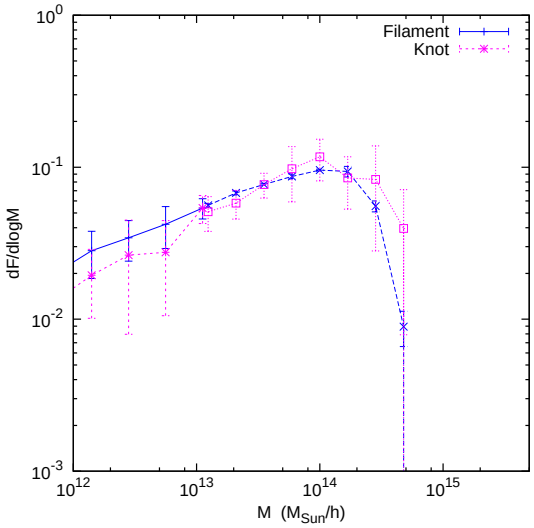

(e) ΛCDM, $\delta_{\rm env} \in [0.45, 0.65]$

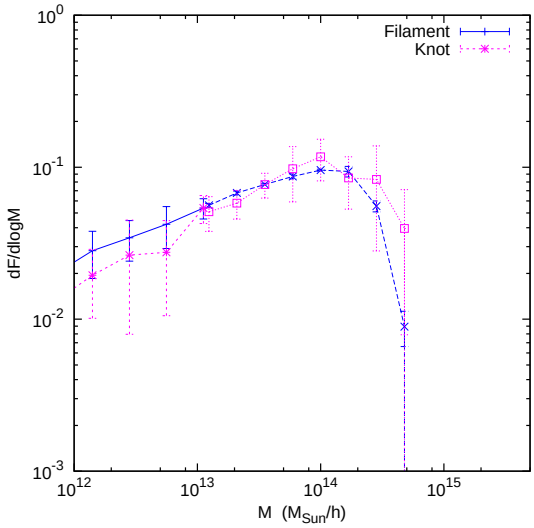

(f) $|f_{\mathcal{R}0}| = 10^{-5}$, $\delta_{\rm env} \in [0.45, 0.65]$

Figure 6.7: Multiplicity at $R_{\rm env} = 10/h$ Mpc after restricting the range of $\delta_{\rm env}$.

than 100 particles per halo. While [65] suggest a cut-off of 300 particles per halo, on the basis of ensuring that the resolution bias is less than 10% compared to the ellipticity result from sampling a halo of 1000 particles, our smaller cut-off produces a maximum resolution bias of $\sim 60\%$, which declines to $\sim 30\%$ as the ellipticity increases. This affects the uncertainty on the shape of the haloes: thus, any difference between ΛCDM and $f(\mathcal{R})$ would have to exceed this uncertainty to be a non-null result. We select only virialised structures by combining the kinetic energy T, gravitational potential energy W and surface pressure term E_S of the halo to define a parameter η such that:

$$2T + W - E_S = 0 \implies \eta = \frac{2T - E_S}{W} + 1 \approx 0 \tag{6.5}$$

The first equality is the virial theorem, which defines a virialised structure by virtue of having reached a state of equilibrium [109]. The possibly non-zero value of η allows for uncertainty in the measurement of the kinetic energy of the halo, so we set haloes with $\eta < 0.2$ to be virialised in accordance with the literature [165]. The decision to remove non-virialised haloes, rather than keeping all gravitationally-bound structures, stems from the different distributions of halo properties within the two classes of haloes [109]. We compute the relative orientation of the halo shape by estimating the inertia tensor of the halo as [66, 165]:

$$I_{ij} \propto \sum_{n=1}^{N_{\rm part}} x_{n,i} x_{n,j} \tag{6.6}$$

where the position of the n-th halo is x_n along each axis $i, j \in [1, 3]$ and the sum is over all particles in the halo. The principal axis of the halo is then defined as the eigenvector corresponding to the largest eigenvalue of $\hat{I}$, the (reduced) inertia tensor. For each halo we then compute μ_{11} and μ_{13}, the cosine of the angle between its principal axis and $\mathbf{e}_1$, and $\mathbf{e}_3$, the eigenvectors of the local tidal field (defined with a smoothing scale $R_{\rm env} = 10\,{\rm Mpc}/h$) corresponding to the largest and smallest eigenvalues respectively. Fig. 6.8 shows the average μ_{11} and μ_{13} as a function of halo mass in the four different environment types. We find no significant difference between ΛCDM and $f(\mathcal{R})$ in the relative halo orientations with respect to the cosmic web. We also performed a similar analysis studying the relative orientation between the principal directions of the cosmic web and the halo spin. We found no significant difference between $f(\mathcal{R})$ and ΛCDM in this case either. Given the interpretation of [71] that the alignment between dark matter haloes and the cosmic web is driven by the dynamics of cosmic flows during the merger history of the haloes, it is unlikely that this behaviour should be altered by modifications to gravity. Specifically, the presence of the scalar field will affect the gravitational interaction during halo mergers, which are the key contributors to the final orientation and spin of the haloes. However, if haloes flow preferentially towards

increasingly collapsed structures, ([71]; *e.g.* along filaments towards knots), then the merger history of these haloes will occur in increasingly screened areas. If the halo formed at early times (even in an unscreened void), each additional contribution to its orientation and/or spin vector will tend towards the ΛCDM equivalent, washing out any initial $f(\mathcal{R})$ modification to the large-mass haloes. In ΛCDM, [71] find that haloes above a threshold of $M > (8 \pm 2) \cdot 10^{12} M_\odot$ exhibit this large-mass behaviour, which is the range we have tested here. Thus our null result is consistent with current interpretations of dark matter halo formation.

It is also customary to define the halo spin parameter [56]

$$\lambda \equiv \frac{|J|}{\sqrt{2G} M^{3/2} R^{1/2}}, \tag{6.7}$$

where $\mathbf{J}$ and R are the halo angular momentum and virial radius respectively. The distribution of λ is known to be only mildly dependent on mass[6] and redshift in ΛCDM [39, 114], and therefore it is interesting to explore departures from this independence in modified gravity theories. Fig. 6.9a shows the spin distribution for all halos in the ΛCDM and $f(\mathcal{R})$ simulations and Fig. 6.9b the ratio of the distributions between both cosmologies for the four different environment types. The spin-parameter is seen to be higher in modified gravity which is in agreement with what was previously found in [153]. We also split the halo catalogue into two samples $M < 3 \cdot 10^{13} M_\odot$ and $M > 3 \cdot 10^{13} M_\odot$ and computed the PDF in each of the samples. For the high-mass sample the PDF is very close to ΛCDM while for the low-mass sample the PDF is as in Fig. 6.9.

This agrees with [153] where the conclusion (for the same $f(\mathcal{R})$ model, but with $|f_{\mathcal{R}0}| = 10^{-6}$) was that modified gravity spins up galactic-sized halos. We can intuitively understand why spin has to be modified via Eq. (6.7). Let us approximate the spin as $|\mathbf{J}| = MR\,|\mathbf{v}|$. Recalling Eq. (2.13), we see that G is enhanced by the factor $(1 + F_{\rm eff})$ with $F_{\rm eff} \in \left[0, \frac{1}{3}\right]$. Thus we indirectly increase $|\mathbf{v}|$, with $v \propto G$ in the linear regime, leading to the approximation $\lambda \propto \sqrt{(1 + F_{\rm eff})G}$. In the absence of screening we would expect $\lambda^{f(\mathcal{R})}/\lambda^{\Lambda\rm CDM} \approx \sqrt{1 + \frac{4}{9}}$, a factor of 1.2. In practice, this is an upper bound because we have neglected the non-linear regime (in which $v \propto G$ does not hold) and the distribution of partial screening. The shift in the PDF we find is roughly $\lambda^{f(\mathcal{R})}/\lambda^{\Lambda\rm CDM} \approx 1.04$ which is within our upper bound. We also see a clear dependence of the spin-parameter in the cosmic web. Fig. 6.9b demonstrates that the spin parameter is boosted mostly in low density environments (in voids and sheets) whereas in high-density environments (in filaments and knots) the value is close to ΛCDM for all

[6] This dependence is described by [39] as "small but real" but the precise nature of it is so dependent upon the halo finder used that they do not quantify the dependence for the FOF finder used in this chapter.

values of λ. This is as expected due to the environmental dependence of screening: a halo that is not screened if placed by itself might still be screened if placed in a high density environment. Given the density ranges in Eq. (4.18), the trend of enhancement with tidal morphology is what we expect from theory.

In Fig. 6.10 we see the dependence on the NFW concentration-mass parameter with mass and environment. The concentration-mass is enhanced in our $f(\mathcal{R})$ model for halos with mass in the range $M \lesssim 10^{14} M_{\odot}/h$, whereas for halos of larger mass the results are close to ΛCDM. This agrees with the results of [168], which only considered cluster-sized halos. There is some dependence on the cosmic web, but it is insignificant in comparison with the scatter in each mass-bin.

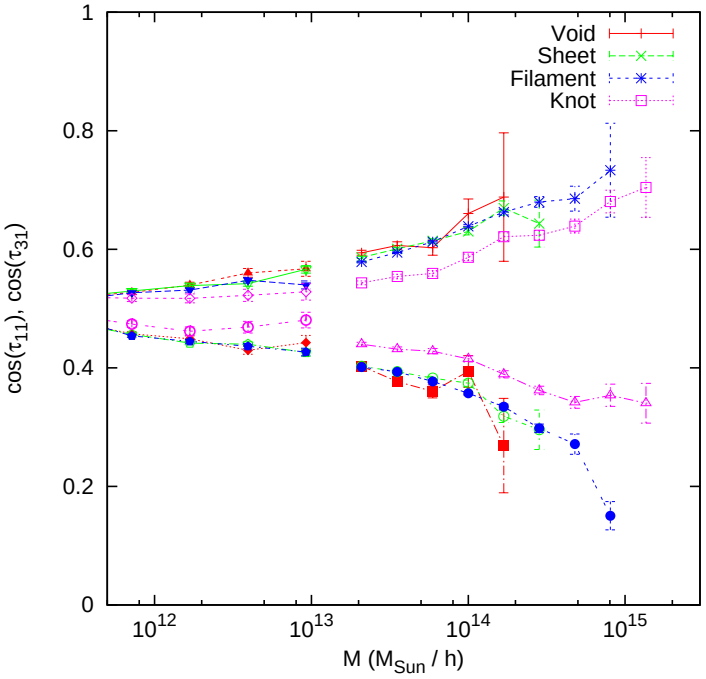

(a) ΛCDM

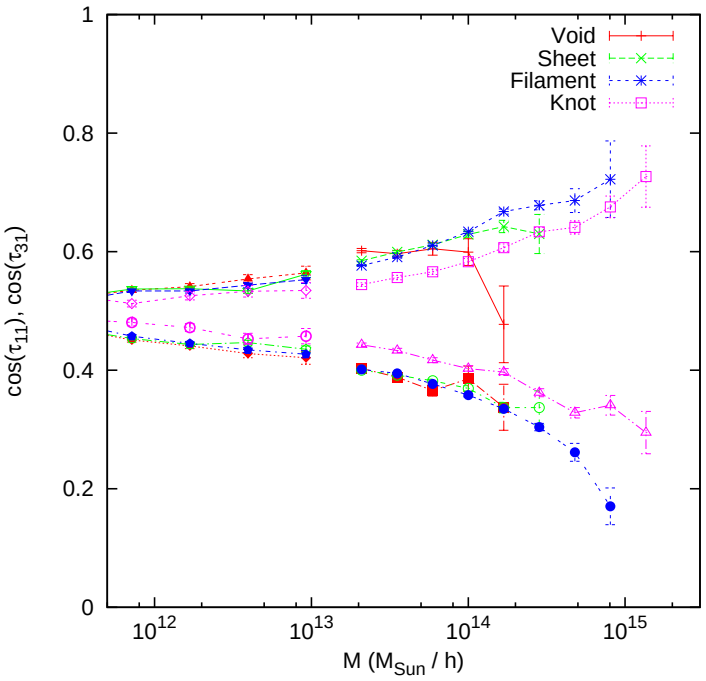

(b) $|f_{\mathcal{R}0}| = 10^{-5}$

Figure 6.8: Alignment between the halos and the environment for ΛCDM (left) and $f(R)$ (right). The angle $\cos(\tau_{ij})$ is between the i-th axis of the halo and the j-th axis of the environment. The smoothing scale here is $R = 10$ Mpc$/h$ and eigenvalue threshold is $\lambda_{\rm th} = 0.1$. The different point types correspond to the different elements of the cosmic web and the connecting lines are to aid the eye.

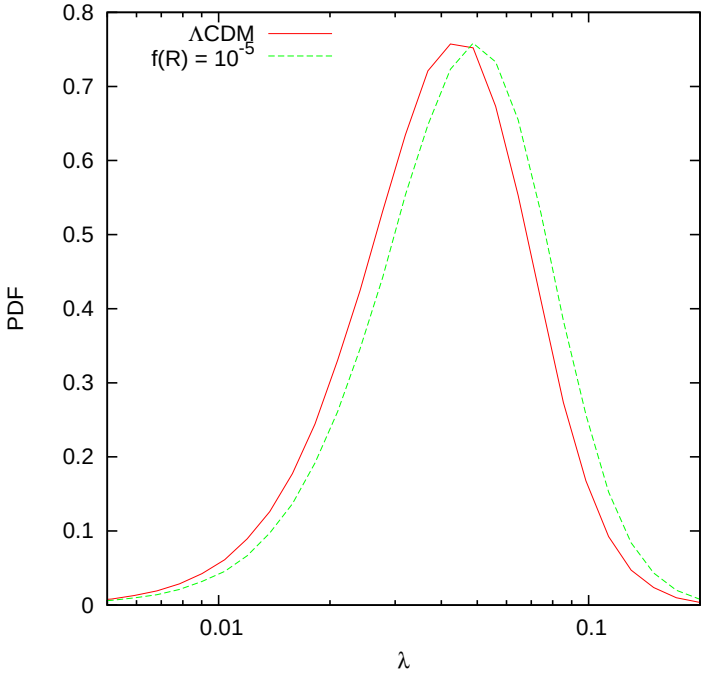

(a)

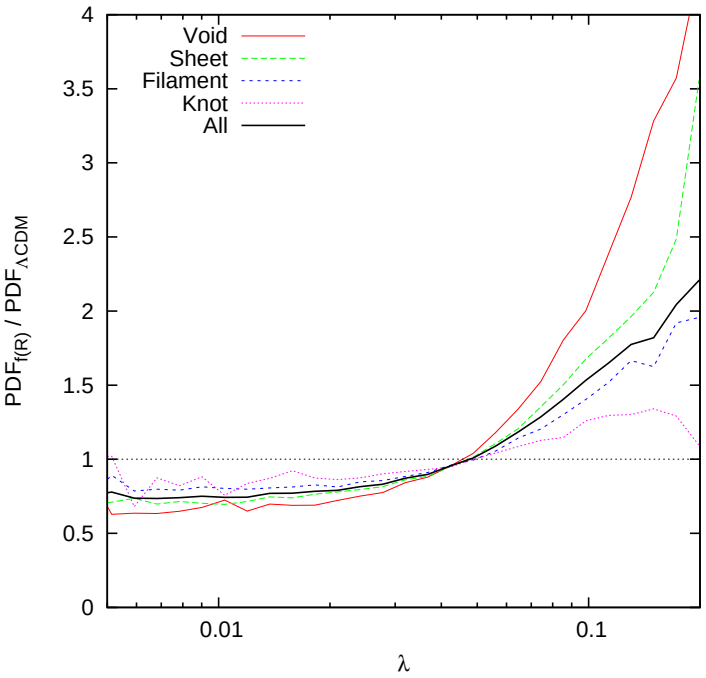

(b)

Figure 6.9: The PDF of spin-parameter (left) for ΛCDM and $f(R)$. We also show the ratio of the PDF in Λ to that in $f(R)$ for the four environments. The smoothing scale here is $R = 10$ Mpc$/h$ and eigenvalue threshold is $\lambda_{\rm th} = 0.1$

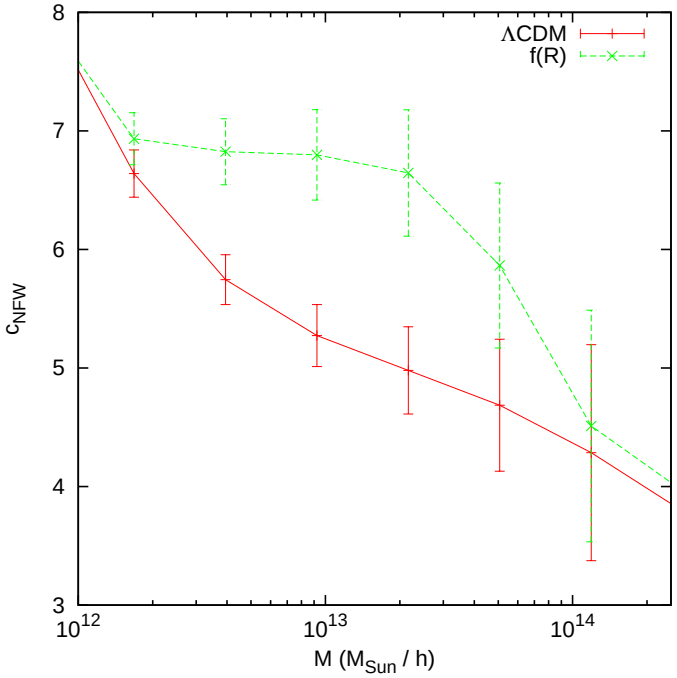

(a)

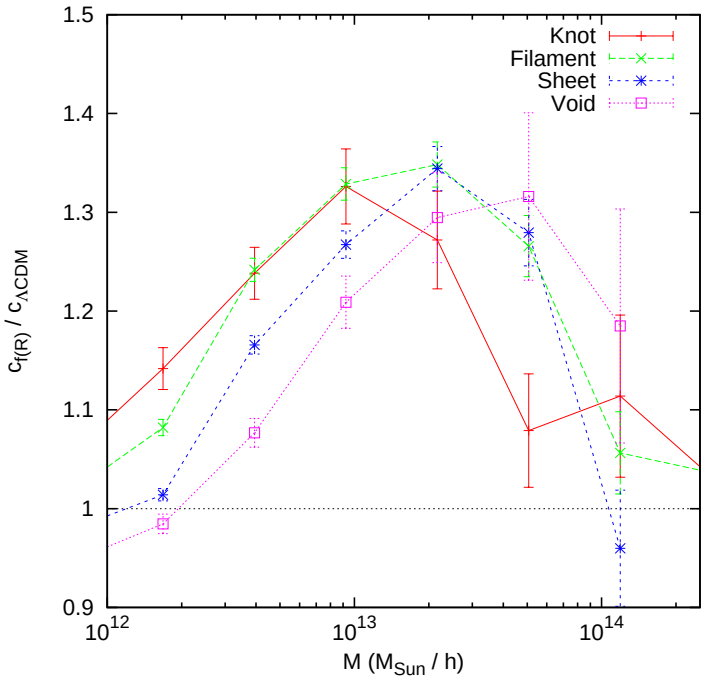

(b)

Figure 6.10: The NFW concentration parameter in $f(\mathcal{R})$ and ΛCDM (left). We also show the ratio of the concentration parameter in ΛCDM to that in $f(\mathcal{R})$ for the four environments (right). The smoothing scale here is $R = 10$ Mpc/h and eigenvalue threshold is $\lambda_{\rm th} = 0.1$

6.5 Discussion

We study the properties of dark matter haloes in the context of the environmental tidal classification of the cosmic web in $f(\mathcal{R})$ theories. This classification defines four different types of environments based on the directionality of the tidal forces: *voids* are defined as regions of space where tidal forces will expand an extended object in all directions, *sheets* and *filaments* have instead one or two compressing directions respectively, and in knots tidal forces will only compress structures. The relation between the gravitational potential and the density field also implies that these environment types will sample partially overlapping ranges of densities, and thus this classification can be a useful tool to study the effect of the chameleon screening, present in viable $f(\mathcal{R})$ theories, on the properties of dark matter haloes.

We have described an approximate method to predict the abundance of dark matter haloes in each environment type. Recall that our purpose was to use excursion set theory to take into account as much of the structure of the cosmic web and the non-linear collapse in $f(R)$ as possible in a semi-analytic model, in order to obtain results that can fit numerical simulations. Thus, we incorporated both the moving barrier of the excursion-set formalism—inherent in screened models—and the analytical description of the mass function conditional upon tidal environment described in [6]. When comparing this prediction with the data from simulations we find that, even though the method is able to reproduce the correct behaviour of modified gravity theories qualitatively, the predictions become unreliable in high-density environment and for mildly non-linear filter scales. The method is, however, able to predict the enhanced abundance of high-mass objects found in low-density environments, a direct consequence of chameleon screening, and the prediction is accurate in voids, where the departure from ΛCDM is largest. The shortcomings of this model are directly related to the inability of the traditional excursion-set formalism to accurately describe the conditional mass function, and we have outlined a number of ways forward to improve the predictions.

In spite of these shortcomings, we have gained further insight into the possible impact of modified gravity on halo properties conditional on environment by directly comparing the results of $f(\mathcal{R})$ and ΛCDM simulations:

- One of the key predictions in ΛCDM is that halo abundances should only depend on the environmental density, and not on the directionality of the tidal forces. Our results show no significant departure from this behaviour in $f(\mathcal{R})$, at least on mildly non-linear filter scales.

- We have identified a number of internal halo properties that are not affected by modified gravity in this context. In particular, we find that the alignment of

halo orientations and spins with respect to the principal tidal directions of the environment.

- We have also seen that, even though the mass-concentration relation is different in $f(\mathcal{R})$ and ΛCDM, its dependence on the tidal environment only shows marginally significant differences between both models.

- We observe a dependence in the distribution of the halo spin parameter upon tidal environment, with stronger deviations from the ΛCDM results in voids and sheets, as expected in the presence of chameleon screening.

Incorporating morphological classification of the cosmic web into the existing analysis of dark matter halo properties increases their utility as a probe of modified gravity. By doing so we can distinguish between the collapsed mass fraction in $f(\mathcal{R})$ and ΛCDM far more than merely using the unconditional result, especially in low-density environments. Furthermore, we can draw a boundary between the halo properties that are affected by screening and those which are not by explicitly examining the results in screened and unscreened regions, rather than averaging the effect over the distribution of environmental properties. While we find three null results, we also have three avenues for detecting the presence of $f(\mathcal{R})$ theories which are designed to evade local tests.

Chapter 7

Conclusions

This chapter highlights the significant elements of the work performed in this thesis. It is useful to remind ourselves of the key points raised in the Introduction. This enables us to place its aims into the wider context of modern cosmology. Having seen that GR is a special case within a broader field of theories, we then focus on the MG theories which are used in this thesis. Next, we summarise the logical flow of the research. Then we summarise the methods developed in each chapter and the corresponding results. Finally, we close with an assessment of how this work can be expanded in the future.

The principles of GR illustrate a shift from a force-based to a geometry-based theory of gravity. The equivalence of inertial and gravitational masses is inherited from Newtonian gravity. Once we add Special Relativity, we are left with a division between observers in inertial reference frames, in which SR holds, and those in non-inertial frames. The combination of these two theories leads to the "tower" of weak, Einstein and strong equivalence principles. We can use the EEP to construct plausible theories of gravity and the SEP to distinguish GR as a "special" case. In this way, the geodesic equation determines the trajectories of objects in a given geometry. Space is no longer an inertial, absolute frame through which gravity distorts that trajectory of masses; instead gravity is a local curvature of space(time) which determines the geodesics of masses. We are left with the inverse problem, namely, to describe the effect of bodies on the geometry of spacetime. The Einstein equation $\mathbf{G} = \kappa\mathbf{T}$ which solves this problem, describes a non-linear, tensor theory of gravity. This is remarkably more complex than the linear, scalar form of Newtonian gravity.

GR has performed remarkably well at predicting and explaining cosmological data. This is particularly surprising given the large range of scales (Solar System to super-horizon),

curvatures (weak- to strong-field) and energies (e.g. evolution of the temperature of the CMB) at which gravity has been tested. In particular, the CMB, BAO, LSS, RSDs, (Type Ia) SNe and weak lensing can all potentially distinguish between GR and extended gravity theories. Current observations have lead to the development of ΛCDM as a description of the Universe which is compatible both with the principles of GR and (to a large degree) with current data. Thus we have an FLRW metric with flat ($\Omega_k = 0$) spatial geometry, so that the Einstein tensor only depends upon the scale factor $a(z)$ and derivatives. The corresponding stress-energy tensor is a perfect fluid consisting of baryonic and cold dark matter and a cosmological constant, with energy densities Ω_b, Ω_c and $\Omega_\Lambda = 1 - (\Omega_b + \Omega_c)$ respectively. The expansion of the Universe is characterised by the last-scattering horizon scale $\theta_{\rm MC}$ and Hubble constant H_0. Linear perturbations require a single scalar potential. On non-linear scales, σ_8 characterises the variance of density fluctuations. This is the concordance cosmology[1] against which we test MG theories.

Given the observational success of GR, we are interested in MG theories whose background evolution agrees with the model provided by ΛCDM. On linear scales, the MG contribution is to remove the equality of the two scalar potentials Φ and Ψ in the perturbed FLRW metric. On non-linear scales, we must turn to the excursion set model of halo formation to test MG.

The aim of Chapter 2 is to characterise GR as one solution amongst a broader class of theories which obey the EEP. We have seen that this large body of MG theories can be classified into families in a number of ways. Lovelock's Theorem implies that any MG theory must relax one or more conditions—four-dimensionality, additional fields, Lorentz invariance, and/or locality—which are characteristic properties of GR. The three theories which we studied in this thesis form a sample across some of these properties. Despite these differences, they share a common trait known as screening. This describes a self-concealing property whereby each theory behaves like GR in the conditions of the local Universe. Only at regions of high energy density (chameleon), large coupling to matter (symmetron) or large derivatives of the scalar field (Vainshtein) does their modified behaviour emerge. The main result of Chapter 2 was the simplification that we can approximate the effects of generalising GR to a modified Poisson equation, provided that we work in the weak-field limit and assume that the quasi-static approximation holds. The effects of this fifth-force interaction on the formation of dark matter haloes is the focus of this work.

Our first task was to prove that these caveats are satisfied in the remainder of this work. Since the weak-field limit is satisfied because we are only concerned with the gravitational collapse of local over-densities into dark matter haloes, we need only

[1]The other parameters, e.g. A_s, n_s, τ are of no particular interest in this work.

look at the quasi-static approximation. In Chapter 3, we examined the efficacy of the quasi-static approximation in chameleon theories of gravity. We used a scalar field with a quintessence and an exponential potential before moving to $f(\mathcal{R})$ gravity. We derived the linear perturbations for the scalar field equations of motion and the Poisson equation in both the synchronous and conformal Newtonian gauges, before carefully applying the two approximations involved in the quasi-static limit. Comparison of the terms in these equations between both gauges illustrated the accuracy (or lack thereof) of the quasi-static approximation compared to the full solution. The essential result was that the performance of the perturbed equations was controlled not by the perturbed quantities but by the background values. In the fast-roll regime of the background field, the scalar field derivatives became non-negligible, leading to an inaccurate quasi-static limit. Conversely, in the slow-roll regime, the derivatives were negligible and the quasi-static approximation performed well. In fact, the slow-rolling field had an accurate quasi-static solution even outside its assumed region of validity, beyond linear scales.

Having established that the quasi-static approximation holds in screening scenarios which are cosmologically plausible, we can now apply the MG Poisson equation in the context of the collapse of overdensities. In Chapter 4 we showed that the equations for collapse of a spherical top-hat overdensity in GR can be modified to the equivalent equation in MG by the addition of a $(1 + F_{\rm eff})$ factor in the non-linear term. (The chameleon screening has the additional complication that we must solve the MG equation for the halo and the GR equation for the environment simultaneously.) Using a bijection scheme we calculated the collapse density and compared to existing results.

Similarly, the excursion set formalism can also be re-used in MG, albeit without the analytic solution arising from a flat barrier in GR. The remainder of Chapter 4 we devoted to solving the integral equations for the drifting-and-diffusing barrier of the collapse density in MG. Moreover, we used this result to also generalise the fitting functions which are derived in ΛCDM N-body simulations to screened MG. While Vainshtein screening (DGP) and symmetron screening prove straightforward, we found a plethora of possible methods to account for the environment-dependence of chameleon screening ($f(\mathcal{R})$). In addition to examining the behaviour of existing methods—namely using the equivalent to Press-Schechter, the unconditional HMF, integrating the conditional HMF over Lagrangian or Eulerian distributions for $p(\delta_{\rm env})$—we also proposed three new methods. The first marginalises over the $\delta_{\rm env}$-dependence when calculating the critical density δ_c rather than the first-crossing distribution $f(S)$. The second scales the unconditional HMF according to the Volterra integral equation which is the MG excursion set equivalent to Press-Schechter. The third involved using the cosmic web effective-ν approach and integrating over the distribution $p(\rho, \theta, \nu_e)$. While the first

two methods provided a more competitive fit than existing proposals, the last was not so effective. Fortunately, the relatively simple (and computationally-expedient) method of scaling the unconditional HMF according to the enhancement from solving the Volterra equation (compared to Press-Schechter), proved to be a good fit to the data. The methodology established in this chapter formed a basis for the next two chapters.

Chapter 5 was devoted to calibrating our MG HMFs with the same rigour as the methods used in ΛCDM. We developed a straightforward method to generalise existing HMFs which are derived in ΛCDM simulations to MG. Our main result was that these HMFs can be utilised in screened MG. Consequently, one does not need to repeat the cumbersome invention of new fitting functions as occurred when improvements to Press-Schechter were required in GR. This is particularly useful in MG because the fifth-force equations make N-body simulations more time-consuming and computationally intensive. Moreover, the framework which we use to generalise the HMFs has a theoretical foundation in excursion set theory, rather than being a purely empirical method. It is remarkable that such a simple physical model provides such a good fit to the complex evolution of dark matter haloes seen in N-body simulations.

However, Chapter 5 also demonstrated some of the caveats of this framework. The calibration process is vulnerable to the choice of likelihood function, the width of the binning and the usual minefield of MCMC settings. Therefore, it was necessary to tune the MCMC routine on artificial data (for which we already knew the correct values) and to confirm that our optimal-binning estimate performed well (i.e. that the bins were neither too narrow nor too wide). In particular, we highlighted the advantage of a Bayesian approach—utilising the Poissonian likelihood appropriate to the problem—compared to a frequentist approach equivalent to using a Gaussian likelihood. This placed us in a position to explore two problems: the potential for MG to be misinterpreted as a change in ΛCDM parameter values and the universality of the HMF in screened MG.

We ran the ΛCDM HMFs using the data from the MG simulations. This illustrated that it was possible for an ΛCDM fitting function to provide a good fit to the MG data. In order to distinguish between ΛCDM and MG in this case, one would have to compute the odds ratios of the evidence. While Dvali-Gabadadze-Porrati and ΛCDM were largely indistinguishable from one another, these theories clustered in a different region of parameter space to the Symmetron and $f(\mathcal{R})$ models. Although one could in principle separate the symmetron/chameleon screened results from the Vainshtein-screened/purely-GR ones, it was not possible to be more specific. Consequently, this is one method by which to probe MG, provided that we have enough halo data at a sufficient mass range. We also used the invariance (or lack thereof) of the best-fit

parameters as a measure of the universality (or not) of HMFs to the underlying theory of gravity. We computed the best-fit parameters for each fitting function using the same MG model for the data and the collapse density δ_c. Our main results were that in most fitting functions, the credible regions for every MG model were in good agreement. In some HMFs, the two Symmetron models were quite distinct from the other five. This behaviour can be attributed to the performance of the spherical collapse model in estimating the non-linear behaviour of the actual halo formation.

Additionally we investigated the behaviour of the HMF in different structures in the cosmic web. We limited ourselves to chameleon $f(\mathcal{R})$ gravity for this chapter. This method, which we already used in our techniques to integrate out environment dependence, can also be used to isolate different environments. The cosmic-web-conditional formula for the HMF depends only on δ_c instead of having to solve the excursion set integral equation. The trade-off is that we have a 3d integral over the eigenvalues of the tidal tensor. By applying different limits to the integral, we classified large-scale structure according to the number of collapsed axes, finding a probability density function for each structure. However, the local environment overdensity was the sole factor controlling the conditional HMF, which was largely independent of the number of collapsed axes (measured by the ellipticity and prolateness along with the overdensity). It was unexpected that $f(\mathcal{R})$ reproduced this result from ΛCDM. Our semi-analytic model had a number of drawbacks compared to simulations. Broadly, it was least successful in dense environments, at very high masses and below weakly-linear scales. Fortunately, it perfomed best in voids, where the chameleon effects are largest and where we expect smaller-mass haloes. However, it performed better when expressed as a relative enhancement of $f(\mathcal{R})$ compared to ΛCDM, because the source of errors was the same in both cosmologies. This showed that the HMF is a potential probe of MG in specific environments as well as overall.

Finally we examined the effects of chameleon screening on a variety of other halo properties. Some internal halo properties remained unaffected by MG, namely the alignment of the halo spin and halo alignment with the local tidal forces. In contrast, the spin parameter of the halo and the mass-concentration relation were different in $f(\mathcal{R})$ compared to ΛCDM. While the former did depend upon the environment, having a stronger deviation from GR in voids and sheets, the latter was largely independent of the local structure. These results were as expected from the theoretical density dependence of chameleon screening.

There are various avenues for generalising and extending the work in this thesis. We are not limited to exploring screened models. If the quasi-static approximation behaves well for other MG theories, according to a similar investigation to Chapter 3, then one could apply the quasi-static and weak-field limit, using first-order perturbation theory

to find a modified Poission equation as per Chapter 2. This could be applied to the same spherical collapse equations as Chapter 4 and subsequently used to investigate the HMF. We have listed improvements mentioned in Chapter 6 to the theoretical environment distributions which are used in the conditional HMF and the cosmic web HMF, which could be applied both in ΛCDM and MG. The theoretical development for MG fitting functions is limited to the spherical collapse model, so it may be possible (albeit difficult, given the fifth-force effects) to investigate ellipsoidal collapse in MG. This will become more relevant as triaxial collapse of haloes becomes more widely investigated. The cosmic web method used to incorporate the drifting-and-diffusing barrier can be applied to any of the MG models we have described. Although we have used it here to incorporate environment-dependence for the $f(\mathcal{R})$ models, $\nu_{\rm eff}$ can be calculated for any given δ_c to isolate the behaviour of the HMF is different elements of LSS. This was already applied to ΛCDM in [6], but has not (yet) been applied to any other types of MG.

Alternatively, one could use voids instead of haloes as a probe of MG. There is already an established excursion set formalism for voids in ΛCDM [261]. [68] have attempted this for chameleon screening. There is no shortage of theoretical work to pursue in this field.

Throughout this thesis, we have seen that there exists a rich variety of MG theories. Even amongst those which use screening to be a viable alternative to GR, we have seen that there are three different possibilities whereby the fifth-force effects can be screened away in the local universe. Moreover, the screening behaviour is produced by relaxing the principles of GR in different ways. In particular, we have focused on chameleon screening produced by changing the geometric response to matter; Vainshtein screening produced by additional spatial dimensions and symmetron screening caused by the addition of new scalar fields. Remarkably, all of these can be represented in the Einstein frame as an additional scalar field. Furthermore, when examining gravitational collapse in the quasi-static, weak-field limit, we obtain a simple, modified Poisson equation. Thanks to this simplification, we can look at the effects of MG in a uniform manner. We have developed novel methods to calculate the distribution of haloes in different theories of gravity, not only for Vainshtein and symmetron screening, which produce a simple function change in the HMF, but also for chameleon screening, whose environment dependence opens many possible techniques for marginalising over this nuisance parameter. Conversely, we have also described how to make the environment a strength rather than a weakness, because it enables us to localise the HMF (and indeed other halo properties) in the large-scale structure. This cosmic web approach permits us to investigate the halo distribution within different structures. We discussed the wide variety of options to apply this method to other MG theories, to improve the current methods, or to apply them to voids instead of haloes. However, some avenues

for improvement are blocked due to conflicting assumptions (particularly incorporating both the excursion set and the cosmic web methods), computational limitations (thoroughly investigating the sensitivity of the HMF in MG N-body simulations to changes in ΛCDM-cosmological parameters), or mathematical overcomplexity (a theoretical framework for ellipsoidal collapse in MG). Despite this, we have also seen that there are many promising avenues for building upon the work in this thesis.

Appendix A

General Relativity

This appendix summarises basic rsults of GR which are useful in MG. We shall see that the principles behind GR (Appendix A.1) lead to a geometric description of gravity. We opt to derive Einstein's tensor equations from a variation-of-least-action principle (Appendix A.2) which places GR in the context of the Standard Model. The complexity of Item 1 is encapsulated in the Einstein field equations (Appendix A.3), which resolve the problematic features of Item 2. We can then address Item 3 by determining the behaviour of observables (matter, photons, *etc.*) under the influence of gravity via the geodesic equation (Appendix A.4).

A.1 Principles of GR

Recall that in the weak-field limit GR (or any extension to it) must reproduce the behaviour of Newtonian gravity. This behaviour can be summarised in a "GR-like" formalism as follows:

Definition A.1 (Newtonian gravity)**.** [107] Let two neighbouring test masses be separated by the 3-vector N, in the presence of a conservative gravitational field g. Since the field g is conservative

$$\nabla \times \mathsf{g} = 0 \implies \mathsf{g} = -\nabla\Phi$$

The Hessian of the potential Φ is the tidal tensor E:

$$\mathsf{E}_{ij} \equiv \partial_i \partial_j \Phi$$

Gauss's law relates the field to its source, namely the (active gravitational) local mass density ρ_a:

$$\nabla \cdot \mathsf{g} = -4\pi G_N \rho_a$$

We have the following corollaries:

$$\begin{aligned}
\frac{\mathrm{d}^2 \mathsf{N}_i}{\mathrm{d}\, t^2} + \mathsf{E}_{ij}\mathsf{N}^j = 0 &\qquad \text{Geodesic equation} \\
\mathsf{E}_{ij} = \mathsf{E}_{ji} &\qquad \text{Symmetry} \\
\nabla_i \mathsf{E}_{jk} - \nabla_j \mathsf{E}_{ik} = 0 &\qquad \text{Bianchi Identity} \\
\mathsf{E}^i{}_i = 4\pi G_N \rho_a = \nabla^2 \Phi &\qquad \text{Field equation}
\end{aligned}$$

□

Under Newtonian gravity the equation of motion of a freely-falling particle can be described in an inertial co-ordinate system x by:

$$m_i \frac{\mathrm{d}^2 \mathsf{N}_i}{\mathrm{d}\, t^2} = m_p \mathsf{g}_i\,(t, \mathsf{x}) \tag{A.1}$$

where the particle has a (passive) gravitational mass m_p and an inertial mass m_i. The experiments of Galileo, Newton and Eotvos [107] show the equality of these masses. Also Newton's 3rd law shows the equality of the active and passive gravitational masses.

Proof. Consider two bodies at $\mathsf{r}_{1,2}$ with active and passive gravitational masses $m_{p1,2}$ and $m_{a1,2}$. Newton's law of gravity gives the force of each object upon the other, while Newton's 3rd law requires these to be equal and opposite:

$$\mathsf{F}_{1 \text{ on } 2} = G_N m_{a1} m_{p2} \frac{\mathsf{r}_1 - \mathsf{r}_2}{|\mathsf{r}_1 - \mathsf{r}_2|^3} \tag{A.2a}$$

$$\mathsf{F}_{2 \text{ on } 1} = G_N m_{p1} m_{a2} \frac{\mathsf{r}_1 - \mathsf{r}_2}{|\mathsf{r}_1 - \mathsf{r}_2|^3} \tag{A.2b}$$

Newton's 3rd law requires these to be equal and opposite, with the consequence that

$$\mathsf{F}_{1 \text{ on } 2} = -\mathsf{F}_{2 \text{ on } 1} \implies \frac{m_{a1}}{m_{p1}} = \frac{m_{a2}}{m_{p2}} \tag{A.2c}$$

Requiring this to be true for any two bodies gives the desired result. This must also be satisfied in GR. □

Thus we obtain:

Theorem A.1 (Equivalence of inertial and gravitational mass)**.** The inertial, active

gravitational and passive gravitational masses of an object are equal: $m_i = m_p = m_a$. □

In addition to the weak-field limit, GR must abide by the postulates of special relativity in any (locally) reference frame.

Definition A.2 (Postulates of special relativity)**.** In the absence of gravity:

1. Space and time form a manifold with metric $g_{\alpha\beta}$ homomorphic to the Euclidean 4-d space $\mathbb{R}^4$.
2. There exist globally inertial reference frames, in which the metric satisfies $\mathbf{g} = \text{diag}\,(-1, 1, 1, 1)$ and $\nabla\mathbf{g} = \mathbf{0}$ on all points on the manifold.
3. In any inertial frame the speed of light is a constant c (*in vacuo*).
4. Moreover the laws of physics are the same in any inertial frame.

□

Consequently, we obtain a (possibly infinite) set of privileged observers, each with their own inertial frame. In order for Items 3 and 4 to be satisfied, this specifies the allowed transformation between the inertial frames specified in Item 2. The invariance postulate Item 4 is known as Lorentz invariance .

Definition A.3 (Lorentz invariance)**.** Consider two inertial frames parametrised by co-ordinate charts $\mathbf{x}$, $\bar{\mathbf{x}}$ at a given points in the metric. Then the most general conversion from one frame to another is given by:

$$\bar{x}^\alpha = L^\alpha{}_\beta x^\beta + T^\alpha \tag{A.3a}$$

where L is a Lorentz transformation matrix satisfying

$$g_{\alpha\beta} = L^\gamma{}_\alpha L^\delta{}_\beta g_{\gamma\delta} \tag{A.3b}$$

T is a translation vector and the metric $\mathbf{g}$ in Eq. (A.3) must—by definition of an inertial frame—be reducible to $\boldsymbol{\eta} = \text{diag}\,(-1, 1, 1, 1)$ in the inertial co-ordinate system, via judicious choice of basis vectors. A physical law which remains unchanged under the transformation Eq. (A.3) is termed **Lorentz invariant**. □

The implications are not merely that definitions of distance and time may change between frames (to ensure the constancy of c) but that this difference between frames is what becomes meaningful, because there is no absolute frame privileged above all

others. These postulates (Definition A.2) must hold locally in GR.

We now have the components for one of the two key results of GR, namely the Einstein Equivalence Principle. This describes the trajectories of particles given the geometry of spacetime and leads to the geodesic equation in Appendix A.4.

Definition A.4 (Equivalence Principles [255])**. Weak EP** Any freely-falling body has a trajectory independent of its internal composition.

Einstein EP Any local, non-gravitational experiment performed in a freely-falling reference frame has an outcome independent of both the velocity of the frame and when it was performed.

Corollary: The WEP is valid for test bodies.

Strong EP Any local experiment performed in a freely-falling reference frame has an outcome independent of the velocity of the apparatus and the time and location of the experiment.

Corollary: The WEP is valid for test bodies and self-gravitating bodies.

□

The only theory which obeys the SEP is GR [255].

Proof. Via the SEP corollary, self-gravitating masses must obey the WEP in a local, gravitational experiment. If there are additional gravitational effects beyond those provided by the metric, then the geodesic equation will hold for test masses but not for self-gravitating ones. Then one could use the local gravitational effects (including the self-interaction of bodies which are not test masses) to distinguish between inertial reference frames. This violates the WEP. Proof by contradiction. □

The opposite problem—how the presence of gravitating bodies determines the curvature of the manifold—is the non-linearity problem mentioned in Appendix A.1. Thus the GR field equations cannot retain the linearity of Newtonian gravity.

Proof. Proof is by contradiction. Suppose that the GR equations are linear. From Newtonian gravity we know that gravity couples to matter. Then two masses will have a field equal to the sum of that produced by the individual. However if they are in different inertial reference frames, part of the rest mass of one will be interpreted by the other as energy-momentum (and vice-versa). So gravity must also couple to energy to satisfy the Lorentz invariance of special relativity. This gravitational energy must contribute to the gravitational field of the two masses. But linear equations would

require this contribution to be zero. Thus GR must include a geometric term related to the metric tensor equivalent to an energy term related to the local mass density. □

Instead, we are forced to construct a metric theory of gravity where the field equations are tensor (rather than scalar). We shall specify these in Appendix A.3.

A.2 The action formalism

The field equations of GR are most elegantly derived from a variation-of-least-action principle. Hilbert presented his action-based derivation contemporaneously with Einstein's tensor-based approach in December 1915 [41]. This demonstrates that the action is independent of any prior knowledge of the field equations. The gravitational and stress-energy parts will be handled separately. We will (mostly) ignore the Gibbons-Hawking-York boundary term as it is an unnecessary complication for the purposes of cosmology.

Let us outline Hilbert's approach. Let the general invariant[1] $H = K + L$ be composed of a source-free gravitational term K and a source term L, which for simplicity shall be purely electrodynamic. Hilbert established two axioms and used what is now known as general covarience to obtain the restrictions (Theorem A.2) which should be placed independently on K, L, hence on H.

Theorem A.2 (Hilbert's axioms [211])**.** Suppose that the Euler-Lagrange equations of a generally covariant variational integral

$$\delta \int H \sqrt{g}\, \mathrm{d}\, \omega = 0 \tag{A.4}$$

for a suitable "world function" H, corresponding to the field equations of GR. Then H can only be composed from:

- The ten gravitational field terms $g_{\mu\nu}$, their first and second derivatives
- The four electromagnetic field terms q_μ and their first derivatives

The "world function" H is invariant with respect to arbitrary transformations of the coordinate chart $\boldsymbol{\omega}$. in the system of n Euler-Lagrange equations in n variables obtained from a generally covariant variational integral, four of the n equations are always a consequence of the other $n - 4$ in the sense that four linear combinations of the n equations and their total derivatives are always identically satisfed. □

[1] We retain Hilbert's notation to avoid sub- and super-script overload.

In Hilbert's paper he defines the electromagnetic Lagrangian via:

$$-2g^{\nu\sigma}\frac{\delta\sqrt{g}L}{\delta g^{\mu\nu}} = T^{\sigma}{}_{\mu} \implies \delta L = -\kappa T^{\mu\nu}\delta g_{\mu\nu} \tag{A.5}$$

where the implication is suggested by [209] and they remove the factor of κ which Hilbert did not explicitly specify. This suggests the now common definition of the stress-energy tensor via the implicit relation [41]:

$$\delta S_M\left[\phi, g_{\mu\nu}\right] = -\frac{1}{2}\int \sqrt{g}\,\mathrm{d}^{\,4}x\; T_{\mu\nu}\delta g^{\mu\nu} \implies T_{\mu\nu} = -\frac{2}{\sqrt{g}}\frac{\delta}{\delta g^{\mu\nu}}S_M\left[\phi, g_{\mu\nu}\right] \tag{A.6}$$

where we have updated to modern notation and defined $\mathbf{T}$ to be the source of the field equations by construction. In this way we automatically obtain the deisrable properties of $\mathbf{T}$ from those of $\mathbf{g}$: symmetry, covariance and conservation.

The complete action for GR in the presence of matter (along with its constraint equations) can be summarised as:

$$S_{\mathrm{GR}} \equiv \frac{1}{16\pi G_N}S_{\mathrm{EH}}\left[g_{\mu\nu}\right] + S_M\left[\phi, g_{\mu\nu}\right] \text{ where } \frac{\delta S_{\mathrm{GR}}}{\delta g^{\mu\nu}} = 0 \tag{A.7}$$

In the next section we will examine the field equations which emerge from this action.

A.3 The field equations

The Euler-Lagrange equations are generated by taking the operation $E^{\mu\nu}$ and demanding that it be zero [70]:

$$E^{\mu\nu}(\mathcal{L}) \equiv \frac{\mathrm{d}}{\mathrm{d}\,x^{\rho}}\left[\frac{\partial\mathcal{L}}{\partial\left(\partial_{\rho}g_{\mu\nu}\right)} - \frac{\mathrm{d}}{\mathrm{d}\,x^{\lambda}}\left(\frac{\partial\mathcal{L}}{\partial\left(\partial_{\lambda\rho}g_{\mu\nu}\right)}\right)\right] - \frac{\partial\mathcal{L}}{\partial g_{\mu\nu}} = 0 \tag{A.8}$$

where the Lagrangian density $\mathcal{L}$ is given by the gravitational and the matter terms [118]:

$$\mathcal{L}_{\mathrm{GR}} = \sqrt{-g}\frac{R - 2\Lambda}{16\pi G_N} + \mathcal{L}_{\mathrm{matter}} \tag{A.9}$$

The first term is the Einstein-Hilbert Lagrangian density. We have normalised it by the factor of $16\pi G_N$ to account for the constant of porportionality κ between the Einstein tensor (obtained by setting the matter term to zero) and the stress-energy tensor (obtained by setting the gravitational term to zero).

On the right hand side, we utilise a fluid-based definition of the stress-energy-momentum tensor $\mathbf{T}$.

Definition A.5 (Fluid stress-energy [96])**.** The generalised stress-energy tensor $\mathbf{T}$ for a fluid takes the form [97, 99]:

$$T^{\alpha\beta} = \rho u^\alpha u^\beta + p\left(u^\alpha u^\beta + g^{\alpha\beta}\right) + \left(q^\alpha u^\beta + u^\alpha q^\beta\right) + \widetilde{\pi}^{\alpha\beta} \tag{A.10}$$

where:

- ρ is the total energy density
- p is the isotropic, mean kinetic pressure
- $\mathbf{q}$ is the energy flux (e.g. diffusion and heat conduction)
- $\widetilde{\boldsymbol{\pi}}$ is the anisotropic matter pressure (e.g. shear viscosity)

□

These components are simplified on cosmological scales to perfect fluids, discussed in Section 1.3.

On the left hand side, the Einstein tensor $\mathbf{G}$ measures the compression of the metric in units of inverse-length squared. The Einstein tensor can also be derived geometrically. Recall that we are concerned with the relative motion between reference frames. The behaviour of infinitesimally-separated reference frames can be characterised by the method of parallel transport. First we establish some definitions, which encapsulate the non-Euclidean geometry of the spacetime manifold.

Definition A.6 (Covariant derivative)**.** For a metric $g_{\alpha\beta}$ with affine connections $\Gamma^\alpha{}_{\beta\gamma}$, the covariant derivative of any (p, q) tensor $\mathbf{T}$ is a $(p, q+1)$ tensor, whose form can be found by induction from the results which we will need:

$$\nabla_\alpha \phi \equiv \partial_\alpha \phi \qquad \text{scalar } \phi \tag{A.11a}$$

$$\nabla_\alpha V^\beta \equiv \partial_\alpha V^\beta + \Gamma^\beta{}_{\alpha\gamma} V^\gamma \qquad \text{vector } V^\nu \tag{A.11b}$$

$$\nabla_\alpha T^\beta{}_\gamma \equiv \partial_\alpha T^\beta{}_\gamma + \Gamma^\beta{}_{\alpha\delta} T^\delta{}_\gamma - \Gamma^\delta{}_{\alpha\gamma} T^\beta{}_\delta \qquad \text{tensor } T^\beta{}_\gamma \tag{A.11c}$$

□

Definition A.7 (Convective derivative)**.** For a worldline $x^\mu(\tau)$ parameterised by the affine parameter τ with tangent vector field $\mathrm{d}_\tau x^\mu(\tau)$, define the derivative to be $X^\mu \nabla_\mu$. If we take X to be the velocity u^α along the worldline, then we define the convective derivative

$$\dot{\mathbf{T}} \equiv u^\alpha \nabla_\alpha \mathbf{T} \tag{A.12}$$

which is the covariant derivative along the worldline. (Equivalent terminology is the

"intrinsic derivative" of [118], the "convective derivative" of [223] and the "effective derivative" of [99].) □

Definition A.8 (Parallel transport)**.** A (p, q) tensor $\mathbf{T}$ is parallel transported if its convective derivative is zero. □

The curvature of the spacetime manifold is described by the Riemann tensor and its contractions, the Ricci tensor and scalar respectively. Covariant derivatives do not commute because the basis vectors are now functions of their co-ordinate chart (a situation familiar from spherical or cylindrical co-ordinates). Having defined the local curvature of the spacetime manifold, we can now construct the Einstein tensor from the metric and its derivatives.

Definition A.9 (Riemann tensor [223])**.** The Riemann tensor quantifies the effect of transporting the vector v^δ along two different curves in the manifold due to its intrinsic curvature at each point along the paths [16].

$$R^\delta{}_{\alpha\beta\gamma} v^\alpha = \left(\nabla_\beta \nabla_\gamma - \nabla_\gamma \nabla_\beta\right) v^\delta$$

The Ricci tensor $\mathbf{R}$ is generated via contraction of the Riemann tensor:

$$R_{\alpha\beta} \equiv R^\gamma{}_{\alpha\beta\gamma} = -\left(\partial_\beta \Gamma^\gamma{}_{\alpha\gamma} - \partial_\gamma \Gamma^\gamma{}_{\alpha\beta} + \Gamma^\gamma{}_{\beta\sigma}\Gamma^\sigma{}_{\alpha\gamma} - \Gamma^\gamma{}_{\gamma\sigma}\Gamma^\sigma{}_{\alpha\beta}\right)$$

Contracting again generates the Ricci scalar R:

$$R \equiv R_{\alpha\beta} g^{\alpha\beta}$$

□

The Einstein tensor $\mathbf{G}$ is:

$$G_{\alpha\beta} \equiv R_{\alpha\beta} - \frac{1}{2} g_{\alpha\beta} \left(R - 2\Lambda\right) \tag{A.13}$$

Thus we have quantified the self-interaction of the spacetime manifold with its contents: the Einstein equation describes the gravitational curvature of spacetime caused by the presence of energy.

Definition A.10 (GR field equations [41, 118, 223])**.** The field equation of GR is the Einstein equation:

$$G_{\alpha\beta} = \frac{c^4}{8\pi G_N} T_{\alpha\beta} \tag{A.14}$$

The integrability condition (the contracted Bianchi identity) combined with the Einstein

equation produces the energy-momentum balance equation

$$G^{\alpha\beta}{}_{\alpha} = 0 \implies T^{\alpha\beta}{}_{\alpha} = 0 \tag{A.15}$$

Thus we have six independent, covariant equations for the metric (ten equations from Eq. (A.14) and four constraint equations Eq. (A.15)). □

A.4 The geodesic equation

In this Section, we define the geodesic equation which described the trajectory of a particle given its local spacetime geometry. This is a straightforward generalisation of the Newtonian geodesic equation which we saw in Definition A.1 to accommodate the non-Euclidean nature of the manifold.

Geodesics are those curves whose covariant acceleration is zero, i.e. which are parallel transported (Definition A.8). Applying the definition of the convective derivative in Definition A.7

$$\dot{a}^{\alpha} = u^{\beta}\nabla_{\beta}u^{\alpha} \tag{A.16}$$

we obtain the geodesic equation directly:

$$\frac{\mathrm{d}^{2}x^{\alpha}}{\mathrm{d}\,\tau^{2}} + \Gamma^{\alpha}{}_{\beta\gamma}\frac{\mathrm{d}\,x^{\beta}}{\mathrm{d}\,\tau}\frac{\mathrm{d}\,x^{\gamma}}{\mathrm{d}\,\tau} = 0 \tag{A.17}$$

If the worldline describes a massive particle then the affine parameter τ is equivalent to the proper time. Thus we see that in the presence of gravity, objects are parallel transported along their worldlines.

References

[1] J. Adamek et al. "General relativity and cosmic structure formation". In: **ArXiv e-prints** (Sept. 2015). arXiv: 1509.01699 (cit. on p. 38).

[2] Julian Adamek, Ruth Durrer, and Martin Kunz. "N-body methods for relativistic cosmology". In: (2014). arXiv: 1408.3352 [astro-ph.CO] (cit. on p. 38).

[3] Julian Adamek et al. "General Relativistic N-body simulations in the weak field limit". In: (2013). arXiv: 1308.6524 [astro-ph.CO] (cit. on pp. 33, 38).

[4] P. A. R. Ade et al. "Planck 2013 results. XVI. Cosmological parameters". In: **Astron. Astrophys.** 571 (2014), A16. DOI: 10.1051/0004-6361/201321591. arXiv: 1303.5076 [astro-ph.CO] (cit. on p. 20).

[5] Jean-Michel Alimi et al. "DEUS Full Observable ΛCDM Universe Simulation: the numerical challenge". In: (2012). arXiv: 1206.2838 [astro-ph.CO] (cit. on p. 35).

[6] David Alonso, Elizabeth Eardley, and John A. Peacock. "Halo abundances within the cosmic web". In: **Mon.Not.Roy.Astron.Soc.** 447 (2015), p. 2683. DOI: 10.1093/mnras/stu2632. arXiv: 1406.4159 [astro-ph.CO] (cit. on pp. 105, 106, 117, 163, 167, 169–171, 176, 184, 191).

[7] F.G. Alvarenga et al. "Dynamics of scalar perturbations in f(R,T) gravity". In: (2013). arXiv: 1302.1866 [gr-qc] (cit. on p. 34).

[8] R. Amanullah et al. "Spectra and Hubble Space Telescope Light Curves of Six Type Ia Supernovae at $0.511 < z < 1.12$ and the Union2 Compilation". In: **apj** 716 (June 2010), pp. 712–738. DOI: 10.1088/0004-637X/716/1/712. arXiv: 1004.1711 [astro-ph.CO] (cit. on p. 20).

[9] L. Amendola and R. Barbieri. "Dark matter from an ultra-light pseudo-Goldsone-boson". In: **Physics Letters B** 642 (Nov. 2006), pp. 192–196. DOI: 10.1016/j.physletb.2006.08.069. eprint: arXiv:hep-ph/0509257 (cit. on p. 57).

[10] L. Amendola, D. Polarski, and S. Tsujikawa. "Are f(R) Dark Energy Models Cosmologically Viable?" In: **Physical Review Letters** 98.13, 131302 (Mar. 2007), p. 131302. DOI: 10.1103/PhysRevLett.98.131302. eprint: astro-ph/0603703 (cit. on p. 47).

[11] L. Anderson et al. “The clustering of galaxies in the SDSS-III Baryon Oscillation Spectroscopic Survey: baryon acoustic oscillations in the Data Releases 10 and 11 Galaxy samples”. In: MNRAS 441 (June 2014), pp. 24–62. DOI: 10.1093/mnras/stu523. arXiv: 1312.4877 (cit. on p. 22).

[12] R. E. Angulo et al. “Scaling relations for galaxy clusters in the Millennium-XXL simulation”. In: **Mon. Not. Roy. Astron. Soc.** 426 (2012), p. 2046. DOI: 10.1111/j.1365-2966.2012.21830.x. arXiv: 1203.3216 [astro-ph.CO] (cit. on p. 35).

[13] R. E. Angulo et al. “Scaling relations for galaxy clusters in the Millennium-XXL simulation”. In: **MNRAS** 426 (Nov. 2012), pp. 2046–2062. DOI: 10.1111/j.1365-2966.2012.21830.x. arXiv: 1203.3216 [astro-ph.CO] (cit. on pp. 112, 150).

[14] I Antoniadis. “Gravity modifications from extra dimensions”. In: **Journal of Physics A: Mathematical and Theoretical** 40.25 (2007), p. 6657. URL: http://stacks.iop.org/1751-8121/40/i=25/a=S10 (cit. on pp. 12–14).

[15] E. Babichev, C. Deffayet, and R. Ziour. “k-Mouflage gravity”. In: **Int. J. Mod. Phys.** D18 (2009), pp. 2147–2154. DOI: 10.1142/S0218271809016107. arXiv: 0905.2943 [hep-th] (cit. on p. 42).

[16] Teresa Baker. “Cosmological Tests of General Relativity”. PhD thesis. University of Oxford: New College, 2013 (cit. on pp. 9–12, 14, 24–28, 200).

[17] M. Baldi. “Dark Energy simulations”. In: **Physics of the Dark Universe** 1 (Nov. 2012), pp. 162–193. DOI: 10.1016/j.dark.2012.10.004. arXiv: 1210.6650 [astro-ph.CO] (cit. on pp. 37, 38).

[18] J. M. Bardeen et al. “The statistics of peaks of Gaussian random fields”. In: ApJ 304 (May 1986), pp. 15–61. DOI: 10.1086/164143 (cit. on p. 170).

[19] R. Barlow. “Asymmetric Statistical Errors”. In: **ArXiv Physics e-prints** (June 2004). eprint: physics/0406120 (cit. on p. 128).

[20] A. Barreira et al. “Halo model and halo properties in Galileon gravity cosmologies”. In: J. Cosmology Astropart. Phys. 4, 029 (Apr. 2014), p. 029. DOI: 10.1088/1475-7516/2014/04/029. arXiv: 1401.1497 (cit. on p. 122).

[21] A. Barreira et al. “Nonlinear structure formation in the cubic Galileon gravity model”. In: J. Cosmology Astropart. Phys. 10, 027 (Oct. 2013), p. 027. DOI: 10.1088/1475-7516/2013/10/027. arXiv: 1306.3219 (cit. on p. 122).

[22] A. Barreira et al. “Spherical collapse in Galileon gravity: fifth force solutions, halo mass function and halo bias”. In: J. Cosmology Astropart. Phys. 11, 056 (Nov. 2013), p. 056. DOI: 10.1088/1475-7516/2013/11/056. arXiv: 1308.3699 (cit. on p. 122).

[23] Alexandre Barreira et al. “Linear perturbations in Galileon gravity models”. In: **Phys. Rev.** D86 (2012), p. 124016. DOI: 10.1103/PhysRevD.86.124016. arXiv: 1208.0600 [astro-ph.CO] (cit. on pp. 33, 34, 92).

[24] Alexandre Barreira et al. “Nonlinear structure formation in the Cubic Galileon gravity model”. In: **JCAP** 1310 (2013), p. 027. DOI: 10.1088/1475-7516/2013/10/027. arXiv: 1306.3219 [astro-ph.CO] (cit. on pp. 33, 92).

[25] Alexandre Barreira et al. “Spherical collapse in Galileon gravity: fifth force solutions, halo mass function and halo bias”. In: **JCAP** 1311 (2013), p. 056. DOI: 10.1088/1475-7516/2013/11/056. arXiv: 1308.3699 [astro-ph.CO] (cit. on pp. 33, 92).

[26] John D. Barrow and S. Cotsakis. “Inflation and the Conformal Structure of Higher Order Gravity Theories”. In: **Phys. Lett.** B214 (1988), pp. 515–518. DOI: 10.1016/0370-2693(88)90110-4 (cit. on p. 46).

[27] Matthias Bartelmann and Peter Schneider. “Weak gravitational lensing”. In: **Phys.Rept.** 340 (2001), pp. 291–472. DOI: 10.1016/S0370-1573(00)00082-X. arXiv: astro-ph/9912508 [astro-ph] (cit. on pp. 29–31).

[28] Nicola Bartolo et al. “Matter bispectrum in cubic Galileon cosmologies”. In: **JCAP** 1303 (2013), p. 034. DOI: 10.1088/1475-7516/2013/03/034. arXiv: 1301.4831 [astro-ph.CO] (cit. on p. 24).

[29] Daniel Baumann. “Part III Cosmology”. In: (2012). URL: http://www.damtp.cam.ac.uk/user/db275/Cosmology/Lectures.pdf (cit. on pp. 17, 18).

[30] Rachel Bean, Pedro G. Ferreira, and Andy Taylor. “A new golden age: testing general relativity with cosmology”. In: **Phil. Trans. R. Soc. A.** 369 (2011), pp. 4941–4946 (cit. on p. 39).

[31] Rachel Bean et al. “Dynamics of Linear Perturbations in f(R) Gravity”. In: **Phys.Rev.** D75 (2007), p. 064020. DOI: 10.1103/PhysRevD.75.064020. arXiv: astro-ph/0611321 [astro-ph] (cit. on pp. 46–48, 65, 66, 70, 71, 79, 81).

[32] P. S. Behroozi, R. H. Wechsler, and H.-Y. Wu. “The ROCKSTAR Phase-space Temporal Halo Finder and the Velocity Offsets of Cluster Cores”. In: ApJ 762, 109 (Jan. 2013), p. 109. DOI: 10.1088/0004-637X/762/2/109. arXiv: 1110.4372 [astro-ph.CO] (cit. on pp. 124–126).

[33] J. Beltrán Jiménez, A. L. Delvas Fróes, and D. F. Mota. “Screening vector field modifications of general relativity”. In: **Physics Letters B** 725 (Oct. 2013), pp. 212–217. DOI: 10.1016/j.physletb.2013.07.032. arXiv: 1212.1923 [astro-ph.CO] (cit. on p. 42).

[34] A. J. Benson. “The mass function of unprocessed dark matter haloes and merger tree branching rates”. In: MNRAS 467 (May 2017), pp. 3454–3466. DOI: 10.1093/mnras/stx343. arXiv: 1610.01057 (cit. on pp. 120, 139, 151).

[35] Daniele Bertacca, Nicola Bartolo, and Sabino Matarrese. “A new approach to cosmological perturbations in f(R) models”. In: **JCAP** 1208 (2012), p. 021. DOI:

10.1088/1475-7516/2012/08/021. arXiv: 1109.2082 [astro-ph.CO] (cit. on p. 63).

[36] E. Berti et al. "Testing general relativity with present and future astrophysical observations". In: **Classical and Quantum Gravity** 32.24, 243001 (Dec. 2015), p. 243001. DOI: 10.1088/0264-9381/32/24/243001. arXiv: 1501.07274 [gr-qc] (cit. on pp. 45, 162).

[37] B. Bertotti, L. Iess, and P. Tortora. "A test of general relativity using radio links with the Cassini spacecraft". In: **Nat** 425 (Sept. 2003), pp. 374–376. DOI: 10.1038/nature01997 (cit. on p. 162).

[38] Edmund Bertschinger. "COSMICS: cosmological initial conditions and microwave anisotropy codes". In: (1995). arXiv: astro-ph/9506070 [astro-ph] (cit. on p. 61).

[39] P. Bett et al. "The spin and shape of dark matter haloes in the Millennium simulation of a Λ cold dark matter universe". In: MNRAS 376 (Mar. 2007), pp. 215–232. DOI: 10.1111/j.1365-2966.2007.11432.x. eprint: astro-ph/0608607 (cit. on p. 179).

[40] S. Bhattacharya et al. "Mass Function Predictions Beyond ΛCDM". In: ApJ 732, 122 (May 2011), p. 122. DOI: 10.1088/0004-637X/732/2/122. arXiv: 1005.2239 (cit. on pp. 4, 120).

[41] Matthias Blau. **Lecture Notes on General Relativity**. 2015. URL: http://www.blau.itp.unibe.ch/lecturesGR.pdf (cit. on pp. 4, 6, 13, 16, 45, 197, 198, 200).

[42] J. R. Bond et al. "Excursion set mass functions for hierarchical Gaussian fluctuations". In: ApJ 379 (Oct. 1991), pp. 440–460. DOI: 10.1086/170520 (cit. on pp. 94, 98, 99, 101).

[43] Michael Boylan-Kolchin et al. "Resolving Cosmic Structure Formation with the Millennium-II Simulation". In: **Mon. Not. Roy. Astron. Soc.** 398 (2009), p. 1150. DOI: 10.1111/j.1365-2966.2009.15191.x. arXiv: 0903.3041 [astro-ph.CO] (cit. on p. 35).

[44] P. Brax et al. "Detecting dark energy in orbit: The cosmological chameleon". In: Phys. Rev. D 70.12, 123518 (Dec. 2004), p. 123518. DOI: 10.1103/PhysRevD.70.123518. eprint: astro-ph/0408415 (cit. on p. 49).

[45] P. Brax et al. "f(R) gravity and chameleon theories". In: Phys. Rev. D 78.10, 104021 (Nov. 2008), p. 104021. DOI: 10.1103/PhysRevD.78.104021. arXiv: 0806.3415 (cit. on p. 48).

[46] P. Brax et al. "Systematic simulations of modified gravity: symmetron and dilaton models". In: J. Cosmology Astropart. Phys. 10, 002 (Oct. 2012), p. 002. DOI: 10.1088/1475-7516/2012/10/002. arXiv: 1206.3568 (cit. on pp. 123, 124).

[47] Philippe Brax, Anne-Christine Davis, and Jeremy Sakstein. "Dynamics of Supersymmetric Chameleons". In: (2013). arXiv: 1302.3080 [astro-ph.CO] (cit. on p. 83).

[48] Philippe Brax et al. "A Unified Description of Screened Modified Gravity". In: **Phys.Rev.** D86 (2012), p. 044015. DOI: 10.1103/PhysRevD.86.044015. arXiv: 1203.4812 [astro-ph.CO] (cit. on p. 64).

[49] Philippe Brax et al. "Chameleon dark energy". In: **AIP Conf.Proc.** 736 (2005), pp. 105–110. DOI: 10.1063/1.1835177. arXiv: astro-ph/0410103 [astro-ph] (cit. on p. 83).

[50] Philippe Brax et al. "f(R) Gravity and Chameleon Theories". In: **Phys. Rev.** D78 (2008), p. 104021. DOI: 10.1103/PhysRevD.78.104021. arXiv: 0806.3415 [astro-ph] (cit. on pp. 78, 80, 81).

[51] Philippe Brax et al. "Systematic simulations of modified gravity: chameleon models". In: (2013). DOI: 10.1088/1475-7516/2013/04/029. arXiv: 1303.0007 [astro-ph.CO] (cit. on pp. 33, 57).

[52] Philippe Brax et al. "Systematic simulations of modified gravity: chameleon models". In: **JCAP** 1304 (2013), p. 029. DOI: 10.1088/1475-7516/2013/04/029. arXiv: 1303.0007 [astro-ph.CO] (cit. on p. 33).

[53] Philippe Brax et al. "Unified description of screened modified gravity". In: **Physical Review D - Particles, Fields, Gravitation and Cosmology** 86 (2012), pp. 1–23. ISSN: 15507998. DOI: 10.1103/PhysRevD.86.044015 (cit. on p. 162).

[54] Johannes Buchner. "A statistical test for Nested Sampling algorithms". In: **Statistics and Computing** 26.1 (2016), pp. 383–392. ISSN: 1573-1375. DOI: 10.1007/s11222-014-9512-y. URL: https://doi.org/10.1007/s11222-014-9512-y (cit. on p. 140).

[55] P. Bull et al. "Beyond Λ CDM: Problems, solutions, and the road ahead". In: **Physics of the Dark Universe** 12 (June 2016), pp. 56–99. DOI: 10.1016/j.dark.2016.02.001. arXiv: 1512.05356 (cit. on pp. 20, 21, 27, 28, 121).

[56] J. S. Bullock et al. "Profiles of dark haloes: evolution, scatter and environment". In: MNRAS 321 (Mar. 2001), pp. 559–575. DOI: 10.1046/j.1365-8711.2001.04068.x. eprint: astro-ph/9908159 (cit. on p. 179).

[57] Clare Burrage and Jeremy Sakstein. "Tests of Chameleon Gravity". In: (2017). arXiv: 1709.09071 [astro-ph.CO] (cit. on pp. 47, 50).

[58] Sean M. Carroll. "The Cosmological Constant". In: **Living Reviews in Relativity** 4.1 (Feb. 2001). DOI: 10.12942/lrr-2001-1. URL: https://doi.org/10.12942/lrr-2001-1 (cit. on p. 23).

[59] M. Cataneo et al. "Cluster abundance in chameleon f(R) gravity I: toward an accurate halo mass function prediction". In: J. Cosmology Astropart. Phys. 12, 024 (Dec. 2016), p. 024. DOI: 10.1088/1475-7516/2016/12/024. arXiv: 1607.08788 (cit. on pp. 102, 109, 127).

[60] Matteo Cataneo et al. "New constraints on $f(R)$ gravity from clusters of galaxies". In: **Phys. Rev.** D92.4 (2015), p. 044009. DOI: 10.1103/PhysRevD.92.044009. arXiv: 1412.0133 [astro-ph.CO] (cit. on p. 47).

[61] J. A. R. Cembranos, A. de la Cruz Dombriz, and L. Olano Garcia. "Complete density perturbations in the Jordan-Fierz-Brans-Dicke theory". In: **Phys. Rev.** D88 (2013), p. 123507. DOI: 10.1103/PhysRevD.88.123507. arXiv: 1307.0521 [gr-qc] (cit. on p. 34).

[62] Kwan Chuen Chan and Román Scoccimarro. "Large-Scale Structure in Brane-Induced Gravity II. Numerical Simulations". In: **Phys. Rev.** D80 (2009), p. 104005. DOI: 10.1103/PhysRevD.80.104005. arXiv: 0906.4548 [astro-ph.CO] (cit. on p. 33).

[63] C. Charmousis. "Higher Order Gravity Theories and Their Black Hole Solutions". In: **Physics of Black Holes**. Vol. 769. Lecture Notes in Physics, Berlin Springer Verlag. 2009, p. 299. DOI: 10.1007/978-3-540-88460-6_8. arXiv: 0805.0568 [gr-qc] (cit. on p. 12).

[64] Takeshi Chiba. "1/R gravity and scalar - tensor gravity". In: **Phys. Lett.** B575 (2003), pp. 1–3. DOI: 10.1016/j.physletb.2003.09.033. arXiv: astro-ph/0307338 [astro-ph] (cit. on p. 46).

[65] N. Chisari et al. "Intrinsic alignments of galaxies in the Horizon-AGN cosmological hydrodynamical simulation". In: MNRAS 454 (Dec. 2015), pp. 2736–2753. DOI: 10.1093/mnras/stv2154. arXiv: 1507.07843 (cit. on p. 178).

[66] Nora Elisa Chisari and Matias Zaldarriaga. "Connection between Newtonian simulations and general relativity". In: **Phys.Rev.** D83 (2011), p. 123505. DOI: 10.1103/PhysRevD.84.089901,10.1103/PhysRevD.83.123505. arXiv: 1101.3555 [astro-ph.CO] (cit. on pp. 62, 178).

[67] Adam J. Christopherson, Juan Carlos Hidalgo, and Karim A. Malik. "Modelling non-dust fluids in cosmology". In: **JCAP** 1301 (2013), p. 002. DOI: 10.1088/1475-7516/2013/01/002. arXiv: 1207.1870 [astro-ph.CO] (cit. on p. 62).

[68] J. Clampitt, Y.-C. Cai, and B. Li. "Voids in modified gravity: excursion set predictions". In: **Mon.Not.Roy.Astron.Soc.** 431 (May 2013), pp. 749–766. DOI: 10.1093/mnras/stt219. arXiv: 1212.2216 [astro-ph.CO] (cit. on p. 191).

[69] Timothy Clifton. "Cosmology without averaging". In: **Classical and Quantum Gravity** 28.16 (2011), p. 164011. URL: http://stacks.iop.org/0264-9381/28/i=16/a=164011 (cit. on p. 52).

[70] Timothy Clifton et al. "Modified Gravity and Cosmology". In: **Phys.Rept.** 513 (2012), pp. 1–189. DOI: 10.1016/j.physrep.2012.01.001. arXiv: 1106.2476 [astro-ph.CO] (cit. on pp. 8, 10, 11, 13, 18, 52, 57, 121, 162, 198).

[71] S. Codis et al. "Connecting the cosmic web to the spin of dark haloes: implications for galaxy formation". In: MNRAS 427 (Dec. 2012), pp. 3320–3336. DOI: 10.1111/j.1365-2966.2012.21636.x. arXiv: 1201.5794 (cit. on pp. 178, 179).

[72] Peter Coles and Bernard Jones. "A lognormal model for the cosmological mass distribution". In: **Monthly Notices of the Royal Astronomical Society** 248.1 (1991), pp. 1–13. DOI: 10.1093/mnras/248.1.1. eprint: http://mnras.oxfordjournals.org/content/248/1/1.full.pdf+html. URL: http://mnras.oxfordjournals.org/content/248/1/1.abstract (cit. on pp. 105, 170).

[73] A. Cooray and R. Sheth. "Halo models of large scale structure". In: Phys. Rep. 372 (Dec. 2002), pp. 1–129. DOI: 10.1016/S0370-1573(02)00276-4. eprint: astro-ph/0206508 (cit. on p. 18).

[74] Edmund J. Copeland, M. Sami, and Shinji Tsujikawa. "Dynamics of dark energy". In: **Int.J.Mod.Phys.** D15 (2006), pp. 1753–1936. DOI: 10.1142/S021827180600942X. arXiv: hep-th/0603057 [hep-th] (cit. on p. 57).

[75] J. Courtin et al. "Imprints of dark energy on cosmic structure formation - II. Non-universality of the halo mass function". In: MNRAS 410 (Jan. 2011), pp. 1911–1931. DOI: 10.1111/j.1365-2966.2010.17573.x. arXiv: 1001.3425 (cit. on pp. 108, 112, 122, 128, 148, 150, 151, 157, 161).

[76] M. Crocce et al. "Simulating the Universe with MICE: the abundance of massive clusters". In: MNRAS 403 (Apr. 2010), pp. 1353–1367. DOI: 10.1111/j.1365-2966.2009.16194.x. arXiv: 0907.0019 (cit. on pp. 109, 112, 150).

[77] A. de la Cruz-Dombriz, A. Dobado, and Antonio Lopez Maroto. "On the evolution of density perturbations in f(R) theories of gravity". In: **Phys.Rev.** D77 (2008), p. 123515. DOI: 10.1103/PhysRevD.77.123515. arXiv: 0802.2999 [astro-ph] (cit. on pp. 34, 70, 71, 91, 92).

[78] T. Damour and Alexander M. Polyakov. "The String dilaton and a least coupling principle". In: **Nucl. Phys.** B423 (1994), pp. 532–558. DOI: 10.1016/0550-3213(94)90143-0. arXiv: hep-th/9401069 [hep-th] (cit. on p. 42).

[79] M. Davis et al. "The evolution of large-scale structure in a universe dominated by cold dark matter". In: ApJ 292 (May 1985), pp. 371–394. DOI: 10.1086/163168 (cit. on p. 125).

[80] K. S. Dawson et al. "The Baryon Oscillation Spectroscopic Survey of SDSS-III". In: AJ 145, 10 (Jan. 2013), p. 10. DOI: 10.1088/0004-6256/145/1/10. arXiv: 1208.0022 (cit. on p. 20).

[81] Kyle S. Dawson et al. "THE BARYON OSCILLATION SPECTROSCOPIC SURVEY OF SDSS-III". In: **The Astronomical Journal** 145.1 (Dec. 2012), p. 10. DOI: 10.1088/0004-6256/145/1/10. URL: https://doi.org/10.1088/0004-6256/145/1/10 (cit. on pp. 21, 22).

[82] A. de Felice, T. Kobayashi, and S. Tsujikawa. "Effective gravitational couplings for cosmological perturbations in the most general scalar-tensor theories with second-order field equations". In: **Physics Letters B** 706 (Dec. 2011), pp. 123–

133. DOI: 10.1016/j.physletb.2011.11.028. arXiv: 1108.4242 [gr-qc] (cit. on p. 45).

[83] W. Dehnen and J. I. Read. "N-body simulations of gravitational dynamics". In: **European Physical Journal Plus** 126, 55 (May 2011), p. 55. DOI: 10.1140/epjp/i2011-11055-3. arXiv: 1105.1082 [astro-ph.IM] (cit. on pp. 36–38).

[84] T. Delubac et al. "Baryon acoustic oscillations in the Lyα forest of BOSS DR11 quasars". In: A&A 574, A59 (Feb. 2015), A59. DOI: 10.1051/0004-6361/201423969. arXiv: 1404.1801 (cit. on pp. 20, 22).

[85] Giulia Despali et al. "The universality of the virial halo mass function and models for non-universality of other halo definitions". In: MNRAS 456.3 (2016), pp. 2486–2504. DOI: 10.1093/mnras/stv2842. arXiv: 1507.05627 [astro-ph.CO] (cit. on p. 122).

[86] C. di Porto, L. Amendola, and E. Branchini. "Growth factor and galaxy bias from future redshift surveys: a study on parametrizations". In: MNRAS 419 (Jan. 2012), pp. 985–997. DOI: 10.1111/j.1365-2966.2011.19755.x. arXiv: 1101.2453 (cit. on p. 27).

[87] Cinzia Di Porto, Luca Amendola, and Enzo Branchini. "Growth factor and galaxy bias from future redshift surveys: a study on parametrizations". In: (2011). arXiv: 1101.2453 [astro-ph.CO] (cit. on p. 27).

[88] J. Diemand et al. "Clumps and streams in the local dark matter distribution". In: **Nature** 454 (2008), pp. 735–738. DOI: 10.1038/nature07153. arXiv: 0805.1244 [astro-ph] (cit. on p. 35).

[89] Guillem Domènech and Misao Sasaki. "Conformal frames in cosmology". In: **Int. J. Mod. Phys.** D25.13 (2016). [,56(2017)], p. 1645006. DOI: 10.1142/9789813203952_0007,10.1142/S0218271816450061. arXiv: 1602.06332 [gr-qc] (cit. on pp. 43, 44).

[90] A. G. Doroshkevich. "Spatial structure of perturbations and origin of galactic rotation in fluctuation theory". In: **Astrophysics** 6 (Oct. 1970), pp. 320–330. DOI: 10.1007/BF01001625 (cit. on p. 163).

[91] G. Dvali, G. Gabadadze, and M. Porrati. "4D gravity on a brane in 5D Minkowski space". In: **Physics Letters B** 485 (July 2000), pp. 208–214. DOI: 10.1016/S0370-2693(00)00669-9. eprint: hep-th/0005016 (cit. on p. 42).

[92] G. R. Dvali, Gregory Gabadadze, and Massimo Porrati. "4-D gravity on a brane in 5-D Minkowski space". In: **Phys. Lett.** B485 (2000), pp. 208–214. DOI: 10.1016/S0370-2693(00)00669-9. arXiv: hep-th/0005016 [hep-th] (cit. on p. 33).

[93] F. W. Dyson, A. S. Eddington, and C. Davidson. "A Determination of the Deflection of Light by the Sun's Gravitational Field, from Observations Made at the Total Eclipse of May 29, 1919". In: **Philosophical Transactions of the Royal Society A: Mathematical, Physical and Engineering Sciences**

220.571-581 (Jan. 1920), pp. 291–333. DOI: 10.1098/rsta.1920.0009. URL: https://doi.org/10.1098/rsta.1920.0009 (cit. on p. 1).

[94] G. Efstathiou. "An anthropic argument for a cosmological constant". In: MNRAS 274 (June 1995), pp. L73–L76. DOI: 10.1093/mnras/274.1.L73 (cit. on p. 150).

[95] G. Efstathiou, W. J. Sutherland, and S. J. Maddox. "The cosmological constant and cold dark matter". In: **Nature** 348.6303 (Dec. 1990), pp. 705–707. DOI: 10.1038/348705a0. URL: https://doi.org/10.1038/348705a0 (cit. on p. 36).

[96] J. Ehlers. "Kinetic theory of gases in general relativity theory". In: **Lectures in Statistical Physics**. Ed. by J. Ehlers et al. Vol. 28. Lecture Notes in Physics, Berlin Springer Verlag. 1974, pp. 78–105. DOI: 10.1007/BFb0008854 (cit. on pp. 37, 38, 199).

[97] Jürgen Ehlers. "Kinetic theory of gases in general relativity theory". In: ed. by J. Ehlers et al. Vol. 28. Lecture Notes in Physics. Berlin, Heidelberg: Springer, 1974, pp. 78–105. ISBN: 978-3-540-06711-5 (cit. on pp. 17, 199).

[98] A. Einstein. "Die grundlage der allgemeinen Relativitätstheorie". In: **Annalen der Physik** 49 (1916), pp. 669–822 (cit. on p. 1).

[99] G. F. R. Ellis. "Relativistic Cosmology". In: **General Relativity and Cosmology**. Ed. by R. K. Sachs. (Reprinted in Gen.Rel.Grav. vol. 41 pp. 581–660). 1971, pp. 104–182 (cit. on pp. 199, 200).

[100] V. Faraoni and S. Nadeau. "(Pseudo)issue of the conformal frame revisited". In: Phys. Rev. D 75.2, 023501 (Jan. 2007), p. 023501. DOI: 10.1103/PhysRevD.75.023501. eprint: gr-qc/0612075 (cit. on pp. 43, 44).

[101] F. Feroz, M. P. Hobson, and M. Bridges. "MULTINEST: an efficient and robust Bayesian inference tool for cosmology and particle physics". In: MNRAS 398 (Oct. 2009), pp. 1601–1614. DOI: 10.1111/j.1365-2966.2009.14548.x. arXiv: 0809.3437 (cit. on pp. 131, 132).

[102] Simone Ferraro, Fabian Schmidt, and Wayne Hu. "Cluster Abundance in f(R) Gravity Models". In: **Phys. Rev.** D83 (2011), p. 063503. DOI: 10.1103/PhysRevD.83.063503. arXiv: 1011.0992 [astro-ph.CO] (cit. on p. 33).

[103] Pedro G. Ferreira and Michael Joyce. "Cosmology with a primordial scaling field". In: **Phys.Rev.** D58 (1998), p. 023503. DOI: 10.1103/PhysRevD.58.023503. arXiv: astro-ph/9711102 [astro-ph] (cit. on pp. 47, 57, 60, 65, 70, 71).

[104] J. E. Forero-Romero et al. "A dynamical classification of the cosmic web". In: MNRAS 396 (July 2009), pp. 1815–1824. DOI: 10.1111/j.1365-2966.2009.14885.x. arXiv: 0809.4135 (cit. on pp. 105, 163).

[105] D. Freedman and P. Diaconis. "On the histogram as a density estimator: L_2 theory". In: **Zeitschrift für Wahrscheinlichkeitstheorie und verwandte Gebiete** (1981), pp. 453–476 (cit. on p. 127).

[106] L. Gao et al. “The Phoenix Project: the Dark Side of Rich Galaxy Clusters”. In: **Mon. Not. Roy. Astron. Soc.** 425 (2012), p. 2169. DOI: 10.1111/j.1365-2966.2012.21564.x. arXiv: 1201.1940 [astro-ph.CO] (cit. on p. 35).

[107] G. W. Gibbons. **Part II General Relativity**. 2006. URL: http://www.damtp.cam.ac.uk/people/g.w.gibbons/ (cit. on pp. 3, 193, 194).

[108] S. P. D. Gill, A. Knebe, and B. K. Gibson. “The evolution of substructure - I. A new identification method”. In: MNRAS 351 (June 2004), pp. 399–409. DOI: 10.1111/j.1365-2966.2004.07786.x. eprint: astro-ph/0404258 (cit. on p. 165).

[109] M. B. Gronke, C. Llinares, and D. F. Mota. “Gravitational redshift profiles in the f(R) and symmetron models”. In: A&A 562, A9 (Feb. 2014), A9. DOI: 10.1051/0004-6361/201322403. arXiv: 1307.6994 (cit. on pp. 37, 178).

[110] J. Guy et al. “SALT: a spectral adaptive light curve template for type Ia supernovae”. In: A&A 443 (Dec. 2005), pp. 781–791. DOI: 10.1051/0004-6361:20053025. eprint: astro-ph/0506583 (cit. on p. 32).

[111] L. Guzzo et al. “The VIMOS Public Extragalactic Redshift Survey (VIPERS). An unprecedented view of galaxies and large-scale structure at 0.5 ¡ z ¡ 1.2”. In: (2013). arXiv: 1303.2623 [astro-ph.CO] (cit. on p. 21).

[112] T. Haugg, S. Hofmann, and M. Kopp. “Newtonian N-body simulations are compatible with cosmological perturbation theory”. In: **ArXiv e-prints** (Oct. 2012). arXiv: 1211.0011 [astro-ph.CO] (cit. on p. 38).

[113] Joel Heinrich. “Coverage of error bars for Poisson data”. In: **CDF Public Note** 6438 (May 2003), pp. 1–30 (cit. on p. 128).

[114] H. Hetznecker and A. Burkert. “The evolution of the dark halo spin parameters λ and λ’ in a ΛCDM universe: the role of minor and major mergers”. In: MNRAS 370 (Aug. 2006), pp. 1905–1914. DOI: 10.1111/j.1365-2966.2006.10616.x. eprint: astro-ph/0505249 (cit. on p. 179).

[115] W. Hillebrandt et al. “Towards an understanding of Type Ia supernovae from a synthesis of theory and observations”. In: **Frontiers of Physics** 8 (Apr. 2013), pp. 116–143. DOI: 10.1007/s11467-013-0303-2. arXiv: 1302.6420 [astro-ph.CO] (cit. on p. 32).

[116] K. Hinterbichler and J. Khoury. “Screening Long-Range Forces through Local Symmetry Restoration”. In: **Physical Review Letters** 104.23, 231301 (June 2010), p. 231301. DOI: 10.1103/PhysRevLett.104.231301. arXiv: 1001.4525 [hep-th] (cit. on pp. 42, 49).

[117] K. Hinterbichler et al. “Symmetron cosmology”. In: Phys. Rev. D 84.10, 103521 (Nov. 2011), p. 103521. DOI: 10.1103/PhysRevD.84.103521. arXiv: 1107.2112 [astro-ph.CO] (cit. on pp. 42, 49, 50).

[118] M. P. Hobson, G. P. Efstathiou, and A. N. Lasenby. **General Relativity: an Introduction for Physicists**. Cambridge University Press, 2006. DOI: 10.2277/0521829518 (cit. on pp. 1, 3–6, 16, 43, 198, 200).

[119] D. W. Hogg, J. Bovy, and D. Lang. "Data analysis recipes: Fitting a model to data". In: **ArXiv e-prints** (Aug. 2010). arXiv: 1008.4686 [astro-ph.IM] (cit. on p. 138).

[120] David W Hogg. "Distance measures in cosmology". In: **arxiv:astro-ph/9905116v4** (2000). eprint: arXiv:astro-ph/9905116. URL: http://lanl.arxiv.org/abs/astro-ph/9905116v4 (cit. on pp. 27, 32).

[121] Alireza Hojjati et al. "Practical solutions for perturbed f(R) gravity". In: **Phys.Rev.** D86 (2012), p. 123503. DOI: 10.1103/PhysRevD.86.123503. arXiv: 1210.6880 [astro-ph.CO] (cit. on pp. 34, 79, 92).

[122] W. Hu. "Structure Formation with Generalized Dark Matter". In: **Astrophys.J.** 506 (Oct. 1998), pp. 485–494. DOI: 10.1086/306274. eprint: arXiv:astro-ph/9801234 (cit. on p. 57).

[123] Wayne Hu and Ignacy Sawicki. "A Parameterized Post-Friedmann Framework for Modified Gravity". In: **Phys.Rev.** D76 (2007), p. 104043. DOI: 10.1103/PhysRevD.76.104043. arXiv: 0708.1190 [astro-ph] (cit. on pp. 47, 48).

[124] Wayne Hu and Ignacy Sawicki. "Models of f(R) Cosmic Acceleration that Evade Solar-System Tests". In: **Phys.Rev.** D76 (2007), p. 064004. DOI: 10.1103/PhysRevD.76.064004. arXiv: 0705.1158 [astro-ph] (cit. on pp. 34, 42, 47, 64, 65, 79, 81).

[125] A. Jenkins et al. "The mass function of dark matter haloes". In: MNRAS 321 (Feb. 2001), pp. 372–384. DOI: 10.1046/j.1365-8711.2001.04029.x. eprint: astro-ph/0005260 (cit. on pp. 108, 109, 112, 127, 146, 150, 151, 155).

[126] Elise Jennings et al. "Redshift space distortions in f(R) gravity". In: **Mon. Not. Roy. Astron. Soc.** 425 (2012), pp. 2128–2143. DOI: 10.1111/j.1365-2966.2012.21567.x. arXiv: 1205.2698 [astro-ph.CO] (cit. on p. 33).

[127] A. Joyce, L. Lombriser, and F. Schmidt. "Dark Energy Versus Modified Gravity". In: **Annual Review of Nuclear and Particle Science** 66 (Oct. 2016), pp. 95–122. DOI: 10.1146/annurev-nucl-102115-044553. arXiv: 1601.06133 (cit. on pp. 14, 25, 26).

[128] Austin Joyce et al. "Beyond the Cosmological Standard Model". In: **Phys. Rept.** 568 (2015), pp. 1–98. DOI: 10.1016/j.physrep.2014.12.002. arXiv: 1407.0059 [astro-ph.CO] (cit. on p. 42).

[129] E. Juan et al. "Halo mass definition and multiplicity function". In: MNRAS 439 (Apr. 2014), pp. 3156–3167. DOI: 10.1093/mnras/stu187. arXiv: 1401.7334 [astro-ph.CO] (cit. on p. 122).

[130] N. Kaiser. "Clustering in real space and in redshift space". In: MNRAS 227 (July 1987), pp. 1–21. DOI: 10.1093/mnras/227.1.1 (cit. on p. 20).

[131] J. Khoury. "Theories of Dark Energy with Screening Mechanisms". In: **ArXiv e-prints** (Nov. 2010). arXiv: 1011.5909 [astro-ph.CO] (cit. on p. 47).

[132] J. Khoury and A. Weltman. "Chameleon cosmology". In: Phys. Rev. D 69.4, 044026 (Feb. 2004), p. 044026. DOI: 10.1103/PhysRevD.69.044026 (cit. on p. 162).

[133] Justin Khoury. "Theories of dark energy with screening mechanisms". In: **arXiv e-prints** (2010). eprint: arXiv:1011.5909 (cit. on p. 162).

[134] Justin Khoury and Amanda Weltman. "Chameleon cosmology". In: **Phys.Rev.** D69 (2004), p. 044026. DOI: 10.1103/PhysRevD.69.044026. arXiv: astro-ph/0309411 [astro-ph] (cit. on pp. 33, 46, 64, 78).

[135] Justin Khoury and Amanda Weltman. "Chameleon cosmology". In: **Phys. Rev.** D69 (2004), p. 044026. DOI: 10.1103/PhysRevD.69.044026. arXiv: astro-ph/0309411 [astro-ph] (cit. on p. 42).

[136] Justin Khoury and Mark Wyman. "N-Body Simulations of DGP and Degravitation Theories". In: **Phys. Rev.** D80 (2009), p. 064023. DOI: 10.1103/PhysRevD.80.064023. arXiv: 0903.1292 [astro-ph.CO] (cit. on p. 33).

[137] Juhan Kim et al. "The New Horizon Run Cosmological N-Body Simulations". In: **J. Korean Astron. Soc.** 44 (2011), pp. 217–234. DOI: 10.5303/JKAS.2011.44.6.217. arXiv: 1112.1754 [astro-ph.CO] (cit. on p. 35).

[138] T. D. Kitching et al. "3D cosmic shear: cosmology from CFHTLenS". In: MNRAS 442 (Aug. 2014), pp. 1326–1349. DOI: 10.1093/mnras/stu934. arXiv: 1401.6842 (cit. on p. 20).

[139] A. Klypin, S. Trujillo-Gomez, and J. Primack. "Halos and galaxies in the standard cosmological model: results from the Bolshoi simulation". In: **Astrophys. J.** 740 (2011), p. 102. DOI: 10.1088/0004-637X/740/2/102. arXiv: 1002.3660 [astro-ph.CO] (cit. on p. 35).

[140] A. Knebe et al. "Haloes gone MAD: The Halo-Finder Comparison Project". In: MNRAS 415 (Aug. 2011), pp. 2293–2318. DOI: 10.1111/j.1365-2966.2011.18858.x. arXiv: 1104.0949 (cit. on pp. 36, 126, 151).

[141] Alexander Knebe et al. "Structure finding in cosmological simulations: the state of affairs". In: **Monthly Notices of the Royal Astronomical Society** 435.2 (2013), p. 1618. DOI: 10.1093/mnras/stt1403. eprint: /oup/backfile/content_public/journal/mnras/435/2/10.1093/mnras/stt1403/2/stt1403.pdf. URL: +http://dx.doi.org/10.1093/mnras/stt1403 (cit. on p. 36).

[142] K. H. Knuth. "Optimal Data-Based Binning for Histograms". In: **ArXiv Physics e-prints** (May 2006). eprint: physics/0605197 (cit. on p. 127).

[143] Michael Kopp et al. "Spherical collapse and halo mass function in $f(R)$ theories". In: **Phys.Rev.** D88.8 (2013), p. 084015. DOI: 10.1103/PhysRevD.88.084015. arXiv: 1306.3233 [astro-ph.CO] (cit. on pp. 96, 122, 163).

[144] K. Koyama. "Cosmological Tests of Gravity". In: **arXiv e-prints** (Apr. 2015). arXiv: 1504.04623 (cit. on p. 162).

[145] Kazuya Koyama and Fabio P Silva. "Nonlinear interactions in a cosmological background in the Dvali-Gabadadze-Porrati braneworld". In: **Phys. Rev. D** 75 (8 Apr. 2007), p. 084040. DOI: 10.1103/PhysRevD.75.084040. URL: https://link.aps.org/doi/10.1103/PhysRevD.75.084040 (cit. on p. 51).

[146] Kazuya Koyama, Atsushi Taruya, and Takashi Hiramatsu. "Non-linear Evolution of Matter Power Spectrum in Modified Theory of Gravity". In: **Phys. Rev.** D79 (2009), p. 123512. DOI: 10.1103/PhysRevD.79.123512. arXiv: 0902.0618 [astro-ph.CO] (cit. on p. 33).

[147] Michael Kuhlen, Mark Vogelsberger, and Raul Angulo. "Numerical simulations of the dark universe: State of the art and the next decade". In: **Physics of the Dark Universe** 1.1-2 (Nov. 2012), pp. 50–93. DOI: 10.1016/j.dark.2012.10.002. URL: https://doi.org/10.1016/j.dark.2012.10.002 (cit. on pp. 35, 36).

[148] C. Lacey and S. Cole. "Merger rates in hierarchical models of galaxy formation". In: **Mon.Not.Roy.Astron.Soc.** 262 (June 1993), pp. 627–649 (cit. on p. 98).

[149] T. Y. Lam and B. Li. "Excursion set theory for modified gravity: correlated steps, mass functions and halo bias". In: MNRAS 426 (Nov. 2012), pp. 3260–3270. DOI: 10.1111/j.1365-2966.2012.21746.x. arXiv: 1205.0059 [astro-ph.CO] (cit. on p. 105).

[150] Tsz Yan Lam et al. "Testing Gravity with the Stacked Phase Space around Galaxy Clusters". In: **Phys. Rev. Lett.** 109 (2012), p. 051301. DOI: 10.1103/PhysRevLett.109.051301. arXiv: 1202.4501 [astro-ph.CO] (cit. on p. 33).

[151] D. Langlois and K. Noui. "Degenerate higher derivative theories beyond Horndeski: evading the Ostrogradski instability". In: J. Cosmology Astropart. Phys. 2, 034 (Feb. 2016), p. 034. DOI: 10.1088/1475-7516/2016/02/034. arXiv: 1510.06930 [gr-qc] (cit. on pp. 9, 11).

[152] Istvan Laszlo and Rachel Bean. "Nonlinear growth in modified gravity theories of dark energy". In: **Phys. Rev.** D77 (2008), p. 024048. DOI: 10.1103/PhysRevD.77.024048. arXiv: 0709.0307 [astro-ph] (cit. on p. 33).

[153] J. Lee et al. "Modified Gravity Spins up Galactic Halos". In: ApJ 763, 28 (Jan. 2013), p. 28. DOI: 10.1088/0004-637X/763/1/28. arXiv: 1204.6608 (cit. on p. 179).

[154] A. Lewis and A. Challinor. "Weak gravitational lensing of the CMB". In: Phys. Rep. 429 (June 2006), pp. 1–65. DOI: 10.1016/j.physrep.2006.03.002. eprint: astro-ph/0601594 (cit. on p. 20).

[155] B. Li and G. Efstathiou. "An extended excursion set approach to structure formation in chameleon models". In: **Mon.Not.Roy.Astron.Soc.** 421 (Apr.

2012), pp. 1431–1442. DOI: 10.1111/j.1365-2966.2011.20404.x. arXiv: 1110.6440 [astro-ph.CO] (cit. on pp. 96, 100, 108, 117, 163).

[156] B. Li and T. Y. Lam. "Excursion set theory for modified gravity: Eulerian versus Lagrangian environments". In: MNRAS 425 (Sept. 2012), pp. 730–739. DOI: 10.1111/j.1365-2966.2012.21592.x. arXiv: 1205.0058 [astro-ph.CO] (cit. on pp. 100, 102, 105, 111, 117).

[157] B. Li et al. "ECOSMOG: an Efficient COde for Simulating MOdified Gravity". In: J. Cosmology Astropart. Phys. 1, 051 (Jan. 2012), p. 051. DOI: 10.1088/1475-7516/2012/01/051. arXiv: 1110.1379 [astro-ph.CO] (cit. on pp. 123, 124).

[158] Baojiu Li et al. "ECOSMOG: An Efficient Code for Simulating Modified Gravity". In: **JCAP** 1201 (2012), p. 051. DOI: 10.1088/1475-7516/2012/01/051. arXiv: 1110.1379 [astro-ph.CO] (cit. on p. 33).

[159] Baojiu Li et al. "ECOSMOG: An Efficient Code for Simulating Modified Gravity". In: **JCAP** 1201 (2012), p. 051. DOI: 10.1088/1475-7516/2012/01/051. arXiv: 1110.1379 [astro-ph.CO] (cit. on p. 36).

[160] Baojiu Li et al. "Simulating the quartic Galileon gravity model on adaptively refined meshes". In: **JCAP** 1311 (2013), p. 012. DOI: 10.1088/1475-7516/2013/11/012. arXiv: 1308.3491 [astro-ph.CO] (cit. on pp. 33, 92).

[161] Y. Li and W. Hu. "Chameleon halo modeling in f(R) gravity". In: Phys. Rev. D 84.8, 084033 (Oct. 2011), p. 084033. DOI: 10.1103/PhysRevD.84.084033. arXiv: 1107.5120 (cit. on p. 122).

[162] E. V. Linder. "Cosmological tests of generalized Friedmann models". In: **aap** 206 (Nov. 1988), pp. 175–189 (cit. on p. 32).

[163] E. V. Linder. "Light propagation in generalized Friedmann universes". In: **aap** 206 (Nov. 1988), pp. 190–198 (cit. on p. 32).

[164] C. Llinares and D. F. Mota. "Releasing Scalar Fields: Cosmological Simulations of Scalar-Tensor Theories for Gravity Beyond the Static Approximation". In: **Physical Review Letters** 110.16, 161101 (Apr. 2013), p. 161101. DOI: 10.1103/PhysRevLett.110.161101. arXiv: 1302.1774 (cit. on p. 124).

[165] C. Llinares, D. F. Mota, and H. A. Winther. "ISIS: a new N-body cosmological code with scalar fields based on RAMSES. Code presentation and application to the shapes of clusters". In: A&A 562, A78 (Feb. 2014), A78. DOI: 10.1051/0004-6361/201322412. arXiv: 1307.6748 (cit. on pp. 36, 52, 123, 124, 164, 176, 178).

[166] Claudio Llinares and David Mota. "Releasing scalar fields: cosmological simulations of scalar-tensor theories for gravity beyond the static approximation". In: (2013). arXiv: 1302.1774 [astro-ph.CO] (cit. on pp. 34, 64, 70, 92).

[167] Claudio Llinares, David F. Mota, and Hans A. Winther. "ISIS: a new N-body cosmological code with scalar fields based on RAMSES. Code presentation and application to the shapes of clusters". In: **Astron. Astrophys.** 562 (2014), A78.

DOI: 10.1051/0004-6361/201322412. arXiv: 1307.6748 [astro-ph.CO] (cit. on p. 33).

[168] L. Lombriser et al. "Chameleon f(R) gravity in the virialized cluster". In: Phys. Rev. D 85.12, 124054 (June 2012), p. 124054. DOI: 10.1103/PhysRevD.85.124054. arXiv: 1203.5125 [astro-ph.CO] (cit. on p. 180).

[169] Lucas Lombriser et al. "Cosmological Constraints on DGP Braneworld Gravity with Brane Tension". In: **Phys. Rev.** D80 (2009), p. 063536. DOI: 10.1103/PhysRevD.80.063536. arXiv: 0905.1112 [astro-ph.CO] (cit. on p. 52).

[170] Lucas Lombriser et al. "Modeling halo mass functions in chameleon f(R) gravity". In: **Phys.Rev.** D87.12 (2013), p. 123511. DOI: 10.1103/PhysRevD.87.123511. arXiv: 1304.6395 [astro-ph.CO] (cit. on pp. 33, 48, 97, 102, 116, 117, 122, 163, 167, 169, 176).

[171] David Lovelock. "The Einstein Tensor and Its Generalizations". In: **Journal of Mathematical Physics** 12.3 (Mar. 1971), pp. 498–501. DOI: 10.1063/1.1665613. URL: https://doi.org/10.1063/1.1665613 (cit. on p. 7).

[172] David Lovelock. "The Four-Dimensionality of Space and the Einstein Tensor". In: **Journal of Mathematical Physics** 13.6 (June 1972), pp. 874–876. DOI: 10.1063/1.1666069. URL: https://doi.org/10.1063/1.1666069 (cit. on p. 7).

[173] Z. Lukić et al. "The Halo Mass Function: High-Redshift Evolution and Universality". In: ApJ 671 (Dec. 2007), pp. 1160–1181. DOI: 10.1086/523083. eprint: astro-ph/0702360 (cit. on pp. 122, 126, 128).

[174] Chung-Pei Ma and Edmund Bertschinger. "Cosmological perturbation theory in the synchronous and conformal Newtonian gauges". In: **Astrophys.J.** 455 (1995), pp. 7–25. DOI: 10.1086/176550. arXiv: astro-ph/9506072 [astro-ph] (cit. on p. 59).

[175] Chung-Pei Ma and Edmund Bertschinger. "Cosmological perturbation theory in the synchronous versus conformal Newtonian gauge". In: **Astrophys. J.** (1994). arXiv: astro-ph/9401007 [astro-ph] (cit. on p. 58).

[176] E. Macaulay, I. K. Wehus, and H. K. Eriksen. "Lower Growth Rate from Recent Redshift Space Distortion Measurements than Expected from Planck". In: **Physical Review Letters** 111.16, 161301 (Oct. 2013), p. 161301. DOI: 10.1103/PhysRevLett.111.161301. arXiv: 1303.6583 (cit. on p. 20).

[177] S. J. Maddox et al. "Galaxy correlations on large scales". In: MNRAS 242 (Jan. 1990), 43P–47P. DOI: 10.1093/mnras/242.1.43P (cit. on p. 36).

[178] Michele Maggiore and Antonio Riotto. "The Halo mass function from excursion set theory. III. Non-Gaussian fluctuations". In: **Astrophys. J.** 717 (2010), pp. 526–541. DOI: 10.1088/0004-637X/717/1/526. arXiv: 0903.1251 [astro-ph.CO] (cit. on p. 108).

[179] Guido Magnano and Leszek M. Sokolowski. "On physical equivalence between nonlinear gravity theories and a general relativistic selfgravitating scalar field". In: **Phys. Rev.** D50 (1994), pp. 5039–5059. DOI: 10.1103/PhysRevD.50.5039. arXiv: gr-qc/9312008 [gr-qc] (cit. on p. 46).

[180] Karim A. Malik and David Wands. "Cosmological perturbations". In: **Phys.Rept.** 475 (2009), pp. 1–51. DOI: 10.1016/j.physrep.2009.03.001. arXiv: 0809.4944 [astro-ph] (cit. on p. 17).

[181] D. J. E. Marsh and P. G. Ferreira. "Ultralight scalar fields and the growth of structure in the Universe". In: **Phys.Rev.** D82.10, 103528 (Nov. 2010), p. 103528. DOI: 10.1103/PhysRevD.82.103528. arXiv: 1009.3501 [hep-ph] (cit. on p. 57).

[182] David J. E. Marsh et al. "Tensor Interpretation of BICEP2 Results Severely Constrains Axion Dark Matter". In: **Phys. Rev. Lett.** 113.1 (2014), p. 011801. DOI: 10.1103/PhysRevLett.113.011801. arXiv: 1403.4216 [astro-ph.CO] (cit. on p. 57).

[183] S. G. Murray, C. Power, and A. S. G. Robotham. "HMFcalc: An online tool for calculating dark matter halo mass functions". In: **Astronomy and Computing** 3 (Nov. 2013), pp. 23–34. DOI: 10.1016/j.ascom.2013.11.001. arXiv: 1306.6721 [astro-ph.CO] (cit. on pp. 121, 126).

[184] M. Musso and R. K. Sheth. "On the Markovian assumption in the excursion set approach: the approximation of Markovian Velocities". In: MNRAS 443 (Sept. 2014), pp. 1601–1613. DOI: 10.1093/mnras/stu1222. arXiv: 1401.8177 (cit. on p. 171).

[185] J. F. Navarro, C. S. Frenk, and S. D. M. White. "A Universal Density Profile from Hierarchical Clustering". In: ApJ 490 (Dec. 1997), p. 493. DOI: 10.1086/304888. eprint: arXiv:astro-ph/9611107 (cit. on p. 19).

[186] J. F. Navarro, C. S. Frenk, and S. D. M. White. "The Structure of Cold Dark Matter Halos". In: ApJ 462 (May 1996), p. 563. DOI: 10.1086/177173. eprint: arXiv:astro-ph/9508025 (cit. on p. 19).

[187] Alberto Nicolis, Riccardo Rattazzi, and Enrico Trincherini. "The Galileon as a local modification of gravity". In: **Phys. Rev.** D79 (2009), p. 064036. DOI: 10.1103/PhysRevD.79.064036. arXiv: 0811.2197 [hep-th] (cit. on p. 33).

[188] Johannes Noller. "Derivative Chameleons". In: **JCAP** 1207 (2012), p. 013. DOI: 10.1088/1475-7516/2012/07/013. arXiv: 1203.6639 [gr-qc] (cit. on pp. 44, 52).

[189] Johannes Noller, Francesca von Braun-Bates, and Pedro G. Ferreira. "Relativistic scalar fields and the quasi-static approximation in theories of modified gravity". In: **Phys.Rev.** D89 (2014), p. 023521. DOI: 10.1103/PhysRevD.89.023521. arXiv: 1310.3266 [astro-ph.CO] (cit. on pp. 5, 47, 54).

[190] Hiroaki Oyaizu. "Non-linear evolution of f(R) cosmologies I: methodology". In: **Phys. Rev.** D78 (2008), p. 123523. DOI: 10.1103/PhysRevD.78.123523. arXiv: 0807.2449 [astro-ph] (cit. on pp. 33, 57).

[191] Lyman A. Page. "Maps of the cosmos: The Cosmic microwave background". In: (2004). [IAU Symp.216,3(2005)]. arXiv: astro-ph/0402547 [astro-ph] (cit. on p. 25).

[192] K. Parfrey, L. Hui, and R. K. Sheth. "Scale-dependent halo bias from scale-dependent growth". In: Phys. Rev. D 83.6, 063511 (Mar. 2011), p. 063511. DOI: 10.1103/PhysRevD.83.063511. arXiv: 1012.1335 [astro-ph.CO] (cit. on pp. 100, 111, 168, 169).

[193] J. A. Peacock. "Testing anthropic predictions for Λ and the cosmic microwave background temperature". In: MNRAS 379 (Aug. 2007), pp. 1067–1074. DOI: 10.1111/j.1365-2966.2007.11978.x. arXiv: 0705.0898 (cit. on pp. 109, 112, 147, 150, 156, 163).

[194] J. A. Peacock and A. F. Heavens. "Alternatives to the Press-Schechter cosmological mass function". In: **MNRAS** 243 (Mar. 1990), pp. 133–143 (cit. on p. 171).

[195] P. J. E. Peebles. "Tests of cosmological models constrained by inflation". In: ApJ 284 (Sept. 1984), pp. 439–444. DOI: 10.1086/162425 (cit. on p. 21).

[196] S. Perlmutter et al. "Measurements of Ω and Λ from 42 High-Redshift Supernovae". In: ApJ 517 (June 1999), pp. 565–586. DOI: 10.1086/307221. eprint: astro-ph/9812133 (cit. on pp. 21, 31, 162).

[197] F. Perrotta and C. Baccigalupi. "Early time perturbations behavior in scalar field cosmologies". In: **Phys.Rev.** D59.12, 123508 (June 1999), p. 123508. DOI: 10.1103/PhysRevD.59.123508. eprint: arXiv:astro-ph/9811156 (cit. on p. 57).

[198] A. Pezzotta et al. "The VIMOS Public Extragalactic Redshift Survey (VIPERS): The growth of structures at $0.5 < z < 1.2$ from redshift-space distortions in the clustering of the PDR-2 final sample". In: (2016). arXiv: 1612.05645 [astro-ph.CO] (cit. on pp. 27, 28).

[199] M. Pietroni. "Dark energy condensation". In: Phys. Rev. D 72.4, 043535 (Aug. 2005), p. 043535. DOI: 10.1103/PhysRevD.72.043535. eprint: astro-ph/0505615 (cit. on p. 49).

[200] Planck Collaboration et al. "Planck 2015 results. XIII. Cosmological parameters". In: A&A 594, A13 (Sept. 2016), A13. DOI: 10.1051/0004-6361/201525830. arXiv: 1502.01589 (cit. on pp. 16, 20, 21, 24, 31, 121).

[201] Francisco Prada et al. "Halo concentrations in the standard LCDM cosmology". In: **Mon. Not. Roy. Astron. Soc.** 423 (2012), pp. 3018–3030. DOI: 10.1111/j.1365-2966.2012.21007.x. arXiv: 1104.5130 [astro-ph.CO] (cit. on p. 35).

[202] W. H. Press and P. Schechter. “Formation of Galaxies and Clusters of Galaxies by Self-Similar Gravitational Condensation”. In: ApJ 187 (Feb. 1974), pp. 425–438. DOI: 10.1086/152650 (cit. on pp. 19, 99, 112, 121, 150).

[203] Ewald Puchwein, Marco Baldi, and Volker Springel. “Modified Gravity-GADGET: A new code for cosmological hydrodynamical simulations of modified gravity models”. In: (2013). arXiv: 1305.2418 [astro-ph.CO] (cit. on p. 36).

[204] Ewald Puchwein, Marco Baldi, and Volker Springel. “Modified Gravity-GADGET: A new code for cosmological hydrodynamical simulations of modified gravity models”. In: **Mon. Not. Roy. Astron. Soc.** 436 (2013), p. 348. DOI: 10.1093/mnras/stt1575. arXiv: 1305.2418 [astro-ph.CO] (cit. on p. 33).

[205] Israel Quiros et al. “The conformal transformation’s controversy: what are we missing?” In: **Gen.Rel.Grav.** 45 (2013), pp. 489–518. DOI: 10.1007/s10714-012-1484-7. arXiv: 1108.5857 [gr-qc] (cit. on p. 43).

[206] D. Reed et al. “Evolution of the mass function of dark matter haloes”. In: MNRAS 346 (Dec. 2003), pp. 565–572. DOI: 10.1046/j.1365-2966.2003.07113.x. eprint: astro-ph/0301270 (cit. on pp. 109, 122, 140, 151).

[207] D. S. Reed et al. “The halo mass function from the dark ages through the present day”. In: MNRAS 374 (Jan. 2007), pp. 2–15. DOI: 10.1111/j.1365-2966.2006.11204.x. eprint: astro-ph/0607150 (cit. on pp. 109, 112, 122, 140).

[208] B. A. Reid et al. “Cosmological constraints from the clustering of the Sloan Digital Sky Survey DR7 luminous red galaxies”. In: MNRAS 404 (May 2010), pp. 60–85. DOI: 10.1111/j.1365-2966.2010.16276.x. arXiv: 0907.1659 [astro-ph.CO] (cit. on pp. 20, 22).

[209] Jürgen Renn and John Stachel. “Hilbert’s foundation of physics : from a theory of everything to a constituent of general relativity”. eng. In: **The genesis of general relativity. Vol. 4 : Gravitation in the twilight of classical physics: the promise of mathematics**. Ed. by Jürgen Renn and Matthias Schemmel. Dordrecht: Springer, 2007, pp. 857–9973 (cit. on p. 198).

[210] A. G. Riess et al. “Observational Evidence from Supernovae for an Accelerating Universe and a Cosmological Constant”. In: AJ 116 (Sept. 1998), pp. 1009–1038. DOI: 10.1086/300499. eprint: astro-ph/9805201 (cit. on pp. 20, 21, 31, 162).

[211] Tilman Sauer and Ulrich Majer, eds. **David Hilbert's Lectures on the Foundations of Physics 1915-1927**. Springer Berlin Heidelberg, 2009. DOI: 10.1007/b12915. URL: https://doi.org/10.1007/b12915 (cit. on p. 197).

[212] David Schlegel, Martin White, and Daniel Eisenstein. “The Baryon Oscillation Spectroscopic Survey: Precision measurements of the absolute cosmic distance scale”. In: (2009). arXiv: 0902.4680 [astro-ph.CO] (cit. on pp. 21, 22).

[213] David J. Schlegel et al. “BigBOSS: The Ground-Based Stage IV Dark Energy Experiment”. In: (2009). arXiv: 0904.0468 [astro-ph.CO] (cit. on pp. 21, 22).

[214] F. Schmidt. "Dynamical masses in modified gravity". In: Phys. Rev. D 81.10, 103002 (May 2010), p. 103002. DOI: 10.1103/PhysRevD.81.103002. arXiv: 1003.0409 [astro-ph.CO] (cit. on p. 162).

[215] F. Schmidt, W. Hu, and M. Lima. "Spherical collapse and the halo model in braneworld gravity". In: Phys. Rev. D 81.6, 063005 (Mar. 2010), p. 063005. DOI: 10.1103/PhysRevD.81.063005. arXiv: 0911.5178 [astro-ph.CO] (cit. on pp. 97, 122).

[216] Fabian Schmidt. "Dynamical Masses in Modified Gravity". In: **Phys. Rev.** D81 (2010), p. 103002. DOI: 10.1103/PhysRevD.81.103002. arXiv: 1003.0409 [astro-ph.CO] (cit. on p. 33).

[217] Fabian Schmidt. "Self-Consistent Cosmological Simulations of DGP Braneworld Gravity". In: **Phys. Rev.** D80 (2009), p. 043001. DOI: 10.1103/PhysRevD.80.043001. arXiv: 0905.0858 [astro-ph.CO] (cit. on p. 33).

[218] Fabian Schmidt, Wayne Hu, and Marcos Lima. "Spherical Collapse and the Halo Model in Braneworld Gravity". In: **Phys. Rev.** D81 (2010), p. 063005. DOI: 10.1103/PhysRevD.81.063005. arXiv: 0911.5178 [astro-ph.CO] (cit. on p. 33).

[219] Aurel Schneider et al. "Matter power spectrum and the challenge of percent accuracy". In: **JCAP** 1604.04 (2016), p. 047. DOI: 10.1088/1475-7516/2016/04/047. arXiv: 1503.05920 [astro-ph.CO] (cit. on pp. 36, 38).

[220] Peter Schneider, Jürgen Ehlers, and Emilio E. Falco. **Gravitational Lenses**. Springer Berlin Heidelberg, 1992. DOI: 10.1007/978-3-662-03758-4. URL: https://doi.org/10.1007/978-3-662-03758-4 (cit. on pp. 29, 30).

[221] D. J. Schwarz. "Thoughts on the Cosmological Principle". In: **Fundamental Interactions: A Memorial Volume for Wolfgang Kummer. Edited by GRUMILLER DANIEL ET AL. Published by World Scientific Publishing Co. Pte. Ltd., 2010. ISBN #9789814277839, pp. 267-276**. Ed. by D. Grumiller and et al. World Scientific Publishing Co, 2010, pp. 267–276. DOI: 10.1142/9789814277839_0015 (cit. on p. 15).

[222] D. W. Scott. "On optimal and data-based histograms". In: **Biometrika** (1979), pp. 605–610 (cit. on p. 127).

[223] R.U. Sexl and H.K. Urbantke. **Gravitation und Kosmologie: Eine Einführung in die Allgemeine Relativitätstheorie**. 5th ed. B.I.-Wissenschaftsverlag, 1975 (cit. on pp. 6, 16, 43, 200).

[224] R. K. Sheth, H. J. Mo, and G. Tormen. "Ellipsoidal collapse and an improved model for the number and spatial distribution of dark matter haloes". In: MNRAS 323 (May 2001), pp. 1–12. DOI: 10.1046/j.1365-8711.2001.04006.x. eprint: astro-ph/9907024 (cit. on pp. 108, 109).

[225] Ravi K. Sheth and Giuseppe Tormen. "An Excursion set model of hierarchical clustering : Ellipsoidal collapse and the moving barrier". In: **Mon.Not.Roy.Astron.Soc.**

329 (2002), p. 61. DOI: 10.1046/j.1365-8711.2002.04950.x. arXiv: astro-ph/0105113 [astro-ph] (cit. on pp. 108, 109, 112, 150, 153).

[226] Alessandra Silvestri, Levon Pogosian, and Roman V. Buniy. "A practical approach to cosmological perturbations in modified gravity". In: (2013). DOI: 10.1103/PhysRevD.87.104015. arXiv: 1302.1193 [astro-ph.CO] (cit. on pp. 33, 34, 64, 92).

[227] S. A. Sim et al. "Synthetic light curves and spectra for three-dimensional delayed-detonation models of Type Ia supernovae". In: MNRAS 436 (Nov. 2013), pp. 333–347. DOI: 10.1093/mnras/stt1574. arXiv: 1308.4833 [astro-ph.HE] (cit. on p. 32).

[228] Fergus Simpson et al. "CFHTLenS: Testing the Laws of Gravity with Tomographic Weak Lensing and Redshift Space Distortions". In: **Mon. Not. Roy. Astron. Soc.** 429 (2013), p. 2249. DOI: 10.1093/mnras/sts493. arXiv: 1212.3339 [astro-ph.CO] (cit. on p. 25).

[229] Volker Springel. "The Cosmological simulation code GADGET-2". In: **Mon. Not. Roy. Astron. Soc.** 364 (2005), pp. 1105–1134. DOI: 10.1111/j.1365-2966.2005.09655.x. arXiv: astro-ph/0505010 [astro-ph] (cit. on p. 35).

[230] Volker Springel et al. "The Aquarius Project: the subhalos of galactic halos". In: **Mon. Not. Roy. Astron. Soc.** 391 (2008), pp. 1685–1711. DOI: 10.1111/j.1365-2966.2008.14066.x. arXiv: 0809.0898 [astro-ph] (cit. on p. 35).

[231] A. Stabile, An. Stabile, and S. Capozziello. "Conformal Transformations and Weak Field Limit of Scalar-Tensor Gravity". In: (2013). arXiv: 1310.7097 [gr-qc] (cit. on p. 43).

[232] Joachim Stadel et al. "Quantifying the heart of darkness with GHALO - a multi-billion particle simulation of our galactic halo". In: **Mon. Not. Roy. Astron. Soc.** 398 (2009), pp. L21–L25. DOI: 10.1111/j.1745-3933.2009.00699.x. arXiv: 0808.2981 [astro-ph] (cit. on p. 35).

[233] N. Suzuki et al. "The Hubble Space Telescope Cluster Supernova Survey. V. Improving the Dark-energy Constraints above $z > 1$ and Building an Early-type-hosted Supernova Sample". In: ApJ 746, 85 (Feb. 2012), p. 85. DOI: 10.1088/0004-637X/746/1/85. arXiv: 1105.3470 [astro-ph.CO] (cit. on p. 20).

[234] L. Taddei, R. Catena, and M. Pietroni. "Spherical collapse and halo mass function in the symmetron model". In: Phys. Rev. D 89.2, 023523 (Jan. 2014), p. 023523. DOI: 10.1103/PhysRevD.89.023523. arXiv: 1310.6175 (cit. on pp. 47, 49, 97, 122).

[235] I. Tereno, E. Semboloni, and T. Schrabback. "COSMOS weak-lensing constraints on modified gravity". In: A&A 530, A68 (June 2011), A68. DOI: 10.1051/0004-6361/201016273. arXiv: 1012.5854 [astro-ph.CO] (cit. on p. 31).

[236] R. Teyssier. "Cosmological hydrodynamics with adaptive mesh refinement. A new high resolution code called RAMSES". In: A&A 385 (Apr. 2002), pp. 337–

364. DOI: 10.1051/0004-6361:20011817. eprint: astro-ph/0111367 (cit. on pp. 123, 164).

[237] Romain Teyssier et al. "Full-Sky Weak Lensing Simulation with 70 Billion Particles". In: **Astron. Astrophys.** 497 (2009), p. 335. DOI: 10.1051/0004-6361/200810657. arXiv: 0807.3651 [astro-ph] (cit. on p. 35).

[238] Mark Thompson. **Graduate Lectures on Statistics**. 2009. URL: http://www.hep.phy.cam.ac.uk/~thomson/lectures/lectures.html (cit. on p. 128).

[239] J. Tinker et al. "Toward a Halo Mass Function for Precision Cosmology: The Limits of Universality". In: ApJ 688, 709-728 (Dec. 2008), pp. 709–728. DOI: 10.1086/591439. arXiv: 0803.2706 (cit. on pp. 109, 112, 121, 122, 150).

[240] F. Tisserand. "Les travaux de Le Verrier". In: **Annales de l'Observatoire de Paris** 15 (1880), pp. 23–43 (cit. on p. 1).

[241] S. de la Torre et al. "The VIMOS Public Extragalactic Redshift Survey (VIPERS). Galaxy clustering and redshift-space distortions at z=0.8 in the first data release". In: **Astron. Astrophys.** 557 (2013), A54. DOI: 10.1051/0004-6361/201321463. arXiv: 1303.2622 [astro-ph.CO] (cit. on p. 30).

[242] S. de la Torre et al. "The VIMOS Public Extragalactic Redshift Survey (VIPERS). Gravity test from the combination of redshift-space distortions and galaxy-galaxy lensing at $0.5 < z < 1.2$". In: **Astron. Astrophys.** 608 (2017), A44. DOI: 10.1051/0004-6361/201630276. arXiv: 1612.05647 [astro-ph.CO] (cit. on p. 29).

[243] S. Tsujikawa. "Modified Gravity Models of Dark Energy". In: **Lecture Notes in Physics, Berlin Springer Verlag**. Ed. by G. Wolschin. Vol. 800. Lecture Notes in Physics, Berlin Springer Verlag. Mar. 2010, pp. 99–145. DOI: 10.1007/978-3-642-10598-2_3. arXiv: 1101.0191 [gr-qc] (cit. on p. 52).

[244] S. Tsujikawa. "Quintessence: a review". In: **Classical and Quantum Gravity** 30.21, 214003 (Nov. 2013), p. 214003. DOI: 10.1088/0264-9381/30/21/214003. arXiv: 1304.1961 [gr-qc] (cit. on pp. 53, 54).

[245] M. S. Turner, F. Wilczek, and A. Zee. "Formation of structure in an axion-dominated universe". In: **Physics Letters B** 125 (May 1983), pp. 35–40. DOI: 10.1016/0370-2693(83)91229-7 (cit. on p. 57).

[246] A.I. Vainshtein. "To the problem of nonvanishing gravitation mass". In: **Physics Letters B** 39.3 (1972), pp. 393 –394. ISSN: 0370-2693. DOI: https://doi.org/10.1016/0370-2693(72)90147-5. URL: http://www.sciencedirect.com/science/article/pii/0370269372901475 (cit. on p. 42).

[247] F. von Braun-Bates and J. Devriendt. "Universality of the halo mass function in screened gravity theories". In: **ArXiv e-prints** (Apr. 2018). arXiv: 1804.05387 (cit. on p. 5).

[248] F. von Braun-Bates et al. "The $f(R)$ halo mass function in the cosmic web". In: J. Cosmology Astropart. Phys. 3, 012 (Mar. 2017), p. 012. DOI: 10.1088/1475-7516/2017/03/012. arXiv: 1702.06817 (cit. on pp. 5, 105, 106, 109, 110, 122).

[249] Johann Georg von Soldner. "Ueber die Ablenkung eines Lichtstrals von seiner geradlinigen Bewegung, durch die Attraktion eines Weltkörpers, an welchem er nahe vorbei geht". In: **Astronomisches Jahrbuch** 180 (Feb. 1804), 161–172 (cit. on p. 1).

[250] M. P. Wand. "Data-based choice of histogram bin width (Corr: 1999V53 p174)". In: **The American Statistician** 51 (1997), pp. 59–64 (cit. on p. 127).

[251] M. S. Warren et al. "Precision Determination of the Mass Function of Dark Matter Halos". In: ApJ 646 (Aug. 2006), pp. 881–885. DOI: 10.1086/504962. eprint: astro-ph/0506395 (cit. on pp. 108, 109, 112, 122, 127, 149, 150, 158, 163).

[252] W. A. Watson et al. "The halo mass function through the cosmic ages". In: MNRAS 433 (Aug. 2013), pp. 1230–1245. DOI: 10.1093/mnras/stt791. arXiv: 1212.0095 (cit. on pp. 112, 150).

[253] S. D. M. White and M. J. Rees. "Core condensation in heavy halos - A two-stage theory for galaxy formation and clustering". In: MNRAS 183 (May 1978), pp. 341–358. DOI: 10.1093/mnras/183.3.341 (cit. on p. 19).

[254] Simon D. M. White et al. "Clusters, filaments, and voids in a universe dominated by cold dark matter". In: **The Astrophysical Journal** 313 (Feb. 1987), p. 505. DOI: 10.1086/164990. URL: https://doi.org/10.1086/164990 (cit. on p. 36).

[255] C. M. Will. "The Confrontation between General Relativity and Experiment". In: **Living Reviews in Relativity** 9, 3 (Mar. 2006), p. 3. DOI: 10.12942/lrr-2006-3. eprint: gr-qc/0510072 (cit. on pp. 3, 196).

[256] C. M. Will. "The Confrontation between General Relativity and Experiment". In: **Living Reviews in Relativity** 9 (Mar. 2006), p. 3. DOI: 10.12942/lrr-2006-3. eprint: gr-qc/0510072 (cit. on pp. 43, 162).

[257] C. M. Will. "The Confrontation between General Relativity and Experiment". In: **Living Reviews in Relativity** 17, 4 (June 2014), p. 4. DOI: 10.12942/lrr-2014-4. arXiv: 1403.7377 [gr-qc] (cit. on p. 41).

[258] H. A. Winther and P. G. Ferreira. "Fast route to nonlinear clustering statistics in modified gravity theories". In: Phys. Rev. D 91.12, 123507 (June 2015), p. 123507. DOI: 10.1103/PhysRevD.91.123507. arXiv: 1403.6492 (cit. on pp. 49, 164).

[259] H. A. Winther, D. F. Mota, and B. Li. "Environment Dependence of Dark Matter Halos in Symmetron Modified Gravity". In: ApJ 756, 166 (Sept. 2012), p. 166. DOI: 10.1088/0004-637X/756/2/166. arXiv: 1110.6438 [astro-ph.CO] (cit. on p. 162).

[260] H. A. Winther et al. “Modified gravity N-body code comparison project”. In: MNRAS 454 (Dec. 2015), pp. 4208–4234. DOI: 10.1093/mnras/stv2253. arXiv: 1506.06384 (cit. on pp. 36, 37, 52, 123, 124, 164).

[261] Andrew R. Zentner. “The Excursion Set Theory of Halo Mass Functions, Halo Clustering, and Halo Growth”. In: **Int.J.Mod.Phys.** D16 (2007), pp. 763–816. DOI: 10.1142/S0218271807010511. arXiv: astro-ph/0611454 [astro-ph] (cit. on pp. 109, 120, 122, 161, 191).

[262] Jun Zhang and Lam Hui. “On random walks with a general moving barrier”. In: **Astrophys. J.** 641 (2006), pp. 641–646. DOI: 10.1086/499802. arXiv: astro-ph/0508384 [astro-ph] (cit. on p. 100).